PROBING VARIATIONS IN THE FUNDAMENTAL CONSTANTS WITH QUASAR ABSORPTION LINES

by

Michael T. Murphy

A thesis submitted in satisfaction of

the requirements for the degree of

Doctor of Philosophy

in the Faculty of Science.

20th of December, 2002

THE UNIVERSITY OF
NEW SOUTH WALES

SYDNEY • AUSTRALIA

Statement of Originality

I hereby declare that this submission is my own work and to the best of my knowledge it contains no materials previously published or written by another person, nor material which to a substantial extent has been accepted for the award of any other degree or diploma at UNSW or any other educational institution, except where due acknowledgement is made in the thesis. Any contribution made to the research by others, with whom I have worked at UNSW or elsewhere, is explicitly acknowledged in the thesis.

I also declare that the intellectual content of this thesis is the product of my own work, except to the extent that assistance from others in the project's design and conception or in style, presentation and linguistic expression is acknowledged.

(Signed) .....

Abstract

Precision cosmology challenges many aspects of fundamental physics. In particular, quasar absorption lines test the assumed constancy of fundamental constants over cosmological time-scales and distances. Until recently, the most reliable technique was the alkali doublet (AD) method where the measured doublet separation probes variations in the fine-structure constant, $\alpha \equiv e^2/\hbar c$. However, the recently introduced many-multiplet (MM) method provides several advantages, including a demonstrated ≈10-fold precision gain. This thesis presents detailed MM analyses of 3 independent Keck/HIRES samples containing 128 absorption systems with $0.2 < z_{\rm abs} < 3.7$. We find $5.6\,\sigma$ statistical evidence for a smaller α in the absorption clouds: $\Delta\alpha/\alpha = (-0.574 \pm 0.102) \times 10^{-5}$. All three samples separately yield consistent, significant $\Delta\alpha/\alpha$. The data marginally prefer constant $\mathrm{d}\alpha/\mathrm{d}t$ rather than constant $\Delta\alpha/\alpha$. The two-point correlation function for α and the angular distribution of $\Delta\alpha/\alpha$ give no evidence for spatial variations. We also analyse 21 Keck/HIRES Si IV doublets, obtaining a 3-fold relative precision gain over previous AD studies: $\Delta\alpha/\alpha = (-0.5 \pm 1.3) \times 10^{-5}$ for $2.0 < z_{\rm abs} < 3.1$.

Our statistical evidence for varying α requires careful consideration of systematic errors. Modelling demonstrates that atmospheric dispersion is *potentially* important. However, the quasar spectra suggest a negligible effect on $\Delta\alpha/\alpha$. Cosmological variation in Mg isotopic abundances may affect $\Delta\alpha/\alpha$ at $z_{\rm abs} < 1.8$. Galactic observations and theory suggest diminished ^{25,26}Mg abundances in the low metallicity quasar absorbers. Removing ^{25,26}Mg isotopes yields *more negative* $\Delta\alpha/\alpha$ values. Overall, known systematic errors can not explain our results.

We also constrain variations in $y \equiv \alpha^2 g_p$, comparing H I 21-cm and millimetre-wave molecular absorption in 2 systems. Fitting *both* the H I and molecular lines yields the tightest, most reliable current constraints: $\Delta y/y = (-0.20 \pm 0.44) \times 10^{-5}$ and $(-0.16 \pm 0.54) \times 10^{-5}$ at $z_{\rm abs} = 0.2467$ and 0.6847 respectively. Possible line-of-sight velocity differences between the H I and molecular absorbing regions dominate these $1\,\sigma$ errors. A larger sample of mm/H I comparisons is required to reliably quantify this uncertainty and provide a potentially crucial check on the MM result.

Contents

List of Tables

List of Figures

Acknowledgments

It is a pleasure to thank my supervisor, John Webb, for such an interesting and subversive PhD project. His insight, guidance, support and good humour throughout my years at UNSW was inspiring, making him a pleasure to work with. Thanks also to Victor Flambaum, my unofficial co-supervisor, who's continued contributions, suggestions and advice were invaluable. We'll make an astrophysicist of him yet.

I am indebted to Chris Churchill, Jason Prochaska & Art Wolfe and Wallace Sargent for providing their large Keck/HIRES datasets. Without their careful and extensive observations, as well as the support of numerous co-observers and data reducers (Tom Barlow, Michael Rauch and Rob Simcoe in particular), this project would not have been possible. I also thank Francoise Combes & Tommy Wiklind for providing their millimetre-wave data and Chris Carilli for his H I spectra. I am also very grateful to Ulf Griesmann, Sveneric Johansson, Rainer Kling, the late Richard Learner, Ulf Litzén, Juliet Pickering and Anne Thorne for conducting laboratory wavelength measurements specifically for the present work and for communicating their results prior to publication.

Many thanks go to Chris Churchill, Jason Prochaska (especially), Wallace Sargent, Art Wolfe and Ray Weymann for organizing and funding my 2002 spoken-word tour of the USA. Thanks also to the Institute of Astronomy for hosting me during two extended visits to Cambridge, UK.

I thank UNSW and the Department of Education, Science and Technology for an Australian Post-graduate Award. I also gratefully acknowledge a Grant-in-Aid of Research from the National Academy of Sciences, administered by SigmaXi, the Scientific Research Society. King's College London furnished me with a generous Bicentennial Scholarship for travel to, and subsistence in, the UK. Thanks also to the Astronomical Society of Australia for smaller, but much needed, travel funds.

I am very grateful to Tom Bida and Steven Vogt who provided much detailed information about Keck/HIRES. For many lively, illuminating and sometimes pleasantly confusing discussions, many thanks go to John Barrow, Michael Bessell, Bob

Carswell, Chris Churchill, Steve Curran, Thibault Damour, Vladimir Dzuba, Rolf Engleman Jr., Alberto Fernández-Soto, John Hearnshaw, Alexander Ivanchik, Walter Johnson, Charley Lineweaver, Jochen Liske, Leon Lucy, João Magueijo, Geoff Marcy, Gillian Nave, Jason Prochaska, Massimo Stiavelli and Art Wolfe.

Warm thanks goes to the entire Department of Astrophysics at UNSW for providing a friendly and stimulating research environment. In particular, I thank Melinda Taylor, the tireless computer guru. To my fellow PhD students, past and present, especially those who had the misfortune to share an office with me, I thank you for your friendship, your patience and sympathetic nodding during my ranting monologues ... and the occasional beverage. I wish you well in your future fields of work/research. It is also a pleasure to thank Russell Standish and the Australian Partnership for Advanced Computing National Facility for numerically intensive computing access.

I especially wish to thank my good friend (and coffee dealer/pusher), Peter Reece, for all his support, encouragement, council and humour. To him and to my other close friends (especially Amanda, Christine, Katalin, Richard and Sara), thank you for making my life outside astrophysics an enjoyable one. Perhaps now I'll be able to talk about something other than my thesis! And finally, I thank my family – Mum, Dad, Jenny, Pooky, Sooty, Pandiiii (and yes, Sofie) – for their love and support throughout these busy years.

Preface

To a large extent, the content of this thesis was (or is to be) published in a series of papers as follows:

- **Murphy et al. (2001a):** *Possible evidence for a variable fine-structure constant from QSO absorption lines: motivations, analysis and results.* Chapter 3.
- **Murphy et al. (2001b):** *Possible evidence for a variable fine-structure constant from QSO absorption lines: systematic effects.* Chapter 4.
- **Murphy et al. (2001c):** *Further constraints on variation of the fine-structure constant from alkali doublet QSO absorption lines.* Chapter 2.
- **Murphy et al. (2001d):** *Improved constraints on possible variation of physical constants from H I 21-cm and molecular QSO absorption lines.* Chapter 5.
- **Murphy et al. (2003c):** *Further evidence for a variable fine-structure constant from Keck/HIRES QSO absorption spectra.* Chapters 3 & 4

Two letters (Webb et al. 2001, 2003) and several refereed conference proceedings (Murphy et al. 2002, 2003a; Webb et al. 2003) summarize the main results.

Although I have retained the use of the first person plural for this thesis, all of the work presented is my own. Throughout the text, previous work and/or contributions from other researchers are described for the sake of completeness. I have endeavored to acknowledge these instances by referring to relevant papers and by referring explicitly to the researchers involved. To further clarify this and to set my work apart, I summarize the major contributions of others below (smaller contributions are specifically acknowledged in the text):

- **Chapter 2:** All of the Keck/HIRES data analysed in this chapter were kindly provided by J. X. Prochaska and A. M. Wolfe in fully reduced, wavelength calibrated form. I performed the additional continuum fitting and corrections to

the wavelength scale (largely explained in Chapter 3). The q coefficients for the Si IV doublet transitions were calculated by V. A. Dzuba and V. V. Flambaum.

- **Chapter 3:** The description of the many-multiplet method (Section 3-1) is my own summary of the references given in that section. All of the q coefficients (Section 3-2.1) were calculated by V. A. Dzuba and V. V. Flambaum. The Keck/HIRES data (Section 3-3.1) were kindly provided in reduced form (including initial wavelength calibration) by C. W. Churchill (sample 1), J. X. Prochaska & A. M. Wolfe (sample 2) and W. L. W. Sargent (sample 3). I performed the additional continuum fitting and corrections to the wavelength scale.

- **Chapter 4:** The discussion of kinematic effects (Section 4-3) was developed in close collaboration with J. K. Webb (my PhD supervisor). The initial thorium–argon and line blending tests were first reported in a thesis for which I received an Honours degree in Physics and Astronomy at UNSW in 1998. These tests were applied to sample 1 at that time. However, the analysis presented here is substantially modified and refined and applies to all three samples (including the very large sample 3). Therefore, I present those analyses as original works here. The ZEMAX modelling of the Keck/HIRES (alluded to in Section 4-11.3), which confirmed my analytical approach, was performed in close collaboration with J. Everett.

- **Chapter 5:** All of the H I 21-cm spectra were kindly provided in reduced form by C. L. Carilli. Likewise, the molecular line spectra were provided by F. Combes and T. Wiklind. I performed all other analyses in this chapter.

Note added after examination: The referees for this thesis recommended that it be accepted without alteration. However, in this copy I have corrected small typographical and grammatical errors and updated the references and Internet addresses. Changes of greater magnitude will be recorded at http://www.ast.cam.ac.uk/~mim/pub.html as they come to light.

All is mutable.

John A. Wheeler (1980)

Chapter 1

Introduction

In this Chapter we briefly introduce the field of varying constants. We define our terms in Section 1-1, emphasizing the importance of dimensionless constants. The early theoretical work on varying constants is outlined in Section 1-2 and more modern theories are discussed in Section 1-3. Section 1-4 briefly reviews the current experimental constraints on possible variations in the fine-structure constant, α, both from local and early universe (redshift $z \gtrsim 1000$) phenomena. Since the majority of this thesis concerns the analysis of QSO spectra, we provide a brief introduction to QSO absorption lines in Section 1-5. We state the aim of our work in Section 1-6 and provide an outline of the following chapters.

1-1 The fundamental constants

1-1.1 Why fundamental? Why constant?

In the late seventeenth century, Newton linked together two seemingly disparate phenomena – falling apples and Planetary motion – with a simple law of physics, the inverse-square law of gravitation. Part of this law's simplicity derived from the empirical fact that the proportionality constant, G, was just that, a constant. It did not depend on position or time or temperature or pressure. It seemed not to depend

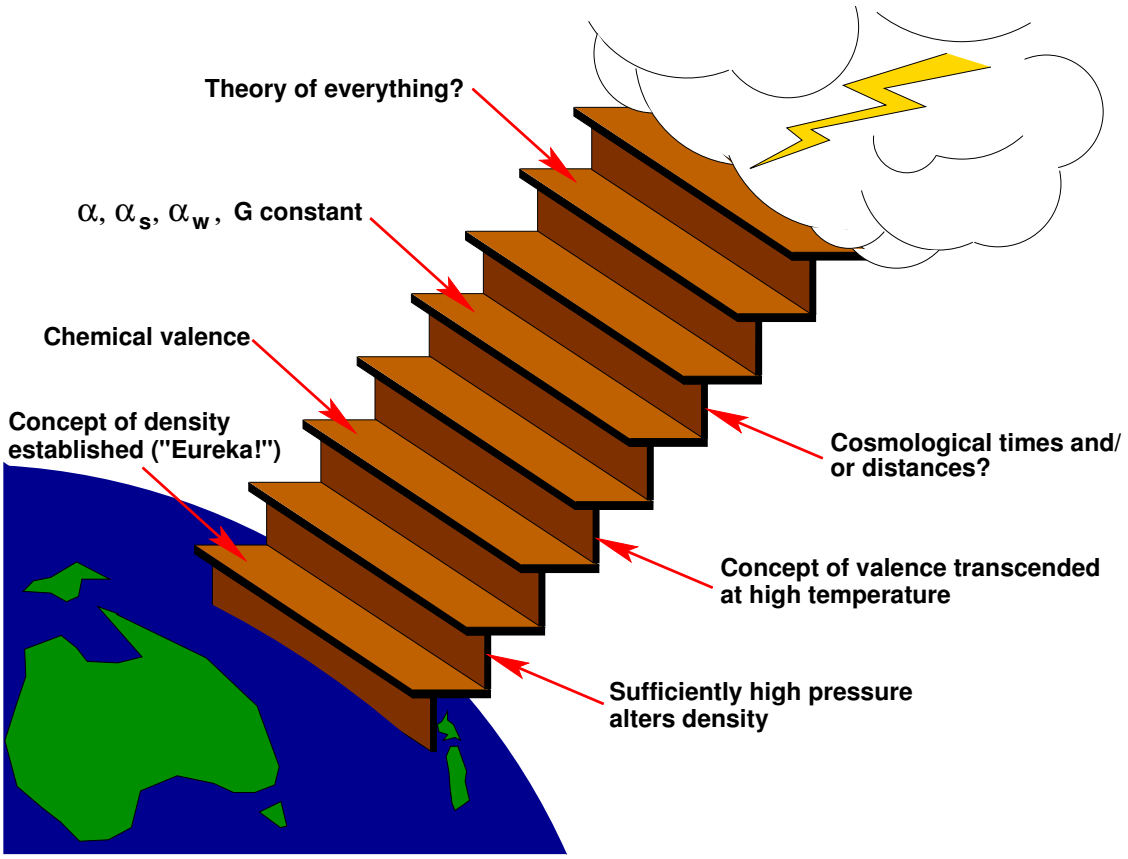

Figure 1.1. Wheeler's staircase of law and law transcended (adapted from Wheeler 1980). Each step represents the discovery of some regularity or constancy in nature. Each riser symbolizes a new environment or extremity of nature where that constancy is transcended. In all experiments to date, the low-energy values of the fundamental constants (e.g. α, $\alpha_{\rm s}$, $\alpha_{\rm w}$, G) seem to be constant. However, this may not be true over large cosmological times and/or distances.

on anything: it was measured to have the same value under all known experimental and natural conditions. Other constants of nature have come and gone (see the classification system of Levy-Leblond 1979). For example, the density of a given material was once regarded as constant, but soon experimenters found it to vary with temperature and pressure – a cherished regularity or constancy in nature was transcended (see Fig. 1.1). With more precise experiments came small but significant deviations from the predictions of Newton's theory. Einstein explained these new observations with his radical revision of gravitation, general relativity. However, G

survived this revolution: it was still central to the theory and still a constant. It was the first of the fundamental constants in use today.

Given that, by definition, the constants of nature have no dependence on other measured parameters, it is perhaps not surprising that we can not explain their values with current physical theories. If one is to predict the value of observables, one must have first measured the values of the constants appearing in the theory. However, all we know of the constants is their value – how is a theory which explains these values to be formulated with so little experimental information? Simpler theories, which explain more observed phenomena, might be regarded as more basic than others. Given a set of basic theories, one has a set of fundamental constants. Why fundamental? Because their values can not be calculated, only measured. Why constant? Because every experiment yields the same value. But if one conducts an experiment with greater precision and/or in an environment more extreme than previously considered, one might observe apparent variations in the constants. This may precipitate a more basic theory which explains the origin and value of the (then variable) constants (see Fig. 1.1).

1-1.2 Which constants? How many?

The current minimal 'standard model' of particle physics contains 19 independent free parameters (Hogan 2000, cf. Weinberg 1983; Cahn 1996; Gaillard et al. 1999). If neutrinos are massive, as currently seems likely, this number may increase by 7. Adding the gravitational interaction (i.e. G) to the standard model gives our current set of basic physical theories (using the language of Section 1-1.1) which contain 20 fundamental constants. The number of ultimately *required* constants in a 'final' physical theory is clearly a separate issue (e.g. Duff et al. 2002).

The coupling constants of electromagnetism, the weak and strong nuclear forces all 'run' with energy in the standard model and so it is common to consider their low-energy limits. In Table 1.1 we define the fundamental constants discussed in

Table 1.1. Some fundamental constants, their measured or defined values and uncertainties (Mohr & Taylor 2000, table 24).

Name	Symbol/definition	Value	Unit
Speed of light	c	299 792 458 (definition)	$\mathrm{m\,s^{-1}}$
Magnetic constant[a]	μ_0	$4\pi \times 10^{-7}$ (definition)	$\mathrm{N\,A^{-1}}$
Electric constant[b]	$\epsilon_0 \equiv 1/\mu_0 c^2$	$8.854\,187\,817\ldots \times 10^{-12}$	$\mathrm{F\,m^{-1}}$
Electron charge	e	$1.602\,176\,462(63) \times 10^{-19}$	C
Planck constant	$\hbar$	$1.054\,571\,596(82) \times 10^{-34}$	J s
Fine-structure constant[c]	$\alpha \equiv e^2/4\pi\epsilon_0\hbar c$	1/137.035 999 58(52)	
Electron mass	m_e	$9.109\,381\,88(72) \times 10^{-31}$	kg
Proton mass	m_p	$1.672\,621\,58(13) \times 10^{-27}$	kg
Proton-to-electron mass ratio	$\mu \equiv m_p/m_e$	1836.152 667 0(39)	
Proton magnetic moment	μ_p	$1.410\,606\,633(58) \times 10^{-26}$	$\mathrm{J\,T^{-1}}$
Nuclear magneton	$\mu_\mathrm{N} \equiv e\hbar/2m_p$	$5.050\,783\,17(20) \times 10^{-27}$	$\mathrm{J\,T^{-1}}$
Proton g-factor	$g_p \equiv 2\mu_p/\mu_\mathrm{N}$	5.585 694 675(57)	

[a] Also known as the permeability of free space. [b] Also known as the permittivity of free space. [c] First introduced by Sommerfeld (1911). e^2 is usually redefined as $e^2/4\pi\epsilon_0$ and so α is defined as $\alpha \equiv e^2/\hbar c$ throughout this work.

this thesis[1] (bold type) and give their measured (low-energy) values and prescribed uncertainties (Mohr & Taylor 2000). We will also often refer to the analogues of the fine-structure constant for the weak and strong forces, $\alpha_{\rm w} \equiv G_{\rm F} m_p^2 c/\hbar^3$ and $\alpha_{\rm s} \equiv g_{\rm s}^2/\hbar c$ where $G_{\rm F}/(\hbar c)^3$ is the Fermi coupling constant and $g_{\rm s}$ is the Yukawa (or strong) coupling constant (at low-energy).

1-1.3 Dimensional and dimensionless constants

Dicke (1962) emphasized that, when discussing variations in the fundamental constants, careful distinction should be made between dimensional and dimensionless constants. Consider measuring the speed of light, c, by finding the time taken for light to travel between two points. Imagine finding two different values on two different days. One might conclude that this implies a varying c. However, varying meter rules and/or varying clocks are equally valid conclusions. One can not measure a change in a dimensional quantity like c without first specifying which units are to be held fixed. For example, Bekenstein (1979) explained why several experimental checks on the constancy of $\hbar c$ were flawed (see also Barrow & Tipler 1986).

In the current literature and in the discussions below, one finds many references to 'varying-G', 'varying-e' and 'varying-c' theories. Given the above, how is one to understand these terms? Barrow & Magueijo (1998) and Magueijo et al. (2002) explain that these names reflect a choice of fixed units which make those theories mathematically simple. For example, each varying-c model is equivalent to a particular varying-e model and varying-G theories could equally well be couched in terms of varying masses. However, one version of the same theory will typically look simpler and/or have a clearer physical interpretation than the other. Barrow & Magueijo (1998) explicitly demonstrate this by expressing the varying-e theory of Bekenstein (1982) (Section 1-3.2) in terms of varying c.

[1] Many of these quantities are not explicitly considered in the standard model but are regarded as 'conventional' fundamental constants (Flowers & Petley 2001).

1-2 Early ideas about varying constants

The constancy of the fundamental constants was first seriously questioned when Milne (1935, 1937) and Dirac (1937) independently suggested that G may vary in cosmological time. Milne proposed a gravitational theory in which different physical 'clocks' – 'ticking' according to different physical processes – 'tick' at different rates as time progresses. The 'bi-metric' varying-c models of today are similar in spirit (Clayton & Moffat 1999, 2000, 2001, see Section 1-3.2). Possible consequences of Milne's hypothesis for biological and geological history were seized upon by Haldane (1937a,b) to explain aspects of their discontinuous development. Dirac's famous Large Numbers Hypothesis (LNH) attracted considerable interest (e.g. Teller 1948; Dicke 1957, 1961; Barrow 1990, 1996). Kothari (1938) and Chandrasekhar (1939) pointed out several astronomical consequences of the LNH which might permit observational tests. The desire to place a varying G on a firmer theoretical footing led to the development of scalar-tensor generalisations of Einstein's general relativity in which the variation of G was described self-consistently by the propagation of a scalar field which also acted as a source of space-time curvature (Brans & Dicke 1961).

Jordan (1937, 1939) first considered how the LNH might be applied to forces other than gravity, but rejected the possibility of time variations in $\alpha_{\rm w}$ or μ. Later, Gamow (1967) showed that the geological problems caused by Dirac's proposed variation in G (first pointed out by Teller 1948) could be avoided by interpreting the LNH as requiring time variation of e rather than G. Observational limits on possible variations of α, $\alpha_{\rm w}$ and $\alpha_{\rm s}$ were more restrictive than those on G but no self-consistent theory permitting the variation of non-gravitational force constants was developed to make the observational limits rigorous. Landau (1955) proposed that α-variation could be connected to renormalization rules in quantum electrodynamics.

1-3 Modern ideas about varying constants

Recent interest in varying constants has seen a huge surge in theoretical activity. We shall not attempt a full review here, deferring the reader to Uzan (2003) for a more thorough discussion and the many theoretical articles in Martins (2003) for very recent work. In recent years, many theories attempting to unify gravity with other interactions have provided strong motivation for varying constants. Bekenstein (1979) scalar theories have also proved interesting. We restrict ourselves to a brief discussion of these two classes of theory below.

1-3.1 Multi-dimensional unification theories

One of the greatest challenges facing modern theoretical physics is the quantization of the gravitational interaction. Early attempts used a geometrization in $(4{+}D)$–dimensional curved space-times in the spirit of the Kaluza-Klein scenario to unite gravity and electromagnetism (Kaluza 1921; Klein 1926). Three-dimensional gauge couplings like α, $\alpha_{\rm w}$, and $\alpha_{\rm s}$ vary as the inverse square of the mean scale of the extra D dimensions. Thus, evolution of the scale size of the extra dimensions is related to variability of the low-energy coupling constants in the 4–dimensional subspace of simple Kaluza-Klein and superstring theories.

Damour & Polyakov (1994) showed that cosmological variation in α may proceed at different rates at different points in space-time (see also Forgács & Horváth 1979; Barrow 1987; Li & Gott 1998). Various functional forms for monotonic time variation of α and G have been derived (e.g. Chodos & Detweiler 1980; Freund 1982; Wu & Wang 1986; Maeda 1988). Marciano (1984) discussed the self-consistency relations required if there are simultaneous variations of different constants in unified gauge theories. He also examined any possible non-monotonic variation in α with t using the running coupling dependence of α, $\alpha_{\rm w}$, and $\alpha_{\rm s}$. Typically, variation in G and α could be linked by relations of the form $(\Delta\alpha/\alpha)^2 \sim \Delta G/G$. However, none of these theories give a natural amplitude for the variation that might be compared with experiments.

The features of extra dimensions mean that in all string theories (and M-theory, of which they are presumed to be limiting cases, see Hořava & Witten 1996; Hořava 1996), any extra dimensions of space need to be held static to avoid conflict with observation. In the currently popular scenarios for M-theory (e.g. Antoniadis et al. 1998; Arkani-Hamed et al. 1998; Randall & Sundrum 1999a,b) only the gravitational force is assumed to act in all (> 3) spatial dimensions (the 'bulk') whilst all other interactions act only in 3-dimensional space (the 'brane'). Observed constancy in the 3-dimensional non-gravitational constants could therefore be of crucial importance in testing this theoretical scenario. Until recently, the extra dimensions were thought to have scales necessarily of order the Planck scale, $\sim 10^{-33}$ cm. However, in the above scenario, they may be as large as ~ 0.01 mm, leading to deviations from Newtonian gravity on these scales. The challenge of testing gravity on sub-millimetre scales is considerable because other forces strongly dominate.

1-3.2 Scalar theories

The first theory of electromagnetism which self-consistently incorporated a varying α, and which reduced to Maxwell's theory in the limit of constant α, was that developed by Bekenstein (1982). He introduced a scalar field whose variation in space and time produces effective variation in e. The form of the propagation equation for evolution of the scalar field is strongly constrained by the natural requirements that it be second order, causal and linearly coupled to the matter density. Bekenstein makes the simplifying assumption that the gravitational sector of the theory is identical to general relativity. This amounts to neglecting the contribution of the Bekenstein scalar's kinetic energy to the expansion dynamics of the universe, a defect that can be avoided in other versions of the theory (Barrow & Magueijo 2000; Magueijo 2000). Bekenstein's theory has been constrained by several astronomical observations (e.g. Livio & Stiavelli 1998; Landau & Vucetich 2002) and used to illustrate consequences of space and time variations of constants (Barrow & O'Toole 2001). The general structure of the theory has also been applied to other couplings. For example, Chamoun et al. (2001) recently studied variations in α_s.

Sandvik et al. (2002) offered a more complete generalization of Bekenstein's theory by self-consistently including varying α in a Λ-dominated, cold dark matter universe's expansion history. They make the assumption that the Bekenstein scalar is coupled to the dark matter energy density. This introduces a free parameter but they provide physical arguments restricting its probable range. The Sandvik et al. theory implies a fractional variation in α at the level $\Delta\alpha/\alpha \sim -1\times10^{-5}$ at late times in the matter dominated epoch (i.e. $z \gtrsim 1$). Observational constraints on $\Delta\alpha/\alpha$ at these redshifts therefore strongly constrain this theory (cf. the multi-dimensional unification theories in Section 1-3.1).

Following the discussion in Section 1-1.3, it is clear that varying-e models are observationally indistinguishable from varying-c models. Thus, scalar varying-speed-of-light theories have also received much attention. The main appeal of varying-c theories is that they provide alternative solutions to the standard cosmological problems such as the flatness, horizon and monopole problems (e.g. Moffat 1993; Barrow & Magueijo 1999a,b; Albrecht & Magueijo 1999; Barrow 1999).

1-4 Non-QSO absorption line limits on varying α

Non-QSO absorption line constraints on $\Delta\alpha/\alpha$ fall into two distinct classes, 'local' and 'early universe'. Uzan (2003) has recently reviewed these constraints and so we provide only brief comments below.

1-4.1 Local constraints

Several limits on α-variation come from the terrestrial (i.e. Earth and Solar system) environment. We discuss the most stringent laboratory, geological and meteoritic constraints below. In Section 6-2 we compare these relatively strong limits with those we obtain from QSO absorption systems in Chapters 2, 3 and 5 (see Fig. 6.1).

1-4.1.1 Atomic clocks

Direct laboratory measurements provide interesting constraints on $\Delta\alpha/\alpha$. Prestage et al. (1995) introduced a new technique, comparing the rates of clocks based on ultra-stable oscillators. The relativistic corrections to the relevant transition energies are of order $(Z_n\alpha)^2$, where Z_n is the nuclear charge. By comparing the frequencies of two clocks based on different atoms (H-maser and Hg I) over a 140 day period, they were able to constrain $|\dot{\alpha}/\alpha| \equiv |(\mathrm{d}\alpha/\mathrm{d}t)/\alpha| \leq 3.7 \times 10^{-14}\,\mathrm{yr}^{-1}$ (i.e. $|\Delta\alpha/\alpha| \leq 1.4 \times 10^{-14}$). Sortais et al. (2001) recently improved this limit by a factor of 5, comparing ^{87}Cs and ^{133}Rb fountains over a 2 year period to obtain $|\dot{\alpha}/\alpha| = (4.2 \pm 6.9) \times 10^{-15}\,\mathrm{yr}^{-1}$ [i.e. $|\Delta\alpha/\alpha| = (0.8 \pm 1.4) \times 10^{-14}$].

However, these measurements assume a constant g_p and do not constrain $\Delta\alpha/\alpha$ directly. Indeed, in using the highly stable ^{87}Cs and ^{133}Rb clocks rather than those with large Z_n differences, Sortais et al. (2001) obtained a tighter constraint on g_p-variation than on α-variation, $|\dot{g}_p/g_p| = (9.5 \pm 16) \times 10^{-16}\,\mathrm{yr}^{-1}$ [i.e. $|\Delta g_p/g_p| = (1.9 \pm 3.2) \times 10^{-15}$].

1-4.1.2 The Oklo phenomenon

Model dependent upper limits on any variation have been claimed from analyses of the Oklo phenomenon – a natural nuclear fission reactor which operated in Gabon, Africa, ∼1.8 billion years ago (Naudet 1974; Maurette 1976; Petrov 1977, see Barrow 2002 for a non-technical description). The relatively high isotopic abundance of ^{235}U at that time[2] allowed a moderated fission reaction to be sustained in water with a high concentration of dissolved U. The neutron absorption cross section of ^{149}Sm is dominated by a resonance capture of thermal neutrons liberated by the ^{235}U fission at ≈0.1 eV. The ^{149}Sm/^{150}Sm abundance ratio measured today therefore constrains the position of the resonance 1.8 Gyr ago.

[2]The half-lives of ^{235}U and ^{238}U are ≈0.7 and ≈4.5 Gyr respectively and so the relative natural isotopic abundance of ^{235}U was ≈3.7% 1.8 Gyr ago compared to about ≈0.72% today.

Shlyakhter (1976) originally constrained the energy of the nuclear resonance level in the ^{149}Sm isotope and related this to upper bounds on $|\Delta\alpha/\alpha|$. Damour & Dyson (1996) have also analysed the problem with different model assumptions and claim[3] $-0.9 \times 10^{-7} < \Delta\alpha/\alpha < 1.2 \times 10^{-7}$. Recently, Fujii et al. (2000) obtained somewhat tighter constraints using new samples from the Oklo reactor: $\Delta\alpha/\alpha = (-0.04 \pm 0.15) \times 10^{-7}$. However, there are considerable uncertainties regarding the complicated Oklo environment and any limits on α derived from it can be weakened by allowing other interaction strengths and mass ratios to vary in time as well (e.g. Flambaum & Shuryak 2002; Olive et al. 2002).

1-4.1.3 β decay

Peebles & Dicke (1962) first suggested that the β-decay rate of ^{187}Re was particularly sensitive to changes in α. Updating the work of Dyson (1967, 1972), Olive et al. (2002) claim that improved measurements of the ^{187}Re β-decay rate (derived from meteoritic ^{187}Re/^{187}Os abundances ratios) imply $|\Delta\alpha/\alpha| < 3\times10^{-7}$ over the 4.56 Gyr history of the Solar system. This assumes that the possible variation in the half-life is equal to its measurement uncertainty. Olive et al. (2002) note that this assumption can be checked by comparing the meteoritic age estimates derived from several different isotopic species.

However, Uzan (2003) notes that the above results assume that variations of the β-decay rate depend entirely on variations in α and not on possible variations in the weak coupling constant $\alpha_{\rm w}$.

1-4.2 Early universe constraints

1-4.2.1 Cosmic microwave background

The power-spectrum of cosmic microwave background (CMB) anisotropies is now well-constrained over angular scales from 6′ (e.g. Sievers et al. 2002) to the full

[3]Throughout this thesis, a negative $\Delta\alpha/\alpha$ represents a smaller α in the past.

sky (COBE, Smoot et al. 1992; Bennett et al. 1996), or multipoles $l = 2$–2000. Hannestad (1999) and Kaplinghat et al. (1999) first pointed out that a different α during last scattering would affect the binding energy of hydrogen, the Thomson scattering cross section and the recombination rates. A smaller value of α in the past would postpone the recombination of electrons and protons, i.e. last-scattering would occur at lower redshift. It would also alter the baryon-to-photon ratio at last-scattering, leading to changes in both the amplitudes and positions of features in the power spectrum, primarily at angular scales $\lesssim 1^\circ$. The strongest current constraints at $z \sim 1000$ from the CMB power spectrum are at the $\Delta\alpha/\alpha \sim 10^{-2}$ level if one considers the uncertainties in, and degeneracies with, the usual cosmological parameters (i.e. $\Omega_{\rm m}$, Ω_Λ etc.) (Avelino et al. 2001; Landau et al. 2001; Martins et al. 2002).

However, Kujat & Scherrer (2000) and Battye et al. (2001) note a crucial degeneracy between variations in α and m_e. Battye et al. suggest that the degeneracy may be partially broken for $l \gtrsim 1500$. However, this degeneracy dramatically weakens the current constraints. Riazuelo & Uzan (2002) also note that variations in G could have similar effects.

1-4.2.2 Big Bang nucleosynthesis

The theory of Big Bang nucleosynthesis (BBN) is one of the corner-stones of the Hot Big Bang cosmology, successfully explaining the abundances of the light elements, D, ^{3}He, ^{4}He and ^{7}Li (see, e.g., Peebles 1993 and Peacock 1999 for detailed discussion). Kolb et al. (1986) first discussed how limits can be placed on $\Delta\alpha/\alpha$ at the time of BBN (corresponding to a redshift $z \sim 10^8 - 10^9$) by assuming a simple scaling between the value of α and the proton-neutron mass difference. Barrow (1987) and Campbell & Olive (1995) considered the simultaneous variation of weak, strong and electromagnetic couplings on BBN.

However, estimates based on the BBN abundance of ^{4}He suffer from a crucial uncertainty as to the electromagnetic contribution to the proton-neutron mass dif-

ference. Much weaker limits are possible if attention is restricted to the nuclear interaction effects on the nucleosynthesis of D, ^{3}He, and ^{7}Li. Bergström et al. (1999) and Nollett & Lopez (2002) considered all light elements up to ^{7}Li. Given the present observational uncertainties in the light element abundances, the most conservative limits are those of Nollett & Lopez (2002): $\Delta\alpha/\alpha = (3 \pm 7) \times 10^{-2}$. However, Uzan (2003) notes that variations in α are degenerate with variations in $\alpha_{\rm w}$, $\alpha_{\rm s}$ and G.

1-5 Quasar absorption lines

In the remainder of this thesis we discuss constraints on varying constants offered by the absorption spectra of quasi-stellar objects (QSOs)[4]. Here we provide a very brief introduction to this field.

The discovery of QSOs by Hazard (1963) and Schmidt (1963) led immediately to intense study of their absorption line spectra. Two seemingly distinct classes of absorption lines were soon identified:

1. Lyman-α forest. Gunn & Peterson (1965) and Bahcall & Salpeter (1965) had first suggested that intergalactic neutral hydrogen (H I) along the line of sight to cosmologically distant objects could be detected by its redshifted ultraviolet (UV) absorption features in optical spectra. Lynds (1971) subsequently suggested that the 'forest' of absorption lines, lying almost exclusively to the blue the QSO Lyman-α emission line, was due to Ly-α absorption by intervening H I.

   From both observations (e.g. Le Brun & Bergeron 1998; Tripp et al. 1998) and simulations (e.g. Miralda-Escude et al. 1996; Theuns et al. 1998a,b; Davé et al. 1999), it has become increasingly clear that the lower H I column density [N(H I)] forest lines arise predominantly in the large-scale filamentary and sheet-like structures in which galaxies are embedded. The higher N(H I) forest lines are probably associated with the dark matter halos or disks of galaxies them-

[4]Quasi-stellar objects (QSOs) and quasars are now known to be the same class of object and so we use the terms interchangeably throughout this work.

selves, as evidenced by their higher metallicities (e.g. Cowie & Songaila 1995; Songaila & Cowie 1996), clustering properties (e.g. Fernandez-Soto et al. 1996) and coincidence in redshift with galaxies (e.g. Lanzetta et al. 1995; Le Brun et al. 1996; Chen et al. 1998; Tripp et al. 1998). Rauch (1998) presents an observational and theoretical review of the Ly-α forest.

2. Metal systems. Initial identification of absorption to the red of the QSO Ly-α emission line (e.g. Burbidge et al. 1966; Stockton & Lynds 1966) suggested the existence of ionized metals (atoms heavier than He) in the absorbing regions. These intervening metal absorption systems are associated with Ly-α absorption systems of very high (though very diverse) $N(\mathrm{H\,I})$ and so are associated with galaxy halos or disks. Damped Ly-α systems (DLAs), defined somewhat arbitrarily by $N(\mathrm{H\,I}) > 2 \times 10^{20}\,\mathrm{cm}^{-1}$, are clearly identified by the damping of the Ly-α absorption line wings. The weaker Lyman limit systems (LLSs) still have high enough column density, $N(\mathrm{H\,I}) \gtrsim 2 \times 10^{17}\,\mathrm{cm}^{-1}$, to cause a clear, sudden drop in transmitted QSO flux below the Lyman limit (at 911.7536 Å in the rest frame).

   The metal absorption lines are much narrower than the corresponding H I lines and high resolution spectroscopy often reveals complicated velocity structure (see lower panel of Fig. 1.2 and Figs. 2.1, 3.4 and 3.5). Detailed studies of the metal abundance patterns (e.g. Lu et al. 1996; Prochaska & Wolfe 1999; Lopez et al. 1999), dust depletion patterns (e.g. Pettini et al. 1997) and kinematic structures (e.g. Prochaska & Wolfe 1997; Churchill & Vogt 2001) aim at understanding the spatial distribution of the absorbing gas and its relationship with the associated galaxy. We briefly discuss different models of the metal systems in Section 4-3. Ultimately, the aim is to provide clues to galaxy formation process and the chemical enrichment history of the universe.

The upper panel of Fig. 1.2 shows the optical spectrum of the QSO GB 1759+7539 (Outram et al. 1999) taken with the High Resolution Spectrograph (HIRES) (Vogt et al. 1994) on the Keck I 10-m telescope on Mauna Kea, Hawaii.

Spectra with such high signal-to-noise (S/N $\sim$ 30), high spectral resolution (FHWM $\sim 7\,\mathrm{kms}^{-1}$, $R \sim 45000$) and practically complete optical coverage are now routinely observed on 8–10-m class telescopes (e.g. Keck/HIRES, VLT/UVES, Subaru/HDS). In the lower panel we focus on a small region which includes the C IV doublet associated with the DLA at a redshift $z_{\rm abs} = 2.6253$. The resolving power is high enough to resolve different velocity components associated with the same absorber. The presence of both doublet transitions facilitates determination of this velocity structure (see Section 3-3.2 for further discussion).

Caption for Fig. 1.2. The full spectrum in the upper panel shows several prominent emission lines intrinsic to the QSO (Lyman-α and β, N V, Si IV and C IV) and the Ly-α forest absorption lines to the blue of the Ly-α emission. In this QSO, two clear high N(H I) absorption systems are seen at $\lambda_{\rm obs} \approx 4400\,$Å and 4750 Å. The former is a damped Lyman-α system, the latter being a [high N(H I)] Lyman-limit system. Many associated metal lines can be seen to the red of the Ly-α emission line. The lower panel highlights a narrow wavelength region containing the C IV $\lambda\lambda$1548/1550 doublet associated with the DLA at $z_{\rm abs} = 2.6253$. Note the complex velocity structure and the differing oscillator strengths of the $\lambda\lambda$1548 and 1550 transitions.

1-6 Aim and outline of thesis

In the context of observations of the local Universe and the CMB at $z \sim 1000$, QSO absorption lines afford us a rare view of physics at intermediate redshifts. The narrow metal lines to the red of the QSO Ly-α emission appear against a 'clean' continuum, not corrupted by the Ly-α forest. Their observed wavelengths, compared with laboratory values, therefore offer an extremely precise probe of electromagnetic interactions throughout much of the history of the universe. This thesis aims to exploit existing, high quality absorption line spectra to search for possible violations of one of the central assumptions of modern physics: the invariance and universality

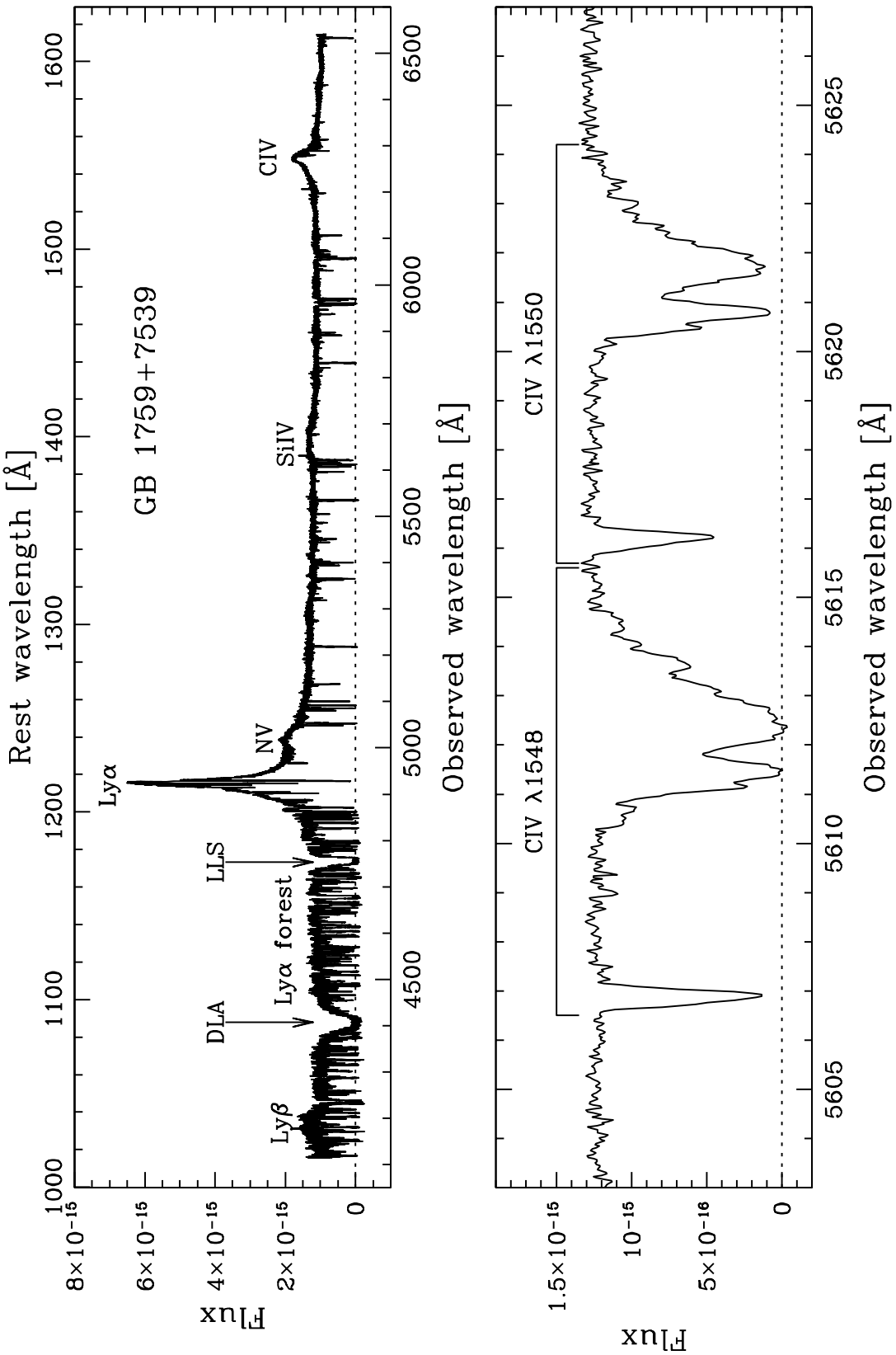

Figure 1.2. A typical optical QSO spectrum observed with Keck/HIRES (Outram et al. 1999). See text for caption.

of fundamental physical constants.

In Chapter 2 we improve existing limits on $\Delta\alpha/\alpha$ from QSO absorption lines using the well-established alkali doublet (AD) technique. This serves as an introduction to Chapter 3 which presents a detailed analysis of 3 large samples of optical QSO spectra using the newly introduced many-multiplet (MM) method. Our results are surprising, implying that α may in fact vary in space-time. We therefore conduct a thorough investigation of possible systematic errors in Chapter 4. We also explore other QSO absorption line techniques in Chapter 5. Specifically, we obtain the tightest constraints on variations in $\alpha^2 g_p$ from comparison of H I 21-cm and millimetre-band molecular rotational absorption lines. We conclude in Chapter 6, summarizing our main results, comparing them with those outlined above and discussing future work aimed at confirming or ruling out our possible detection of varying α.

Thus, to ignore the possibility that some constants may vary is to risk having a distorted view of the universe; no better motivation is needed for delving into the possible forms of variability.

Jacob D. Bekenstein (1979)

Chapter 2

$\Delta\alpha/\alpha$ from the alkali doublet (AD) method

In this Chapter we describe the alkali doublet (AD) method for obtaining constraints on α-variation from QSO spectra. After discussing the most stringent constraints in the literature, we use Keck/HIRES spectra to improve on these limits by a factor of 3. We also eliminate systematic errors due to uncertain laboratory measurements that dominated previous results.

We give only brief descriptions of the observational data (Section 2-2) and analysis methods (Section 2-3), deferring a thorough discussion to Chapter 3 (Sections 3-3.1.2 and 3-4 respectively) where the main optical (many-multiplet) results of this thesis are presented. Due to the somewhat surprising nature of those results, we prefer to present thoroughly all relevant information in that Chapter. Similarly, we defer our analysis of possible systematic effects relevant to the AD method to Chapter 4 (Section 4-14), preferring to compare them with those important to the many-multiplet results.

2-1 Introduction

The relative wavelength separation between the two transitions of an alkali doublet (AD) is proportional to α^2 (e.g. Bethe & Salpeter 1977). Savedoff (1956) first analysed AD separations seen in Seyfert galaxy emission spectra to obtain constraints on α-variation. Absorption lines in intervening clouds along the line of sight to QSOs are substantially narrower than intrinsic emission lines and therefore provide a more precise probe. Bahcall et al. (1967) first used AD spacings of gas seen in absorption which seemed to be intrinsic to the QSO. They obtained the constraint $\Delta\alpha/\alpha \equiv (\alpha_z - \alpha_0)/\alpha_0 = (-2 \pm 5) \times 10^{-2}$ at an absorption redshift $z_{\rm abs} \approx 1.95$. Here, α_z and α_0 are the values of α in the absorption cloud(s) and in the laboratory respectively.

Narrower still are metal absorption lines from DLAs and LLSs. Wolfe et al. (1976) first analysed Mg II doublets from a DLA at $z_{\rm abs} \approx 0.524$. Since then, several authors (e.g. Cowie & Songaila 1995; Varshalovich et al. 1996) have applied the AD method to doublets of several different species (e.g. C IV, Si II, Si IV, Mg II and Al III) arising from intervening absorption clouds at significantly lower redshift than the background QSO.

The most recent and stringent constraint using the AD method was obtained by Varshalovich et al. (2000, hereafter VPI00) using the Si IV $\lambda\lambda$1393 and 1402 doublet. A small change in α (i.e. $\Delta\alpha/\alpha \ll 1$) will lead to a change in the doublet separation given by (VPI00, correcting a typographical error)

$$\Delta\alpha/\alpha = \frac{c_r}{2}\left[\frac{(\Delta\lambda)_z}{(\Delta\lambda)_0} - 1\right] . \qquad (2.1)$$

Here, $(\Delta\lambda)_z$ and $(\Delta\lambda)_0$ are the relative doublet separations in the absorption cloud (at redshift z) and in the laboratory respectively and $c_r \approx 1$ is a constant taking into account higher order relativistic corrections. From 16 absorption systems (towards 6 QSOs) they obtained a mean $\Delta\alpha/\alpha = (-4.6 \pm 4.3) \times 10^{-5}$ using a line fitting method. The error quoted here is statistical only. VPI00 augment this with an additional systematic error term, $\pm 1.4 \times 10^{-5}$, due to uncertainties in the laboratory doublet separation, $(\Delta\lambda)_0$, assumed in their analysis (see Table 2.1). This

estimate of the potential systematic error seems optimistic considering that the error in the laboratory wavelength separation was previously quoted at $\delta(\Delta\lambda)_0 \sim 1\,\mathrm{m\AA}$ by Ivanchik et al. (1999). From equation 2.1, the corresponding systematic error in $\Delta\alpha/\alpha$ is

$$|\delta(\Delta\alpha/\alpha)| \approx -\frac{c_r}{2}\frac{\delta(\Delta\lambda)_0}{(\Delta\lambda)_0} \approx 5\times10^{-5}\,, \tag{2.2}$$

consistent with the Ivanchik et al. (1999) value ($\sim 8\times10^{-5}$).

There are three ways in which the above constraints can be significantly improved without the need for a much larger sample of QSO spectra:

1. Improved spectral resolution. Many of the spectra used by VPI00 have FWHM $\sim 20\,\mathrm{kms}^{-1}$ (e.g. Petitjean et al. 1994; Varshalovich et al. 1996) while many absorption systems are known to contain Si IV lines with b-parameters (i.e. Doppler widths) $\sim 5\,\mathrm{kms}^{-1}$ (e.g. Outram et al. 1999). FWHM $\sim 7\,\mathrm{kms}^{-1}$ is now routinely used for QSO observations with, for example, the Keck/HIRES and the VLT/UVES. Therefore, such spectra offer the opportunity to significantly improve constraints on $\Delta\alpha/\alpha$.

2. Improved signal-to-noise ratio (S/N). Many of the spectra used by VPI00 have S/N ~ 15 per pixel. With the advent of 8–10-m telescopes, significantly greater S/N can be achieved (e.g. Prochaska & Wolfe 1996, 1997, 1999).

3. Improved laboratory wavelength measurements. Griesmann & Kling (2000) have increased the absolute precision of the laboratory Si IV $\lambda\lambda$1393 and 1402 wavelengths by more than two orders of magnitude. Table 2.1 compares the new values with those used by VPI00 (Kelly 1987; Morton 1991, 1992). Note that even our conservative estimate of the systematic error on $\Delta\alpha/\alpha$ in equation 2.2 is too small. The new measurements imply that the VPI00 result in equation 2.1 should be corrected by $\approx +11.3\times10^{-5}$ to $\Delta\alpha/\alpha \approx (7\pm4)\times10^{-5}$. If the error in the difference between the doublet wavelengths is equal to the absolute uncertainty (i.e. 4×10^{-5} Å) then a precision limit of $\delta(\Delta\alpha/\alpha) \approx 0.2\times10^{-5}$ can now be reached. This should be true of Griesmann & Kling's measurement since sta-

Table 2.1. Atomic data for the Si IV $\lambda\lambda$1393 and 1402 lines. We give the ground and excited state configurations and compare the new laboratory wavelength measurements with those used by VPI00. We also give the oscillator strengths, f, used in our profile fitting algorithm and the relativistic coefficients q_1 and q_2 used in equation 2.3.

Transition	Ground	Upper state	Old λ_0 (Å)[a]	New λ_0 (Å)[b]	New ω_0 (cm^{-1})[b]	f [a]	q_1 (cm^{-1})[c]	q_2 (cm^{-1})[c]
Si IV λ1393	$2p^6 3s\ ^2S_{1/2}$	$2p^6 3p\ ^2P_{3/2}$	1393.755(6)	1393.76018(4)	71748.355(2)	0.5140	766	48
Si IV λ1402		$2p^6 3p\ ^2P_{1/2}$	1402.770(6)	1402.77291(4)	71287.376(2)	0.2553	362	−8

[a]Martin & Zalubas (1983) and Kelly (1987); [b]Griesmann & Kling (2000); [c]Dzuba et al. (1999a)

tistical errors in the line positions dominated their error budget (U. Griesmann, private communication).

We apply the above improvements in the following sections with the aim of increasing both the accuracy and precision of $\Delta\alpha/\alpha$ as measured using the Si IV AD method.

2-2 Keck/HIRES spectra

The data used here were kindly provided in reduced form by Jason X. Prochaska and Arthur M. Wolfe and are detailed in Prochaska & Wolfe (1996, 1997, 1999). Outram et al. (1999) have also kindly contributed their spectrum of Q 1759+75 taken in July 1997. Here we provide only a brief description of the observations and data reduction, deferring a more detailed discussion to Section 3-3.1.2.

All the QSO spectra were obtained at the Keck I 10-m telescope on Mauna Kea with the HIRES facility (Vogt et al. 1994) over several observing runs from 1994 to 1997. The QSOs were generally quite faint ($m_V \lesssim 19.0$) so several $\sim$1–2 hour exposures were co-added for each object. Most of the data were reduced using the HIRES data reduction package written by T. Barlow, MAKEE[1]. This package converts the two-dimensional echelle images to fully reduced, one-dimensional, wavelength–calibrated spectra.

Thorium–argon (ThAr) spectra were taken before and after the QSO exposures and co-added to provide a calibration spectrum. ThAr lines were selected and centroided to form the wavelength solution. Some of the QSO spectra were reduced when MAKEE had no wavelength calibration facility. In these cases, wavelength calibration was carried out using IRAF[2] routines. Spectra not reduced in MAKEE were fully reduced within IRAF. $1\,\sigma$ error arrays were generated assuming Poisson count-

[1] Available at http://www2.keck.hawaii.edu:3636/inst/hires/makeewww.

[2] IRAF is distributed by the National Optical Astronomy Observatories, which are operated by the Association of Universities for Research in Astronomy, Inc., under cooperative agreement with the National Science Foundation.

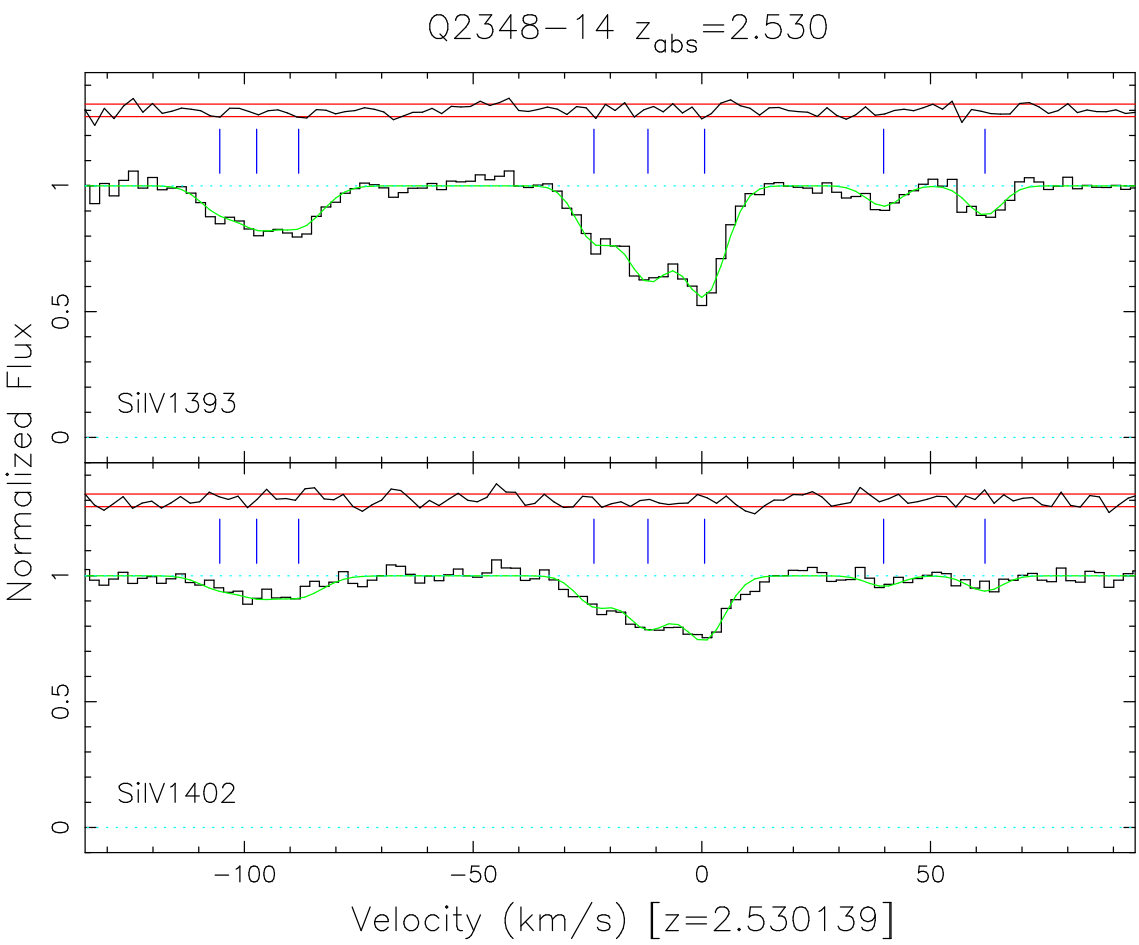

Figure 2.1. Si IV absorption system at $z_{\rm abs} = 2.530$ towards Q2348−1444. The data have been normalized by a fit to the continuum and plotted as a histogram. Our Voigt profile fit (solid curve) and the residuals (i.e. [data]−[fit]), normalized to the $1\,\sigma$ errors (horizontal solid lines), are also shown. The tick–marks above the continuum indicate individual velocity components.

ing statistics. We fitted continua to regions of each spectrum containing either or both of the Si IV doublet transitions by fitting Legendre polynomials to $\sim$500 kms^{-1} sections.

The sample comprises 21 Si IV absorption systems (towards 8 QSOs) over a redshift range $z = 2.0$–3.1 (mean redshift $\langle z_{\rm abs}\rangle = 2.6$). The S/N per pixel ranges from 15–40 with most spectra having S/N $\sim$ 30 and FWHM $\lesssim 7.5$ kms^{-1} ($R = 34000$). We provide an example absorption system in Fig. 2.1. We plot all 21 absorption systems in Appendix B.

2-3 Analysis

Although equation 2.1 is a simple approach to the specific case of an alkali doublet, a more general approach is to write down the energy equation for any individual transition, within any multiplet and for any species. Dzuba et al. (1999a,b) and Webb et al. (1999) suggested the convenient formulation

$$\omega_z = \omega_0 + q_1 x_z + q_2 y_z \,, \tag{2.3}$$

where ω_z is the wavenumber in the rest-frame of the cloud, at redshift z, in which α_z/α_0 may not equal unity. ω_0 is the wavenumber as measured in the laboratory and x_z and y_z contain the information about $\Delta\alpha/\alpha$:

$$x_z \equiv \left(\frac{\alpha_z}{\alpha_0}\right)^2 - 1 \quad \text{and} \quad y_z \equiv \left(\frac{\alpha_z}{\alpha_0}\right)^4 - 1. \tag{2.4}$$

The q_1 and q_2 coefficients represent the relativistic corrections to the energy for a particular transition. The q_1 coefficients are typically an order of magnitude larger than the q_2 coefficients and so it is the relative magnitudes of q_1 for different transitions that characterizes our ability to constrain $\Delta\alpha/\alpha$. This equation forms the basis of the MM method and will be discussed in detail in Chapter 3. In the case of a single alkali doublet and $\Delta\alpha/\alpha \ll 1$, equation 2.3 reduces to equation 2.1 with

$$c_r \approx \frac{\delta q_1 + \delta q_2}{\delta q_1 + 2\delta q_2} \tag{2.5}$$

where δq_1 and δq_2 are the differences between the q_1 and q_2 coefficients for the doublet transitions. The values for q_1 and q_2 for Si IV $\lambda\lambda$1393 and 1402 have been calculated by Dzuba et al. (1999a) and are shown in Table 2.1. For the Si IV doublet, $c_r \approx 0.9$ as used by VPI00.

The technique for extracting $\Delta\alpha/\alpha$ from each absorption system is based on a simultaneous χ^2 minimization analysis of multiple component Voigt profile fits to the Si IV absorption features. We discuss this technique in detail in Section 3-4. Briefly, consider a QSO spectrum containing a single velocity component of a specific transition. Three parameters describe the Voigt profile fit to such a component: the

column density N, the Doppler width or b-parameter and the redshift $z_{\rm abs}$ of the absorbing gas cloud. For the present case, we add another free parameter to the fit: $\Delta\alpha/\alpha$.

We have used the program VPFIT (v5, Webb 1987)[3] to fit absorption profiles to the spectra. We have modified VPFIT to include $\Delta\alpha/\alpha$ as a free parameter. Parameter errors can be calculated from the diagonal terms of the final parameter covariance matrix (Fisher 1958). The reliability of these errors has been confirmed using Monte Carlo simulations of a variety of different combinations of transitions and velocity structures (see Section 3-4 and Appendix A for detailed discussion).

VPFIT imposes a (user-adjustable) cut-off point in parameter space such that very weak velocity components are removed from the fit when they no longer significantly affect the value of χ^2. Conceivably, dropping even very weak components could affect the determination of $\Delta\alpha/\alpha$. Therefore, in such cases we observed the trend in the values of $(\Delta\alpha/\alpha)_i$ at each iteration i of the minimization routine to see if this trend was significantly altered due to line dropping. If components were dropped during a fit then we also re-ran the VPFIT algorithm, keeping the dropped components by fixing their column density at the value just before they were dropped from the original fit. No cases were found where the values of $\Delta\alpha/\alpha$ from the different runs differed significantly.

We impose several consistency checks before we accept a value of $\Delta\alpha/\alpha$. Firstly, the value of χ^2 per degree of freedom must be $\sim$1. Secondly, we calculated $\Delta\alpha/\alpha$ for each absorption system using a range of different first-guess values for $\Delta\alpha/\alpha$ to ensure that the VPFIT algorithm was finding global minima in the χ^2 parameter space.

[3]Available at http://www.ast.cam.ac.uk/~rfc/vpfit.html

2-4 Results

We present our results in Table 2.2, giving the values of $\Delta\alpha/\alpha$ for each absorption cloud together with the $1\,\sigma$ errors derived in the VPFIT algorithm. To illustrate the distribution of $\Delta\alpha/\alpha$, we plot these results in Fig. 2.2 as a function of the absorption cloud redshift, $z_{\rm abs}$, and the corresponding fractional look-back time. The weighted mean of the sample is

$$\Delta\alpha/\alpha = (-0.5 \pm 1.3) \times 10^{-5}\,. \tag{2.6}$$

The value of χ^2 per degree of freedom, χ^2_ν, about this weighted mean value is 0.95, giving no evidence to suggest that we may have incorrectly estimated the individual $1\,\sigma$ errors on $\Delta\alpha/\alpha$. We checked that the distribution of $\Delta\alpha/\alpha$ values shows no gross deviation from a Gaussian distribution (although with only 21 data points this is not a rigorous check). We also note that the unweighted $[\Delta\alpha/\alpha = (-0.12 \pm 1.4) \times 10^{-5}]$ and weighted means are consistent with each other, again suggesting no substantial deviation from Gaussianity.

2-5 Discussion

Our new Si IV AD results represent a 3.3-fold increase in precision over those of VPI00. The increase in precision is due to improved data quality, i.e. higher spectral resolution and S/N. The $1\,\sigma$ statistical uncertainty we quote in equation 2.6 dominates the potential $\pm 0.2 \times 10^{-5}$ systematic uncertainty due to the $1\,\sigma$ errors in the (greatly improved) laboratory wavelengths of Griesmann & Kling (2000).

We have seen how the VPI00 result, originally consistent with $\Delta\alpha/\alpha = 0$, was severely affected by (underestimated) systematic errors in the Si IV laboratory wavelengths. Therefore, despite equation 2.6 being consistent with $\Delta\alpha/\alpha = 0$, it is important to consider other possible systematic errors. We carry out a thorough search for systematic errors in the Si IV AD method in Section 4-14, identifying several which could cause a spurious $|\Delta\alpha/\alpha| \lesssim 0.3 \times 10^{-5}$.

One possible avenue for future AD constraints may be the C IV λ1548/1550

Table 2.2. Si IV alkali doublet results. The raw results from the χ^2 minimization procedure are shown for each QSO absorption system. We identify the QSO emission redshift, $z_{\rm em}$, the absorption cloud redshift, $z_{\rm abs}$, and the value of $\Delta\alpha/\alpha$ for each absorption cloud with the associated $1\,\sigma$ error.

QSO	$z_{\rm em}$	$z_{\rm abs}$	$\Delta\alpha/\alpha$ (10^{-5})
0100+13	2.68	2.299	-3.05 ± 7.30
		2.309	8.96 ± 10.39
0149+33	2.43	2.065	-4.47 ± 16.81
		2.140	-12.93 ± 12.69
		2.204	-5.89 ± 6.68
0201+36	2.49	2.457	-4.50 ± 3.57
0347−38	3.24	2.810	3.04 ± 7.43
		2.899	-10.90 ± 10.87
		3.025	-4.05 ± 6.78
1759+75	3.05	2.624[a]	-5.98 ± 2.98
		2.849[a]	2.56 ± 3.29
		2.849	2.74 ± 3.88
		2.911	6.00 ± 9.89
		2.911[a]	0.65 ± 4.75
2206−20	2.56	2.014	-3.84 ± 6.59
		2.128	-3.48 ± 7.41
2231−00	3.02	2.641	0.20 ± 10.65
		2.986	4.23 ± 17.74
2348−14	2.94	2.279	10.38 ± 6.05
		2.530	3.76 ± 6.53
		2.775	14.04 ± 7.10

[a]These absorbers contributed by Outram et al. (1999).

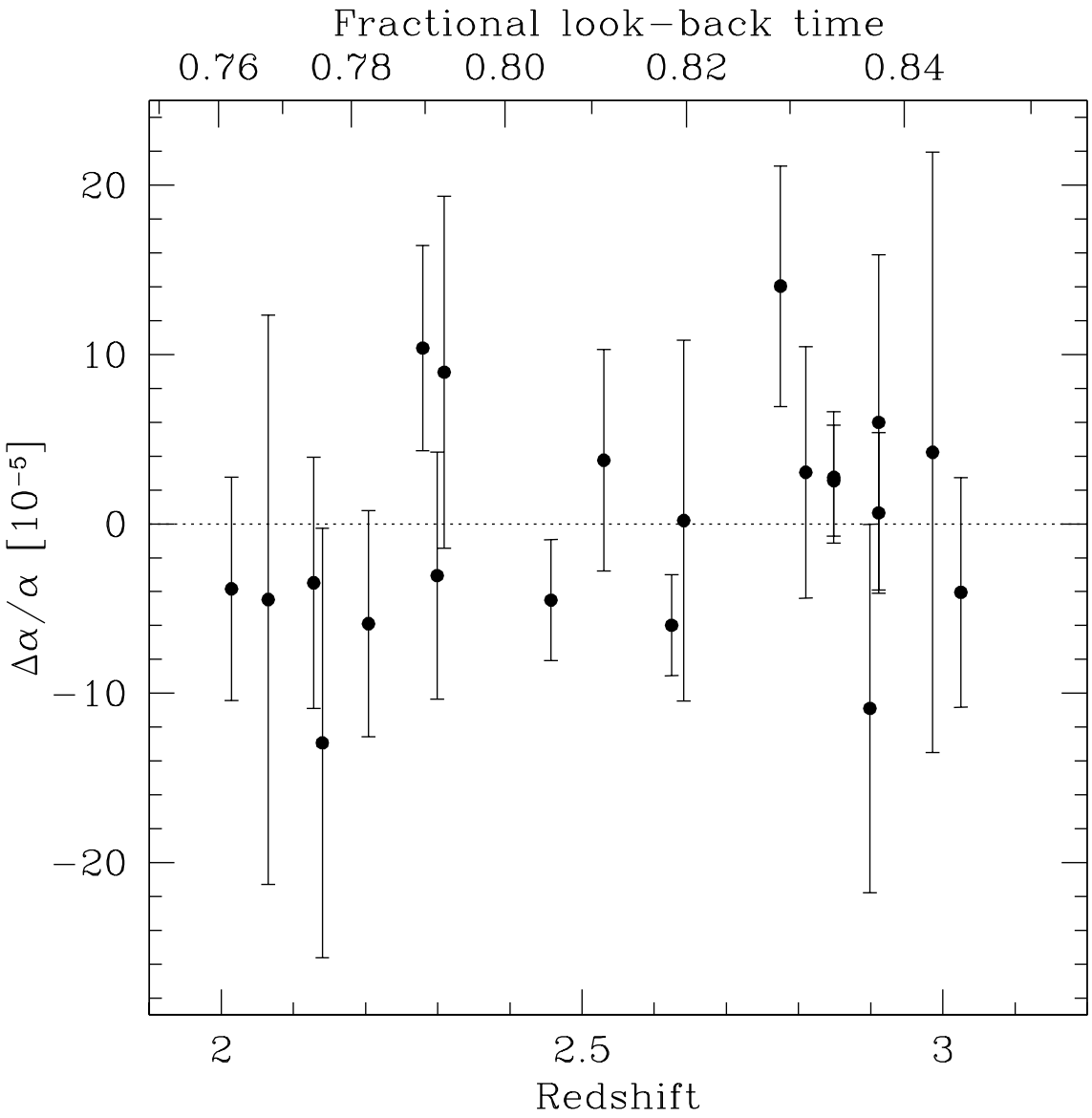

Figure 2.2. 21 Si IV alkali doublet constraints. We plot $\Delta\alpha/\alpha$ with $1\,\sigma$ errors for each absorption cloud against absorption redshift and fractional look-back time ($H_0 = 70\,\mathrm{kms^{-1}Mpc^{-1}}$, $\Omega_\mathrm{m} = 0.3$, $\Omega_\Lambda = 0.7 \rightarrow t_0 = 13.47\,\mathrm{Gyr}$). The weighted mean of the sample is $\Delta\alpha/\alpha = (-0.5 \pm 1.3) \times 10^{-5}$.

doublet, absorption from which is detected more often than Si IV absorption (e.g. Cowie et al. 1995). However, the q_1 coefficients for the C IV doublet transitions – calculated in Dzuba et al. (1999a) – are smaller than those for the Si IV values. This weakens the potential constraints on $\Delta\alpha/\alpha$. Despite this, a modest increase in precision could easily be achieved with present data if the C IV doublet labora-

tory wavelengths were known to high enough precision. Griesmann & Kling (2000) have increased the laboratory precision by an order of magnitude but the statistical uncertainty is still $\gtrsim 0.04\,\mathrm{cm}^{-1}$. This corresponds to an accuracy $\Delta\alpha/\alpha \sim 20\times10^{-5}$.

Despite the increase in precision achieved here, the many multiplet (MM) method described in Chapter 3 provides a further precision gain of up to an order of magnitude (per absorption system) with similar quality data. To reach this improved precision with the AD method, S/N $\gtrsim 200$ would be required. Moreover, the effect of systematic errors in the MM method is approximately the same as for the AD method. Therefore, once these systematic errors are understood and can be reliably removed from QSO absorption data, the MM method is certainly preferred for probing $\Delta\alpha/\alpha$ to high precision at high redshift.

An idea that is not dangerous is unworthy to be called an idea at all.

Elbert Hubbard (1856–1915)

Chapter 3

A non-zero $\Delta\alpha/\alpha$ from the many-multiplet (MM) method

Here we describe the recently-introduced many-multiplet (MM) method of constraining $\Delta\alpha/\alpha$ with QSO absorption lines. We apply this technique to 3 independent samples of Keck/HIRES spectra containing a total of 128 absorption systems over the redshift range $0.2 < z_{\rm abs} < 3.7$. This analysis leads to the main result of this thesis: $5.6\,\sigma$ statistical evidence for a smaller α in the QSO absorption clouds.

3-1 The many-multiplet (MM) method

3-1.1 Theoretical basis

Introduced by V. Dzuba, V. V. Flambaum and J. K. Webb in Webb et al. (1999, hereafter W99) and Dzuba et al. (1999b), the many-multiplet (MM) method is a generalization of the AD method, allowing an order of magnitude precision gain from similar quality data. The full details behind this technique are presented in Dzuba et al. (1999a, 2001b, 2002). Therefore, we only outline the salient features of the method below.

We begin with a simple analytic approach to estimate the relativistic effects in transition frequencies. If we consider a many-electron atom/ion then the relativistic correction, Δ, to the energy of the external electron can be written as

$$\Delta \propto (Z_n\alpha)^2 \, |E|^{3/2} \left[\frac{1}{j+1/2} - C(j,l) \right] , \tag{3.1}$$

where Z_n is the nuclear charge, E is the electron energy ($E < 0$, $|E|$ is the ionization potential) and j and l are the total and orbital electron angular momenta. The contribution to the relativistic correction from many-body effects is described by $C(j,l)$. For s and p orbitals, $C(j,l) \approx 0.6$ and is of similar magnitude for d orbitals. Equation 3.1 therefore provides a general strategy for probing the relativistic corrections in resonance transitions.

For example, consider comparison of the transition energies of two s–p transitions, one in a light ion, the other in a heavy ion (i.e. low and high Z_n respectively). The Z_n^2 term dominates so the relativistic corrections to the transition energies will differ greatly. Thus, comparison of the spectra of light and heavy species is a sensitive probe of α-variation.

As a further example, consider an s–p and a d–p transition in a heavy species. The corrections will be large in each case but will be of opposite sign since the many-body corrections, $C(j,l)$, begin to dominate with increasing j. This situation also allows tight constraints to be placed on changes in α.

Thus, comparing spectra of transitions from different multiplets and different atoms or ions, provides a sensitive method for probing variations in α. In comparison, the fine splitting of an s–p doublet will be substantially smaller than the absolute shift in the s–p transition energy since the excited p electron, with relatively small $|E|$, will have much smaller relativistic corrections than the s electron (see Fig. 3.1). Therefore, the AD method is relatively insensitive to variations in α.

More formally, the energy equation for a transition from the ground state, within a particular multiplet, at a redshift z, can be written as

$$E_z = E_c + Q_1 Z_n^2 \left[\left(\frac{\alpha_z}{\alpha_0} \right)^2 - 1 \right] + K_1(\mathbf{LS}) Z_n^2 \left(\frac{\alpha_z}{\alpha_0} \right)^2 + K_2(\mathbf{LS})^2 Z_n^4 \left(\frac{\alpha_z}{\alpha_0} \right)^4 , \tag{3.2}$$

where α_z may or may not be equal to the laboratory value, α_0. Here, **L** and **S** are the electron total orbital angular momentum and total spin respectively and E_c is the energy of the configuration centre. Q_1, K_1 and K_2 are relativistic coefficients which have been accurately computed in Dzuba et al. (1999a, 2001a,b, 2002) using *ab initio* many-body calculations to include all dominant relativistic effects. Equation 3.2 forms the basis of the MM method.

For our purposes, the most convenient form of equation 3.2 is written as

$$\omega_z = \omega_0 + q_1 x_z + q_2 y_z \,, \tag{3.3}$$

where ω_z is the wavenumber in the rest-frame of the cloud, at redshift z, ω_0 is the wavenumber as measured on Earth and x_z and y_z contain the information about a possible non-zero $\Delta\alpha/\alpha$:

$$x_z \equiv \left(\frac{\alpha_z}{\alpha_0}\right)^2 - 1 \quad \text{and} \quad y_z \equiv \left(\frac{\alpha_z}{\alpha_0}\right)^4 - 1 \,. \tag{3.4}$$

If $\alpha_z \neq \alpha_0$ then x_z and y_z are non-zero and the magnitude and sign of q_1 and q_2 determine the shift in the transition wavenumber. Since we only consider $\Delta\alpha/\alpha \ll 1$, we may write

$$\omega_z = \omega_0 + q x_z \,, \tag{3.5}$$

where we consolidate q_1 and q_2 into $q \equiv q_1 + 2q_2$. The q coefficient represents all the relativistic corrections for the transition of interest and varies both in magnitude and sign from transition to transition (see Fig. 3.3). That is, if $\Delta\alpha/\alpha \neq 0$, the QSO absorption lines will be shifted in a distinct pattern with respect to their laboratory values.

3-1.2 Comparison with the AD method

Fig. 3.1 illustrates the difference between the AD and MM methods. The AD method is simple, but inefficient. The s ground state is most sensitive to changes in α (i.e. it has the largest relativistic corrections) but is common to both transitions (Fig. 3.1a). The MM method compares transitions from different multiplets and/or atoms, allowing the ground states to constrain $\Delta\alpha/\alpha$ (Fig. 3.1b).

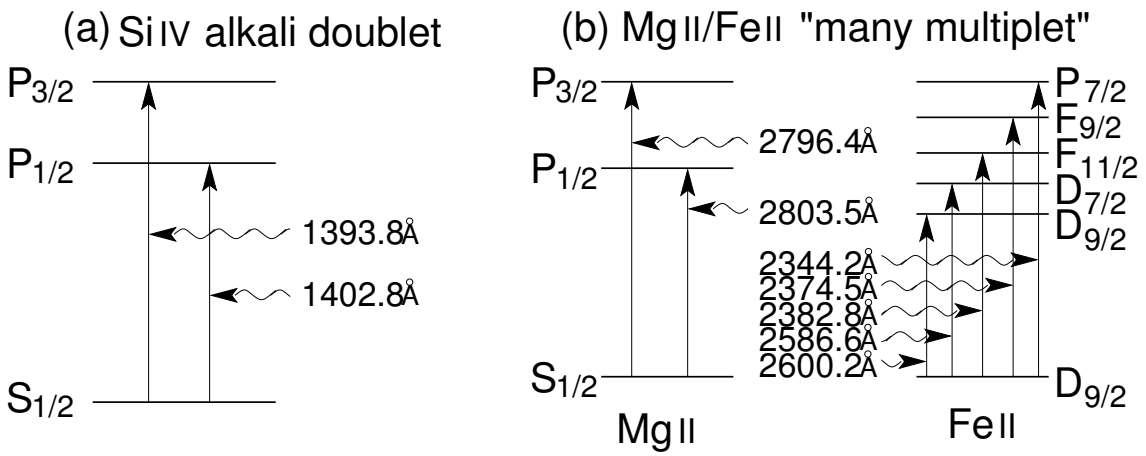

Figure 3.1. **(a)** The AD method is not sensitive to the maximal relativistic corrections in the common s ground state. **(b)** Comparison of different ions increases sensitivity to $\Delta\alpha/\alpha$, increases statistics and decreases systematic errors.

We may summarize the advantages of the MM method over the AD method as follows:

1. By including *all* relativistic corrections (i.e. including those for the ground state) there is a sensitivity gain of around an order of magnitude compared to the AD method.

2. In principle, all transitions appearing in a QSO absorption system may be used. This provides an obvious statistical gain and a more precise constraint on $\Delta\alpha/\alpha$ compared to using a single AD alone.

3. A further advantage of using many transitions is that the velocity structure is determined with much greater reliability due to the larger range of line strengths (see Section 3-3.2 for further explanation).

4. A very important advantage is that comparison of transitions with positive and negative q coefficients minimizes systematic effects (see Section 3-3.2 in particular).

3-1.3 First application to QSO absorption systems

W99 first applied the MM method to 30 Keck/HIRES QSO absorption systems (towards 14 QSOs) in the absorption redshift range $0.5 < z_{\rm abs} < 1.6$, fitting the Mg I λ2853 line, the Mg II $\lambda\lambda$2796/2803 doublet and the five strongest Fe II lines between λ2344 and λ2600 (see Fig. 3.1). The Z_n^2 dependence in equation 3.2 means that the Mg lines act as anchors against which the large shifts in the Fe II lines can be used to constrain $\Delta\alpha/\alpha$. The difference in q values ($\Delta q \approx 1200\,{\rm cm}^{-1}$) is much larger than for the Si IV transitions in the AD method ($\Delta q \approx 500\,{\rm cm}^{-1}$, see Table 2.1) and so the MM method allows significantly increased precision. Additionally, analysing the 5 Fe II and 3 Mg transitions allows a statistical gain over the AD method. W99 explicitly demonstrated this increased precision, obtaining the first tentative evidence for a smaller α in the absorption clouds:

$$\Delta\alpha/\alpha = (-1.09 \pm 0.36) \times 10^{-5}\,. \tag{3.6}$$

The 'detection' was dominated by the 14 systems above $z_{\rm abs} = 1$ [$\Delta\alpha/\alpha = (-1.88 \pm 0.53) \times 10^{-5}$] whereas $\Delta\alpha/\alpha$ was consistent with zero at lower redshifts [$\Delta\alpha/\alpha = (-0.17 \pm 0.39) \times 10^{-5}$].

In this chapter we extend the W99 analysis to a much larger sample of Mg/Fe II systems in a similar redshift range. We also apply the MM method to higher redshift absorption systems in which we detect transitions of many different species.

3-2 Atomic data

We summarize all relevant atomic data for the MM transitions of interest in Table 3.1, discussing the key quantities, q and ω_0, below.

[1] Available at http://kingpin.ucsd.edu/~hiresdla.

Table 3.1. Atomic data for the MM transitions in our analysis. Information for isotopic and hyperfine components is given in italics. Column 2 shows the nucleon number for each species. The origin of the laboratory wavenumbers (ω_0) and wavelengths (λ_0) is summarized in Section 3-2.2. Columns 5 and 6 show the ground and excited state electronic configurations. The ID letters in column 7 are used in Table 3.4 to indicate the transitions used in our fits to each absorption system. The ionization potential, (IP)[a], is given in column 8. Column 9 shows the oscillator strengths, f, from the DLA database[1] of Prochaska et al. (2001) or the relative strengths of the isotopic (Rosman & Taylor 1998) or hyperfine components (italics). The q coefficients are from Dzuba et al. (1999a,b, 2001b, 2002) and the uncertainties are discussed in Section 3-2.1. The Si II, Al II and Al III wavenumbers have been scaled from their literature values due to the Norlén/Whaling et al. calibration difference (see Section 3-2.2).

Ion	A	λ_0 (Å)	ω_0 (cm^{-1})	Ground	Upper	ID	IP (eV)	f or %	q (cm^{-1})
Mg I	24.32	2852.96310(8)	35051.277(1)[b]	$3s^2\ ^1S_0$	$3s3p\ ^1P_1$	a	–	1.81	86(10)
	26	*2852.95977*	*35051.318*[b]					*11.0*	
	25	*2852.96316*	*35051.295*[b]					*10.0*	
	24	*2852.96359*	*35051.271*[b]					*79.0*	
Mg II	24.32	2796.3543(2)	35760.848(2)[b]	$3s\ ^2S_{1/2}$	$3p\ ^2P_{3/2}$	b	7.7	0.6123	211(10)
	26	*2796.3473*	*35760.937*[b]					*11.0*	
	25	*2796.3492*	*35760.913*[b]					*5.8*	
	25	*2796.3539*	*35760.853*[b]					*4.2*	
	24	*2796.3553*	*35760.835*[b]					*79.0*	

Table. 3.1 – *continued.* Atomic data for the MM transitions.

Ion	A	λ_0 (Å)	ω_0 (cm^{-1})	Ground	Upper	ID	IP (eV)	f or %	q (cm^{-1})
Mg II	24.32	2803.5315(2)	35669.298(2)[b]		$3p\ ^2P_{1/2}$	c		0.3054	120(10)
	26	*2803.5244*	*35669.388*[b]					*11.0*	
	25	*2803.5258*	*35669.370*[b]					*3.0*	
	25	*2803.5266*	*35669.360*[b]					*2.8*	
	25	*2803.5305*	*35669.310*[b]					*1.5*	
	25	*2803.5313*	*35669.300*[b]					*2.7*	
	24	*2803.5324*	*35669.286*[b]					*79.0*	
Al II	27.00	1670.7887(1)	59851.972(4)[c]	$3s^2\ ^1S_0$	$3s3p\ ^1P_1$	d	6.0	1.88	270(30)
Al III	27.00	1854.71841(3)	53916.540(1)[c]	$3s\ ^2S_{1/2}$	$3p\ ^2P_{3/2}$	e	18.9	0.539	464(30)
		1854.70910(3)	*53916.8111(8)*[c]					*41.7*	
		1854.72483(2)	*53916.3536(6)*[c]					*58.3*	
		1862.79126(7)	53682.880(2)[c]		$3p\ ^2P_{1/2}$	f		0.268	216(30)
		1862.78046(5)	*53683.1915(15)*[c]					*41.7*	
		1862.79871(4)	*53682.6654(12)*[c]					*58.3*	

Table. 3.1 – *continued.* Atomic data for the MM transitions.

Ion	A	λ_0 (Å)	ω_0 (cm^{-1})	Ground	Upper	ID	IP (eV)	f or %	q (cm^{-1})
Si II	28.11	1526.70709(2)	65500.4492(7)[c]	$3s^2 3p\ ^2\mathrm{P}^\mathrm{o}_{1/2}$	$3s^2 4s\ ^2\mathrm{S}_{1/2}$	g	8.2	0.127	68(30)
	30	*1526.7040*	*65500.583*					*3.1*	
	29	*1526.7055*	*65500.517*					*4.7*	
	28	*1526.7073*	*65500.442*					*92.2*	
		1808.01301(1)	55309.3365(4)[c]		$3s3p^2\ ^2\mathrm{D}_{3/2}$	h		0.00218	531(30)
	30	*1808.0094*	*55309.446*					*3.1*	
	29	*1808.0113*	*55309.390*					*4.7*	
	28	*1808.0132*	*55309.330*					*92.2*	
Cr II	52.06	2056.25693(8)	48632.055(2)[d]	$3d^5\ ^6\mathrm{S}_{5/2}$	$3d^4 4p\ ^6\mathrm{P}^\mathrm{o}_{7/2}$	i	6.8	0.105	−1107(150)
		2062.23610(8)	48491.053(2)[d]		$3d^4 4p\ ^6\mathrm{P}^\mathrm{o}_{5/2}$	j		0.078	−1251(150)
		2066.16403(8)	48398.868(2)[d]		$3d^4 4p\ ^6\mathrm{P}^\mathrm{o}_{3/2}$	k		0.0515	−1334(150)

Table. 3.1 – *continued.* Atomic data for the MM transitions.

Ion	A	λ_0 (Å)	ω_0 (cm^{-1})	Ground	Upper	ID	IP (eV)	f or %	q (cm^{-1})
Fe II	55.91	1608.45085(8)	62171.625(3)[e]	$3d^64s\ a^6\mathrm{D}_{9/2}$	$3d^54s4p\ y^6\mathrm{P}^\mathrm{o}_{7/2}$	l	7.9	0.0580	−1200(300)
		1611.20034(8)	62065.528(3)[e]		$3d^64p\ y^4\mathrm{F}^\mathrm{o}_{7/2}$	m		0.00136	1050(300)
		2344.2130(1)	42658.2404(2)[f]		$3d^64p\ z^6\mathrm{P}^\mathrm{o}_{7/2}$	n		0.114	1254(150)
		2374.4603(1)	42114.8329(2)[f]		$3d^64p\ z^6\mathrm{F}^\mathrm{o}_{9/2}$	o		0.0313	1640(150)
		2382.7642(1)	41968.0642(2)[f]		$3d^64p\ z^6\mathrm{F}^\mathrm{o}_{11/2}$	p		0.320	1498(150)
		2586.6496(1)	38660.0494(2)[f]		$3d^64p\ z^6\mathrm{D}^\mathrm{o}_{7/2}$	q		0.06918	1520(150)
		2600.1725(1)	38458.9871(2)[f]		$3d^64p\ z^6\mathrm{D}^\mathrm{o}_{9/2}$	r		0.23878	1356(150)
Ni II	58.76	1709.6042(1)	58493.071(4)[d]	$3d^9\ ^2\mathrm{D}_{5/2}$	$3d^84p\ z^2\mathrm{F}^\mathrm{o}_{5/2}$	s	7.6	0.0324	−20(250)
		1741.5531(1)	57420.013(4)[d]		$3d^84p\ z^2\mathrm{D}^\mathrm{o}_{5/2}$	t		0.0427	−1400(250)
		1751.9157(1)	57080.373(4)[d]		$3d^84p\ z^2\mathrm{F}^\mathrm{o}_{7/2}$	u		0.0277	−700(250)
Zn II	65.47	2026.13709(8)	49355.002(2)[d]	$3d^{10}4s\ ^2\mathrm{S}_{1/2}$	$3d^{10}4p\ ^2\mathrm{P}^\mathrm{o}_{3/2}$	v	9.4	0.489	2479(25)
		2062.66045(9)	48481.077(2)[d]		$3d^{10}4p\ ^2\mathrm{P}^\mathrm{o}_{1/2}$	w		0.256	1577(25)

[a]IP is defined here to be the energy required to form the ion in question from the ion with a unit lower charge; [b]Pickering et al. (1998); [c]Griesmann & Kling (2000); [d]Pickering et al. (2000); [e]Pickering et al. (2002); [f]Nave et al. (1991).

3-2.1 The q coefficients

The values of q for Mg I and Mg II are taken from Dzuba et al. (1999a,b) and those for Al II and Al III are from Dzuba et al. (2001b). All other q coefficients are from updated calculations of the type detailed in Dzuba et al. (2002), kindly provided by V. Dzuba. The uncertainties in q are typically $\lesssim 30\,\mathrm{cm}^{-1}$ for the Mg, Si, Al and Zn transitions but are $\lesssim 300\,\mathrm{cm}^{-1}$ for those of Cr, Fe and Ni due to the more complicated electronic configurations involved. These represent conservative error estimates made by comparing other calculated quantities (e.g. energy intervals, g-factors) with their experimental values and by comparing the results of several different calculation techniques. Thus, the errors quoted in Table 3.1 should be reliable but should not be treated as statistical.

It is important to note that, in the absence of systematic effects in the QSO spectra, the form of equation 3.5 ensures that errors in the q coefficients can not lead to a non-zero $\Delta\alpha/\alpha$.

From equation 3.2 we see that q will be much larger in heavier ions due to the Z_n^2 dependence. Indeed, one can see in Table 3.1 several *combinations of transitions from different ions*, of very different mass, showing large differences between their respective q coefficients. As described in Section 3-1.3, W99 combined the Mg I λ2852 line, the Mg II doublet and the five Fe II lines between λ2344 and λ2600 since the Fe II q coefficients are typically an order of magnitude larger than those of the Mg lines. For comparison, we present the line shifts in wavenumber, wavelength and velocity space arising from a shift of $\Delta\alpha/\alpha = +10^{-5}$ in Table 3.2.

Further examination of the q coefficients in Table 3.1 reveals several other very useful combinations of lines. In particular, note the large *negative* values for the Cr II lines. A comparison between Cr II spectra and that of Zn II – the λ2026 transition having the largest magnitude value of q – provides the most sensitive combinations for probing non-zero $\Delta\alpha/\alpha$. Also, note the coefficients for Ni II. Here, within the same species (but different multiplets), we have both very small and very large (negative) values for q. This is due to the very complicated multiplet structure of

Table 3.2. Shift in the rest frame wavenumber, wavelength and velocity space for $\Delta\alpha/\alpha = +10^{-5}$

Transition	$\Delta\omega$ ($10^{-2}\,\mathrm{cm}^{-1}$)	$\Delta\lambda$ (10^{-3} Å)	Δv (kms^{-1})
Mg I λ2853	0.21	0.17	−0.018
Mg II λ2796	0.42	0.33	−0.035
Mg II λ2803	0.24	0.19	−0.020
Al II λ1670	0.54	0.15	−0.027
Al III λ1854	0.93	0.32	−0.052
Al III λ1862	0.43	0.15	−0.024
Si II λ1526	0.10	0.023	−0.0046
Si II λ1808	1.04	0.34	−0.056
Cr II λ2056	−2.22	−0.94	0.137
Cr II λ2062	−2.56	−1.09	0.158
Cr II λ2066	−2.72	−1.16	0.168
Fe II λ1608	−2.60	−0.67	0.125
Fe II λ1611	2.20	0.57	−0.106
Fe II λ2344	2.42	1.33	−0.170
Fe II λ2374	3.18	1.79	−0.226
Fe II λ2383	2.92	1.66	−0.209
Fe II λ2587	2.98	1.99	−0.231
Fe II λ2600	2.66	1.80	−0.207
Ni II λ1709	−0.04	−0.012	0.0021
Ni II λ1741	−2.80	−0.85	0.146
Ni II λ1751	−1.40	−0.43	0.074
Zn II λ2026	4.98	2.04	−0.302
Zn II λ2062	3.17	1.35	−0.196

Ni II, as discussed in detail in Dzuba et al. (2001b). Also, the Fe II $\lambda\lambda$1608 and 1611 lines have large q values of opposite sign.

3-2.2 Laboratory wavelengths

If we are to fully utilize the increased precision offered by the MM method for a single absorption system, the laboratory wavenumbers of the MM transitions – ω_0 in equation 3.5 – must be known to a precision of $\delta\omega_0 \sim 0.03\,\mathrm{cm}^{-1}$. Typical absolute errors for most important transitions are $\gtrsim 0.05\,\mathrm{cm}^{-1}$ (Morton 1991). If we are to avoid significant systematic errors when averaging over ∼100 absorption systems then we require $\delta\omega_0 \lesssim 0.003\,\mathrm{cm}^{-1}$ for each MM transition of interest. Since the existing precision is too low for our work, laboratory measurements were performed by several different groups using Fourier transform spectrometry (FTS) specifically for use with the MM method. We discuss the measurements for each ion below, concentrating on those issues most relevant to our analysis.

1. Mg I and Mg II: These spectra have recently been measured by Pickering et al. (1998). The spectra of Ni I and Ni II were excited along with those of Mg I and Mg II and several of these lines were used for calibration. The Ni I spectrum of Litzen et al. (1993) was used for reference which itself was calibrated from the Fe I and Fe II lines of Nave et al. (1991). The Mg II λ2796 wavelength has been measured previously by Drullinger et al. (1980) and Nagourney & Dehmelt (1981) and the wavenumbers are in excellent agreement. Also, a confirmation of the Pickering et al. (1998) wavenumbers has been made and is described briefly in Pickering et al. (2000).

   Since Mg is a relatively light atom, the isotopic structure of the line profile must be taken into account (see equation 3.7). Pickering et al. (1998) used the isotopic spacings measured by Hallstadius (1979) to obtain absolute wavelengths for the isotopes. They also included the hyperfine spacings found by Drullinger et al. (1980). These values are listed in Table 3.1 and the full isotopic/hyperfine structures are used in our analysis.

2. Si II, Al II and Al III: These spectra have recently been measured by Griesmann & Kling (2000). The C IV and Si IV spectra were also measured and all spectra were calibrated using the Ar II spectrum of Whaling et al. (1995). At present, there are no other similarly precise measurements of these spectra.

   To our knowledge, the isotopic spacings for the Si II transitions have not been measured. The mass and specific isotopic shifts should dominate the volume isotopic shift in such a light ion. The λ1526 transition is very similar to those of Mg II and so the specific shift should be of the same order. Thus, to estimate the isotopic spacings in Si II λ1526 we have scaled the spacings of Mg II λ2796 by the mass shift:

   $$\Delta\omega_i \propto \omega_0/m_i^2 \tag{3.7}$$

   for $\Delta\omega_i$ the wavenumber shift for a given isotope i where m_i is the atomic mass. We have used these spacings to fit a synthetic Gaussian emission line (centred at the composite wavelength) in order to estimate the absolute wavenumbers for the isotopes. We present the results in Table 3.1. We performed similar calculations for the Si II λ1808 transition. However, the assumption that the specific shift for λ1808 is similar to that for the Mg II transitions is not so justified in this case since the transitions are of quite different type. Preliminary calculations for both transitions (J. Berengut, private communication) suggest that the specific shifts are of opposite sign to the normal mass shift and so the shifts in Table 3.1 are probably overestimates. We discuss any effect our approximation may have on the values of $\Delta\alpha/\alpha$ in Section 4-10, finding that it should be negligibly small.

3. Cr II and Zn II: These spectra have been measured independently using two different Fourier transform spectrometers: one at Imperial College, the other at Lund University. The two experiments are described in Pickering et al. (2000). The wavenumber calibration was based on the Fe I and II standards of Nave et al. (1991) in both cases.

4. Fe II: This spectrum, from 1750–3850 Å, is presented in Nave et al. (1991). The

wavelength calibration was done by comparison with the Norlén (1973) Ar II spectrum. No other (similarly precise) catalogues of Fe II lines exist in the literature. The Fe II $\lambda\lambda$1608 and 1611 wavenumbers come from similar experiments described briefly in Pickering et al. (2002).

5. Ni II: This spectrum was recently measured by Pickering et al. (2000). The original spectra were measured during the Mg I and II experiments by Pickering et al. (1998). Wavenumber calibration was done using the Ni II standards of Litzen et al. (1993) which cover the region down to about 2000 Å. The Ni I lines between 1750 Å and 2000 Å were calibrated with the Fe I and II lines so as to be used as calibration lines for the Ni II spectrum. R. Kling (private communication) has confirmed these wavenumbers, albeit with lower precision.

All wavelength calibrations above rely on the Ar II spectrum measured by either Norlén (1973) or Whaling et al. (1995). However, the Norlén and Whaling et al. calibrations systematically disagree. The Whaling et al. wavenumbers are larger and the difference between them is proportional to the wavenumber:

$$\delta\omega = 7 \times 10^{-8}\omega\,. \tag{3.8}$$

Note that this difference is linear in velocity space. Therefore, as long as we normalize all measured wavenumbers to the one calibration scale, any systematic error will be completely absorbed into the redshift parameter when we centroid corresponding velocity components in different transitions in the absorption systems (see Section 3-4 for further explanation). We choose to normalize all measured wavenumbers to the Norlén calibration scale and so the wavelengths of the Si II, Al II and Al III transitions in Table 3.1 have been scaled accordingly.

Also of note is that we only take into account the isotopic structures for the lightest two elements, Mg and Si. In the optically thin limit, the centroids of the isotopic structures described in Table 3.1 (italics) reduce to the composite values. When a line becomes optically thick, differential saturation of the isotopic components causes the centroid of the composite line to shift. This effect is discussed in

detail in Section 4-10.1: we find that neglecting the (unknown) isotopic structures for the heavier ions will have negligible effects on $\Delta\alpha/\alpha$.

It is interesting to note that, with the exception of the Fe II spectrum, the wavelengths presented in Table 3.1 are systematically longer than those compiled in Morton (1991) – a widely used list of resonance transition wavelengths. For a particular transition, the wavelengths are generally consistent but, taken altogether, a systematic trend is noted.

3-3 Keck/HIRES QSO spectra

3-3.1 Three independent samples

We analyse 128 absorption systems, observed towards 68 different QSOs using the high resolution spectrograph (HIRES, Vogt et al. 1994) on the Keck I 10-m telescope on Mauna Kea, Hawaii. The absorption redshifts cover the range $0.2 < z_{\rm abs} < 3.7$. The observations were carried out by three different groups and we segregate these independent samples throughout this thesis. We characterize each sample below. 7 of these absorption systems (towards 7 QSOs) were observed by two different groups, bringing the total number of independent Keck/HIRES spectra to 75.

3-3.1.1 Sample 1: 16 QSOs, 28 absorption systems, $0.5 < z_{\rm abs} < 1.8$.

These data were observed, reduced and kindly provided by C. W. Churchill. This sample comprises the same dataset analysed in W99 (though our analysis differs in some respects, see Section 3-4).

The observations were taken in July 1994, January 1995 and July 1996. The S/N per pixel ranged from 15–50 with most spectra having S/N $\sim$ 30 (see Fig. 3.2). The FWHM was $\sim$6.6 kms^{-1}($R = 45000$). The QSOs were generally bright ($m_{\rm V} \lesssim 17.5$) and so several short ($\sim$1000 s) exposures were taken of each object. Primarily, the data were reduced by Chris Churchill within IRAF[2]. Individual frames were overscan

[2]IRAF is distributed by the National Optical Astronomy Observatories, which are operated by

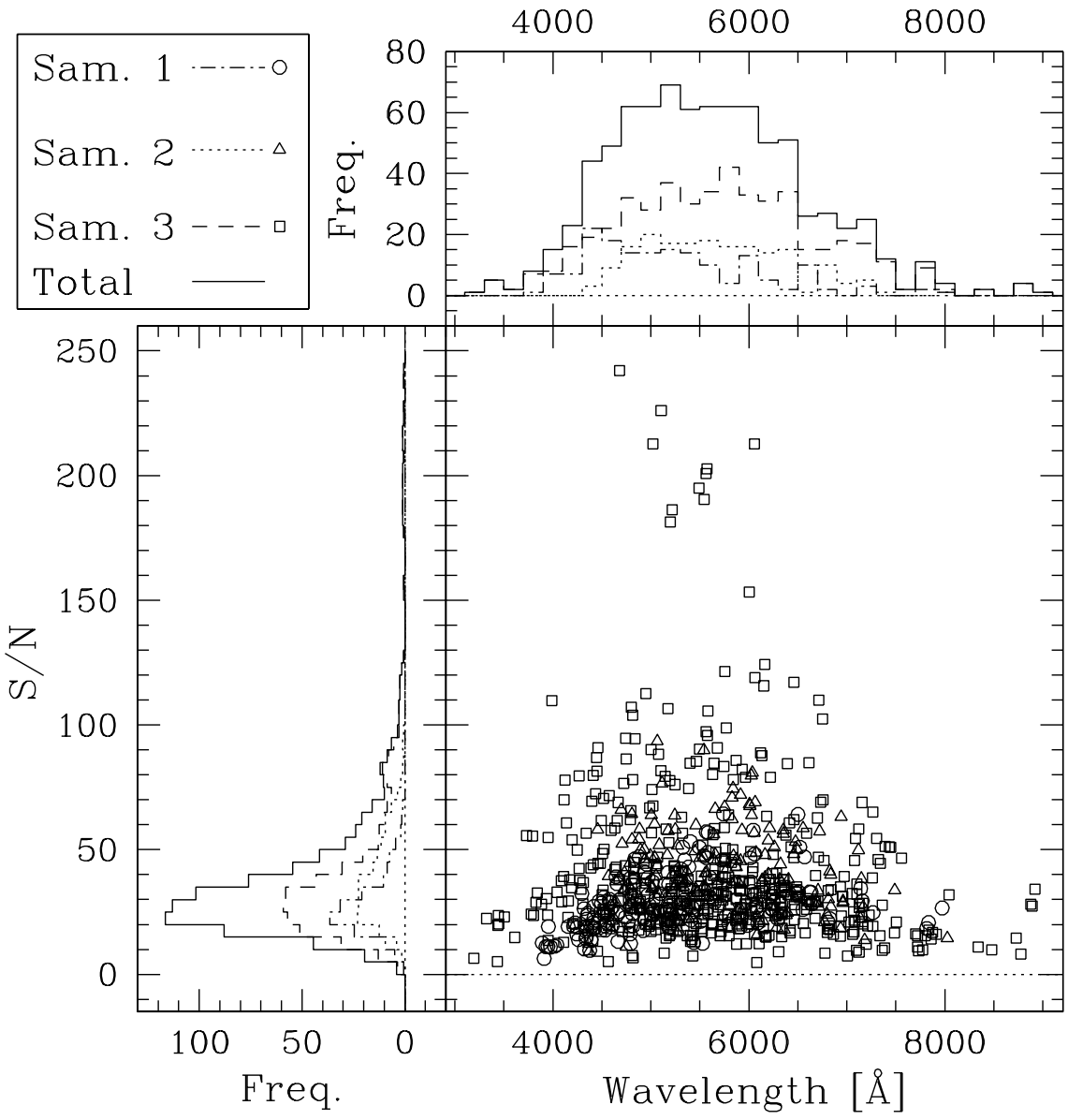

Figure 3.2. The distribution of S/N and central wavelength for the spectral regions of interest in the three samples of QSO spectra.

subtracted, bias frame corrected and flatfielded. Cosmic rays were removed by median filtering and the frames were averaged to form the final image. $1\,\sigma$ error arrays were generated assuming Poisson counting statistics. Full details of the reduction process are given in Churchill et al. (2000a). We fitted continua to regions of each spectrum containing any of the relevant transitions by fitting Legendre polynomials

the Association of Universities for Research in Astronomy, Inc., under cooperative agreement with the National Science Foundation.

to $\sim$500-kms^{-1} sections.

Wavelength calibration was carried out within IRAF: thorium–argon (ThAr) lamp exposures, taken before and after the QSO exposures, were co-added to provide a calibration spectrum. Centroiding selected ThAr lines yielded a wavelength solution. We note that no image rotator was installed during these observations and so the spectrograph slit was not perpendicular to the horizon in general. We present a detailed analysis of these points and their effect on $\Delta\alpha/\alpha$ in Section 4-11.

3-3.1.2 Sample 2: 13 QSOs, 23 absorption systems, $0.9 < z_{\rm abs} < 3.5$.

These data were observed, reduced and kindly provided by J. X. Prochaska and A. M. Wolfe. The observations were spread over many observing runs from 1994 to 1997. The S/N per pixel ranges from 15–40 with most spectra having S/N $\sim$ 30 (see Fig. 3.2). The spectral resolution was FWHM $\lesssim$ 7.5 kms^{-1} ($R = 34000$). The QSOs themselves are at higher redshift than those of sample 1 and so appear much fainter: $m_{\rm V} \lesssim 19.0$. Consequently, the total integration times were much longer and many more frames were co-added during the reduction process. An image rotator was installed in August 1996 and so only about half of the observations were carried out with the slit perpendicular to the horizon (see Section 4-11).

Most of the data were reduced using MAKEE[3], the HIRES data reduction package written by T. Barlow. This package converts the two-dimensional echelle images to fully reduced, one-dimensional, wavelength calibrated spectra (calibration spectra were taken in the same way as for sample 1). Some of the spectra were reduced when MAKEE had no wavelength calibration facility. In these cases, wavelength calibration was carried out using IRAF routines. The remainder of the spectra were fully reduced within IRAF. $1\,\sigma$ error arrays were generated assuming Poisson counting statistics. We fitted continua to regions of each spectrum containing any of the relevant transitions by fitting Legendre polynomials to $\sim$500-kms^{-1} sections. Full details of the reduction procedures can be found in Prochaska & Wolfe (1996, 1997,

[3]See http://www2.keck.hawaii.edu:3636/inst/hires/makeewww.

1999). Outram et al. (1999) have also kindly provided their spectrum of Q1759+75 which was taken in July 1997.

3-3.1.3 Sample 3: 46 QSOs, 78 absorption systems, $0.2 < z_{\rm abs} < 3.7$.

These data were observed, reduced and kindly provided by W. L. W. Sargent and collaborators (notably T. Barlow, M. Rauch and R. Simcoe). The observations were carried out during numerous observing runs from November 1993 to November 1999. All spectra were reduced with the MAKEE package. QSO exposure times ranged from 1000–6000 s depending on the QSO magnitude and between 3–16 separate exposures were combined to form the final spectrum. $1\,\sigma$ error arrays were generated assuming Poisson counting statistics. For each QSO spectrum we identified all absorption systems which contained enough MM transitions to yield meaningful constraints on $\Delta\alpha/\alpha$. We selected $\sim$500-kms^{-1} sections around each transition and defined a continuum by fitting a Legendre polynomial. The average S/N per pixel for these spectral regions of interest ranged from 4–240, with most sections having S/N ~ 30 (see Fig. 3.2). The spectral resolution for most spectra was FWHM $\approx 6.6\,$kms^{-1} ($R = 45000$). ThAr emission lamp spectra, taken both before and after the QSO exposures, were used to calibrate the wavelength scale.

All 3 samples are affected by a small but important error in the IRAF and MAKEE wavelength calibration software. This error concerns the conversion between air and vacuum wavelength scales and is discussed in detail in Section 4-5.

3-3.2 Low-z vs. high-z systems

Fig. 3.3 illustrates the distribution of q coefficients in (rest) wavelength space for the transitions in Table 3.1. The transitions of species with generally high abundances (i.e. Mg II, Al II, Si II and Fe II) fall into two, widely spaced wavelength regions, $\lambda < 1700\,$Å and $\lambda > 2300\,$Å. Detectable column densities of these species can be observed in the lower N(H I) (i.e. more common) Lyman limit systems (LLSs).

The remaining species are usually only detectable in the high N(H I), less common, damped Lyman-α systems (DLAs). Therefore, in systems at low-z ($z_{\rm abs} < 1.8$), we typically only detect transitions of Mg II and Fe II. This convenient delineation is further emphasized by the fact that sample 1 was targeted specifically at Mg/Fe II systems and sample 2 at high-z DLAs.

The low-z and high-z systems have several different properties due to the transitions involved (Table 3.3) and the arrangement of q coefficients (Fig. 3.3):

- **Low-z ($z_{\rm abs} < 1.8$)**: Sample 1 comprises only low-z systems containing Mg and Fe II transitions whereas some low-z systems in sample 3 contain other transitions. Sample 2 contains 3 low-z Mg/Fe II systems. We plot an example Mg/Fe II system from sample 3 in Fig. 3.4. Note that fitting a large number of transitions allows for a reliable determination of the velocity structure of the absorption complex. This is further facilitated by the range of line-strengths due to the differing Fe II oscillator strengths (see Table 3.1). In some cases the Mg II lines are saturated and so the Mg II lines themselves provide only weak constraints on $\Delta\alpha/\alpha$. However, the weak Mg I λ2852 line then often serves to provide a good constraint on the velocity structure.

  The arrangement of q coefficients for the Mg/Fe II systems is particularly simple: the Mg lines act as anchors against which the large potential shifts in the Fe II lines can be measured. For example, if $\Delta\alpha/\alpha < 0$, the Fe II lines shift redwards while the Mg lines remain relatively fixed (see Table 3.2). However, this situation may be mimicked by a relatively simple systematic error, i.e. one producing an overall compression of the wavelength scale with respect to the ThAr calibration frames.

- **High-z ($z_{\rm abs} > 1.8$)**: The high-z systems are characterized by a diverse range of transitions from different ionic species. Table 3.3 shows that the strong Si II λ1526, Al II λ1670 and Fe II λ1608 transitions are the most common. Fig. 3.5 illustrates a particularly high column density absorber where these ions are saturated in many components and the lower abundance species – Cr II, Ni II

Table 3.3. The frequency of occurrence for each transition in the different samples of QSO absorbers. For sample 3, we define low-z as $z_{\rm abs} < 1.8$ and high-z as $z_{\rm abs} > 1.8$. Sample 1 adheres to this definition but sample 2 does contain 3 low-z systems. The low-z samples are dominated by the Mg/Fe II transitions. The high-z systems contain a diverse range of transitions and species but the strong Si II λ1526, Al II λ1670 and Fe II λ1608 transitions are the most common.

Transition	Frequency of occurrence						
	low-z samples			high-z samples			Total
	1	3	Tot.	2	3	Tot.	
Mg I λ2852	6	21	27	1	0	1	28
Mg II λ2796	25	36	61	2	0	2	63
Mg II λ2803	26	37	63	3	1	4	67
Al II λ1670	0	5	5	11	30	41	46
Al III λ1854	0	6	6	6	11	17	23
Al III λ1862	0	6	6	4	9	13	19
Si II λ1526	0	3	3	19	26	45	48
Si II λ1808	0	3	3	15	8	23	26
Cr II λ2056	0	2	2	9	7	16	18
Cr II λ2062	0	1	1	10	7	17	18
Cr II λ2066	0	0	0	8	7	15	15
Fe II λ1608	0	4	4	19	28	47	51
Fe II λ1611	0	1	1	9	6	15	16
Fe II λ2344	21	26	47	5	7	12	59
Fe II λ2374	10	20	30	3	2	5	35
Fe II λ2382	22	34	56	3	5	8	64
Fe II λ2587	20	34	54	3	3	6	60
Fe II λ2600	25	36	61	3	3	6	67

Table. 3.3 – *continued.* The frequency of occurrence for each transition.

Transition	Frequency of occurrence						
	low-z samples			high-z samples			Total
	1	3	Tot.	2	3	Tot.	
Ni II λ1709	0	0	0	7	7	14	14
Ni II λ1741	0	1	1	12	6	18	19
Ni II λ1751	0	1	1	12	8	20	21
Zn II λ2026	0	1	1	7	6	13	14
Zn II λ2062	0	1	1	7	6	13	14

and Zn II – can be used to constrain the velocity structure. Theoretically, the large magnitude of the q coefficients for the transitions of these species makes them very important for constraining $\Delta\alpha/\alpha$ (see Fig. 3.3). However, since their optical depths are typically $\lesssim 0.3$ and since they are not detected in all high-z systems, their influence over $\Delta\alpha/\alpha$ is reduced.

In 25 spectra we have also fitted either or both of the two Al III transitions. Variations in the incident radiation field could give rise to changes in the relative column densities when comparing species with ionization potentials above and below the Lyman limit. In our sample, the Al III velocity structures corresponded well with those of the singly ionized atoms, consistent with the conclusions of Wolfe & Prochaska (2000). In some cases, however, some velocity components in the Al III profiles were much weaker or stronger relative to the other components when compared with the profiles of singly ionized species. In one case (sample 2), our fitting algorithm removed many weak Al III components from the fit (see Section 3-4) and so we removed the Al III data in this instance.

The arrangement of q coefficients for the high-z systems is far more complex than for the low-z Mg/Fe II systems. Any systematic effects which lead to low-order distortions of the wavelength scale (i.e. a compression or expansion) will have a varied and complex effect on $\Delta\alpha/\alpha$ depending on which transitions are

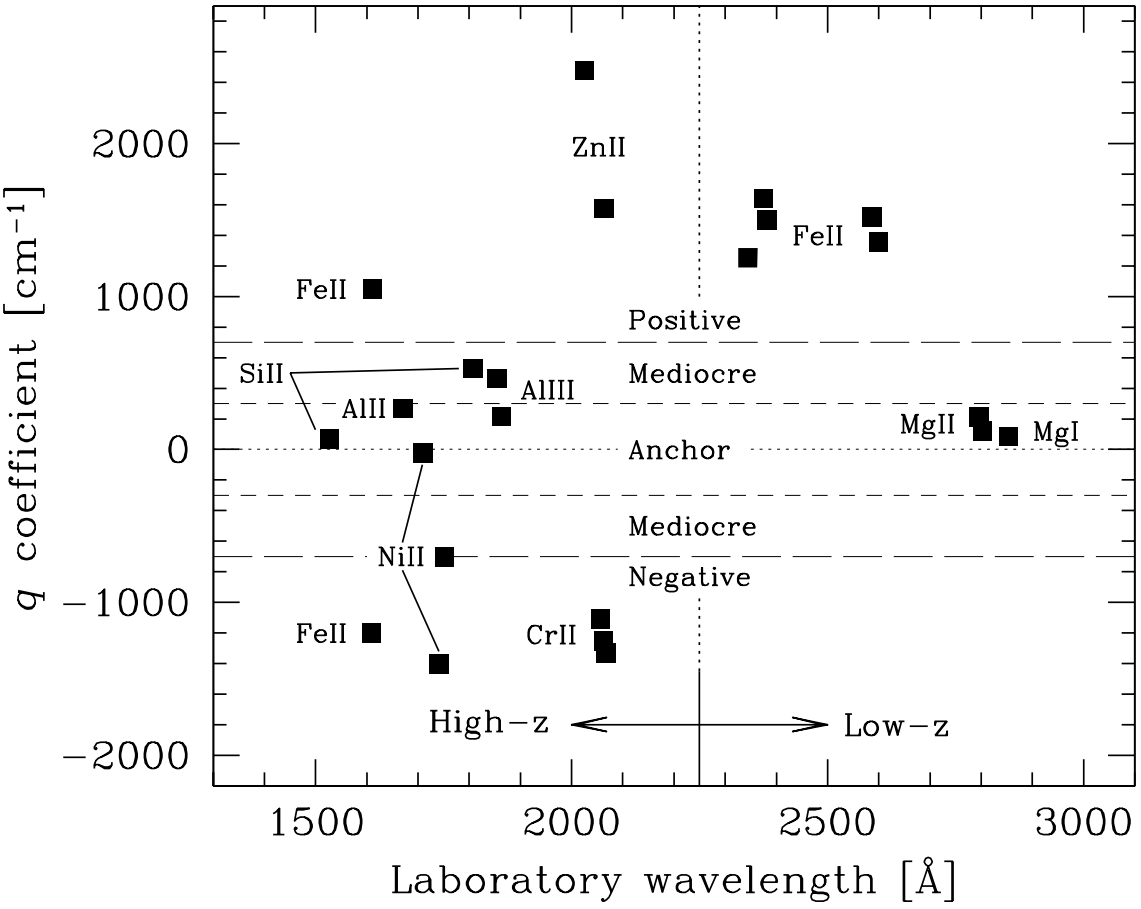

Figure 3.3. The distribution of q coefficients in (rest) wavelength space for the low- and high-z samples. Note the simple arrangement for the low-z Mg/Fe II systems: the Mg transitions are used as anchors against which the large, positive shifts in the Fe II transitions can be measured. Compare this with the complex arrangement for the high-z systems: low-order distortions to the wavelength scale will have a varied and complex effect on $\Delta\alpha/\alpha$ depending on which transitions are fitted in a given absorption system. In general, the complexity at high-z will yield more robust values of $\Delta\alpha/\alpha$. The transitions and q coefficients used here are listed in Table 3.1. For the discussion in Sections 4-12.2 and 4-12.3 we define several different 'q-types' as follows: positive-shifters ($q \geq 700\,\mathrm{cm}^{-1}$), negative-shifters ($q \leq -700\,\mathrm{cm}^{-1}$), anchors ($|q| < 300\,\mathrm{cm}^{-1}$) and mediocre-shifters ($300 \leq |q| < 700\,\mathrm{cm}^{-1}$).

fitted in a given absorption system. In general, the complex arrangement of q values at high-z will yield more robust values of $\Delta\alpha/\alpha$.

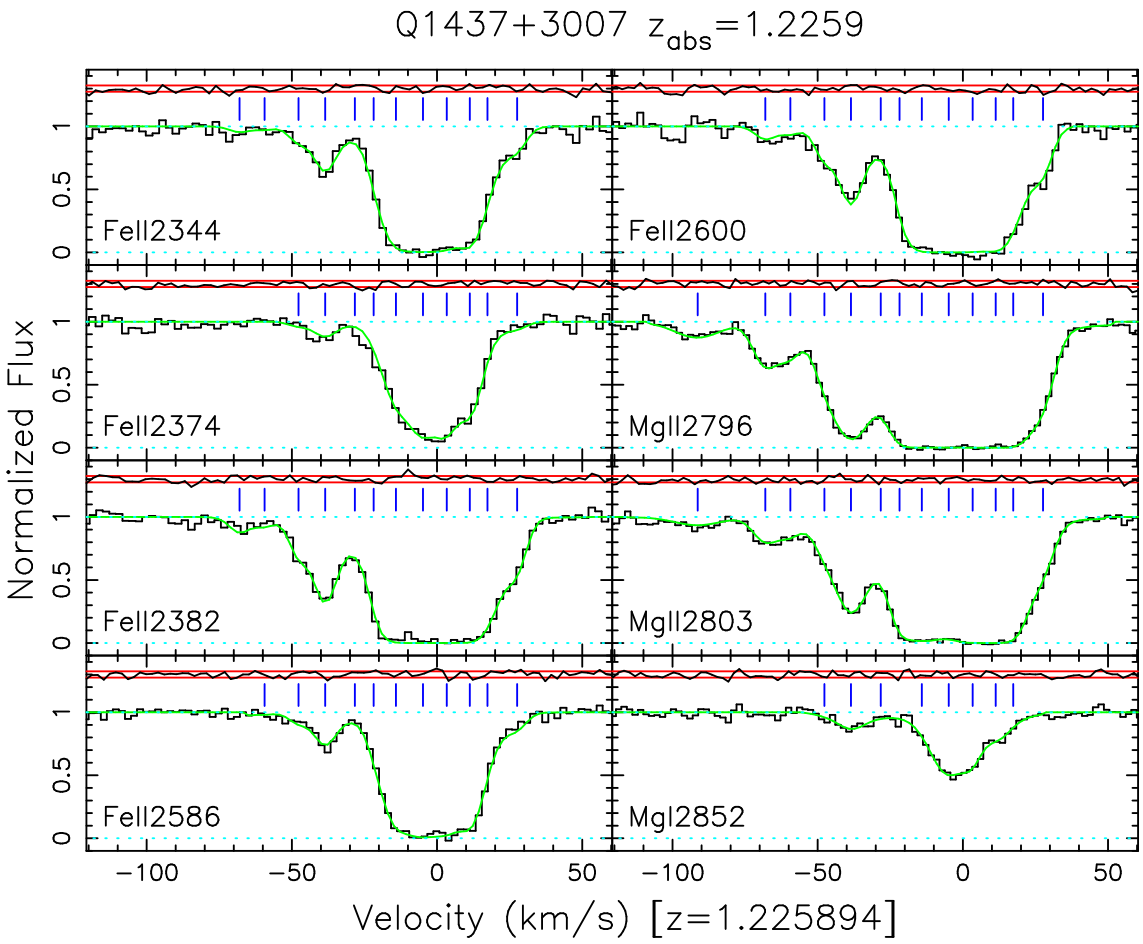

Figure 3.4. Mg/Fe II absorption system towards Q1437+3007 at $z_{\rm abs} = 1.2259$. The data have been normalized by a fit to the continuum and plotted as a histogram. Our Voigt profile fit (solid curve) and the residuals (i.e. [data]−[fit]), normalized to the 1σ errors (horizontal solid lines), are also shown. The tick–marks above the continuum indicate individual velocity components. Note the range of line-strengths in Fe II, facilitating determination of the velocity structure. The large number of Fe II transitions and the large number of velocity components allows for tight constraints to be placed on $\Delta\alpha/\alpha$. The Mg I λ2853 and Fe II λ2374 transition constrain $\Delta\alpha/\alpha$ with the velocity $\approx 0\,{\rm kms}^{-1}$ components whereas the Mg II and remaining Fe II transitions constrain $\Delta\alpha/\alpha$ with the velocity $\approx -40\,{\rm kms}^{-1}$ component.

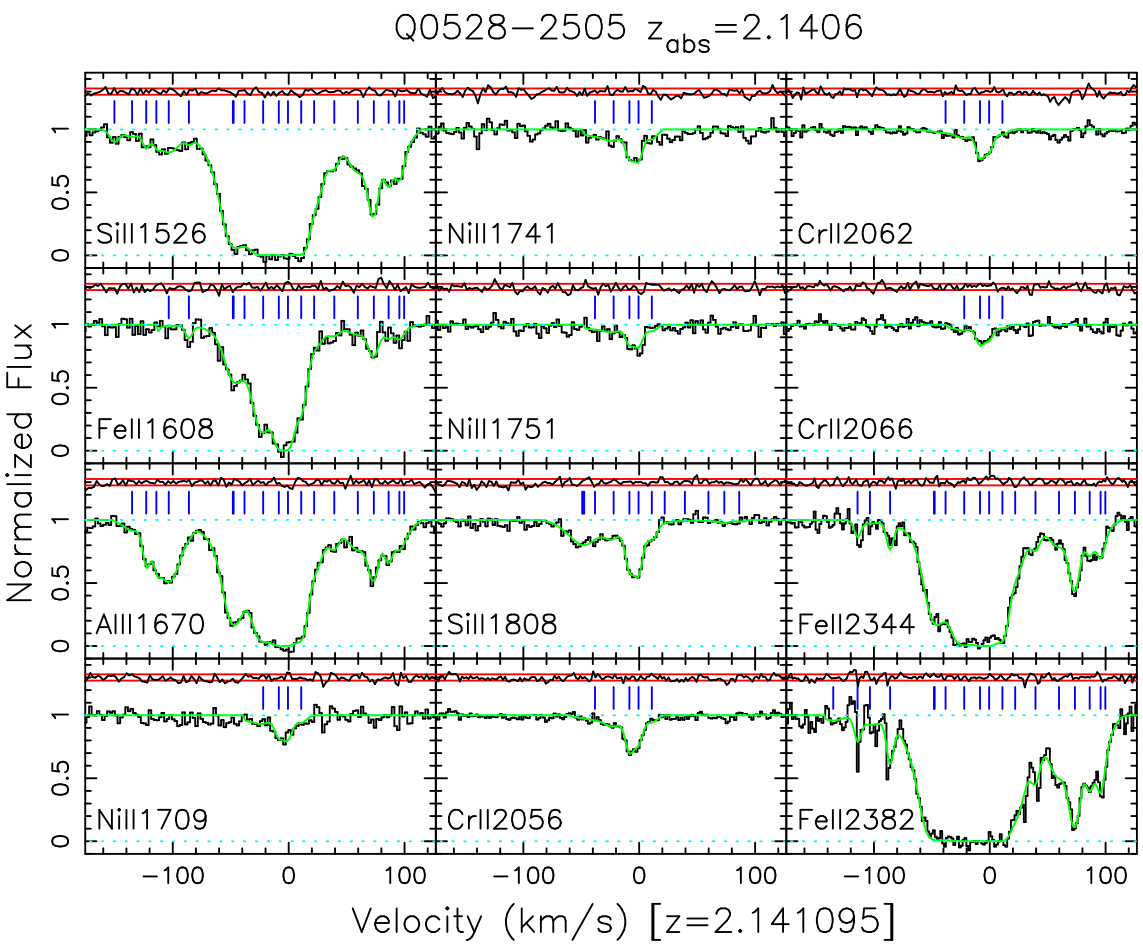

Figure 3.5. Heavy element absorption lines in the damped Lyman-α system towards Q0528−2505 at $z_{\rm abs} = 2.1406$. The data have been normalized by a fit to the continuum and plotted as a histogram. Our Voigt profile fit (solid curve) and the residuals (i.e. [data]−[fit]), normalized to the 1σ errors (horizontal solid lines), are also shown. The tick–marks above the continuum indicate individual velocity components. Note the large range in line-strengths for the different transitions. The velocity structure is well-constrained by Si II λ1526, Al II λ1670 and Fe II λ1608 while the Ni II and Cr II transitions are strong enough to constrain $\Delta\alpha/\alpha$ with the velocity $\approx 0\,{\rm kms}^{-1}$ components. This system is at low enough redshift for the Fe II $\lambda\lambda$2344 and 2382 transitions to be detected. These combine with Si II λ1526, Al II λ1670 and Fe II λ1608 to constrain $\Delta\alpha/\alpha$ with the components at velocity $\approx 80\,{\rm kms}^{-1}$.

3-4 Voigt profile analysis

Our analysis technique is based on a χ^2 minimization of multiple component Voigt profile fits to the absorption features using VPFIT (v5, Webb 1987)[4]. We discuss the Voigt profile and its computation in Appendix A (Section A-1). Consider a QSO spectrum containing a single velocity component of a single transition. Three parameters describe the Voigt profile fit to such a component: the column density, the Doppler width or b-parameter and the redshift of the absorbing gas cloud, $z_{\rm abs}$. In general, however, each absorption system contains many blended velocity components appearing in many different transitions. To find the best fitting value of $\Delta\alpha/\alpha$ one must tie together the $z_{\rm abs}$ parameters of the corresponding velocity components in different transitions while minimizing χ^2. This significantly reduces the number of free parameters in a particular fit since the redshift of corresponding velocity components in different transitions need only be specified once. However, tieing together the absorption redshifts in this way assumes negligible proper motion between the absorbing gas of different ionic species. We discuss this assumption in detail in Section 4-3.

Further restrictions can be placed on the number of free parameters when fitting different transitions simultaneously since the b-parameters of corresponding velocity components in different ionic species are physically related. We may write

$$b_i^2 = \frac{2kT}{m_i} + b_{\rm turb}^2 \tag{3.9}$$

as the b-parameter of an ionic species i which has a mass m_i. The first term describes the thermal broadening within a gas cloud which has a kinetic temperature T and the second term describes an additional turbulent motion which affects all ions equally (Struve & Elvey 1934). If we assume that either thermal or turbulent broadening dominates for a particular component then again we reduce the number of free parameters. If we fit transitions of at least two ions with different masses then we can determine T and $b_{\rm turb}$ for each velocity component.

[4]Available at http://www.ast.cam.ac.uk/~rfc/vpfit.html

For the present case, we wish to add another free parameter to the fit: $\Delta\alpha/\alpha$. From equation 3.5 we can see that $\Delta\alpha/\alpha$ will be constrained by the difference $\omega_z - \omega_0$ for each transition if we fit two or more transitions simultaneously[5].

For each absorption system we construct multiple velocity component Voigt profile fits to the data using VPFIT. We discuss the χ^2 minimization technique employed by VPFIT in Appendix A (Section A-2). We have modified VPFIT to include $\Delta\alpha/\alpha$ as a free parameter: for each transition we alter the rest wavelength using equation 3.5 so that all velocity components shift in concert. This differs from the analysis in W99 where $\Delta\alpha/\alpha$ was varied externally to VPFIT. The main advantage is a significant gain in computational speed, allowing us to fit more complicated systems that would have taken prohibitively long using the method in W99. This increased speed also allows us to conduct detailed Monte Carlo simulations to test the reliability of VPFIT itself (Section A-3) and to model the effects of different systematic errors (Sections 4-12.2 and 4-12.3).

We present the final Voigt profile fits to the absorption systems comprising all three samples in Appendix C.

Parameter errors are calculated from the diagonal terms of the final parameter covariance matrix (Fisher 1958). We have performed Monte Carlo simulations of absorption systems of varying complexity (i.e. different numbers of velocity components and transitions fitted) and with a range of input values of $\Delta\alpha/\alpha$ to verify that VPFIT returns the correct values and $1\,\sigma$ errors for $\Delta\alpha/\alpha$ (see Appendix A). The results of selected simulations are presented in Figs. A.2 and A.3 (see also Section 4-12.2, Fig. 4.13).

We employed the following general procedure for fitting each absorption system:

1. The transition which best appeared to constrain the velocity structure was fitted first. Generally, this was the strongest unsaturated transition. For the low-z Mg/Fe II systems, this was usually Mg II λ2796 as this transition generally has

[5] We require two or more transitions since fitting only one would render z and $\Delta\alpha/\alpha$ degenerate for a single component and nearly degenerate for multiple components.

highest line-strength. In cases where this transition was strongly saturated, one of the series of Fe II lines generally provided a clear view of the velocity structure (e.g. Fig. 3.4). For the high-z systems, one of the strong Al II λ1670, Si II λ1526 and Fe II λ1608 transitions provided the basis for fitting. In cases where these transitions were strongly saturated (e.g. Fig. 3.5), the weak Si II λ1808 and strong Si II λ1526 lines provided a convenient combination. A minimal number of velocity components were fitted in order that $\chi^2_\nu \sim 1$.

2. This initial velocity structure was then applied to weaker transitions in the complex. Extra components were added when justified by this additional data (i.e. if adding the extra components significantly decreased χ^2).

3. This secondary velocity structure was applied to the stronger transitions (e.g. ones exhibiting saturated components). Very often, weaker, optically thin components flanking the main, strong components were required (e.g. the velocity $\sim -100\,\mathrm{kms}^{-1}$ components in Fig. 3.5). However, in general, we did not fit extra, strong components near those found in the secondary velocity structures in step 2. This allows the 'good' fits found there for the weaker transitions to constrain $\Delta\alpha/\alpha$ most reliably and repeatably.

The reader will note that the above procedure seems somewhat 'subjective' since one does not know *a priori* how many velocity components to fit. Indeed, the Voigt profile fits are not unique and several weaker velocity components may exist in the data which are not fitted. This problem is endemic to Voigt profile fitting. For example, a systematic bias occurs when attempting to estimate column densities from Voigt profile fits to saturated profiles with many components. Therefore, adopting a particular fitting 'philosophy' will lead to systematic effects in the total column density, even for a large number of systems. However, such ambiguities can not systematically affect the best fitting values of $\Delta\alpha/\alpha$ given a large number of velocity components and systems. The magnitude of the effect for an individual system is also reduced since the constraints on $\Delta\alpha/\alpha$ are naturally weighted by the optically thin components in the χ^2 minimization. We discuss random errors that may be

introduced into the values of $\Delta\alpha/\alpha$ for different systems in Section 3-5.2.

We impose two self-consistency checks on each absorption system before accepting a value of $\Delta\alpha/\alpha$. Firstly, we require the value of χ^2 per degree of freedom, χ^2_ν, to be $\sim$1. Secondly, we construct two fits to the data with different constraints on the b-parameters: (i) entirely thermal broadening and (ii) entirely turbulent broadening[6]. We require that the values of $\Delta\alpha/\alpha$ derived from both fits be consistent with each other since the choice above should not greatly affect $\Delta\alpha/\alpha$ (i.e. the redshifts of velocity components will not change systematically). We rejected only 4 systems in this way.

VPFIT imposes a user-adjustable cut-off point in parameter space such that very weak velocity components are removed from the fit when they no longer significantly affect the value of χ^2. This presents a problem for our method since a given component may be weak in one transition (and so can be regarded as dispensable with respect to χ^2) but may be strong in another. An example of this can be seen in Fig. 3.5 where the velocity $\sim -100\,\mathrm{kms}^{-1}$ components do not appear in the weaker transitions. Conceivably, dropping even very weak components could affect our determination of $\Delta\alpha/\alpha$. Therefore, in such cases we observed the trend in the values of $(\Delta\alpha/\alpha)_i$ at each iteration i of the minimization routine to see if this trend was significantly altered due to line dropping. If components were dropped during a fit then we also re-ran the VPFIT algorithm, keeping the dropped components by fixing their column density at the value just before they were dropped from the original fit. No cases were found where the values of $\Delta\alpha/\alpha$ from the different runs differed significantly.

[6]For samples 1 and 2 we also constructed a third fit for each absorption system where the thermal and turbulent component of the b-parameters were determined by goodness of fit. Previously, VPFIT did not allow one to vary T and $b_{\rm turb}$ for each component independently, but dealt only with b_i. We have therefore modified VPFIT to include T and $b_{\rm turb}$ explicitly as free parameters. Such a fit is more computationally intensive and, in general, the thermal and turbulent b-parameters are poorly determined. We found that this fit did not lead to any inconsistent values of $\Delta\alpha/\alpha$ and so fits (i) and (ii) provide a sufficient consistency check.

3-5 Results

3-5.1 Raw QSO results

We present the χ^2 minimization results in Table 3.4 for the three different Keck/HIRES samples. We list the QSO (B1950) name, the emission redshift, $z_{\rm em}$, the absorption redshift, $z_{\rm abs}$, and $\Delta\alpha/\alpha$ for each absorption system with the associated $1\,\sigma$ statistical error. The transitions fitted in each system are indicated with the ID letters defined in Table 3.1. We present basic statistics for the different samples in Table 3.5: $\langle\Delta\alpha/\alpha\rangle_{\rm w}$ is the weighted mean with $1\,\sigma$ error, $\langle\Delta\alpha/\alpha\rangle$ is the unweighted mean, S_0 is the significance of the departure of the weighted mean from zero, rms is the root-mean-square deviation from the mean of $\Delta\alpha/\alpha$, $\langle\delta(\Delta\alpha/\alpha)\rangle$ is the mean $1\,\sigma$ error and χ^2_ν is the value of χ^2 per degree of freedom with $\langle\Delta\alpha/\alpha\rangle_{\rm w}$ as the model.

The statistics in Table 3.5 indicate a smaller α over the redshift range $0.2 < z_{\rm abs} < 3.7$ at the $5.6\,\sigma$ significance level:

$$\Delta\alpha/\alpha = (-0.574 \pm 0.102) \times 10^{-5}\,. \tag{3.10}$$

Note the consistency between the three independent samples. Breaking the sample down into low-z ($z_{\rm abs} < 1.8$) and high-z ($z_{\rm abs} > 1.8$) subsamples also yields consistent results. We also see an overall agreement between the weighted and unweighted means, indicating that the results are not dominated by a small number of highly significant points. This is supported by the histograms in Fig. 3.6 which show a symmetric, roughly Gaussian distribution for the values of $\Delta\alpha/\alpha$ and for the significance of $\Delta\alpha/\alpha$ with respect to the weighted mean value, $S_{-0.574}$.

We illustrate the distribution of $\Delta\alpha/\alpha$ over redshift and cosmological time in Fig. 3.7. The upper panel shows the values of $\Delta\alpha/\alpha$ (with their $1\,\sigma$ error bars) for each sample separately. The middle panel shows an arbitrary binning of each sample such that each bin has an equal number of points [aside from the final (highest z) bin which also contains the remaining points after dividing the total number by the number of bins]. We plot the weighted mean for each bin with the associated $1\,\sigma$

Table 3.4. The results from the χ^2 minimization procedure. For each absorption system in the three samples we identify the QSO emission redshift, $z_{\rm em}$, the absorption cloud redshift, $z_{\rm abs}$, the transitions fitted and the value of $\Delta\alpha/\alpha$ with associated $1\,\sigma$ statistical error.

Object	$z_{\rm em}$	$z_{\rm abs}$	Transitions[a]	$\Delta\alpha/\alpha$ (10^{-5})
Sample 1				
0002+0507	1.90	0.85118	bcnopqr	-0.346 ± 1.279
0117+2118	1.49	0.72913	abcqr	0.084 ± 1.297
		1.0479	bcnpr	-0.223 ± 2.200
		1.3246	bcpqr	0.695 ± 0.803
		1.3428	cnpq	-1.290 ± 0.948
0420−0127	0.915	0.63308	abcr	4.211 ± 4.076
0450−1312	2.25	1.1743	bnopr	-3.070 ± 1.098
		1.2294	bcnpqr	-1.472 ± 0.836
		1.2324	bcp	1.017 ± 2.752
0454+0356	1.34	0.85929	acnoprq	0.405 ± 1.325
		1.1534	bcnqr	-0.749 ± 1.782
0823−2220	0.91[b]	0.91059	bcnpqr	-0.394 ± 0.609
1148+3842	1.30	0.55339	bcqr	-1.861 ± 1.716
1206+4557	1.16	0.92741	bcnopqr	-0.218 ± 1.389
1213−0017	2.69	1.3196	abcnopqr	-0.738 ± 0.760
		1.5541	bcnopqr	-1.268 ± 0.892
1222+2251	2.05	0.66802	bcnpr	0.067 ± 1.474
1225+3145	2.22	1.7954	abcnopr	-1.296 ± 1.049
1248+4007	1.03	0.77292	bcnopqr	2.165 ± 1.191
		0.85452	bcnpqr	-0.021 ± 1.268
1254+0443	1.02	0.51934	abcqr	-3.371 ± 3.247
		0.93426	bcnpqr	1.485 ± 1.908

Table. 3.4 – *continued.* MM results for samples 1 (continued) and 2.

Object	$z_{\rm em}$	$z_{\rm abs}$	Transitions[a]	$\Delta\alpha/\alpha$ (10^{-5})
1317+2743	1.01	0.66004	bcnpqr	0.590 ± 1.515
1421+3305	1.91	0.84324	bcnopqr	0.099 ± 0.847
		0.90301	bcnopqr	-0.998 ± 1.783
		1.1726	bcnpr	-2.844 ± 1.448
1634+7037	1.34	0.99010	bcnpqr	1.094 ± 2.459
Sample 2				
0019−1522	4.53	3.4388	ghl	0.925 ± 3.958
0100+1300	2.68	2.3095	efgjklmvw	-3.941 ± 1.368
0149+3335	2.43	2.1408	defghijklmstu	-5.112 ± 2.118
0201+3634	2.49	1.4761	cnoqr	-0.647 ± 1.219
		1.9550	ehil	1.989 ± 1.048
		2.3240	deghl	0.758 ± 1.592
		2.4563	dgl	-3.731 ± 2.285
		2.4628	ghiltu	0.572 ± 1.719
0347−3819	3.23	3.0247	gl	-2.795 ± 3.429
0841+1256	2.55	2.3742	dghijtuvw	2.277 ± 3.816
		2.4761	dghijklmtu	-4.304 ± 1.944
1215+3322	2.61	1.9990	defghijlmtuvw	5.648 ± 3.131
1759+7539	3.05	2.6253	eghklmstu	-0.750 ± 1.387
		2.6253[c]	dglmstu	-0.492 ± 1.645
2206−1958	2.56	0.94841	bcnpqr	-3.659 ± 1.855
		1.0172	abcnopqr	-0.322 ± 0.732
		1.9204	dghijklmstuvw	1.878 ± 0.702
2230+0232	2.15	1.8585	dghjlnpstu	-5.407 ± 1.179
		1.8640	ghijklmnostuvw	-0.998 ± 0.492

Table. 3.4 – *continued.* MM results for samples 2 (continued) and 3.

Object	$z_{\rm em}$	$z_{\rm abs}$	Transitions[a]	$\Delta\alpha/\alpha$ (10^{-5})
2231−0015	3.02	2.0653	ghjklmtuvw	-2.604 ± 1.015
2348−1444	2.94	2.2794	ghl	1.346 ± 4.180
2359−0216	2.31	2.0951	dghijklstuvw	-0.068 ± 0.722
		2.1539	dfgl	4.346 ± 3.338
Sample 3				
0000−2620	4.11	1.4342	bcpr	-1.256 ± 1.167
		3.3897	dglm	-7.666 ± 3.231
0002+0507	1.90	0.59137	bcnpqr	-3.100 ± 2.428
		0.85118	efnopqr	0.494 ± 1.021
0055−2659	3.66	1.2679	abcpqr	1.669 ± 2.745
		1.3192	bcpqr	-2.642 ± 2.457
		1.5337	abcnopqr	-1.319 ± 1.072
0058+0155	1.96	0.61256	bcnopqr	0.374 ± 1.189
		0.72508	bcnpqr	-2.637 ± 3.522
0119−0437	1.95	0.65741	bcnopqr	7.123 ± 4.599
0153+7427	2.33	0.74550	bcnpqr	-2.168 ± 0.778
0207+0503	4.19	3.6663	dgl	-0.748 ± 3.468
0216+0803	2.99	1.7680	eflnopqr	0.044 ± 1.235
0237−2321	2.23	1.3650	deghlnop	-0.197 ± 0.565
0241−0146	4.04	2.0994	dnop	-0.739 ± 2.675
0302−2223	1.41	1.0092	abcnopqr	-0.189 ± 1.008
0449−1325	3.09	1.2667	abcnopq	-1.212 ± 1.430
0528−2505	2.77	0.94398	bcr	0.759 ± 2.335
		2.1406	dghijklnpstu	-0.853 ± 0.880
		2.8114	defgijklmstuvw	0.850 ± 0.846

Table. 3.4 – *continued.* MM results for sample 3 (continued).

Object	$z_{\rm em}$	$z_{\rm abs}$	Transitions[a]	$\Delta\alpha/\alpha$ (10^{-5})
0636+6801	3.17	1.2938	bcpqr	-1.392 ± 0.623
0741+4741	3.21	1.6112	abcnpq	-1.299 ± 1.726
		3.0173	dghl	0.794 ± 1.796
0757+5218	3.24	2.6021	defl	-1.396 ± 1.955
		2.8677	dgl	3.837 ± 3.288
0841+1256	2.55	1.0981	bnopr	-3.589 ± 1.203
		1.1314	abcnpqr	0.562 ± 0.787
		1.2189	abcnopqrvw	-0.522 ± 0.542
		2.3742	deghijknqrtuvw	1.435 ± 1.227
0930+2858	3.42	3.2351	dgl	0.867 ± 1.777
0940−1050	3.05	1.0598	abcnpqr	-0.453 ± 1.572
0956+1217	3.31	2.3103	defl	-2.161 ± 5.977
1009+2956	2.62	1.1117	bcnpqr	-5.461 ± 2.518
1011+4315	3.10	1.4162	bcnopqr	-0.892 ± 0.552
		2.9587	deghlmsu	2.475 ± 1.706
1055+4611	4.12	3.3172	dgl	2.706 ± 5.677
1107+4847	2.97	0.80757	abcpq	1.199 ± 1.222
		0.86182	abcqr	-2.030 ± 1.632
		1.0158	abcp	-2.086 ± 0.934
1132+2243	2.88	2.1053	defgl	6.323 ± 3.622
1202−0725	4.70	1.7549	bcqr	-1.465 ± 2.182
1206+4557	1.16	0.92741	abcnopqr	-0.275 ± 0.776
1223+1753	2.94	2.4653	hijkmsuvw	1.635 ± 1.919
		2.5577	dglnp	0.546 ± 1.199
1225+3145	2.22	1.7954	defghl	1.352 ± 1.388
1244+3142	2.95	0.85048	bcpr	-6.897 ± 7.012
		2.7504	dgl	2.414 ± 4.110

Table. 3.4 – *continued.* MM results for sample 3 (continued).

Object	$z_{\rm em}$	$z_{\rm abs}$	Transitions[a]	$\Delta\alpha/\alpha$ (10^{-5})
1307+4617	2.13	0.22909	abcr	2.551 ± 5.392
1337+1121	2.97	2.7955	dhl	4.103 ± 8.538
1425+6039	3.20	2.7698	dgl	-0.688 ± 1.843
		2.8268	dgl	0.433 ± 0.827
1437+3007	3.00	1.2259	abcnopqr	0.308 ± 1.460
1442+2931	2.76	2.4389	dgl	-0.882 ± 1.473
1549+1919	2.83	1.1425	cfnpqr	-0.076 ± 0.671
		1.3422	nopq	-0.740 ± 1.232
		1.8024	def	-3.050 ± 2.473
1626+6433	2.32	0.58596	bcr	-1.977 ± 4.529
		2.1102	defgl	-0.705 ± 1.068
1634+7037	1.34	0.99010	abcdnopqr	-2.194 ± 1.343
1850+4015	2.12	1.9900	ghijklmnopqrvw	-1.663 ± 0.859
1946+7658	3.02	1.7385	efhijmntu	-0.212 ± 1.857
		2.8433	dgl	-4.743 ± 1.289
2145+0643	1.00	0.79026	bcnopqr	0.087 ± 0.589
2206−1958	2.56	1.0172	abcqr	1.354 ± 0.883
		2.0762	dl	1.429 ± 3.022
2231−0015	3.02	1.2128	abcopqr	1.223 ± 1.465
		2.0653	efghijklmstuvw	1.707 ± 1.249
		2.6532	dglstu	-3.348 ± 1.904
2233+1310	3.30	2.5480	dgl	2.942 ± 5.207
		2.5548	defgl	1.732 ± 6.349
		3.1513	dgl	-4.005 ± 3.301
2343+1232	2.52	0.73117	abcoqr	-1.211 ± 0.975
		1.5899	acdefgqr	0.453 ± 1.187
		2.1711	cdefnp	-0.961 ± 1.295

Table. 3.4 – *continued.* MM results for sample 3 (continued).

Object	$z_{\rm em}$	$z_{\rm abs}$	Transitions[a]	$\Delta\alpha/\alpha$ (10^{-5})
2343+1232	2.52	2.4300	dgijklnqrstuvw	-1.224 ± 0.389
2344+1228	2.77	1.0465	abcinopqr	-0.747 ± 1.530
		1.1161	abcopqr	0.009 ± 1.963
		2.5378	dgl	-3.205 ± 2.094

[a]Transitions identified as in Table 3.1; [b]This QSO is a BL Lac object and so the emission redshift has a large uncertainty. Indeed, the literature value for $z_{\rm em}$ shown here is less than the measured absorption redshift. [c]This absorber contributed by Outram et al. (1999).

error bar. The lower panel combines all three samples. Note the expanded scales on the lower two panels.

3-5.2 Extra scatter at high-z?

In Table 3.5 we note that the scatter in the total low-z sample is consistent with that expected from the size of the error bars [i.e. rms $\approx \langle\delta(\Delta\alpha/\alpha)\rangle$ and $\chi^2_\nu \approx 1$]. However, at higher z, Fig. 3.7 shows several values of $\Delta\alpha/\alpha$ which are significantly different from one another, particularly around $z_{\rm abs} \approx 1.9$. Indeed, Table 3.5 shows that rms $> \langle\delta(\Delta\alpha/\alpha)\rangle$ and $\chi^2_\nu > 1$ for the total high-z sample and that sample 2 dominates these statistics. We emphasize that only a few systems dominate this extra scatter: if one removes from sample 2 the 8 systems with $1.8585 \leq z_{\rm abs} \leq 2.1408$ then the scatter is significantly reduced. The statistics for sample 2 after removing these 8 systems are as follows: $\langle\Delta\alpha/\alpha\rangle_{\rm w} = -0.980 \pm 0.415$, $\langle\Delta\alpha/\alpha\rangle = -0.694 \pm 0.636$, rms $= 2.462$, $\langle\delta(\Delta\alpha/\alpha)\rangle = 2.298 \pm 0.282$ (all in units of 10^{-5}) and $\chi^2_\nu = 1.303$.

There are also several reasons why *we may expect extra scatter*. Consider fitting two transitions, arising from different species, with significantly different line-strengths (e.g. Al II λ1670 and Ni II λ1709 in Fig. 3.5). Weak components in the high optical depth portions of strong species' profiles are not necessary to obtain good

Table 3.5. Statistics for the raw QSO results and several tests for systematic errors. The three samples are described in Section 3-3.1. For sample 3 and the total sample, "low-z" refers to $z_{\rm abs} < 1.8$ and "high-z" refers to $z_{\rm abs} > 1.8$. For each sample, $\langle z_{\rm abs}\rangle$ is the mean absorption redshift, $N_{\rm abs}$ is the number of absorption systems, $\langle\Delta\alpha/\alpha\rangle_{\rm w}$ is the weighted mean, $\langle\Delta\alpha/\alpha\rangle$ is the unweighted mean, S_0 is the significance of the weighted mean (with respect to zero), rms is the root-mean-square deviation from the mean, $\langle\delta(\Delta\alpha/\alpha)\rangle$ is the mean $1\,\sigma$ error and χ^2_ν is χ^2 per degree of freedom using $\langle\Delta\alpha/\alpha\rangle_{\rm w}$ as the model.

Sample	$\langle z_{\rm abs}\rangle$	$N_{\rm abs}$	$\langle\Delta\alpha/\alpha\rangle_{\rm w}$	$\langle\Delta\alpha/\alpha\rangle$	S_0	rms	$\langle\delta(\Delta\alpha/\alpha)\rangle$	χ^2_ν
QSO results								
Raw results (Fig. 3.7)								
1	1.00	27	-0.513 ± 0.224	-0.305 ± 0.304	$2.28\,\sigma$	1.579	1.554 ± 0.153	0.981
2	2.17	23	-0.672 ± 0.244	-0.656 ± 0.601	$2.76\,\sigma$	2.880	1.951 ± 0.232	3.082
3 (low-z)	1.11	44	-0.537 ± 0.159	-0.652 ± 0.321	$3.37\,\sigma$	2.131	1.757 ± 0.204	1.123
3 (high-z)	2.60	34	-0.623 ± 0.224	-0.053 ± 0.473	$2.78\,\sigma$	2.755	2.604 ± 0.318	1.533
3 (total)	1.76	78	-0.566 ± 0.130	-0.391 ± 0.276	$4.36\,\sigma$	2.441	2.126 ± 0.186	1.284
low-z	1.07	74	-0.539 ± 0.130	-0.562 ± 0.226	$4.24\,\sigma$	1.941	1.663 ± 0.134	1.051
high-z	2.50	54	-0.637 ± 0.172	-0.227 ± 0.389	$3.72\,\sigma$	2.862	2.400 ± 0.224	2.179
Total	**1.67**	**128**	$\mathbf{-0.574 \pm 0.102}$	$\mathbf{-0.421 \pm 0.210}$	$\mathbf{5.62\sigma}$	**2.379**	$\mathbf{1.974 \pm 0.127}$	**1.515**

Table. 3.5 – *continued.* Statistics for the raw QSO results and several tests for systematic errors.

Sample	$\langle z_{\rm abs}\rangle$	$N_{\rm abs}$	$\langle\Delta\alpha/\alpha\rangle_{\rm w}$	$\langle\Delta\alpha/\alpha\rangle$	S_0	rms	$\langle\delta(\Delta\alpha/\alpha)\rangle$	χ^2_ν
Angular variations (Fig. 3.10)								
$b < 0°$	1.70	64	-0.533 ± 0.140	-0.519 ± 0.299	$3.80\,\sigma$	2.394	1.916 ± 0.156	1.742
$b > 0°$	1.65	64	-0.619 ± 0.149	-0.322 ± 0.295	$4.16\,\sigma$	2.360	2.032 ± 0.200	1.310
$l < 150°$	1.64	74	-0.608 ± 0.130	-0.669 ± 0.278	$4.67\,\sigma$	2.395	1.907 ± 0.162	1.770
$l > 150°$	1.72	54	-0.519 ± 0.164	-0.080 ± 0.315	$3.16\,\sigma$	2.314	2.065 ± 0.202	1.189
Systematic error tests								
ThAr calibration test: $(\Delta\alpha/\alpha)_{\rm ThAr}$ (Fig. 4.3)								
1	1.00	27	0.016 ± 0.021	0.034 ± 0.045	$0.74\,\sigma$	0.234	0.129 ± 0.008	3.697
2	2.10	18	-0.013 ± 0.020	-0.015 ± 0.059	$0.66\,\sigma$	0.250	0.165 ± 0.043	3.212
3 (low-z)	1.14	41	-0.008 ± 0.014	-0.003 ± 0.036	$0.59\,\sigma$	0.229	0.123 ± 0.016	3.095
3 (high-z)	2.63	32	0.019 ± 0.014	0.016 ± 0.052	$1.38\,\sigma$	0.293	0.148 ± 0.022	2.714
3 (total)	1.79	73	0.006 ± 0.010	0.005 ± 0.030	$0.57\,\sigma$	0.259	0.134 ± 0.013	2.915
low-z	1.08	71	-0.006 ± 0.011	0.006 ± 0.027	$0.54\,\sigma$	0.230	0.124 ± 0.010	3.286
high-z	2.52	47	0.014 ± 0.012	0.013 ± 0.041	$1.24\,\sigma$	0.284	0.159 ± 0.022	2.827
Total	**1.66**	**118**	$\mathbf{0.004 \pm 0.008}$	$\mathbf{0.009 \pm 0.023}$	$\mathbf{0.48\sigma}$	**0.253**	$\mathbf{0.138 \pm 0.011}$	**3.091**

Table. 3.5 – *continued.* Statistics for the raw QSO results and several tests for systematic errors.

Sample	$\langle z_{\rm abs}\rangle$	$N_{\rm abs}$	$\langle\Delta\alpha/\alpha\rangle_{\rm w}$	$\langle\Delta\alpha/\alpha\rangle$	S_0	rms	$\langle\delta(\Delta\alpha/\alpha)\rangle$	χ^2_ν
Composite wavelengths only: $(\Delta\alpha/\alpha)_{\rm comp}$ (Fig. 4.5, top panel)								
1	1.00	27	-0.802 ± 0.227	-0.557 ± 0.334	$3.54\,\sigma$	1.736	1.567 ± 0.156	1.094
2	2.17	23	-0.736 ± 0.243	-0.731 ± 0.608	$3.03\,\sigma$	2.918	1.929 ± 0.230	3.178
3 (low-z)	1.11	44	-0.550 ± 0.161	-0.609 ± 0.329	$3.42\,\sigma$	2.184	1.779 ± 0.209	1.060
3 (high-z)	2.60	34	-0.650 ± 0.224	-0.085 ± 0.456	$2.90\,\sigma$	2.660	2.636 ± 0.326	1.457
3 (total)	1.76	78	-0.584 ± 0.131	-0.380 ± 0.274	$4.47\,\sigma$	2.417	2.152 ± 0.191	1.218
low-z	1.07	74	-0.650 ± 0.128	-0.648 ± 0.238	$5.08\,\sigma$	2.045	1.681 ± 0.138	1.098
high-z	2.50	54	-0.667 ± 0.172	-0.251 ± 0.380	$3.89\,\sigma$	2.792	2.411 ± 0.229	2.129
Total	**1.67**	**128**	$\mathbf{-0.656 \pm 0.103}$	$\mathbf{-0.481 \pm 0.212}$	$\mathbf{6.39\sigma}$	**2.397**	$\mathbf{1.989 \pm 0.129}$	**1.520**
Strong isotopes only: $(\Delta\alpha/\alpha)_{\rm iso}$ (Fig. 4.5, middle panel)								
1	1.00	27	-1.204 ± 0.228	-0.885 ± 0.353	$5.29\,\sigma$	1.834	1.567 ± 0.157	1.257
2	2.17	23	-0.738 ± 0.244	-0.734 ± 0.619	$3.03\,\sigma$	2.967	1.928 ± 0.226	3.210
3 (low-z)	1.11	44	-0.860 ± 0.159	-0.834 ± 0.323	$5.40\,\sigma$	2.145	1.768 ± 0.206	1.279
3 (high-z)	2.60	34	-0.634 ± 0.224	-0.077 ± 0.463	$2.84\,\sigma$	2.700	2.626 ± 0.325	1.494
3 (total)	1.76	78	-0.784 ± 0.130	-0.504 ± 0.275	$6.04\,\sigma$	2.432	2.142 ± 0.190	1.363

Table. 3.5 – *continued.* Statistics for the raw QSO results and several tests for systematic errors.

Sample	$\langle z_{\rm abs}\rangle$	$N_{\rm abs}$	$\langle\Delta\alpha/\alpha\rangle_{\rm w}$	$\langle\Delta\alpha/\alpha\rangle$	S_0	rms	$\langle\delta(\Delta\alpha/\alpha)\rangle$	χ^2_ν
Strong isotopes only: – *continued.*								
low-z	1.07	74	-0.984 ± 0.128	-0.913 ± 0.239	$7.71\,\sigma$	2.055	1.674 ± 0.137	1.300
high-z	2.50	54	-0.638 ± 0.171	-0.231 ± 0.384	$3.72\,\sigma$	2.824	2.404 ± 0.228	2.143
Total	**1.67**	**128**	$\mathbf{-0.861 \pm 0.102}$	$\mathbf{-0.626 \pm 0.215}$	$\mathbf{8.41\sigma}$	**2.433**	$\mathbf{1.982 \pm 0.128}$	**1.663**
Atmospheric dispersion corrected: $(\Delta\alpha/\alpha)_{\rm adc}$ (Fig. 4.9)								
1	1.00	27	-0.098 ± 0.225	0.142 ± 0.339	$0.43\,\sigma$	1.762	1.554 ± 0.153	1.208
2	2.17	23	-0.637 ± 0.244	-0.668 ± 0.583	$2.61\,\sigma$	2.794	1.951 ± 0.232	2.979
3 (low-z)	1.11	44	-0.416 ± 0.159	-0.557 ± 0.319	$2.61\,\sigma$	2.118	1.757 ± 0.204	1.050
3 (high-z)	2.60	34	-0.740 ± 0.224	-0.189 ± 0.472	$3.31\,\sigma$	2.755	2.604 ± 0.318	1.545
3 (total)	1.76	78	-0.525 ± 0.130	-0.397 ± 0.274	$4.48\,\sigma$	2.423	2.126 ± 0.186	1.266
low-z	1.07	74	-0.288 ± 0.127	-0.309 ± 0.232	$2.27\,\sigma$	1.999	1.663 ± 0.134	1.118
high-z	2.50	54	-0.764 ± 0.172	-0.363 ± 0.386	$4.45\,\sigma$	2.837	2.400 ± 0.224	2.099
Total	**1.67**	**128**	$\mathbf{-0.457 \pm 0.102}$	$\mathbf{-0.332 \pm 0.211}$	$\mathbf{4.48\sigma}$	**2.389**	$\mathbf{1.974 \pm 0.127}$	**1.558**

Table. 3.5 – *continued.* Statistics for the raw QSO results and several tests for systematic errors.

Sample	$\langle z_{\rm abs}\rangle$	$N_{\rm abs}$	$\langle\Delta\alpha/\alpha\rangle_{\rm w}$	$\langle\Delta\alpha/\alpha\rangle$	S_0	rms	$\langle\delta(\Delta\alpha/\alpha)\rangle$	χ^2_ν
Total systematic error corrected: $(\Delta\alpha/\alpha)_{\rm sys}$ (Fig. 4.20)								
1	1.00	27	-0.796 ± 0.224	-0.437 ± 0.386	$3.54\,\sigma$	2.008	1.553 ± 0.153	1.462
2	2.17	23	-0.653 ± 0.244	-0.532 ± 0.562	$2.68\,\sigma$	2.696	1.951 ± 0.232	2.831
3 (low-z)	1.11	44	-0.750 ± 0.159	-0.739 ± 0.321	$4.71\,\sigma$	2.126	1.756 ± 0.204	1.152
3 (high-z)	2.60	34	-0.749 ± 0.224	-0.212 ± 0.463	$3.35\,\sigma$	2.699	2.604 ± 0.318	1.511
3 (total)	1.76	78	-0.750 ± 0.130	-0.509 ± 0.273	$5.78\,\sigma$	2.407	2.125 ± 0.186	1.291
low-z	1.07	74	-0.746 ± 0.127	-0.663 ± 0.243	$5.88\,\sigma$	2.089	1.662 ± 0.134	1.291
high-z	2.50	54	-0.736 ± 0.172	-0.272 ± 0.370	$4.29\,\sigma$	2.722	2.400 ± 0.224	1.993
Total	**1.67**	**128**	$\mathbf{-0.742 \pm 0.102}$	$\mathbf{-0.498 \pm 0.211}$	$\mathbf{7.28\sigma}$	**2.385**	$\mathbf{1.974 \pm 0.127}$	**1.574**

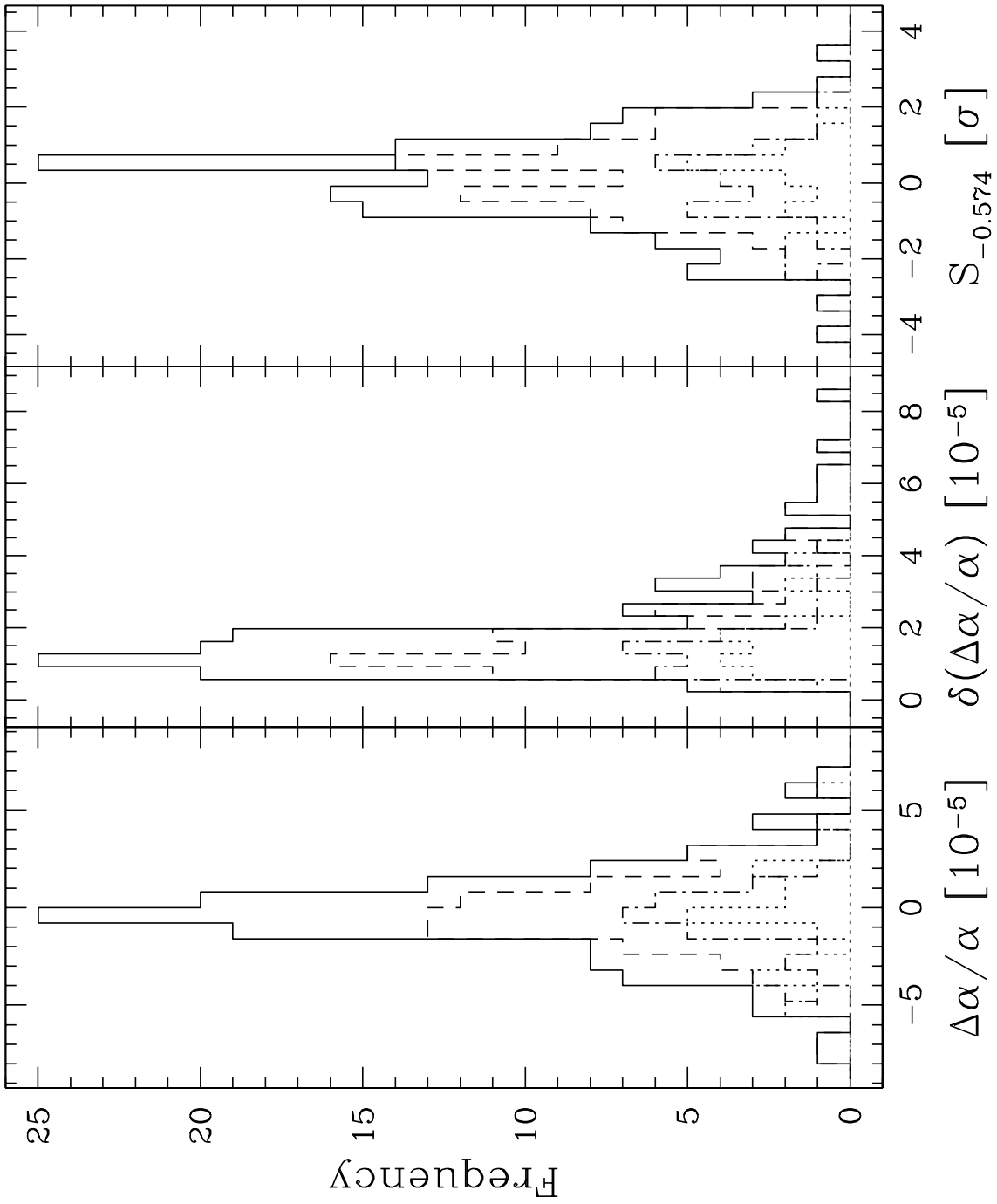

Figure 3.6. Histograms of results from Table 3.4. The left panel shows the distribution of $\Delta\alpha/\alpha$ for sample 1 (dot-dashed line), sample 2 (dotted line) and sample 3 (dashed line) together with the overall distribution (solid line). The middle panel shows the distribution of $1\,\sigma$ errors in $\Delta\alpha/\alpha$, $\delta(\Delta\alpha/\alpha)$, and the right panel shows that of the significance with respect to the overall weighted mean (equation 3.10), $S_{-0.574}$. Note the symmetric, roughly Gaussian profiles in the left and right panels.

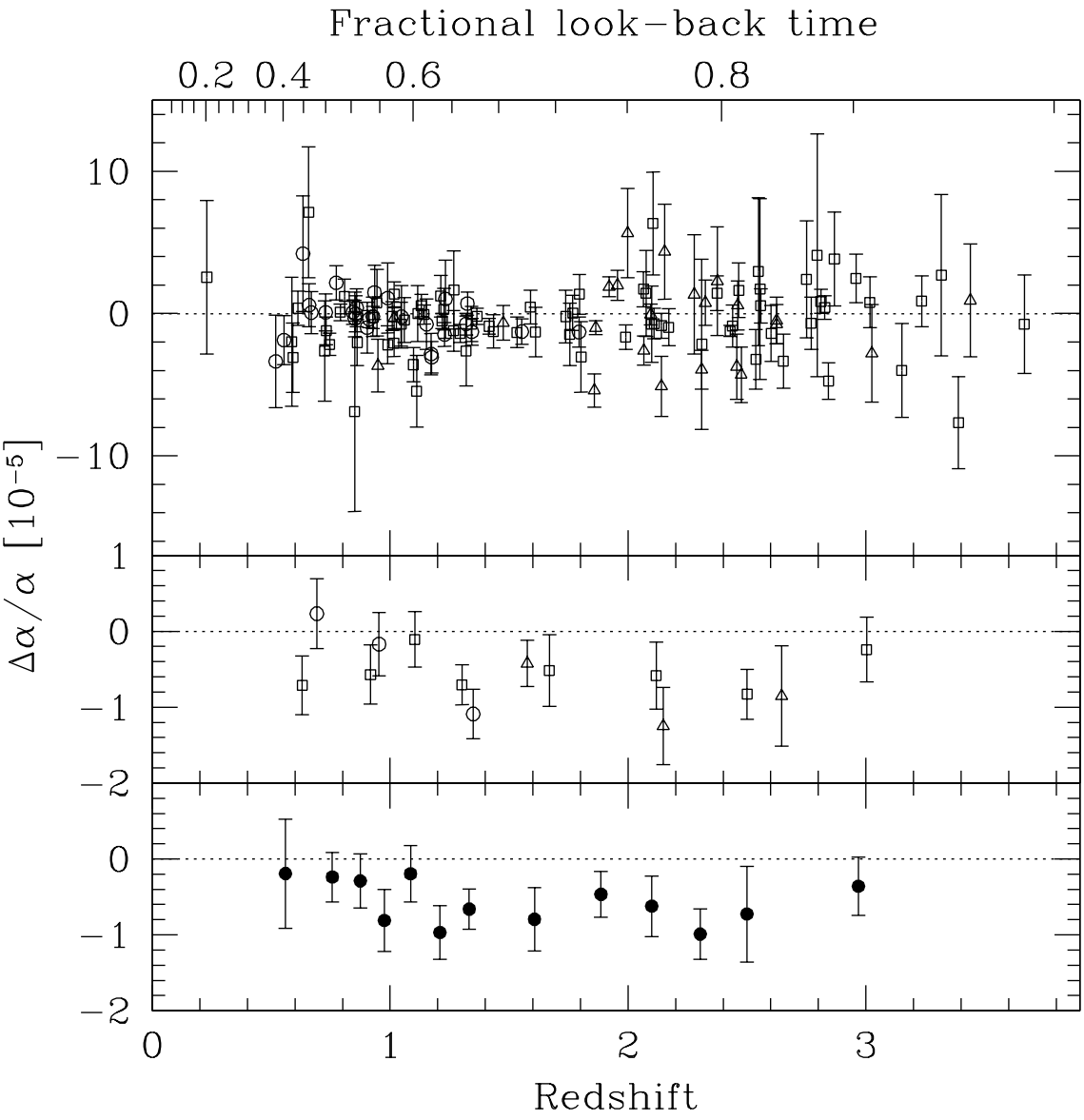

Figure 3.7. $\Delta\alpha/\alpha$ versus absorption redshift for sample 1 (open circles), sample 2 (open triangles) and sample 3 (open squares). The upper panel shows the raw results and $1\,\sigma$ error bars. The middle panel shows an arbitrary binning of each sample and the lower panel combines all three samples. The redshifts of the points are taken as the mean absorption redshift within each bin and the value of $\Delta\alpha/\alpha$ is the weighted mean with its associated $1\,\sigma$ error bar. The upper scale is the fractional look-back time to the absorber ($H_0 = 70\,\mathrm{kms^{-1}Mpc^{-1}}$, $\Omega_\mathrm{m} = 0.3$, $\Omega_\Lambda = 0.7 \rightarrow t_0 = 13.47\,\mathrm{Gyr}$).

fits to the data. Even though the VPFIT χ^2 minimization ensures that constraints on $\Delta\alpha/\alpha$ primarily derive from the optically thin velocity components, these weak

components missing from the fit will cause small line shifts. The resulting shift in $\Delta\alpha/\alpha$ is random (though correlated) from component to component: the effect of missing components will be to increase the random scatter in the individual $\Delta\alpha/\alpha$ values. We expect this effect to be greater in the high-z sample for several reasons:

1. At high-z, a larger number of different species are generally available for fitting compared to lower z. Also, the range in optical depths for corresponding velocity components is significantly larger than for the low-z Mg/Fe II systems (compare Figs. 3.4 and 3.5).

2. The high-z sample is dominated by DLAs. If these have a more complex velocity structure, i.e. the number of absorbing components per kms^{-1} is higher than for the Me/Fe II systems, Voigt profile decomposition would be more difficult, increasing the scatter in $\Delta\alpha/\alpha$.

3. In the high-z systems, we fit more heavy, i.e. low-b, species. Absorption features are therefore closer to the resolution of the instrument, increasing the systematic bias against finding the weaker components.

Section 4-3.1 discusses disk+halo models for the QSO absorbers. In these models, a larger number of velocity components is expected in DLAs, illustrating point (ii) above. This possibility is further explored in Fig. 3.8 which shows the number of independent velocity components, $N_{\rm comp}$, in each absorption system which contribute to constraints on $\Delta\alpha/\alpha$. The histogram in the upper panel reveals that the high-z systems in our sample indeed tend to have larger $N_{\rm comp}$. This is confirmed in the middle panel which indicates a correlation between $z_{\rm abs}$ and $N_{\rm comp}$. There is also evidence of increased scatter in $\Delta\alpha/\alpha$ for systems with $N_{\rm comp} \gtrsim 8$: for the 54 systems with $N_{\rm comp} < 8$, $\chi^2_\nu = 0.988$ about the weighted mean, $\Delta\alpha/\alpha = (-0.485 \pm 0.201) \times 10^{-5}$; for the 84 systems with $N_{\rm comp} \geq 8$, $\chi^2_\nu = 1.800$ about the weighted mean, $\Delta\alpha/\alpha = (-0.621 \pm 0.116) \times 10^{-5}$. However, note that there is no clear correlation between $\Delta\alpha/\alpha$ and $N_{\rm comp}$.

[7] $P(r_{\rm s})$ is the probability that $|r_{\rm s}|$ could have been exceeded by chance.

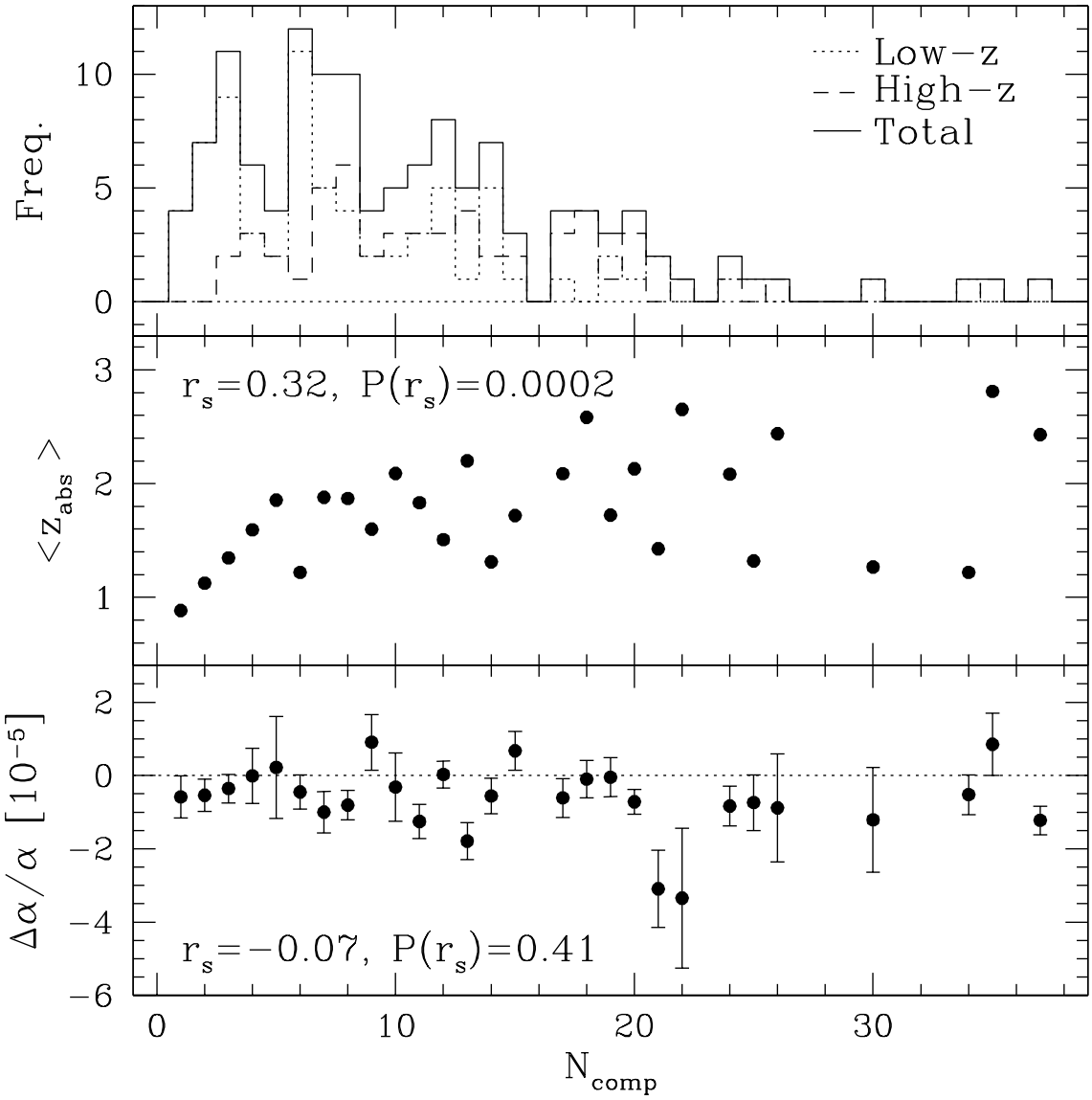

Figure 3.8. Exploring correlations with the number of fitted velocity components. The upper panel shows the number of systems containing $N_{\rm comp}$ independent velocity components which constrain $\Delta\alpha/\alpha$ for the low-z, high-z and total samples. On average, the low-z systems have lower $N_{\rm comp}$. This can also be seen in the middle panel where the Spearman rank correlation coefficient, $r_{\rm s}$, and associated probability, $P(r_{\rm s})$[7], indicates a distinct correlation between $N_{\rm comp}$ and the mean redshift, $\langle z_{\rm abs}\rangle$, in each $N_{\rm comp}$ bin. We do not see clear evidence for such a correlation if we consider the low- and high-z samples separately [low-z: $r_{\rm s} = 0.16$, $P(r_{\rm s}) = 0.17$; high-z: $r_{\rm s} = -0.08$, $P(r_{\rm s}) = 0.56$]. There is also no clear correlation between $\Delta\alpha/\alpha$ and $N_{\rm comp}$.

If we assume the extra scatter observed at high-z is due to the above effects, we may increase the size of the individual $1\,\sigma$ errors on $\Delta\alpha/\alpha$ until $\chi^2_\nu = 1$ in order to obtain a more conservative estimate for the overall $\Delta\alpha/\alpha$. We achieve this by adding $S = 1.68 \times 10^{-5}$ in quadrature to the high-z error bars. This does not appreciably change the weighted mean value for the high-z systems: $\Delta\alpha/\alpha = (-0.598 \pm 0.342) \times 10^{-5}$ [compared to $\Delta\alpha/\alpha = (-0.637 \pm 0.172) \times 10^{-5}$ before increasing the errors (Table 3.5)]. By including the (unaltered) low-z values, the overall weighted mean becomes $\Delta\alpha/\alpha = (-0.546 \pm 0.119) \times 10^{-5}$, still a $4.6\,\sigma$ effect. One may also remove significant points from the high-z sample until $\chi^2_\nu = 1$. We σ-clipped 23 points in this way and the final weighted mean is $\Delta\alpha/\alpha = (-0.561 \pm 0.193) \times 10^{-5}$ for the remaining high-z values.

3-5.3 Temporal variations in α?

In Fig. 3.9 we overlay the binned data from Fig. 3.7 with several fits to the raw values of $\Delta\alpha/\alpha$ versus $z_{\rm abs}$ and look-back time. Note that for the constant $\dot{\alpha}/\alpha \equiv (\mathrm{d}\alpha/\mathrm{d}t)/\alpha$ model we fix $\Delta\alpha/\alpha$ to zero at $z_{\rm abs} = 0$. The values of χ^2 for the constant $\Delta\alpha/\alpha$ and constant $\dot{\alpha}/\alpha$ fits are $\chi^2 = 192.4$ and 191.5 respectively. This indicates that a linear increase in α with cosmological time, t,

$$\dot{\alpha}/\alpha = (6.41 \pm 1.12) \times 10^{-16}\,\mathrm{yr}^{-1}\,, \tag{3.11}$$

is preferred over a constant $\Delta\alpha/\alpha$. We estimate the significance of this preference using a bootstrap technique. Each value of $\Delta\alpha/\alpha$ is randomly assigned to one of the measured absorption redshifts and the best fitting constant $\dot{\alpha}/\alpha$ is determined. Constructing many such bootstrap samples yields a distribution of χ^2 for the constant $\dot{\alpha}/\alpha$ fits. In this procedure we construct low- and high-z bootstrap samples separately since the distributions of $\Delta\alpha/\alpha$ in the real low- and high-z samples may differ (Section 3-5.2). The χ^2 distribution indicates that 38% of χ^2 values were < 192.4 and 17% were < 191.5. Thus, the constant $\dot{\alpha}/\alpha$ model is preferred over the constant $\Delta\alpha/\alpha$ model only at the 55% confidence level. The latter is preferred over a linear evolution of α with z at the 59% level. Not distinguishing the low- and

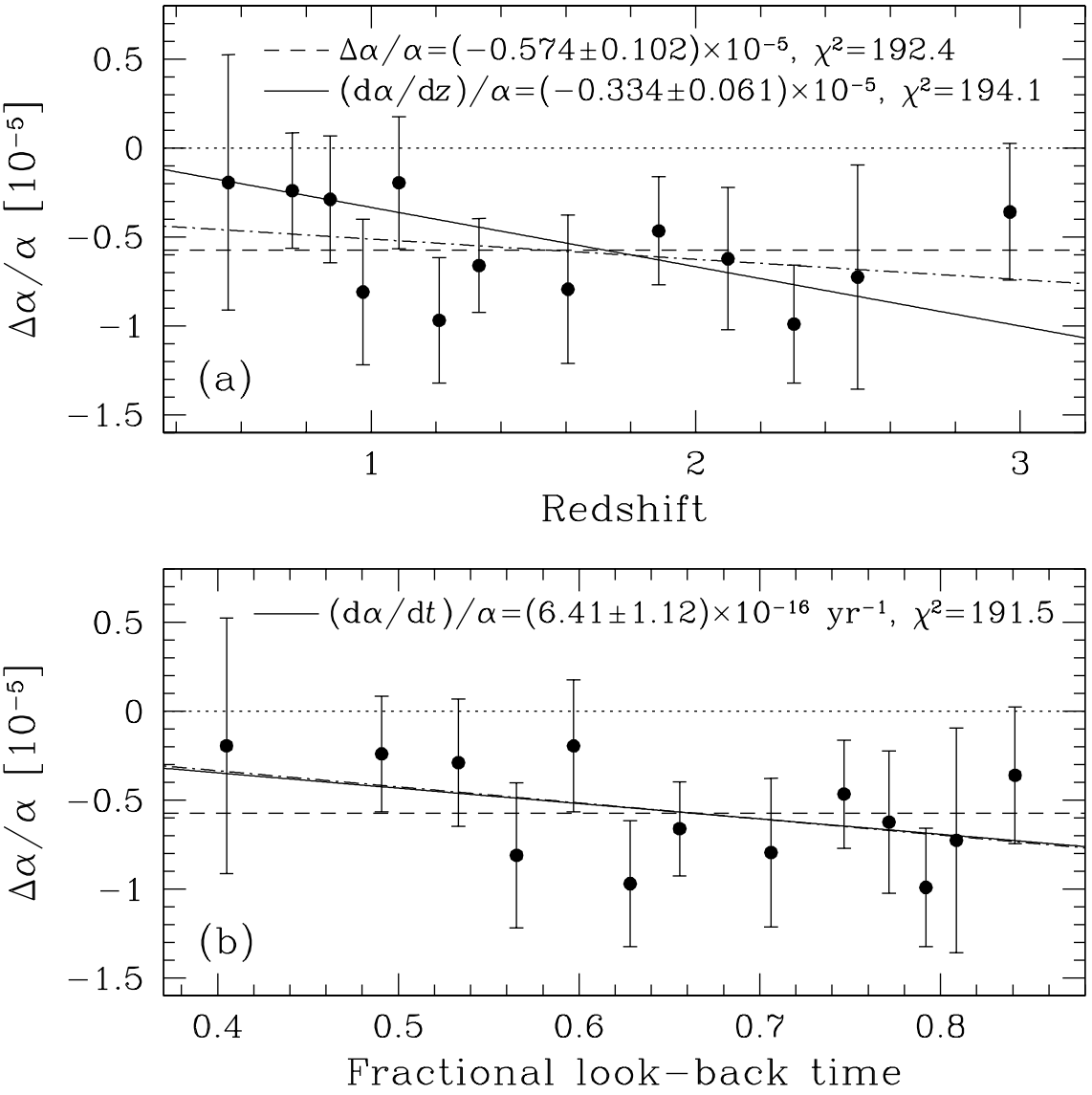

Figure 3.9. Temporal variation in α? **(a)** The points are the binned values of $\Delta\alpha/\alpha$ for the total sample plotted versus redshift. The dashed line is the weighted mean and the solid line is a fit to the raw (i.e. unbinned) data fixed to $\Delta\alpha/\alpha = 0$ at $z_{\rm abs} = 0$. The dot-dashed line is a fit with the $z_{\rm abs} = 0$ value allowed to vary. The values of χ^2 may indicate that the constant $\Delta\alpha/\alpha$ model is preferred. **(b)** Same as (a) but plotted versus fractional look-back time. The values of χ^2 may indicate that an evolving $\Delta\alpha/\alpha$ is preferred.

high-z samples gives lower confidence levels, i.e. 32% for both cases.

However, the constant $\dot{\alpha}/\alpha$ model should be treated with caution. Fixing $\Delta\alpha/\alpha$ to

zero (i.e. fixing α to the laboratory value) at $z_{\rm abs} = 0$ may not be valid because of the potential for spatial variations in α. For example, if α varies over $\sim$100 Mpc spatial scales and our Galaxy resides in a region with a slightly larger α than the 'universal mean', then we should expect to measure a constant (negative) $\Delta\alpha/\alpha$ rather than an evolution of α with time. Bekenstein (1979) and Barrow & O'Toole (2001) also note that it is difficult to compare values of $\Delta\alpha/\alpha$ in areas of different gravitational potential without a detailed theory giving both time *and* space variations of α. If we allow the $z_{\rm abs} = 0$ value of $\Delta\alpha/\alpha$ to vary, the linear fit against cosmological time is barely altered, though somewhat poorly constrained.

3-5.4 Angular variations in α?

The results in Table 3.4 can also be used to search for spatial variations in α. If very large scale ($\sim$10 Gpc) spatial variations exist, one might expect $\Delta\alpha/\alpha$ to be different in different directions on the sky. We plot the distribution of $\Delta\alpha/\alpha$ over Galactic coordinates (l, b) in Fig. 3.10. We remove all redshift information by collapsing all absorption systems along a single QSO sight-line to a single value of $\Delta\alpha/\alpha$. We also combine independent values from the same QSO in different observational samples (see Section 3-5.6). The colour-scale indicates the weighted mean $\Delta\alpha/\alpha$ and the size of each point scales with the significance with respect to the overall weighted mean, $S_{-0.574}$.

In Table 3.5 we compare statistics for the (Galactic) southern ($b < 0°$) and northern ($b > 0°$) halves of the sample. The weighted means for the two samples are consistent. This is also true if one divides the sky along $(l, b) = (150°, 0°)$. Thus, a simple analysis yields no evidence for bipolar angular variation of $\Delta\alpha/\alpha$. We have also used a χ^2 minimization algorithm to find the best-fit dipole in the angular $\Delta\alpha/\alpha$ distribution. We first constructed a grid of directions in equatorial coordinates, (RA, DEC). For each direction, a cosine fit to $\Delta\alpha/\alpha$ as a function of the angular distance, ϕ, to each $\Delta\alpha/\alpha$ point, yields an amplitude for the dipole,

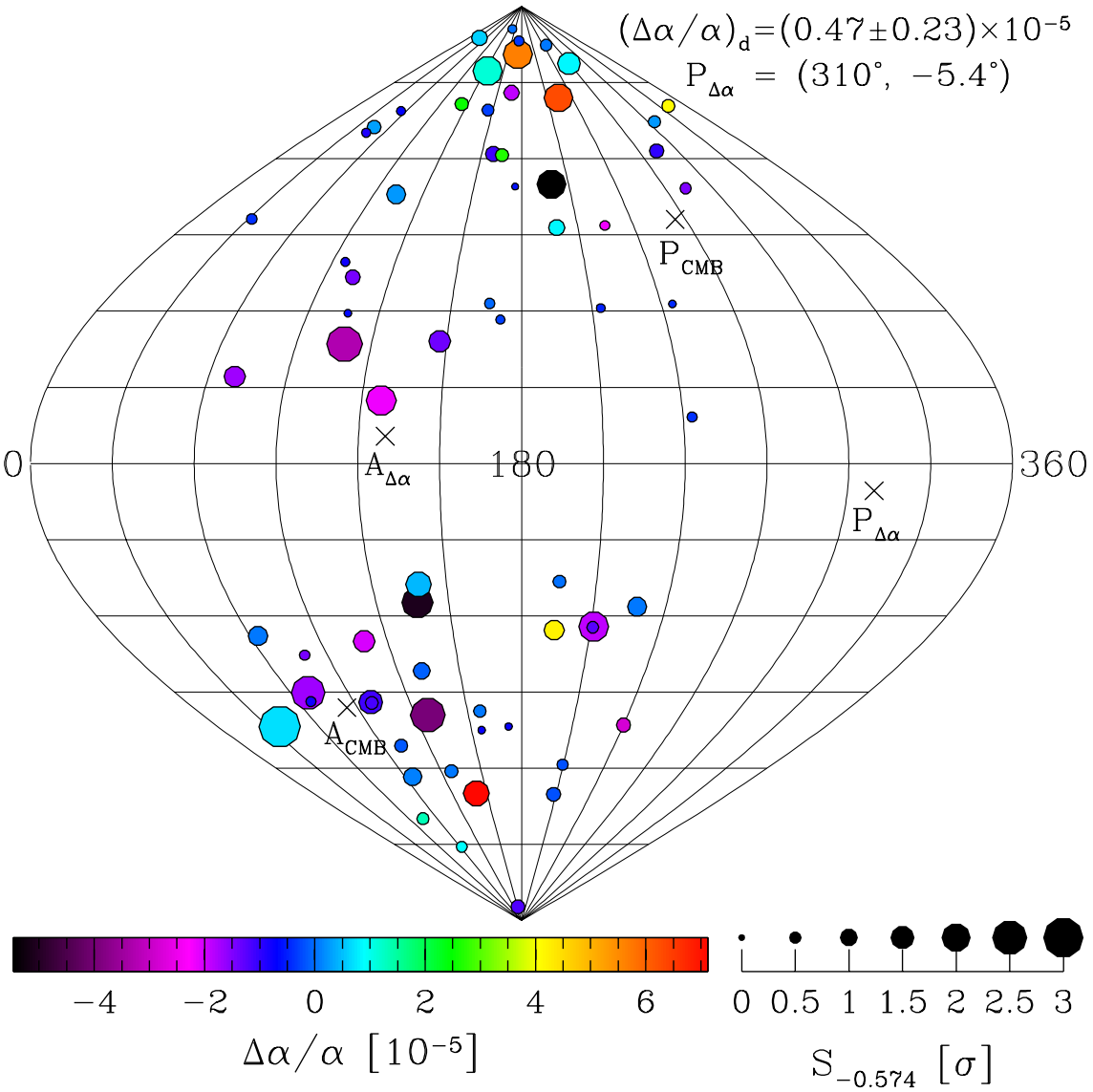

Figure 3.10. The distribution of $\Delta\alpha/\alpha$ in Galactic coordinates (l, b). All values along a single QSO sight-line (i.e. for many absorption clouds and/or repeated, independent QSO observations) are collapsed to a single weighted mean. $\Delta\alpha/\alpha$ is given by the colour-scale and the size of each point scales with the significance, $S_{-0.547}$, of the departure from the overall weighted mean. There is no evidence for a bipolar difference in $\Delta\alpha/\alpha$ for samples delineated by $(l, b) = (l, 0)$ or $(l, b) = (150, b)$. The best-fit dipole has an amplitude $(\Delta\alpha/\alpha)_{\rm d} = (0.47\pm0.23)\times10^{-5}$ with its pole and anti-pole in the directions $P_{\Delta\alpha}$ and $A_{\Delta\alpha}$. However, a bootstrap analysis indicates that the dipole model is preferred over the constant $\Delta\alpha/\alpha$ model at only the 60% confidence level. We plot the CMB pole and anti-pole for comparison.

$(\Delta\alpha/\alpha)_{\rm d}$, defined by

$$\frac{\Delta\alpha}{\alpha}(\phi) = \left\langle \frac{\Delta\alpha}{\alpha} \right\rangle_{\rm w} + \left(\frac{\Delta\alpha}{\alpha}\right)_{\rm d} \cos\phi\,. \tag{3.12}$$

Fig. 3.11 shows the best-fit dipole which has an amplitude $(\Delta\alpha/\alpha)_{\rm d} = (0.47\pm0.23)\times 10^{-5}$. The pole is in the direction $P_{\Delta\alpha}({\rm RA, DEC}) = (14\,{\rm hr}, -67^\circ)$ or $P_{\Delta\alpha}(l,b) = (310^\circ, -5.4^\circ)$ as marked on Fig. 3.10. We also mark the anti-pole, $A_{\Delta\alpha}$, and the cosmic microwave background (CMB) pole and anti-pole directions ($P_{\rm CMB}$ and $A_{\rm CMB}$, Lineweaver et al. 1996) for comparison.

The limited range of angular separations in Fig. 3.11 severely limits the dipole interpretation. Although the dipole amplitude is significant at the $2\,\sigma$ level, a bootstrap analysis, similar to that in the previous section, indicates that the dipole model is not significantly preferred over the constant $\Delta\alpha/\alpha$ (i.e. monopole) model. Bootstrap samples were formed by randomizing the values of $\Delta\alpha/\alpha$ over the QSO sight-line directions. Again, we treated the low- and high-z samples separately, combining them only to find the best-fit dipole directions. The resulting χ^2 distribution indicates that the dipole model is preferred only at the 60% confidence level. Therefore, the data do not support significant angular variations in α. There is also no evidence for angular variations in the low-z and high-z samples taken separately.

3-5.5 Spatial variations in α?

If spatial variations in α do exist at the $\Delta\alpha/\alpha \sim 10^{-5}$ level then one expects to see additional scatter in the raw values of $\Delta\alpha/\alpha$ in Fig. 3.7. However, as noted previously, the statistics in Table 3.5 indicate that the scatter at low z is consistent with the size of the error bars and so we have no evidence for spatial variations in α for $z_{\rm abs} < 1.8$. At higher z we have noted the additional scatter introduced by the absorption systems in sample 2 with $1.8585 \le z_{\rm abs} \le 2.1408$. These systems may provide evidence for spatial variations but the lack of such evidence at other redshifts casts doubt on this conclusion.

We performed a more thorough search for spatial variations by calculating the two-point correlation function for α. Consider two absorption systems with values

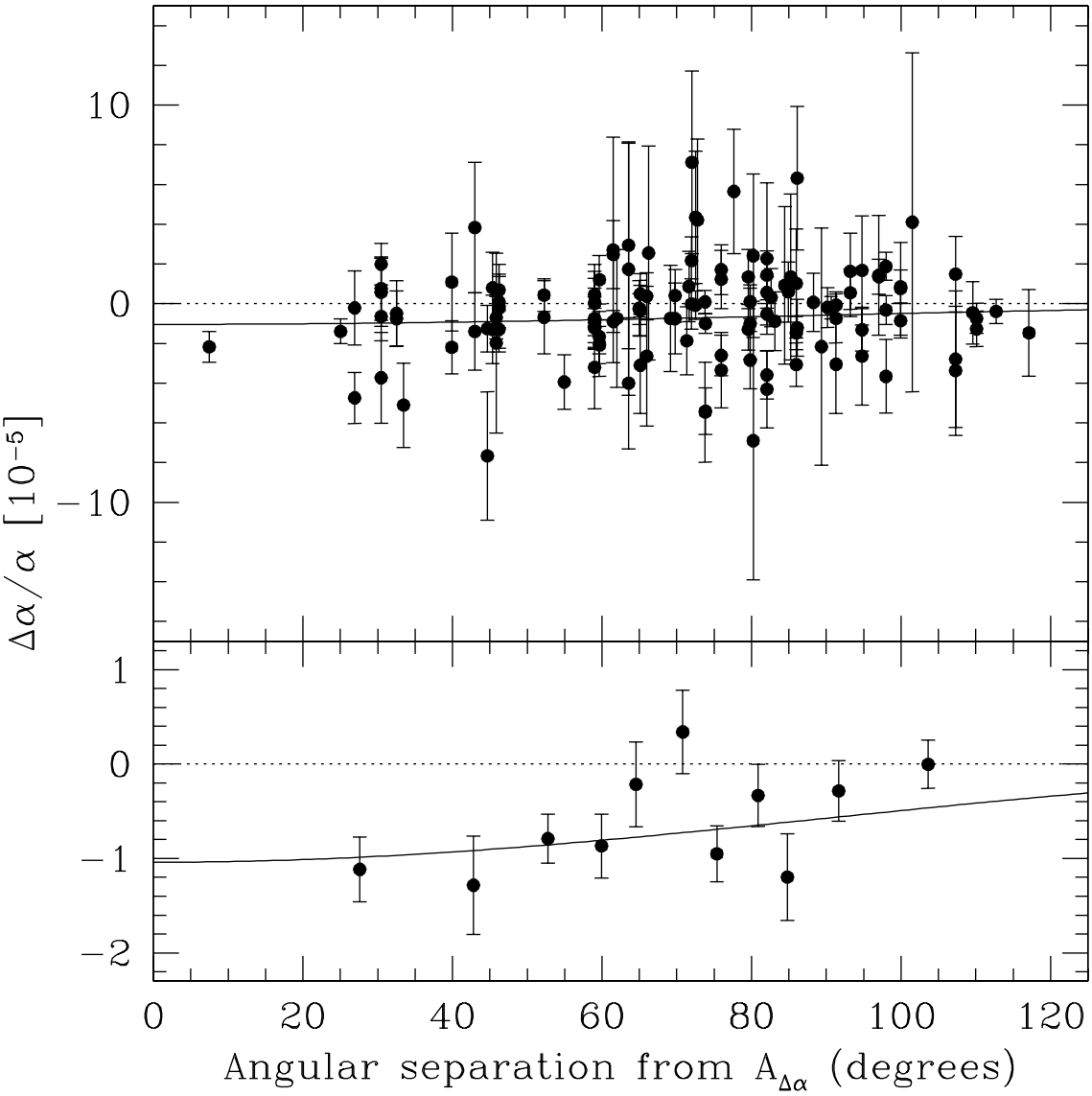

Figure 3.11. Best-fit dipole to the angular distribution of $\Delta\alpha/\alpha$ in Fig. 3.10. The pole lies in the direction $P_{\Delta\alpha}(l, b) = (310°, -5.4°)$. The upper panel shows the distribution of $\Delta\alpha/\alpha$ with angular separation from the anti-pole, $A_{\Delta\alpha}$. The lower panel shows a binning of the results. The solid line is the best-fit cosine with an amplitude $(\Delta\alpha/\alpha)_{\rm d} = (0.47 \pm 0.23) \times 10^{-5}$. However, the limited angular coverage of QSO sight-lines clearly undermines confidence in this dipole interpretation.

of α, α_1 and α_2, as calculated in Table 3.4. The two-point correlation function, C_{12}, is then

$$C_{12} = \frac{(\alpha_1 - \alpha_{\rm m})\,(\alpha_2 - \alpha_{\rm m})}{\alpha_{\rm m}^2}\,, \tag{3.13}$$

where $\alpha_{\rm m}$ is the mean value of α over the entire sample.

In Fig. 3.12 we plot the correlation function versus the comoving separation between the absorption systems (e.g. Liske 2003), χ_{12}. We used a Monte Carlo technique to estimate the mean $C_{12}(\chi_{12})$ and 68% confidence interval for each bin. Synthetic values of α were drawn randomly from Gaussian distributions centred on the measured values with $1\,\sigma$ widths equal to the measured $1\,\sigma$ errors. Where independent observations of an absorption system exist (Section 3-5.6), we centred the Gaussian on the weighted mean value and used the $1\,\sigma$ error in the weighted mean. For each bin, the mean C_{12} was found from all pairs of absorption systems with comoving separations within the bin. In Fig. 3.12 we plot the mean and rms of this quantity, represented by a point and error bar. Fig. 3.12 shows no evidence for significant spatial correlations in α over 0.2–13 Gpc (comoving) scales.

3-5.6 Repeated observations

Several QSOs in the sample have been observed independently by two different groups: sample 3 contains 7 absorption systems which are also (independently) contained in either sample 1 or 2. Two independent spectra of the $z_{\rm abs} = 2.6253$ system towards GB 1759+7539 are also contained in sample 2. We compare the values of $\Delta\alpha/\alpha$ for these repeated systems in Fig. 3.13. The lower panel may indicate some evidence for systematic errors in individual points (i.e. some additional scatter may exist). However, the value of χ^2 with respect to zero difference is $\chi^2 = 13.33$ which, for 7 degrees of freedom, has a 6.4% probability of being exceeded by chance. Evidence for additional scatter is therefore rather marginal.

3-6 Summary

We have used the MM method to analyse 3 samples of Keck/HIRES QSO spectra containing a total of 128 absorption systems over the redshift range $0.2 < z_{\rm abs} < 3.7$. All 3 samples independently yield consistent, non-zero values of $\Delta\alpha/\alpha$ (Table 3.5,

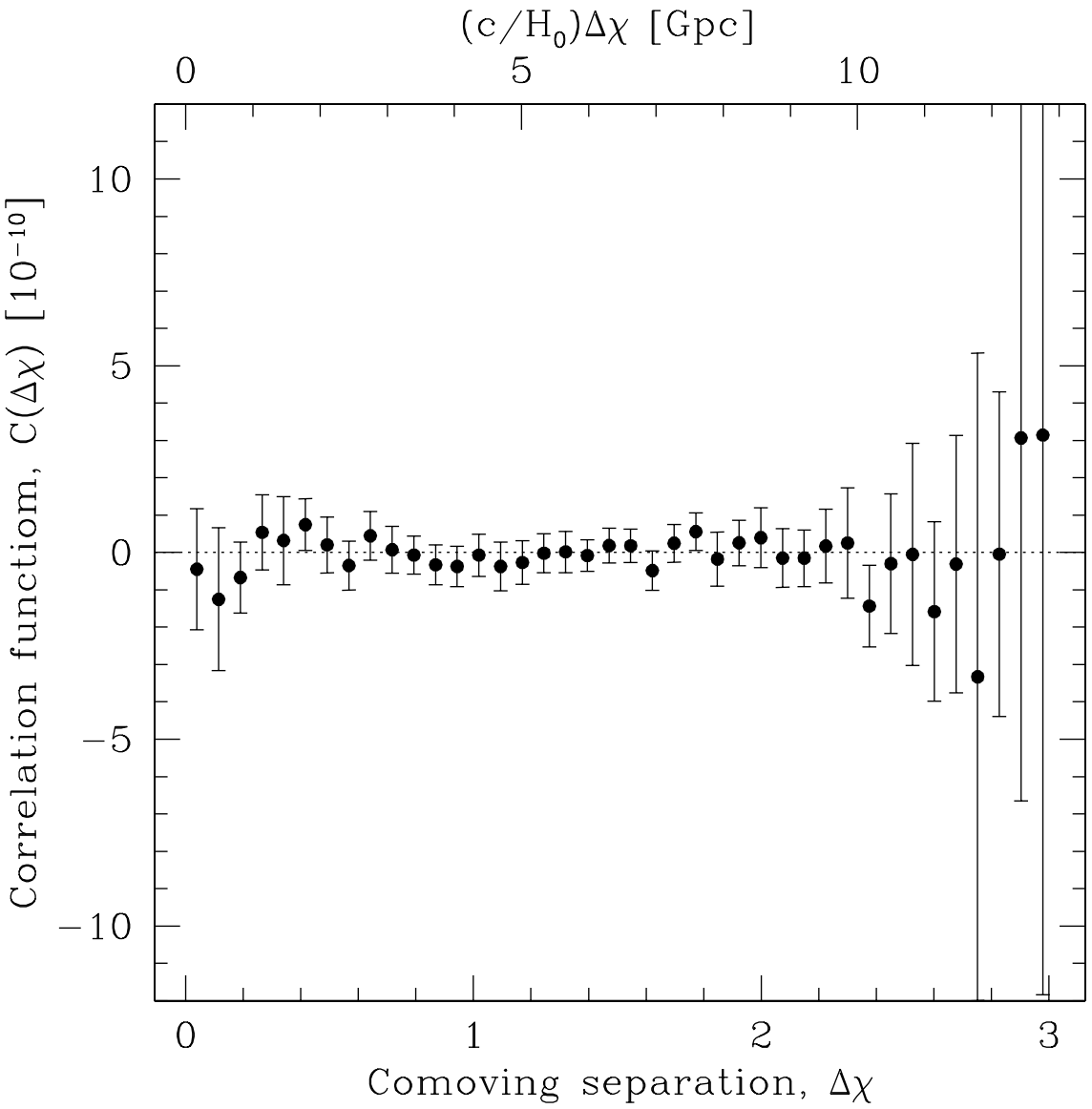

Figure 3.12. The two-point correlation function for α, $C_{12}(\chi_{12})$, as a function of comoving separation between absorption clouds, χ_{12} ($H_0 = 70\,\mathrm{kms}^{-1}\mathrm{Mpc}^{-1}$, $\Omega_\mathrm{m} = 0.3$, $\Omega_\Lambda = 0.7$). The values and errors were obtained with a Monte Carlo technique. However, since each value of $\Delta\alpha/\alpha$ may contribute to many bins, the bins are not independent.

Fig. 3.7). Combining the samples gives a weighted mean $\Delta\alpha/\alpha = (-0.574 \pm 0.102) \times 10^{-5}$, representing $5.6\,\sigma$ statistical evidence for a smaller α in the QSO absorption systems. If one assumes that $\Delta\alpha/\alpha = 0$ at $z_\mathrm{abs} = 0$ then a constant increase in α with time is preferred over a constant $\Delta\alpha/\alpha$ at the 55% confidence level: $\dot{\alpha}/\alpha =$

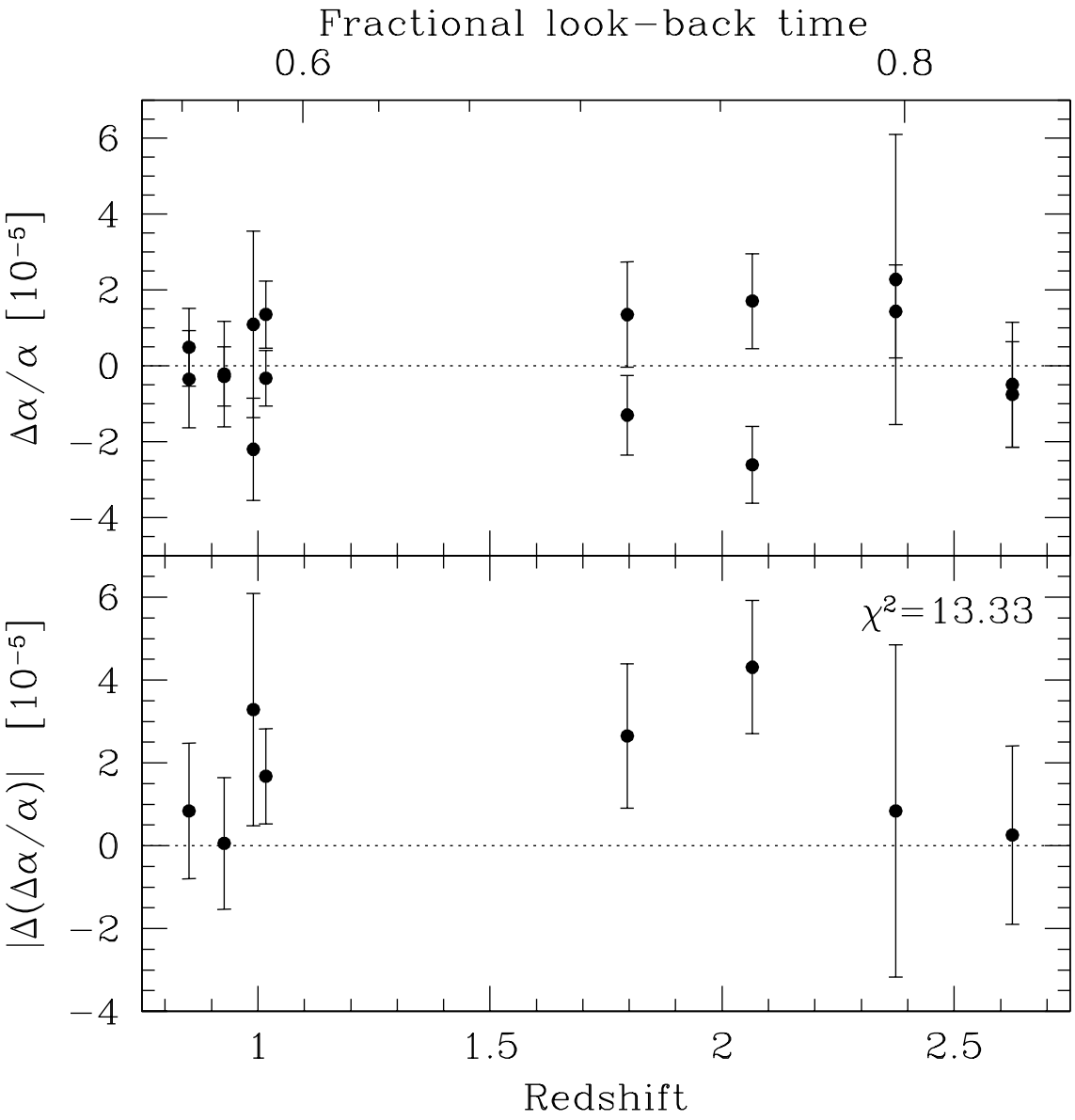

Figure 3.13. Repeated absorption systems. The upper panel shows the values of $\Delta\alpha/\alpha$ for those systems which have been observed independently by different groups. The absolute difference is shown in the lower panel.

$(6.41 \pm 1.12) \times 10^{-16}\,\mathrm{yr}^{-1}$. However, we find no evidence for spatial variations from the angular distribution of $\Delta\alpha/\alpha$ (Fig. 3.10) and no evidence for spatial correlations in α from the two-point correlation function (Fig. 3.12).

Anything that can go wrong, will go wrong.

Finagle's law of dynamic negatives

Corollary:
Never attribute to malice that which can be adequately explained by stupidity.

Hanlon's razor

Chapter 4

Detailed analysis of systematic errors

In the previous chapter we presented $5.6\,\sigma$ evidence for a variable α. Specifically, we found that the value of α in the QSO absorption clouds was systematically smaller than the laboratory value: $\Delta\alpha/\alpha = (-0.574 \pm 0.102) \times 10^{-5}$. In this chapter we conduct a thorough search for systematic errors which could potentially explain this surprising result. We consider a wide range of instrumental and astrophysical systematic errors that may mimic significant non-zero (positive or negative) values of $\Delta\alpha/\alpha$: laboratory wavelength errors, heliocentric velocity errors/variations, kinematic effects, magnetic fields, air-vacuum wavelength conversion, wavelength miscalibration, instrumental profile variations, spectrograph temperature variations, line blending, isotopic and hyperfine structure effects and atmospheric dispersion effects. Many of these can be excluded with high confidence with general arguments while others require a much more detailed analysis. We have also conducted several line-

removal tests which constrain systematic errors of unknown origin. Finally, Section 4-14 considers a similar range of systematic errors in the Si IV alkali doublet (AD) method.

4-1 Laboratory wavelength errors

Errors in the values of ω_0 will lead directly to errors in any single determination of $\Delta\alpha/\alpha$. If, for example, the laboratory wavelengths of the Mg II lines were all shifted to the blue or red then this would systematically bias the values of $\Delta\alpha/\alpha$ for the low-z sample. We summarized the measurements of all values of ω_0 in Section 3-2.2. Most measurements were repeated independently and good agreement was obtained in those cases. A typical measurement accuracy of ω_0 from these laboratory measurements is $\sim 2 \times 10^{-3}\,\mathrm{cm}^{-1}$, which could only introduce a maximum error in $\Delta\alpha/\alpha$ around an order of magnitude below the observed deviation from zero. In practice, since we use several transitions (particularly for the high-z sample), any associated errors are likely to be smaller. We therefore consider it unlikely that the systematic shift in $\Delta\alpha/\alpha$ is due to errors in the values of ω_0.

4-2 Heliocentric velocity variations and errors

During a one hour exposure, representative of the QSO integrations for the samples we have used (Section 3-3.1), the heliocentric velocity may change by as much as $\sim 0.1\,\mathrm{kms}^{-1}$. This will act to smear any spectral feature: the instantaneous spectrum is convolved with a top-hat function in velocity space. However, since we fit a redshift parameter to the spectrum when determining $\Delta\alpha/\alpha$, a velocity-space smearing is completely absorbed into the redshift parameter. Heliocentric smearing will have no effect on measurements of $\Delta\alpha/\alpha$. Similarly, errors in the heliocentric velocity will have no effect on the value of $\Delta\alpha/\alpha$ for a given system. Such errors may be introduced if the reduction software (predominantly MAKEE, Section 3-3.1) calculates the heliocentric velocity for a time other than the flux weighted average

time of observation. In summary, heliocentric velocity variations and/or errors lead to systematic errors in the estimated redshifts of the different velocity components, not in $\Delta\alpha/\alpha$.

4-3 Kinematic effects

In order to measure $\Delta\alpha/\alpha$ with the MM method, one must assume that corresponding velocity components of different ionic species have the same intrinsic redshift. The low-z Mg/Fe II systems would be more sensitive to velocity segregation between species due to the simple arrangement of q coefficients (see Fig. 3.3). For the high-z systems, the effect on $\Delta\alpha/\alpha$ for an individual system would be minimized due to the diversity and complicated arrangement of q coefficients. Velocity segregation could arise through chemical abundance gradients combined with differential velocity fields. These effects may also generate departures from Voigt profiles.

Inhomogeneous photoionization throughout the absorption complex is also a possibility. With the exception of Mg I and Al III (discussed in Section 3-3.2), the species in our analysis are singly ionized and have very similar ionization potentials below the Lyman limit (see Table 3.1). Thus, the absorption from different ionic species, associated with a given velocity component, should arise co-spatially. However, variations in the incident radiation field could cause weak components in the singly ionized species to appear very strong in Mg I or Al III. Spurious shifts in $\Delta\alpha/\alpha$ could be introduced if a strong Mg I or Al III component was mistakenly tied to a nearby ($|\Delta v| \sim 0.5\,\mathrm{km s^{-1}}$) singly ionized component[1].

However, these kinematic shifts in $\Delta\alpha/\alpha$ are themselves random over a large ensemble of random sight-lines. If kinematic effects are significant, they act only to increase the scatter in the values of $\Delta\alpha/\alpha$ beyond what is expected on the basis of the statistical errors alone. The value of χ^2_ν for the low-z sample in Table 3.5 is ≈ 1 and so the low-z data present no evidence for significant kinematic effects. One

[1]We have no evidence for these effects since the there is no additional scatter in $\Delta\alpha/\alpha$ for systems containing Mg I or Al III.

may interpret the extra scatter in $\Delta\alpha/\alpha$ observed at high-z as evidence for such effects, though we discuss other, more likely, mechanisms for producing this scatter in Section 3-5.2.

Despite the random nature of kinematic effects over a large number of velocity components and absorption systems, we discuss below the contributory factors to potential effects on small velocity scales for individual velocity components.

4-3.1 Small-scale velocity structure and equilibrium in QSO absorbers

Detailed kinematic studies of QSO absorbers (Briggs et al. 1985; Lanzetta & Bowen 1992; Wolfe & Prochaska 2000; Churchill & Vogt 2001), indicate that a disk+halo model provides a reasonable description of the absorption systems. Alternative models exist, including multiple merging clumps bound to dark matter halos (Haehnelt et al. 1998; McDonald & Miralda-Escudé 1999; Maller et al. 1999) and outflows from supernovae winds (Nulsen et al. 1998; Schaye 2001). For disk+halo models of Mg/Fe II systems, the disk component is strongly saturated and spread over small velocity scales whereas the halo component is broadly spread in velocity space and causes the lower column density absorption. The constraints on $\Delta\alpha/\alpha$ in the Mg/Fe II systems are therefore dominated by velocity components arising in the outer parts of galaxy halos. The constraints on $\Delta\alpha/\alpha$ from DLAs arise either from low abundance, hence unsaturated, species (e.g. Ni II, Cr II, Zn II), or from optically thin components flanking the saturated ones (e.g. Fe II λ1608 or Al II λ1670).

However, the large-scale properties of the absorbing gas have no influence on estimates of $\Delta\alpha/\alpha$. Galactic rotation or large-scale galactic winds are unimportant. The fact that we find excellent agreement between the redshifts of individual velocity components down to $\lesssim 0.3\,\mathrm{kms}^{-1}$ illustrates this. Any contribution to the scatter in $\Delta\alpha/\alpha$ comes only from the detailed properties of gas on velocity scales typical of the observed b-parameters, i.e. $\lesssim 5\,\mathrm{kms}^{-1}$.

Given the importance of small-scale properties in the determination of $\Delta\alpha/\alpha$, it

is relevant to ask whether the gas is in dynamic equilibrium on these scales. For the low-z Mg/Fe II systems, a recent detailed study (Churchill et al. 2003a) suggests that the column density ratio N(Mg II)/N(Fe II) appears not to change systematically across an absorption complex. A similar chemical uniformity is found for the majority of high-z systems (Prochaska 2003; Churchill et al. 2003b). This implies that, if not in equilibrium, the gas is well mixed, i.e. absorption lines of different species arise co-spatially. Furthermore, DLAs show no significant evolution in their number density per unit redshift interval (Rao & Turnshek 2000). Photoionization models also suggest gas in photoionization equilibrium with an ambient extragalactic UV background. If this is correct, local equilibrium may be valid. Any redshift evolution of the number of absorption lines per unit redshift interval, over and above that expected due to cosmology alone, could be explained by cosmological evolution of the integrated background UV flux.

Thus, there is evidence to suggest that no gross changes in physical conditions occur over large velocity scales across an absorption complex. This may imply that we should not expect to find abundance variations and non-equilibrium on small scales. If this is incorrect, one expects departures from a Maxwellian velocity distribution in the absorbers, the assumption of which is inherent in fitting Voigt profiles (see Appendix A, Section A-1). We note in passing that no evidence currently exists for non-Voigt profiles (e.g. Outram et al. 1999), despite expectations from hydrodynamic simulations of large-scale structure formation (Outram et al. 2000).

4-3.2 Comparison with the ISM

In contrast to the previous section, analogy with the interstellar medium (ISM) in our own Galaxy suggests that non-equilibrium could apply on very small scales. Andrews et al. (2001) use stars in a background globular cluster, M92, to probe the kinematics on scales defined by the separation between the lines of sight at the absorber. They find significant variations in Na I column densities in the ISM on scales as small as 1600 AU (or $\sim$ 0.01 pc). Even smaller-scale details come

from measurements of temporal variation of Na I and K I absorption lines, implying non-equilibrium scales $\sim 10 - 100\,\mathrm{AU}$ (Crawford et al. 2000; Lauroesch et al. 2000; Price et al. 2000). Although these ISM cloud sizes are small compared to estimates of the sizes of individual QSO absorption cloud components, ∼10–100 pc (Churchill & Vogt 2001), the characteristic size for a QSO continuum emission region may be $\sim 10^{-3}\,\mathrm{pc}$. The lines-of-sight to opposite edges of the QSO therefore probe similar size scales as the Galactic ISM studies. However, it should be noted that the gas densities are very different and so the comparison should be treated with caution.

The ISM analogy may also allow us to estimate an upper limit on the velocity segregation in QSO absorption clouds. Some theories argue that gravity may be important for cloud confinement on small size scales in the Galactic ISM (e.g. Walker & Wardle 1998). If gravity plays a significant role in QSO absorption systems on similar scales, we could apply a simple stability condition on the velocity dispersion, $v^2 = GM/R$, where M and R are the cloud mass and radius. Estimates for individual cloud sizes vary but adopting $R = 10\,\mathrm{pc}$ and $M = 30\,M_\odot$ (Churchill & Vogt 2001) we find $v \lesssim 0.1\,\mathrm{kms}^{-1}$. This provides an upper limit on the velocity shift between different species. For one single Mg/Fe II velocity component, this translates into an error on an individual $\Delta\alpha/\alpha$ measurement of roughly $\Delta\alpha/\alpha \sim 0.3 \times 10^{-5}$. However, this would be randomized over ∼100 observations (and over many velocity components), producing a maximum effect which is 20 times smaller than that observed.

4-4 Magnetic fields

Shifting of ionic energy levels due to large magnetic fields may also be a possibility. If very large scale magnetic fields exist in the intergalactic medium and QSO light is polarized, this could result in correlated values of $\Delta\alpha/\alpha$ in neighbouring regions of the universe. However, the absorption clouds studied here are separated by comoving distances of 0.2–13 Gpc (see Fig. 3.12). Furthermore, even in Abell clusters, intra-

cluster magnetic field strengths are typically $\sim\mu$G (e.g. Feretti et al. 1999), roughly 9 orders of magnitude below the strength required to cause substantial effects. We consider this possibility to be very unlikely.

4-5 Air–vacuum wavelength conversion

Most thorium-argon (ThAr) line lists are presented as air wavelengths. The usual data reduction procedure is to carry out the wavelength calibration fits to the data using air wavelengths and then convert the calibrated spectrum to vacuum wavelengths. For example, MAKEE, which was used to calibrate the majority of spectra in samples 2 and 3, uses air wavelengths for a selection of lines from the thorium spectral atlas of Palmer & Engleman (1983) and from the argon lines of Norlén (1973). The same list is used in IRAF which was used to calibrate the majority of spectra in sample 1. In the latter case, the spectra were actually calibrated with a set of vacuum wavelengths, $\lambda_{\rm vac}$, that IRAF states is derived from the air wavelengths, $\lambda_{\rm air}$, by using the Edlen (1966) formula for the refractive index, n,

$$10^8\,[n(\lambda_{\rm vac})-1] = 8342.13 + \frac{2406030}{(130-\sigma^2)} + \frac{15997}{(38.9-\sigma^2)} \qquad (4.1)$$

at 15°C and atmospheric pressure. Instead of using $\sigma \equiv 10^4/\lambda_{\rm vac}$, IRAF makes the approximation, $\sigma \approx 10^4/\lambda_{\rm air}$. MAKEE converts the final air wavelength calibrated QSO frames to vacuum using the Cauchy dispersion formula (e.g. Weast 1979),

$$10^7\,[n(\lambda_{\rm air})-1] = 2726.43 + \frac{12.288}{10^{-8}\lambda_{\rm air}^2} + \frac{0.3555}{10^{-16}\lambda_{\rm air}^4} \qquad (4.2)$$

at 15°C and atmospheric pressure. $\lambda_{\rm vac}$ and $\lambda_{\rm air}$ are both measured in angstroms in the above equations. This difference begs the question: 'What is the absolute and relative accuracy of these conversion formula?'.

First let us refine this question. The measurements reported by Palmer & Engleman (1983) and Norlén (1973) were all carried out in vacuum. The air wavelengths they quote are calculated using the Edlen formula. Thus, IRAF and MAKEE will only produce 'correct' vacuum wavelength scales if they invert the

Edlen formula to calculate the refractive index. As stated above, this is not the case. Therefore, to re-state the above question, what error does the IRAF and MAKEE air–vacuum wavelength conversion introduce into the resulting QSO wavelength scale? To illustrate the answer to this we plot the various conversion formulae commonly used in the literature, including those discussed above, in Fig. 4.1. We also include the original Edlen (1953) formula[2] for comparative purposes. Peck & Reeder (1972) published a fit to revised refractive index data, proposing a 4-parameter formula:

$$10^8\,[n(\lambda_{\rm vac})-1] = \frac{5791817}{(238.0185-\sigma^2)} + \frac{167909}{(57.362-\sigma^2)} \qquad (4.3)$$

at 15°C and atmospheric pressure with $\sigma \equiv 10^4/\lambda_{\rm vac}$ (again, $\lambda_{\rm vac}$ is in angstroms).

From Fig. 4.1 we see that the Cauchy formula seriously deviates from the other formulas. Furthermore, the difference between the Edlen and Cauchy dispersions is strongly wavelength dependent. Thus, spectra calibrated with MAKEE may have systematically non-zero values of $\Delta\alpha/\alpha$ due to this distortion. We have corrected all the affected spectra in samples 2 and 3 by converting the wavelength scale back to air wavelengths using the (inverted) Cauchy formula and then back to vacuum using the (inverted) Edlen formula. From Fig. 4.1 we also note the small distortion to the wavelength scale introduced by the approximation made within IRAF. We have corrected the affected spectra in sample 1 for this effect even though the difference is below our level of precision.

4-6 Wavelength miscalibration

The QSO CCD images are wavelength calibrated by comparison with the ThAr emission spectra which are generally taken both before and after each QSO exposure. A polynomial wavelength solution is obtained by centroiding a standard set of ThAr lines which are strong and (appear to be) unblended in the particular ThAr lamp in

[2]The 1953 formula is of the same form as the 1966 formula (equation 4.1) but has slightly different parameters: 6432.8, 2949810, 146, 25540 and 41 in order from left to right, numerator to denominator.

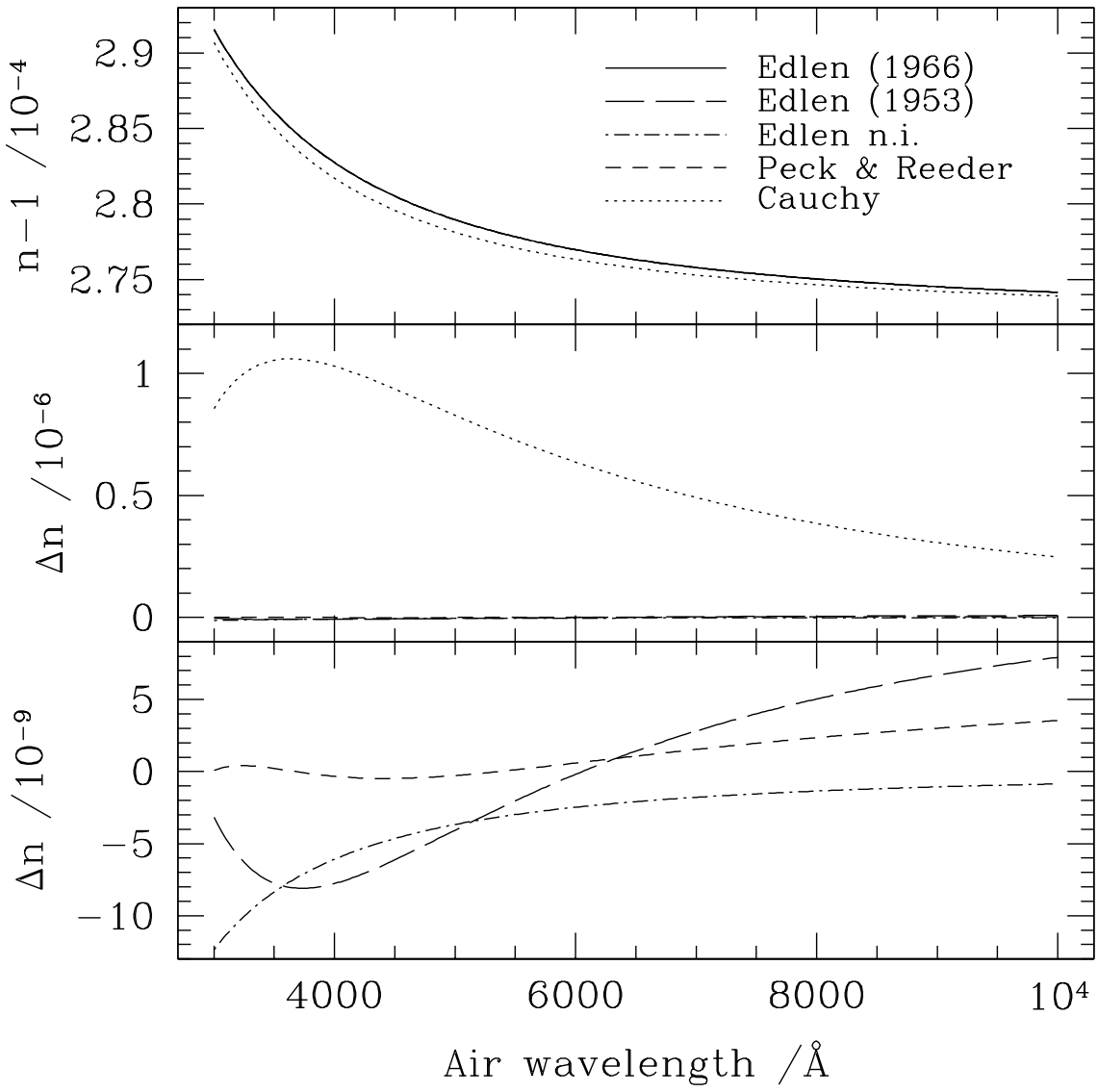

Figure 4.1. Comparison of the various air dispersion formulas used in the literature (all for 15°C and atmospheric pressure). We use the Edlen (1966) formula as our reference since the atlases of Palmer & Engleman (1983) and Norlén (1973) use this to convert their vacuum wavelengths to air wavelengths. The top panel shows the dispersion for the Edlen (1966) and Edlen (1953) formulas together with that of Peck & Reeder (1972) and the Cauchy formula (Weast 1979). We also plot the approximation made within IRAF where the Edlen formula has not been inverted to convert air wavelengths to vacuum (denoted "Edlen n.i."). The middle and lower panels show the difference between the Edlen (1966) refractive index, $n_{\rm E}$, and that derived from the other formulae, $n_{\rm X}$: $\Delta n \equiv n_{\rm E} - n_{\rm X}$.

use. We consider errors in the laboratory wavelengths of the selected ThAr lines to be negligible as their absolute values are known to greater precision than our values of λ_0: $\delta\lambda_{\rm ThAr} \sim 5 \times 10^{-5}$ Å (Palmer & Engleman 1983).

However, there may be inaccuracies in the wavelength calibration software used to reduce the spectra. Also, human error cannot be ruled out. One or more of the ThAr lines in the standard set could be misidentified or, in a more subtle way, lead to long range miscalibrations of the wavelength scale. Misidentifications could also be applied to the rest of the spectra taken over the same series of observations (i.e. applied to the spectra of many QSOs in one or all three samples). This effect would be particularly problematic in the low-z absorption systems where all values of $\Delta\alpha/\alpha$ would be affected in the same sense by such a low-order distortion of the wavelength scale (see Fig. 3.3). Webb et al. (1999, hereafter W99) stated that a drift in the wavelength calibration by an amount corresponding to ~ 2.5 times the mean wavelength-pixel residuals over the range of the CCD could result in a significant error in their results from low-z Mg/Fe II systems.

Thus, *a priori*, we cannot rule out the possibility that the wavelength scale has been set improperly in this process and that a systematic shift in α has not been mimicked. Such a potential effect needs careful investigation. Below we directly quantify the effect of any wavelength calibration errors on $\Delta\alpha/\alpha$. We analyse sets of ThAr emission lines in the same way we analyse sets of QSO absorption lines. If no calibration error exists then one should obtain $(\Delta\alpha/\alpha)_{\rm ThAr} = 0$ for each absorption system.

4-6.1 The thorium-argon calibration test

For each QSO spectrum, we selected $\sim$15 Å sections of ThAr spectra at wavelengths corresponding to the observed absorption lines in the QSO spectra. Each $\sim$15 Å section contains several (typically up to $\sim$10) ThAr lines. Error arrays were generated assuming Poisson counting statistics. We fitted continua to these ThAr sections, dividing the raw spectra by the continua to obtain normalized spectra. Several in-

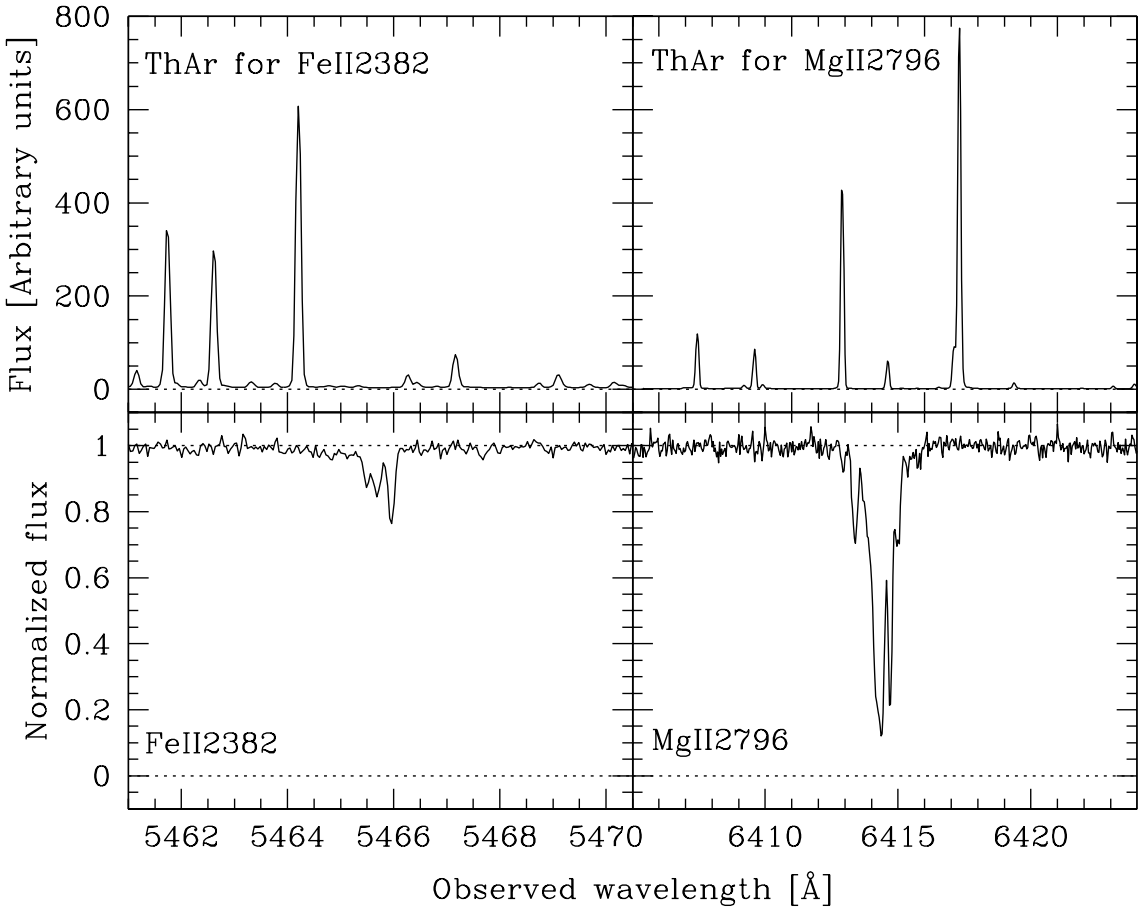

Figure 4.2. The ThAr calibration test. The lower panels show two sections of QSO spectra from the $z_{\rm abs} = 1.2938$ Mg/Fe II system towards Q0636+6801 (sample 3). The upper panels show the corresponding sections of ThAr spectra used to calibrate the wavelength scale. We may ascribe the q coefficients of the QSO absorption lines (Mg II λ2796 and Fe II λ2382 in this case) to pairs of ThAr lines which have well known laboratory wavelengths. The value of $(\Delta\alpha/\alpha)_{\rm ThAr}$ so derived may be compared directly with $\Delta\alpha/\alpha$ derived from the absorption lines.

dependent[3] sets of ThAr emission lines were selected from each section of spectra. Each set of lines therefore corresponds to, and has been selected in an analogous way to, one QSO absorption system. Fig. 4.2 illustrates the ThAr lines associated with a particular Mg/Fe II absorption system. Selecting several (typically 3–7) different sets of ThAr lines allows a more robust estimate of $(\Delta\alpha/\alpha)_{\rm ThAr}$ for each absorption

[3]Each set of ThAr lines never included any of the ThAr lines from any other set.

system and provides a cross-check on its $1\,\sigma$ uncertainty.

We fit Gaussian profiles to the emission lines with the same modified version of VPFIT used to fit Voigt profiles to the QSO absorption lines (see Section 3-4). We adopted the ThAr wavelengths from Palmer & Engleman (1983) and Norlén (1973) for values of ω_0 in equation 3.5. In order to relate any measured ThAr line shifts directly to a value of $(\Delta\alpha/\alpha)_{\rm ThAr}$, we assign to each ThAr line the q coefficient corresponding to the QSO absorption line falling in that part of the spectrum (Fig. 4.2). That is, we treat the ThAr lines as if they *were* QSO absorption lines and derive a value of $(\Delta\alpha/\alpha)_{\rm ThAr}$ using the MM method. The free parameters involved in each fit are the line-width (assumed the same for all ThAr lines in a given set, although the results were insensitive to this assumption), 'redshift' (numerically close to zero) and peak intensity.

4-6.2 Results and discussion

ThAr spectra were readily available for 118 of the 128 absorption systems in the total sample. We applied the above ThAr test to these spectra and obtain the results presented in Fig. 4.3. Comparing the QSO results in panel (a) with the ThAr results in panel (b) we immediately see that miscalibrations of the wavelength scale did not systematically affect the overall value of $\Delta\alpha/\alpha$. This is particularly emphasized in panel (e) which compares binned values of $\Delta\alpha/\alpha$ and $(\Delta\alpha/\alpha)_{\rm ThAr}$. We tabulate various statistics for the ThAr test in Table 3.5 for direct comparison with the QSO results. Notably, the overall weighted mean value, $(\Delta\alpha/\alpha)_{\rm ThAr} = (0.4 \pm 0.8) \times 10^{-7}$, is two orders of magnitude below the observed value of $\Delta\alpha/\alpha$.

Caption for Fig. 4.3. Comparison between the QSO results [panel (a)] and the ThAr calibration error [panel (b)] for sample 1 (open circles), sample 2 (open triangles) and sample 3 (open squares). The $(\Delta\alpha/\alpha)_{\rm ThAr}$ scale is expanded by a factor of 10 in panel (c). Panel (d) shows binned values for the three sub-samples and panel (e) compares the binned values for the total ThAr (solid circles) and QSO (open circles)

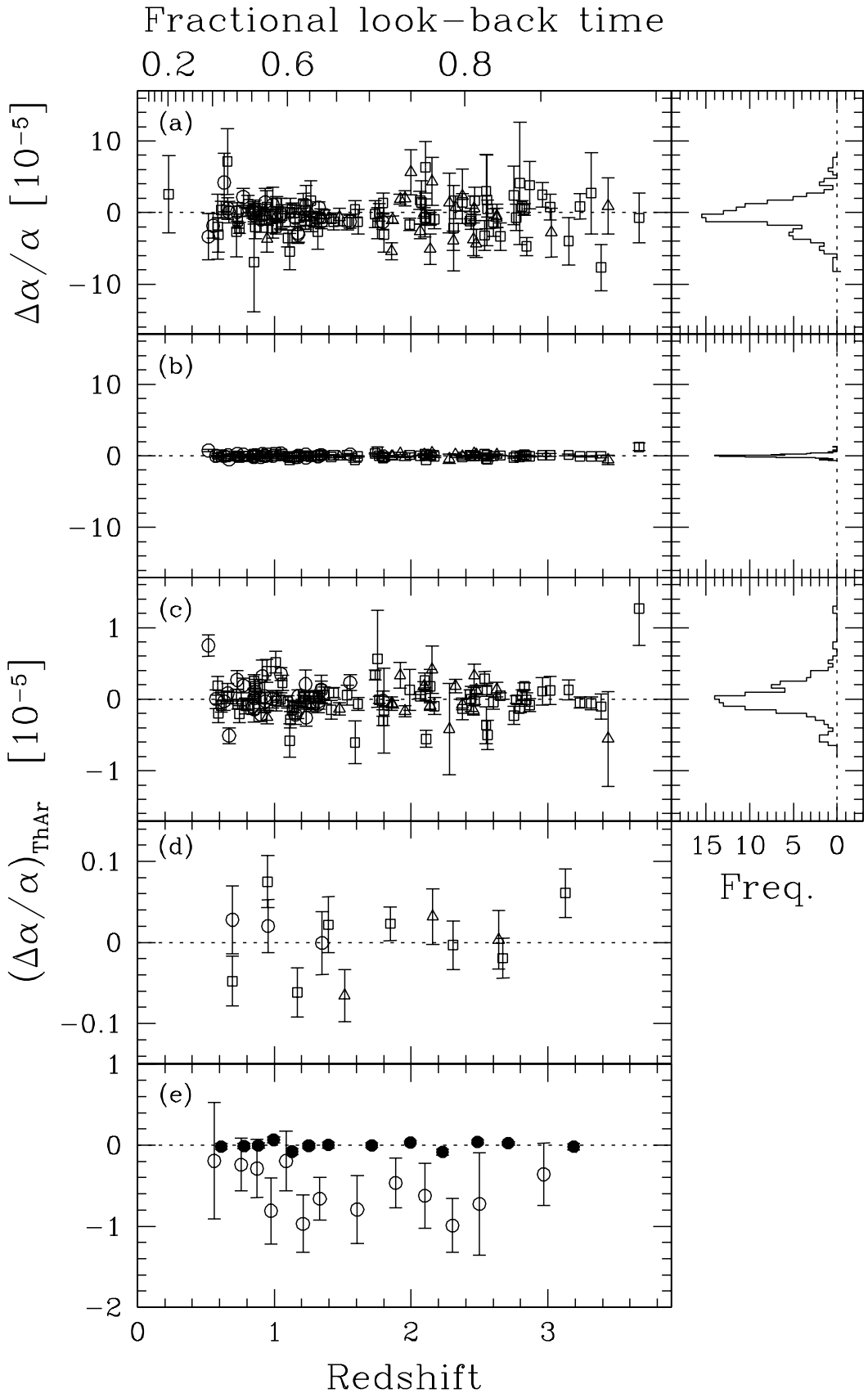

Figure 4.3. ThAr calibration test results. See text for caption.

samples. The weighted mean of the ThAr results is $(\Delta\alpha/\alpha)_{\rm ThAr} = (0.4 \pm 0.8) \times 10^{-7}$.

Panel (c) of Fig. 4.3 shows an expanded view of the ThAr results which demonstrates a similar 'extra scatter' to the high-z QSO sample (see Section 3-5.2). The extra scatter has a similar origin as for the high-z QSO results: close inspection of any portion of ThAr spectrum reveals a plethora of weak emission lines and so the fit to any given (strong) ThAr emission line will be affected by weak blends. The ThAr lines are of such high S/N that significant extra scatter ensues. This effect would produce uncorrelated deviations in $(\Delta\alpha/\alpha)_{\rm ThAr}$ from point to point, as observed. Another interpretation may be that the extra scatter presents evidence for ThAr line misidentifications. However, if these were important, one would expect systematically correlated deviations [i.e. an overall non-zero offset in $(\Delta\alpha/\alpha)_{\rm ThAr}$)] and this is not observed. One might also expect a correlation between $(\Delta\alpha/\alpha)_{\rm ThAr}$ and $\Delta\alpha/\alpha$ in this case. Fig. 4.4 shows no such correlation.

On inspection of some of the ThAr spectra in sample 1, we noted that some ThAr lines towards the blue end of the spectrum were slightly asymmetric. This may indicate a degradation in the polynomial fits near the edges of the fitting regions. These may also indicate an intrinsic asymmetry in the HIRES instrumental profile (IP) and this is discussed in Section 4-7.

We conclude this section by emphasizing the reliability of the wavelength scale as derived from the ThAr spectra: we directly measure the effect of any ThAr miscalibrations on $\Delta\alpha/\alpha$ and find it to be negligible. One objection to the reliability of the MM method has been that fitting transitions which fall on different echelle orders may lead to systematic errors (Varshalovich et al. 2000; Ivanchik et al. 2002). The ThAr test in Fig. 4.3 clearly demonstrates that this concern is unfounded.

[4] $P(r_{\rm s})$ is the probability that $|r_{\rm s}|$ could have been exceeded by chance.

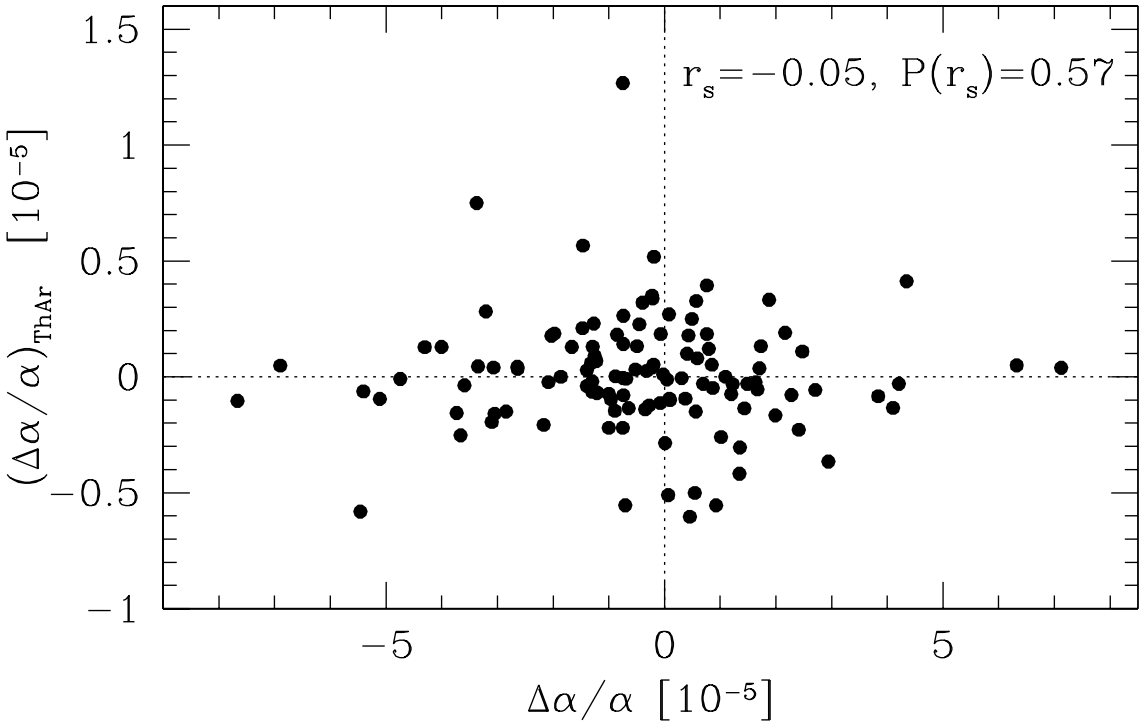

Figure 4.4. Is $(\Delta\alpha/\alpha)_{\rm ThAr}$ correlated with $\Delta\alpha/\alpha$? If the significant scatter in the ThAr calibration test results (Fig. 4.3) were due to ThAr line misidentifications then one might expect a correlation between $(\Delta\alpha/\alpha)_{\rm ThAr}$ and $\Delta\alpha/\alpha$. Here, the Spearman rank correlation coefficient, $r_{\rm s}$, and associated probability, $P(r_{\rm s})$[4] indicate no significant correlation.

4-7 Instrumental profile (IP) variations

If the IP of HIRES shows significant *intrinsic* asymmetries then we expect absorption line centroids to be incorrectly estimated. If the asymmetry varies with wavelength, this could mimic a non-zero $\Delta\alpha/\alpha$. Valenti et al. (1995) have derived the HIRES IP for several positions along a single echelle order, finding that the IP is slightly asymmetric and that this asymmetry varies slightly along the order. Valenti et al. do not quantify the asymmetry variation across orders, though this is likely to be comparable to the variation along the orders.

The ThAr calibration test results in Fig. 4.3 also illuminates discussion of potential IP variations and their effect on $\Delta\alpha/\alpha$. To a first approximation, the ThAr

and QSO light paths through the spectrograph are the same. If such asymmetry variations exist then they should also apply to the QSO spectra. The ThAr results in Fig. 4.3 therefore strongly suggest that IP asymmetries (and variations thereof) do not contribute significantly or systematically to $\Delta\alpha/\alpha$. One possibility is that the ThAr and QSO light follow slightly different and possibly wavelength dependent paths through the spectrograph to the CCD. We explore this possibility in Section 4-11 in the context of atmospheric dispersion effects.

4-8 Spectrograph temperature variations

The refractive index of air within the spectrograph depends on temperature (and also on pressure but this is a smaller effect). If a QSO spectrum is calibrated with only a single ThAr exposure taken at a different spectrograph temperature, we expect a systematic miscalibration of the QSO frame's wavelength scale. Consider a QSO frame taken at 15°C which is calibrated with a ThAr exposure taken at 0°C and similar pressure. Any wavelength separation in the QSO exposure will be overestimated. For example, the difference between the wavelength separations of vacuum $\lambda\lambda$4000 and 7000 at 15°C and 0°C is 43×10^{-3} Å (using the tables in Weast 1979). A comparison with values of $\Delta\lambda$ in Table 3.2 indicates that this would result in $\Delta\alpha/\alpha \gtrsim +1 \times 10^{-5}$ for a typical low-z Mg/Fe II system.

Note that a systematically non-zero $\Delta\alpha/\alpha$ can only be introduced for the Mg/Fe II systems if $T_{\rm QSO}$ is systematically higher or lower than $T_{\rm ThAr}$. This is possible if the ThAr exposures were always taken before or after the QSO frames and the temperature evolves monotonically throughout the night. However, the effect can be greatly reduced if the ThAr calibration exposures are taken immediately before and/or after the QSO exposures or if the spectrograph is temperature stabilized (e.g. VLT/UVES). The former was generally the case for our observations. We have used image header information to calculate $\Delta T = \langle T_{\rm QSO}\rangle - \langle T_{\rm ThAr}\rangle$ for each QSO in each sample, where the average is taken over all QSO and ThAr exposures. We find mean values of $\Delta T = 0.04 \pm 0.02$ K, $\Delta T = 0.2 \pm 0.1$ K and $\Delta T = 0.013 \pm 0.006$ K

for samples 1, 2 and 3 respectively. Taking into account that, on average, rest-frame separations between the transitions of interest are $\lesssim 300$ Å, it is clear that our values of $\Delta\alpha/\alpha$ are not affected by spectrograph temperature variations.

4-9 Line blending

The errors in $\Delta\alpha/\alpha$ presented in Table 3.4 take into account errors from signal-to-noise and spectral resolution considerations and the velocity structure of the profile fits. The errors are also reduced when more lines are fitted simultaneously. However, we have assumed that we have deconvolved each absorption system into the correct number of velocity components. There may have been weak, interloping, unresolved lines which could have produced a shift in the fitted line wavelengths of all velocity components of one or more transitions. The importance of such an effect diminishes as the number of transitions used in each fit is increased. Therefore, the effect, if present, should be smaller in our high-z sample. Below we describe a detailed search for potential blends with the MM transitions of interest. We first distinguish between *random* and *systematic* line blending.

4-9.1 Random blends

Random blends can occur when many absorption clouds lie along the line of sight to the QSO, including any interstellar material and the Earth's atmosphere. In general, random blends can only have a random effect on $\Delta\alpha/\alpha$ and so can not have caused the systematically non-zero values observed. Two distinct categories of random blend can be identified:

1. Strong blends. Lyman-α forest absorption lines would cause numerous strong blends. However, if MM transitions fell into the Lyman-α forest region, we generally did not fit them. If the velocity structure of one of our MM transitions is obviously affected by a random blend then we modify our fit for that transition according to the identity of the interloper. If the interloper is a MM transition

(i.e. one with a precise laboratory wavelength listed in Table 3.1), and its velocity structure can be constrained using other associated MM transitions at the interloper's redshift, then we include the interloper in the fit. In general, the laboratory wavelengths of non-MM transitions (e.g. C IV $\lambda\lambda$1548 and 1550) are not known to high precision. Therefore, if the interloper and/or the associated transitions are not MM transitions, possible errors in the laboratory wavelengths could have a significant effect on $\Delta\alpha/\alpha$. In these cases, and if the velocity structure of the interloper was both simple and clear, we freed its redshift parameters, not tieing it to any associated transitions. In all other cases, we either masked the blended data out of the fit or simply rejected that MM transition altogether.

2. Weak blends. It is possible that weak, random interlopers exist in our data but were not identified in our analysis. For example, numerous broad (FWHM = 20–2000 kms^{-1}), weak (equivalent width $\lesssim 0.1$ Å), diffuse interstellar absorption bands have been discovered in stellar spectra (e.g. Herbig 1975; Jenniskens & Desert 1994). The narrower of these lines may blend with some velocity components of individual MM transitions, causing slight, apparent line shifts. However, since our absorption systems lie at a range of redshifts and since many different transitions are fitted to arrive at a final value of $\Delta\alpha/\alpha$, it is unlikely that such weak interlopers have significantly affected the results.

4-9.2 Systematic blends

A systematic blend occurs when two ionic species are in the same absorption cloud and have transitions with similar rest wavelengths. Such a blend could mimic a systematic shift in α. We have explored two approaches to this problem:

1. We attempted to identify candidate blends by searching atomic line databases for transitions lying close to the laboratory wavelengths of the MM transitions. Simulations of various blends indicated that, in order to cause a significant, systematic shift in α, the interloping transition must lie within $\Delta v \approx 10\,\mathrm{kms}^{-1}$ of the 'host' line. If the separation is larger, the interloper blends with other

'host' velocity components, causing random effects on $\Delta\alpha/\alpha$ which depend on the velocity structure of the 'host' transition. No possible blending transitions satisfying the $\Delta v \approx 10\,\mathrm{kms}^{-1}$ criterion could be found in Moore (1971) or the Vienna Atomic Line Database[5] (VALD, Piskunov et al. 1995; Kupka et al. 1999).

We have extended our search criterion to include potential interlopers lying up to $100\,\mathrm{kms}^{-1}$ away from the host MM transitions and have identified two possible interlopers lying to the red of the Zn II λ2026 transition:

(a) Cr II λ2026.269 ($\Delta v \approx 19\,\mathrm{kms}^{-1}$) has an oscillator strength $f = 0.0047$ (VALD). We simulated this blend's effect on the high-z sample: using the largest value of N(Cr II)/N(Zn II) directly from the absorption line data, we generated a synthetic, single velocity component spectrum containing Zn II λ2026 and the Cr II interloper. We also generated several other lines typically observed in the high-z DLAs. We produced synthetic spectra with several different values of $\Delta\alpha/\alpha$ and used VPFIT to measure $\Delta\alpha/\alpha$. The result was that the measured value of $\Delta\alpha/\alpha$ was always consistent with the nominal value, that is, we could detect no significant effect due to the interloping Cr II transition.

(b) Mg I λ2026.477 ($\Delta v \approx 50\mathrm{kms}^{-1}$) has an oscillator strength $f = 0.1154$ (Morton 1991) and was apparent in six of the high-z systems. However, in four cases the velocity structure is narrow enough that the Mg I interloper does not overlap and blend with the Zn II line. In the remaining two cases we fitted the Mg I interloper and left the redshift parameters free (i.e. we did not tie the Mg I velocity structure to that of the other MM transitions). This has the effect of removing any constraints the blended Zn II components may have on $\Delta\alpha/\alpha$. We checked the resulting values of $\Delta\alpha/\alpha$ against those found after completely masking out the blended portion of the Zn II velocity structure and found them to be consistent.

Note that the atomic line databases searched are not complete and that we have

[5]Available at http://www.astro.univie.ac.at/~vald.

not considered molecular interlopers, although the QSO absorbers are known to have very low molecular fractions (e.g. Black et al. 1987; Curran et al. 2002a, 2003a,b; Murphy et al. 2003b). We therefore compliment the treatment above with the following test.

2. To asses the significance of any unknown blends, we may separately remove most transitions from the analysis and re-fit to find a new value of $\Delta\alpha/\alpha$. If the new and old values of $\Delta\alpha/\alpha$ are significantly different then one interpretation is that the transition removed is affected by an unknown systematic blend. We conduct this line-removal analysis in Section 4-12.1 and find no evidence for shifts in $\Delta\alpha/\alpha$ caused by individual transitions or ionic species.

In summary, we find that neither random nor systematic line blending has significantly affected the values of $\Delta\alpha/\alpha$.

4-10 Isotopic and hyperfine structure effects

As stated in Section 3-2, the only species for which full isotopic and hyperfine structures are known are Mg I, Mg II and Al III. We obtained an estimate of the Si II isotopic structures by scaling the Mg II λ2796 structure by the mass shift (equation 3.7). In this section we investigate systematic errors that could result from ignorance of the isotopic/hyperfine structures for other species and from any evolution of the isotopic ratios and/or hyperfine level populations.

4-10.1 Differential isotopic saturation

For the transitions of Cr II, Fe II, Ni II and Zn II, the laboratory wavelengths in Table 3.1 are *composite* values only. The composite wavelengths are only strictly applicable in the optically thin regime (linear part of the curve of growth). Consider an absorption line with several isotopes. As the dominant (highest abundance) isotope saturates, the weaker isotopes will have increased influence on the fitted line centroid. This could lead to systematic errors in $\Delta\alpha/\alpha$.

Table 4.1. The percentage terrestrial isotopic abundances of the atoms used in our analysis (Rosman & Taylor 1998). The second column shows the mass number, A, of the isotope with the highest abundance and ΔA is defined relative to this (negative values representing lighter isotopes). Finally, for the discussion in Section 4-10.2, we also give the magnetic moment, $\mu_{\rm m}$ (in units of $\mu_{\rm N}$, the nuclear magneton), for each atom (Mills et al. 1988).

Atom	A	ΔA							$\mu_{\rm m}$
		-2	0	$+1$	$+2$	$+3$	$+4$	$+6$	
Mg	24		79.0	10.0	11.0				-0.85546
Al	27		100.0						3.641504
Si	28		92.229	4.683	3.087				-0.55529
Cr	52	4.3	83.8	9.5	2.4				-0.47454
Fe	56	5.8	91.8	2.1	0.3				0.09062294
Ni	58		68.08		26.22	1.14	3.63	0.93	-0.75002
Zn	64		49		28	4	19	1	0.875479

Table 4.1 shows the terrestrial isotopic abundances for the atoms used in the MM method. Note that the abundance is quite distributed and asymmetric for Ni, Zn and, to a lesser extent, Cr. If the isotopic components of the transitions of these species were widely spaced in wavelength then differential isotopic saturation may be an important effect. However, the Cr, Ni and Zn lines were always weak in our QSO spectra, typically absorbing only $\lesssim$20% of the continuum. Using only the composite wavelengths for transitions of these species is therefore justified.

Although the Fe abundance is strongly centered on the ^{56}Fe isotope, the Fe II transitions in our QSO spectra are often saturated. The possible effect of differential isotopic saturation for Fe should therefore be tested. The mass isotopic shift (equation 3.7) for Fe transitions should be $\gtrsim 5$ times smaller than for those of Mg. Therefore, using only composite wavelengths of Mg and Si transitions in our analysis (instead of the full isotopic structures) should place a firm upper limit on the possible effect from Fe II.

We have conducted such a test with our total sample: we use composite wavelengths for the Mg I, Mg II and Si II isotopic structures and refit our spectra to find values of $(\Delta\alpha/\alpha)_{\rm comp}$. We also use composite wavelengths for the Al III hyperfine structures (see Section 4-10.2). What is the expected magnitude of $\Delta(\Delta\alpha/\alpha) = (\Delta\alpha/\alpha)_{\rm comp} - \Delta\alpha/\alpha$? Imagine a single velocity component and consider finding $\Delta\alpha/\alpha$ from, say, the Mg II λ2796 and Fe II λ2344 lines only. One might estimate the maximum effect of differential isotopic saturation by assuming that when all isotopes of Mg II are saturated, the line centroid would lie at the unweighted mean isotopic wavelength. This would result in a correction to $\Delta\alpha/\alpha$ of $\sim -1 \times 10^{-5}$ (i.e. the observed value would become more negative when the correction is applied).

However, several factors will reduce this correction in reality. Firstly, once a line begins to saturate, then because the intrinsic line-width (i.e. the b-parameter) is far greater than the isotopic separations, the weaker isotopes are swamped by the dominant one. This reduces the effect on $\Delta\alpha/\alpha$. Secondly, if the velocity structure is more complex (i.e. if it contains more than one velocity component) the unsaturated components, which do not suffer from the differential isotopic saturation problem, will provide much stronger constraints on $\Delta\alpha/\alpha$. Finally, as more unsaturated transitions (e.g. Fe II) are incorporated into the fit of a particular QSO absorption system, the effect is further reduced since some constraints on $\Delta\alpha/\alpha$ come from shifts between the Fe II lines.

The top panel of Fig. 4.5 compares values of $(\Delta\alpha/\alpha)_{\rm comp}$ (solid triangles) for the total sample with those found using the full isotopic/hyperfine structures (dotted circles). We see that isotopic saturation has only a small effect on $\Delta\alpha/\alpha$, even for the Mg/Fe II systems at low-z. This is confirmed when comparing the statistics for this test in Table 3.5 with the fiducial values. It is therefore clear that differential isotopic saturation of Fe II transitions is unlikely to have significantly affected our results.

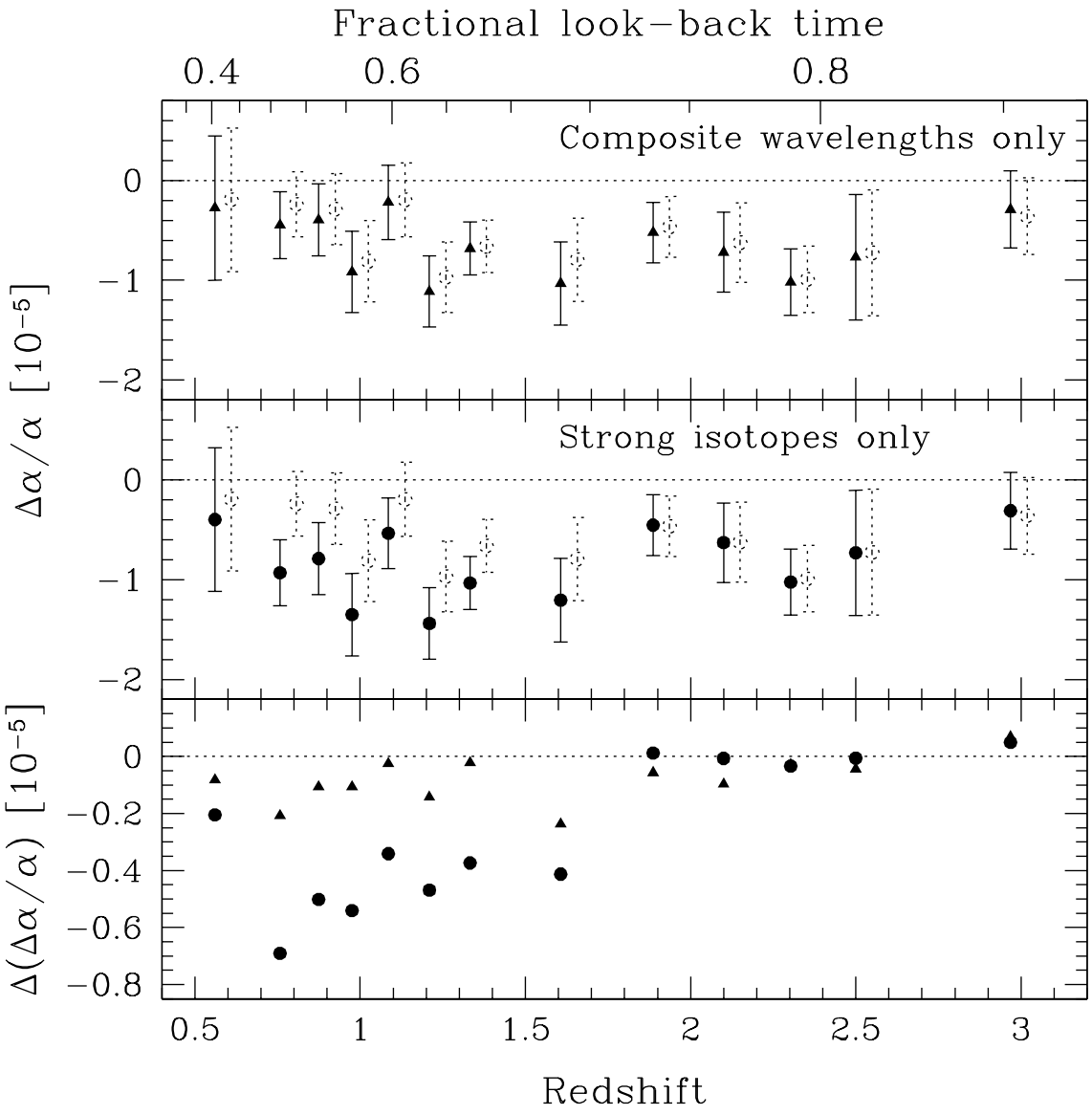

Figure 4.5. Upper limits on the effects of differential isotopic saturation and isotopic abundance evolution. The top panel compares the binned values of $\Delta\alpha/\alpha$ derived using only the composite laboratory wavelengths (solid triangles) from Table 3.1 and the fiducial values (dotted circles, slightly shifted for clarity). The solid circles in the middle panel are derived using only the strongest isotopic components of the Mg I, Mg II and Si II transitions. The lower panel shows the differences between these composite and single isotope values of $\Delta\alpha/\alpha$ and the fiducial values.

4-10.2 Differential hyperfine saturation

Hyperfine splitting of energy levels occurs only in species with odd mass numbers (i.e. odd proton or neutron numbers – note that most isotopes in Table 4.1 have even A). Different hyperfine components will have different transition probabilities but the composite wavelength of a line will be unchanged by the splitting (i.e. the centre of gravity of the hyperfine components is constant with increased splitting). However, a similar differential saturation effect will occur for the hyperfine components as for the isotopic components discussed in Section 4-10.1.

Table 4.1 shows that Al has the largest magnetic moment by a factor of ∼5. The s-wave ground state of Al III has non-zero spin and so the hyperfine structure should be quite prominent. Indeed, the two hyperfine components are clearly resolved in the laboratory experiments of Griesmann & Kling (2000). We take this Al III hyperfine structure into account in our fits to the QSO data (see Table 3.1). The high-z composite wavelength results in Fig. 4.5 therefore provide an upper limit on the effect of hyperfine saturation effects for all other transitions. The only other hyperfine structures taken into account in our fitting process are those of the ^{25}Mg transitions (since they have been measured, see Section 3-2.2). These are so closely separated that they would have a negligible effect on $\Delta\alpha/\alpha$ (especially considering the small effect of differential *isotopic* saturation in Fig. 4.5).

Significant effects on $\Delta\alpha/\alpha$ from saturation effects in other (odd A) species are unlikely due either to their low magnetic moments (for Fe II in particular) or the nature of the ground- and excited-state wavefunctions (e.g. Al II λ1670 has zero electron spin in both states) and, in some cases, low abundances (e.g. Zn II). All the above arguments imply a negligible effect due to differential hyperfine saturation.

4-10.3 Isotopic abundance variations

We assumed the terrestrial isotopic abundances in Table 4.1 when fitting Mg and Si absorption lines. However, if the isotopic abundances in the QSO absorbers are different, small apparent shifts in the absorption lines would be introduced,

potentially mimicking a non-zero $\Delta\alpha/\alpha$. This effect will be greatest for changes in the isotopic abundances of Mg I, Mg II and Si II since the mass shift (equation 3.7) implies these ions will have the largest isotopic separations. As an example, consider the case where the ^{25}Mg and ^{26}Mg abundances are zero in a given absorption cloud. The isotopic structure given in Table 3.1 implies that we would incorrectly infer a more positive $\Delta\alpha/\alpha$ by fitting Mg II spectra of such a cloud with the terrestrial isotopic abundances. In the simple case of finding $\Delta\alpha/\alpha$ from Mg II λ2796 and Fe II λ2344, we would expect to find $\Delta\alpha/\alpha \approx 0.6 \times 10^{-5}$ in the absence of any real variation in α.

Observations of Mg (Gay & Lambert 2000) and theoretical estimates for Si (Timmes & Clayton 1996) in stars clearly show a decrease in the isotopic abundances with decreasing metallicity. For example, at relative metal abundances [Fe/H] ~ -1, ^{25}Mg/^{24}Mg $\approx$ ^{26}Mg/^{24}Mg ≈ 0.1, which is about 20% below terrestrial values (see Table 4.1). Theoretical estimates suggest even larger decreases. All the absorption systems in our analysis are likely to have sub-solar metallicities: the Mg/Fe II systems at low-z have $Z = -2.5$–0.0 (Churchill & Le Brun 1998; Churchill et al. 2000a,b) and the DLAs at high-z have $Z \approx -0.6$ (Prochaska & Wolfe 1999, 2000). Therefore, we expect significantly lower isotopic abundances of ^{25,26}Mg and ^{29,30}Si in our QSO absorption systems.

Considering the above, refitting all our spectra using only the strong isotopes of Mg and Si (i.e. ^{24}Mg and ^{28}Si) should place an upper limit on the effect of possible isotopic abundance variations on $\Delta\alpha/\alpha$. The values of $\Delta\alpha/\alpha$ from fitting only the strong isotopes, $(\Delta\alpha/\alpha)_{\rm iso}$ (solid circles), are compared with the fiducial values (dotted circles) in the middle panel of Fig. 4.5. The lower panel also shows the size of the correction, $\Delta(\Delta\alpha/\alpha) = (\Delta\alpha/\alpha)_{\rm iso} - \Delta\alpha/\alpha$. Fig. 4.5 clearly demonstrates that strong isotopic abundance evolution in Mg and Si can not explain our results. Indeed, $\Delta\alpha/\alpha$ becomes more negative when we remove this potential systematic effect. Note that removing ^{25}Mg and ^{26}Mg only affects the low-z Mg/Fe II systems whereas removing ^{29}Si and ^{30}Si only affects the high-z systems. The largest effect is for the low-z Mg/Fe II systems. This is expected because (a) the isotopic separations

for Mg transitions are larger than those for Si transitions (equation 3.7), (b) the relative terrestrial abundances of ^{25}Mg and ^{26}Mg are larger than ^{29}Si and ^{30}Si (Table 4.1) and (c) a large number of different species are fitted in the high-z systems, i.e. a systematic effect in just one species (in this case Si II) is unlikely to significantly affect $\Delta\alpha/\alpha$.

The above test estimates the maximum effect of strong isotopic abundance evolution for Mg and Si transitions. Although we emphasize that the effect for heavier species should be reduced by the mass shift, we point out that isotopic (and hyperfine) structures for transitions of other species are not known. It is possible that large specific isotopic shifts exist for some transitions. If this is combined with strong isotopic ratio evolution then small apparent line shifts would be measured in the QSO spectra. However, this possibility is unlikely given the results of removing single transitions or entire species in Section 4-12.1.

4-10.4 Hyperfine level population variations

Once again, consider the prominent hyperfine structure of the Al III transitions. If the populations of the ground-state hyperfine levels are not equal in the absorption clouds, as they are in the laboratory measurements of Griesmann & Kling (2000), we would measure small apparent shifts for the Al III transitions. A lower bound on the relative population is set by interaction with CMB photons, $\exp[-hc\Delta\omega/k_{\rm B}T_{\rm CMB}(z)]$, where $\Delta\omega \approx 0.5\,{\rm cm}^{-1}$ is the hyperfine splitting for the Al III $\lambda\lambda$1854 and 1862 transitions. At $z_{\rm abs} \sim 2.0$, the relative population is $\approx$0.9, leading to a shift in the line centroid of $\sim$0.01 cm^{-1} ($\sim 5 \times 10^{-4}$ Å). This corresponds to $\Delta\alpha/\alpha = +1 \times 10^{-5}$ for the Al III lines alone. Clearly, including other transitions will reduce the effect on $\Delta\alpha/\alpha$ for a particular system.

Two caveats significantly lessen concern in this case: (i) Even without a detailed calculation of the critical density for the Al III hyperfine levels, the wavelength separation is so small that collisional excitation processes should drive the relative populations to equality; (ii) removing either or both of the Al III transitions from

our analysis has a very small effect on $\Delta\alpha/\alpha$ (see Section 4-12.1). We therefore consider systematic errors from variations in the hyperfine level populations to be negligible.

4-11 Atmospheric dispersion effects

Below we describe how atmospheric dispersion could have distorted the wavelength scale and instrumental profile (IP) of the QSO spectra. However, in Section 4-11.2 *we find no evidence for atmospheric dispersion effects in our data*. Nevertheless, we model the potential effect on our QSO spectra in Section 4-11.3, finding further evidence that atmospheric dispersion effects can not explain our results.

4-11.1 Distortions from atmospheric dispersion

As noted in Section 3-3.1, the Keck/HIRES was only fitted with an image rotator in August 1996. Therefore, prior to this time, the spectrograph slit could not be held perpendicular to the horizon during observations and so the atmosphere will have dispersed QSO light with some component across the slit. We illustrate this situation in Fig. 4.6. This can lead to a low-order distortion of the wavelength scale since different wavelengths will follow slightly different paths through the spectrograph. Also, since the seeing discs for different wavelengths will be centred at different positions across the slit, the effective IP of the spectrograph will be asymmetric and this asymmetry will be wavelength dependent. These effects will not be applied to the ThAr calibration frames since the ThAr lamp will illuminate the spectrograph slit uniformly in all cases.

All of the 27 absorption systems in sample 1 were observed before August 1996 when the image rotator was installed on the Keck/HIRES. Similarly, 11 systems in sample 2 and half (39) of sample 3 were observed 'pre-rotator'. Therefore, for the total sample, 77 of the 128 absorption systems could be affected by atmospheric dispersion effects.

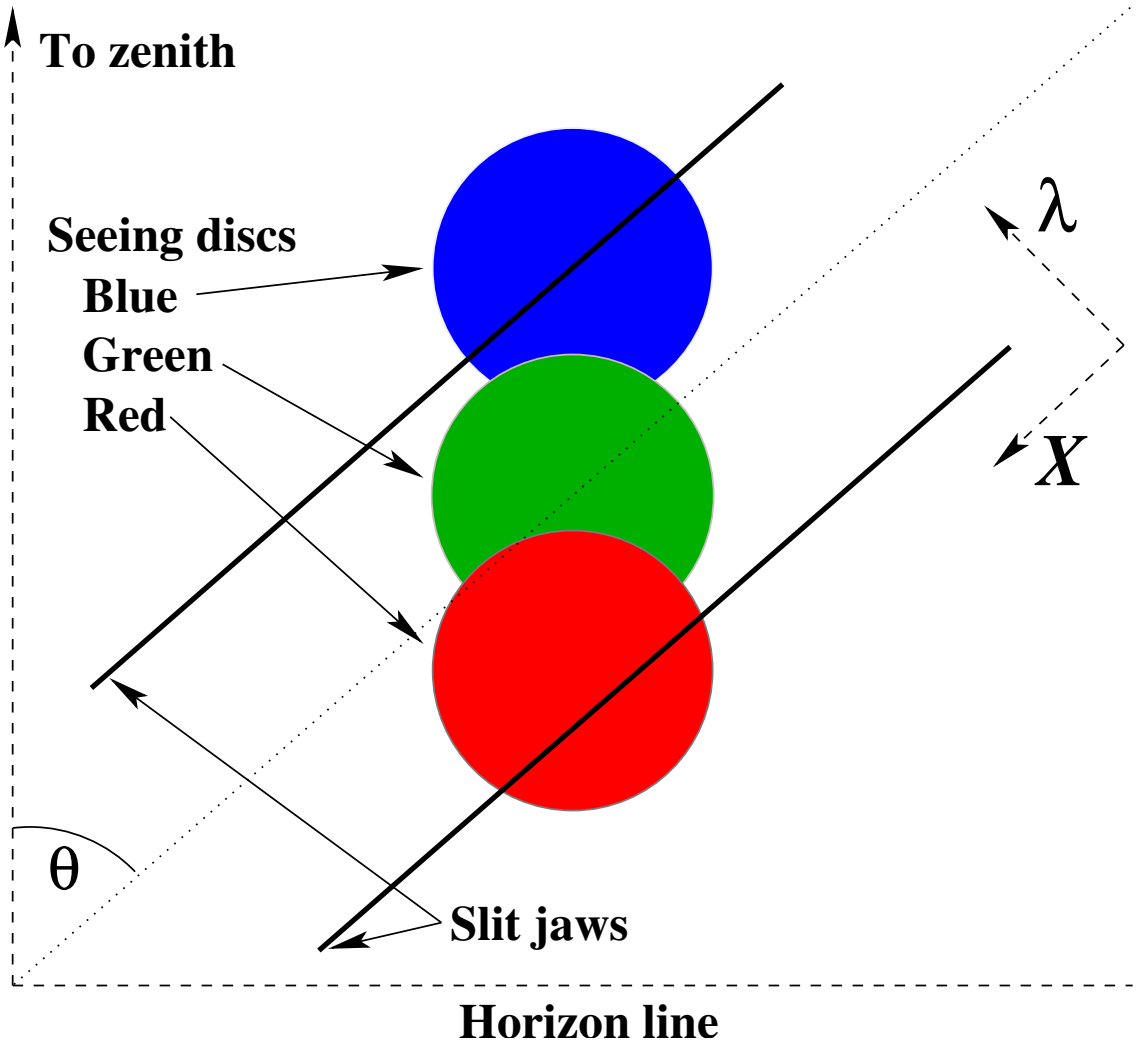

Figure 4.6. Schematic diagram showing the effects of atmospheric dispersion. The HIRES slit is projected onto the sky so that we see the seeing discs of blue, red and green light from a point source dispersed with some component along the spectral direction of the slit. The spectral direction is indicated by λ and the spatial direction by X. Note that the refraction is worse in the blue.

4-11.2 Evidence for atmospheric dispersion effects?

Atmospheric dispersion increases with increasing zenith distance, ξ. For the Keck/HIRES, the angle, θ, between the vertical and the slit axis (as projected on the sky) is equal to the zenith distance, $\theta = \xi$ (see Fig. 4.6). Therefore, for the pre-rotator observations, the effect atmospheric dispersion will have on $\Delta\alpha/\alpha$

should increase with the zenith distance of the QSO observation. If this effect is present in the pre-rotator spectra, we should observe a correlation between $\Delta\alpha/\alpha$ and ξ for the pre-rotator sample, particularly for the low-z Mg/Fe II systems which are more susceptible to low-order distortions of the wavelength scale.

To search for such a correlation we plot $\Delta\alpha/\alpha$ against the mean ξ for each absorption system in Fig. 4.7. The Spearman rank correlation coefficient, r_s, and associated probability, $P(r_s)$[4], for the pre-rotator sample give no evidence to suggest a correlation between $\Delta\alpha/\alpha$ and ξ. We also see no correlation for the low-z or high-z subsamples of the pre-rotator points. This suggests that atmospheric dispersion has a negligible effect on $\Delta\alpha/\alpha$.

We may also test for atmospheric dispersion effects by comparing the value of $\Delta\alpha/\alpha$ for the (77) pre- and (51) post-rotator values of $\Delta\alpha/\alpha$. In the top panel of Fig. 4.8 we identify these subsamples and plot binned values in the middle panel. There is no clear discrepancy between the pre- and post-rotator samples. This is confirmed in Table 4.2 where we compare the weighted mean values of $\Delta\alpha/\alpha$ for the pre- and post-rotator observations. Even for the low-z systems, which should be most susceptible to atmospheric dispersion effects, we see no evidence for a discrepancy. We also consider sample 3 separately in the lower panel of Fig. 4.8 where exactly half of the systems are pre-rotator observations. Again, in Table 4.2, the weighted mean values of $\Delta\alpha/\alpha$ are consistent.

To summarize this section, we see no evidence for the effects of atmospheric dispersion. No correlation between $\Delta\alpha/\alpha$ and the zenith angle of the QSO observations is observed (Fig. 4.7) and the pre- and post- rotator samples give completely consistent results (Fig. 4.8 and Table 4.2). Nevertheless, we consider a detailed model of atmospheric dispersion in the following section in an effort to understand the potential effects on the Keck/HIRES wavelength scale and effective IP.

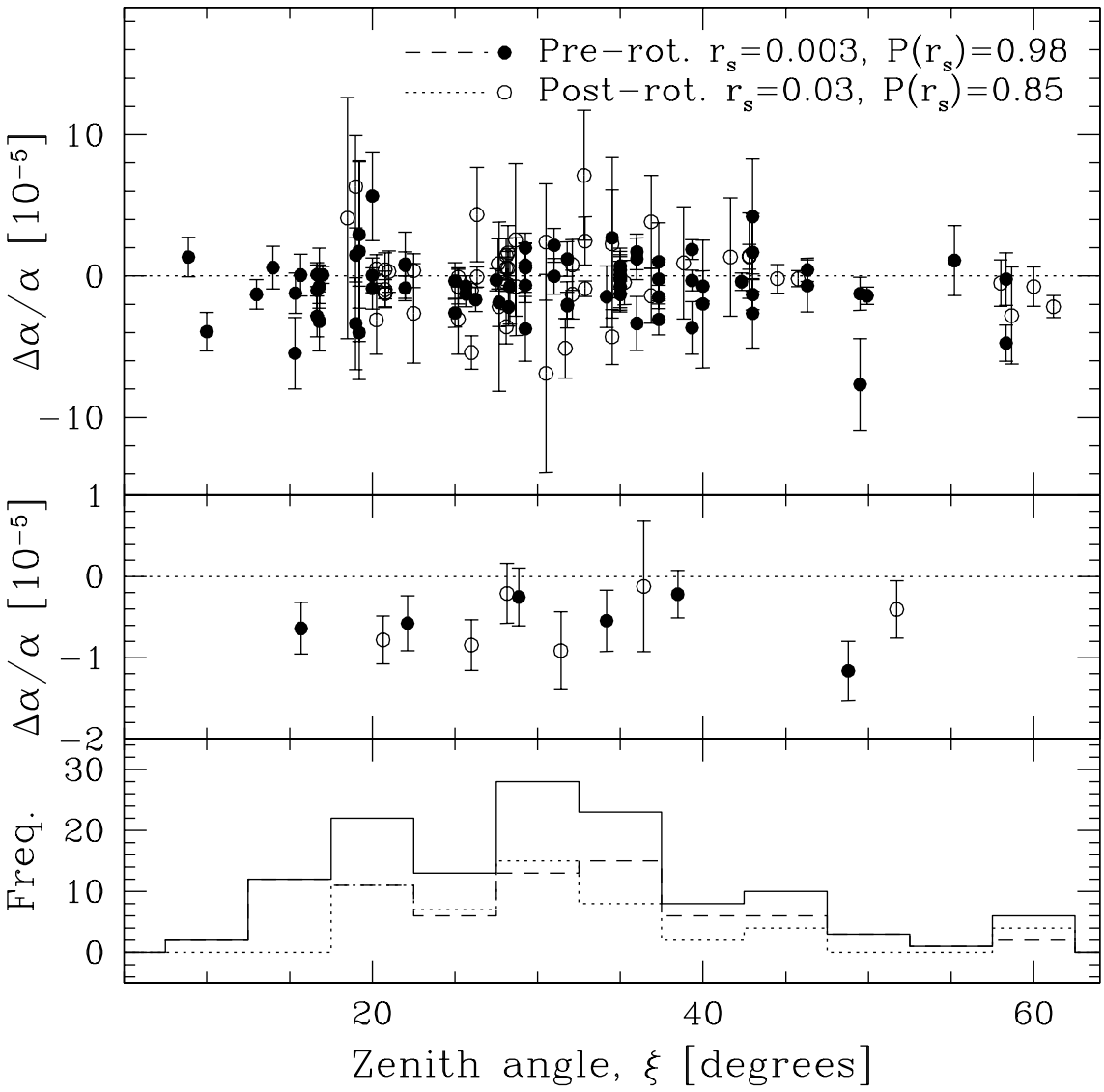

Figure 4.7. Is $\Delta\alpha/\alpha$ correlated with zenith angle? The lower panel shows the distribution of absorption systems over average zenith angle for the pre-rotator (dashed line), post-rotator (dotted line) and total (solid line) samples. The upper panel shows $\Delta\alpha/\alpha$ as a function of zenith angle, ξ, for the pre- and post-rotator samples. The Spearman rank correlation coefficient (and corresponding probability) indicates no correlation for the pre-rotator sample, as might be expected if the atmospheric dispersion effect was significant (see Fig. 4.10). For the pre-rotator sample, we also see no correlation for the low-z [$z < 1.8$: $r_{\rm s} = -0.01$, $P(r_{\rm s}) = 0.92$] or high-z [$z > 1.8$: $r_{\rm s} = -0.06$, $P(r_{\rm s}) = 0.77$] subsamples. The middle panel shows the binned results, also giving no hint of correlation.

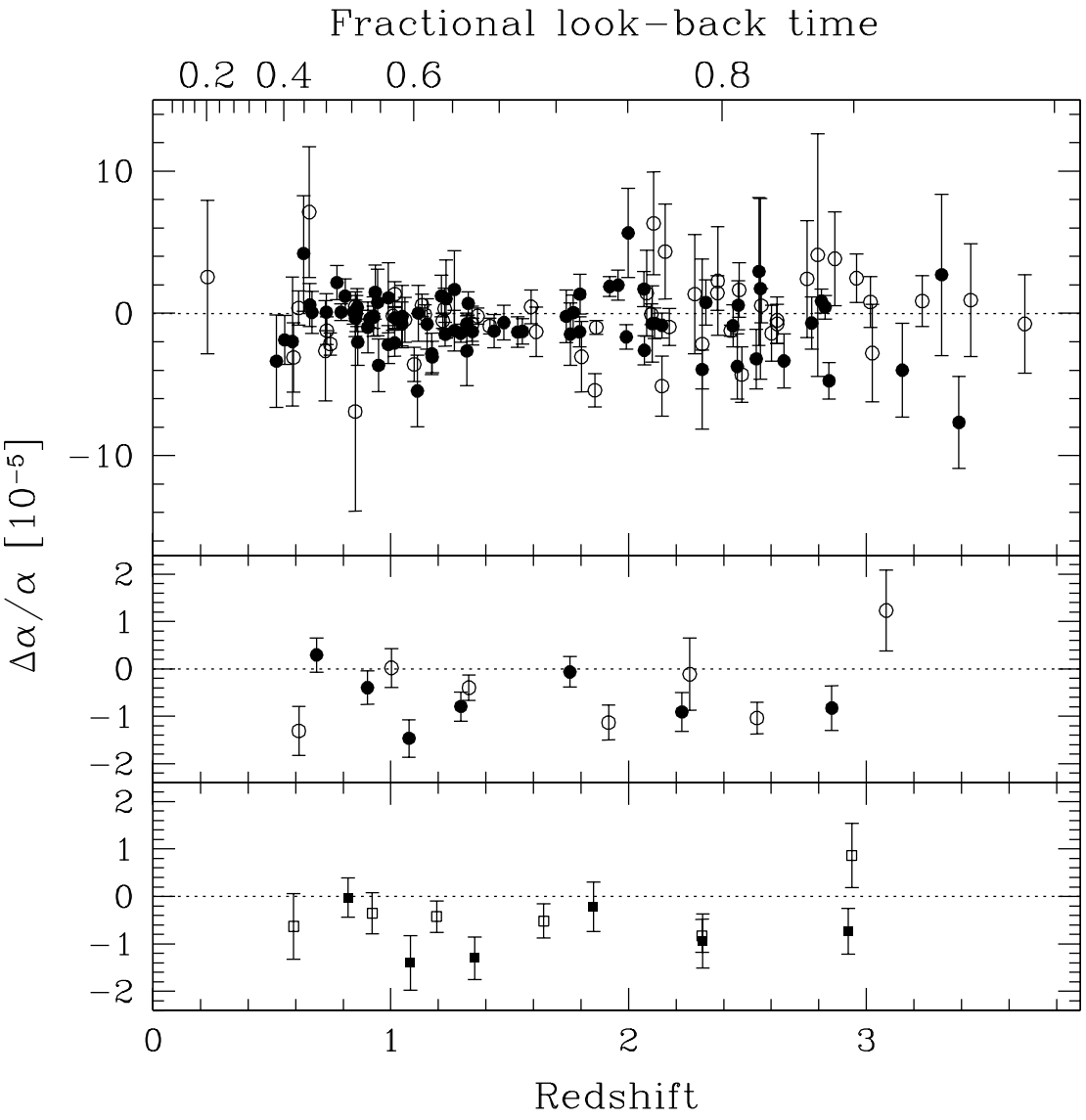

Figure 4.8. Comparison of the pre- and post-rotator systems. The upper panel compares values of $\Delta\alpha/\alpha$ for the pre-rotator (solid circles, 77 points) and post-rotator (open circles, 51 points) samples. The weighted means are consistent: $\Delta\alpha/\alpha = (-0.54 \pm 0.14) \times 10^{-5}$ and $\Delta\alpha/\alpha = (-0.62 \pm 0.15) \times 10^{-5}$ respectively. The middle panel bins the results in the same fashion as for the main results in Fig. 3.7. We see no evidence for a significant systematic effect due to atmospheric dispersion. The lower panel compares the pre-rotator (solid squares, 39 points) and post-rotator (open squares, 39 points) subsamples of sample 3 alone. Again, we see no evidence for the atmospheric dispersion effect. Table 4.2 presents the weighted mean values of $\Delta\alpha/\alpha$.

Table 4.2. Comparison of weighted mean values of $\Delta\alpha/\alpha$ for the pre- and post-rotator systems.

Sample	Pre-rotator		Post-rotator	
	$N_{\rm abs}$	$\Delta\alpha/\alpha$	$N_{\rm abs}$	$\Delta\alpha/\alpha$
Total sample (Fig. 4.8, middle panel)				
low-z	52	-0.60 ± 0.16	22	-0.45 ± 0.20
high-z	25	-0.39 ± 0.26	29	-0.83 ± 0.23
Total	77	-0.54 ± 0.14	51	-0.62 ± 0.15
Sample 3 only (Fig. 4.8, lower panel)				
low-z	22	-0.67 ± 0.25	22	-0.45 ± 0.20
high-z	17	-0.77 ± 0.33	17	-0.50 ± 0.31
Total	39	-0.71 ± 0.20	39	-0.46 ± 0.17

4-11.3 Modelling of atmospheric dispersion effects

As mentioned above, before the image rotator was installed, the angle of the Keck/HIRES slit to the vertical, θ, was directly related to the zenith angle by $\theta = \xi$. That is, the slit lies with its axis along the horizon at $\xi = 90°$. The component of atmospheric dispersion along the spectral direction of the slit (i.e. across its axis) therefore increases with increasing ξ both because atmospheric dispersion *and* θ increase with ξ. This will lead to two effects on the wavelength scale:

1. Compression. Due to the angular separation of different wavelengths as they enter the spectrograph, the QSO spectrum will be distorted relative to the ThAr calibration frames. Consider two wavelengths, λ_1 and λ_2 ($\lambda_2 > \lambda_1$), entering the spectrograph slit separated by an angle $\Delta\psi$ in the vertical direction. The spectral separation of the two wavelengths in the extracted, calibrated spectrum will be

$$\Delta\lambda \approx \lambda_2 - \lambda_1 - \frac{a\Delta\psi \sin\theta}{\delta}\,, \tag{4.4}$$

where a is the CCD pixel size in angstroms and δ is the projected slit width in

arcseconds per pixel (for HIRES, $\delta = 0\farcs287$ per pixel). We checked the accuracy of this equation with ZEMAX models of the Keck/HIRES provided by Steve Vogt. If $\Delta\psi \neq 0$ then the spectral separation between any two wavelengths will decrease, i.e. the spectrum is compressed. If $\Delta\psi$ is due to atmospheric dispersion then it is a function of the atmospheric conditions and can be estimated using the refractive index of air at the observer and the zenith distance of the QSO (e.g. Filippenko 1982). Note that equation 4.4 assumes that the seeing profiles at λ_1 and λ_2 are not truncated by the slit edges.

2. Wavelength dependent IP asymmetry. If tracking errors or seeing effects do cause profile truncation at the slit edges then the truncation will be asymmetric and this asymmetry will depend on wavelength. For example, the optical design of Keck/HIRES is such that a blue spectral feature will have its red wing truncated and a red feature will be truncated towards the blue. The asymmetry and the severity of its dependence on wavelength will increase with increasing $\Delta\psi$ and with θ (and therefore, ξ). Note that when we centroid absorption features in QSO spectra, we will find larger wavelength separations due to this effect, i.e. a positive term is effectively added to the right-hand-side of equation 4.4 due to this wavelength dependent asymmetry.

For the low-z Mg/Fe II systems, these two effects will have an opposite effect on $\Delta\alpha/\alpha$: the compression will produce $\Delta\alpha/\alpha < 0$ and the wavelength dependent asymmetry will result in $\Delta\alpha/\alpha > 0$. It is important to note that both effects rely mainly on the same parameters for each observation (i.e. $\Delta\psi$ and $\theta = \xi$) and so their relative strength is fixed by our model. The one free parameter is the seeing, which determines the strength of the wavelength asymmetry effect and not the compression effect. We discuss this below.

For each QSO observed without the image rotator we have calculated an effective seeing profile at the spectrograph slit. In general, each QSO spectrum is the combination of several exposures and each exposure was taken at a different ξ. For each

exposure we assume typical observing conditions at the telescope[6] and use the mean value of ξ calculated from the recorded image headers to obtain the relative angular separations, $\Delta\psi$, between all observed wavelengths. Then, to reconstruct the full dispersion pattern relative to the slit edges, we assumed that light of wavelength $\lambda = 5500\,\text{Å}$ was centred on the slit axis. This corresponds to the mean wavelength of the response curve for the acquisition camera used to guide the Keck/HIRES on the QSO.

For each exposure we assumed a seeing of FWHM $= 0\farcs75$ to produce a Gaussian intensity profile at the slit for each observed wavelength. Although this is a realistic assumption, we have no detailed information about the seeing conditions for each observation[7]. Tracking errors will broaden the intensity profile so the above assumption is effectively a conservative one: if FWHM $> 0\farcs75$ then the effect of wavelength dependent IP asymmetry on $\Delta\alpha/\alpha$ will reduce because each wavelength will illuminate the slit more uniformly.

For each QSO observation and at each observed wavelength we average the slit intensity profiles for all exposures. For each observed wavelength (i.e. each observed MM transition) a high S/N, high spectral resolution synthetic spectrum is constructed based on the Voigt profile fits to the QSO data. We convolve each spectrum with the corresponding intensity profile, truncated by the slit edges. Finally, we convolve with a Gaussian instrumental response of width FHWM $\approx 2.2\,\text{kms}^{-1}$ (Valenti et al. 1995). We vary this parameter slightly depending on the observed wavelength so as to ensure constant velocity resolution to match the real QSO data. Finally, we re-bin the simulated spectra to match the real QSO spectral dispersion.

The above procedure provides synthetic QSO spectra with $\Delta\alpha/\alpha = 0$ but which contain effects due to our model of atmospheric dispersion. We fit these spectra

[6] We assumed the following observational parameters in our atmospheric dispersion model: temperature $= 280\,\text{K}$, atmospheric pressure $= 600\,\text{mbar}$ and relative humidity $= 10\%$.

[7] In principle, one could find a reliable estimate of the seeing for each exposure by integrating the object profile in the spatial direction along the echelle orders. In general, we did not have access to the unextracted, 2-dimensional object exposures and so could not perform such an analysis. However, our conclusions below would be unchanged.

and determine $(\Delta\alpha/\alpha)_{\rm ad}$, an estimate of the effect of atmospheric dispersion on the values of $\Delta\alpha/\alpha$ derived from the real QSO spectra. The results are plotted in the top panel of Fig. 4.9 for the 77 systems observed without the image rotator. In the low-z Mg/Fe II systems, atmospheric dispersion causes $\Delta\alpha/\alpha < 0$ (i.e. the compression effect dominates the wavelength dependent IP asymmetry effect) and so, once the effect is modelled and removed, $\Delta\alpha/\alpha$ increases. At high z not all values of $\Delta\alpha/\alpha$ react the same way to atmospheric dispersion since different transitions are fitted in each absorption system. However, on average, the high-z values of $\Delta\alpha/\alpha$ decrease after removing atmospheric dispersion effects.

The middle panel of Fig. 4.9 shows the corrected values of $\Delta\alpha/\alpha$, i.e. $(\Delta\alpha/\alpha)_{\rm adc} \equiv \Delta\alpha/\alpha - (\Delta\alpha/\alpha)_{\rm ad}$ (solid squares) including those systems not affected by atmospheric dispersion effects [$(\Delta\alpha/\alpha)_{\rm ad} = 0$, open squares]. The lower panel compares the binned values of $(\Delta\alpha/\alpha)_{\rm adc}$ with the fiducial values from Fig. 3.7. Clearly, atmospheric dispersion effects (as modelled above) can not explain our results. Indeed, on average, the overall compression of the wavelength scale has an *opposite effect on the low-z and high-z systems*. This is further borne out by the simulations in Section 4-12.2 (see Fig. 4.13).

In the top panel of Fig. 4.10 we plot the estimates of $(\Delta\alpha/\alpha)_{\rm ad}$ versus the mean value of ξ for each absorption system affected by atmospheric dispersion. Note the clear anticorrelation for the low-z systems (solid squares). We did not observe this anticorrelation in Section 4-11.2 (see Fig. 4.7) and so argued that there was no evidence for atmospheric dispersion effects in our data. This is further confirmed in the lower panel where we search for a correlation between $(\Delta\alpha/\alpha)_{\rm ad}$ and the fiducial values of $\Delta\alpha/\alpha$. No correlation exists for the low-z systems. For the high-z systems (open squares) there is no clear evidence for a correlation between $\Delta\alpha/\alpha$ and ξ and so one can not use the lack of such a correlation in the real data (again, see Fig. 4.7) to rule out effects from atmospheric dispersion. There is possibly a weak correlation between $(\Delta\alpha/\alpha)_{\rm ad}$ and $\Delta\alpha/\alpha$ (lower panel). However, recall the lack evidence for atmospheric dispersion effects in the high-z sample from direct comparison between the pre- and post-rotator systems in Fig. 4.8 and Table 4.2.

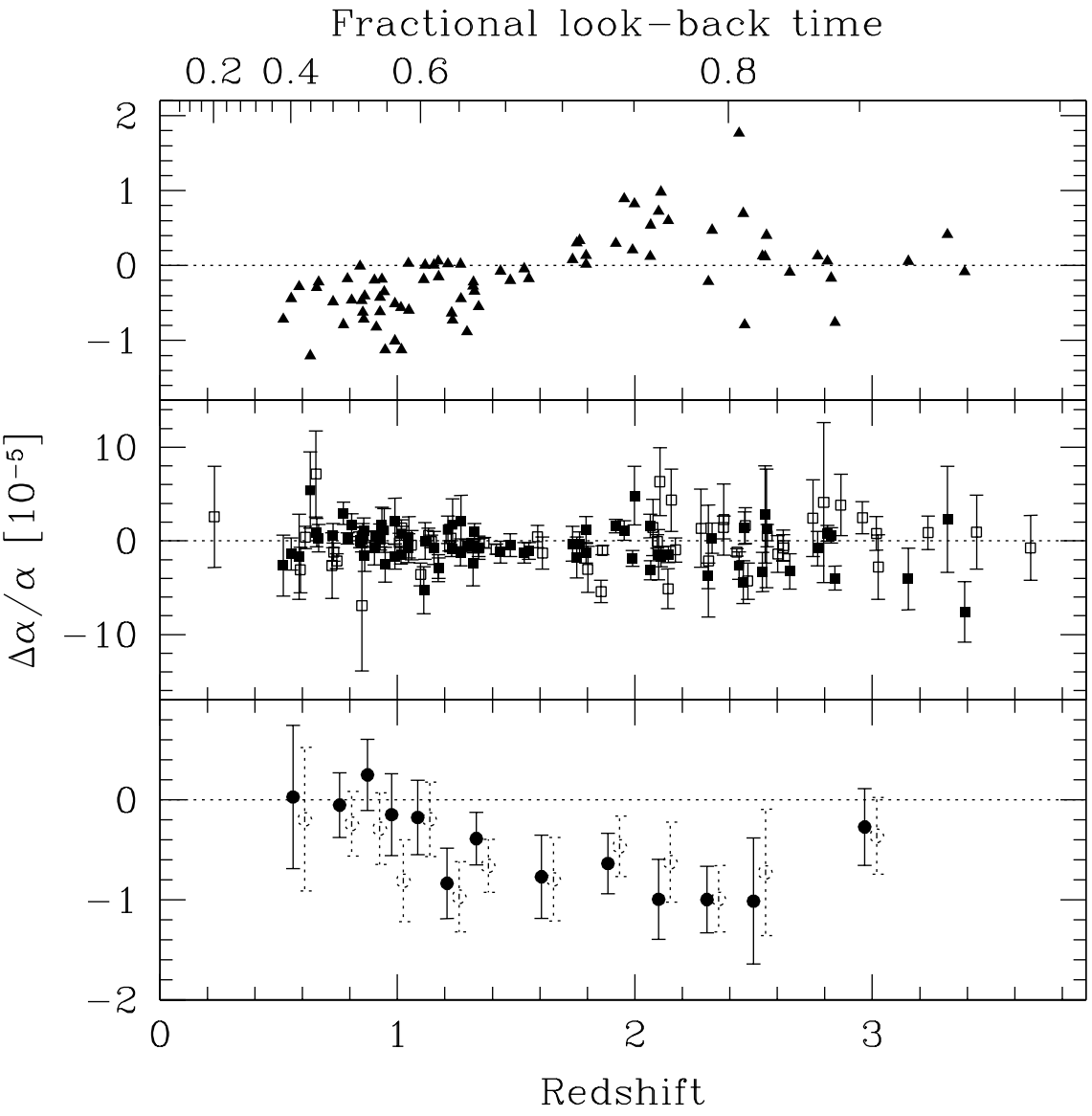

Figure 4.9. Correcting for atmospheric dispersion effects. The upper panel shows values of $(\Delta\alpha/\alpha)_{\rm ad}$ derived from simulated spectra with our model for atmospheric dispersion applied. We have corrected the relevant values of $\Delta\alpha/\alpha$ in the middle panel (solid squares) which also shows the unaffected values (open squares). The lower panel compares the binned values from the middle panel (solid circles) with those of the fiducial values (open circles). The new overall weighted mean is $\Delta\alpha/\alpha = (-0.46 \pm 0.10) \times 10^{-5}$.

To summarize this section, it is clear that atmospheric dispersion effects can not explain the observed values of $\Delta\alpha/\alpha$. There is no evidence for such effects in the

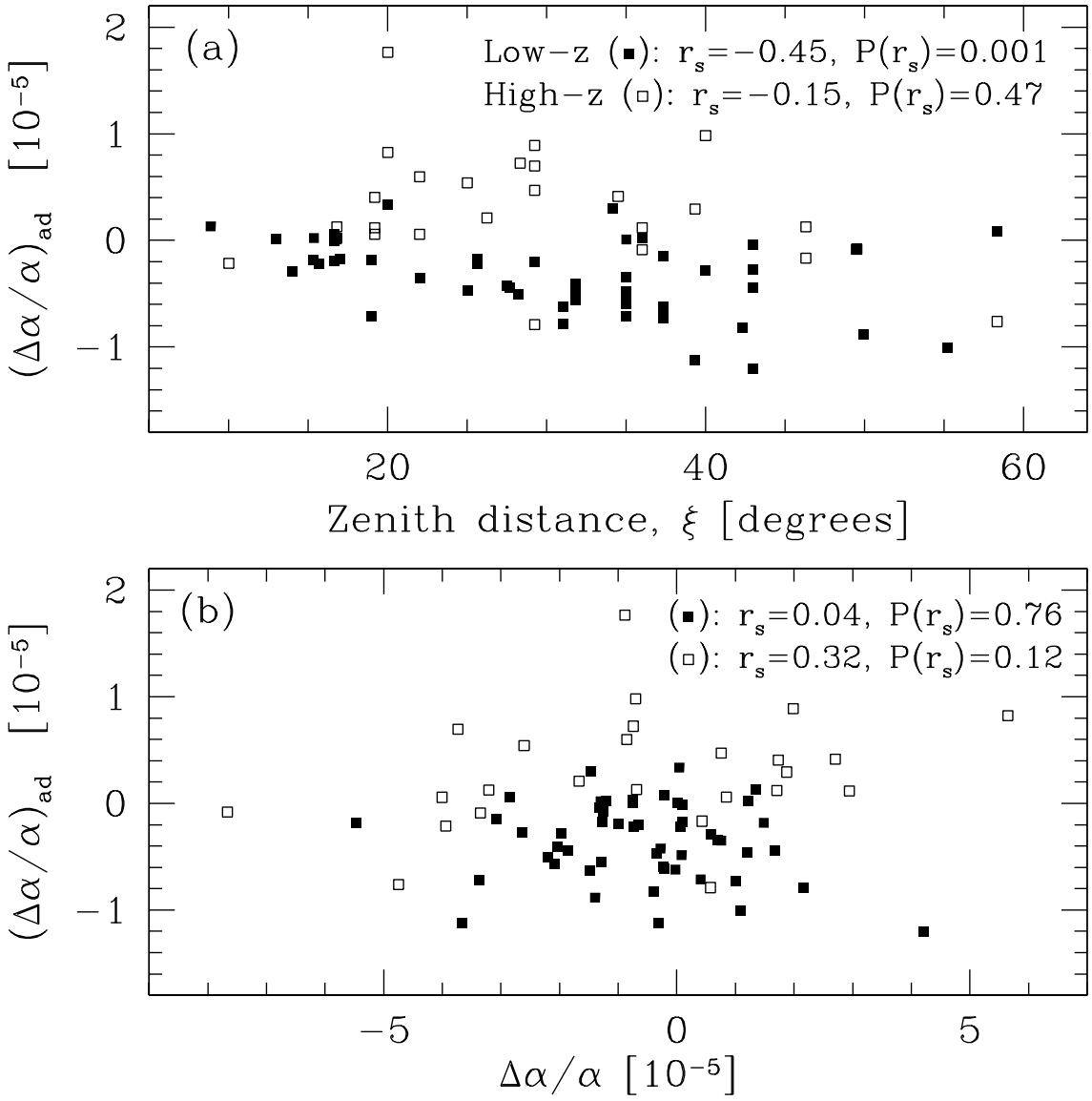

Figure 4.10. **(a)** Distribution of $(\Delta\alpha/\alpha)_{\rm ad}$ over zenith angle for the low-z ($z_{\rm abs} < 1.8$, solid squares) and high-z ($z_{\rm abs} > 1.8$, open squares) systems in the pre-rotator sample. The Spearman rank correlation coefficient (and associated probability) indicates a strong anticorrelation for the low-z systems. **(b)** $(\Delta\alpha/\alpha)_{\rm ad}$ is not correlated with $\Delta\alpha/\alpha$ for the low-z systems but a correlation may exist for the high-z systems.

QSO data. Detailed modelling confirms this conclusion.

4-12 Line–removal tests

A non-zero $\Delta\alpha/\alpha$ manifests itself as a distinct pattern of line shifts (see Fig. 3.3). For a given absorption system, with a given set of fitted transitions, we can remove one or more transitions and still obtain a value of $\Delta\alpha/\alpha$. In the absence of systematic errors associated with the transition removed or with the wavelength scale of the QSO spectra, $\Delta\alpha/\alpha$ should not change systematically over all absorption systems. Removing a single transition or distinct groups of transitions from our analysis therefore allows us to search for systematic errors without specific knowledge of their origin. Note that removing one or more transitions will result in a slightly modified estimate of the velocity structure, revising the estimate of $\Delta\alpha/\alpha$ for each system. However, this will have a random effect on $\Delta\alpha/\alpha$; the real question is, how robust are the values of $\Delta\alpha/\alpha$, averaged over the entire sample, to this line removal process?

Below we construct three different line removal tests, each sensitive to different types of systematic errors.

4-12.1 Single transition and species removal

Removing a single transition (e.g. Mg II λ2796) from our fits to the QSO data allows us a direct means to search for systematic errors due to systematic line blending (Section 4-9.2), isotopic and hyperfine structure effects (Section 4-10) and large errors in the measured laboratory wavelengths in Table 3.1. Removing entire species (e.g. all transitions of Si II) is also a test for isotopic and hyperfine structure effects.

Given an absorption system, with a certain set of fitted transitions, we only remove transitions that *can* be removed. To clarify this, consider removing the Mg II λ2796 transition. For the low-z Mg/Fe II systems, a well-constrained value of $\Delta\alpha/\alpha$ can only be obtained when at least one Mg line is fitted since there is only a small difference between the q coefficients for the different (low-z) Fe II transitions (see Fig. 3.3). Therefore, if the only anchor line present is Mg II λ2796 then we can

not remove it from the system. Similarly, we only remove the entire Mg II species if the Mg I λ2852 line is fitted.

In Fig. 4.11 we present line removal results for the total sample. The transition/species removed is given on the vertical axis and the number of systems, n, where removal was possible is also given. The left panel compares the weighted mean value of $\Delta\alpha/\alpha$ before removing the transition/species (dotted error bar) with that obtained afterwards (solid error bar) for these n systems. The right panel shows the effect of removing the transition/species on the weighted mean $\Delta\alpha/\alpha$ for the sample as a whole (i.e. including those systems where the transition in question could not be removed).

Caption for Fig. 4.11. The left panel compares the values of $\Delta\alpha/\alpha$ before (dotted error bar) and after (solid error bar) line removal. The transitions or species removed are listed on the left together with the number of systems, n, for which line removal was possible. The right panel shows the impact of line removal on the value of $\Delta\alpha/\alpha$ for the entire sample. The vertical lines indicate the fiducial value of $\Delta\alpha/\alpha$ (dashed line) and $1\,\sigma$ error range (dotted lines). Note that some confusion may arise due to the occasional blending of the Cr II and Zn II λ2062 lines: '(Cr II + Zn II) λ2062' refers to cases where both transitions had to be removed simultaneously; 'Cr II + Zn II λ2062' refers to cases when all Cr II transitions were removed along with the blended ZnII λ2062 line; a similar definition applies to 'Zn II + Cr II λ2062'; 'Cr II' and 'Zn II' refer only to removal of the Cr II and Zn II species in cases where the Cr II and Zn II λ2062 lines were not blended.

Fig. 4.11 provides no evidence to suggest that systematic errors associated with any one transition or species have significantly affected $\Delta\alpha/\alpha$. This strongly suggests that isotopic/hyperfine saturation or evolution effects are not important for the transitions of interest. This is particularly important information for the majority of transitions for which the isotopic structures are not known (see Section 4-10). The line removal results also confirm that systematic blending with unidentified

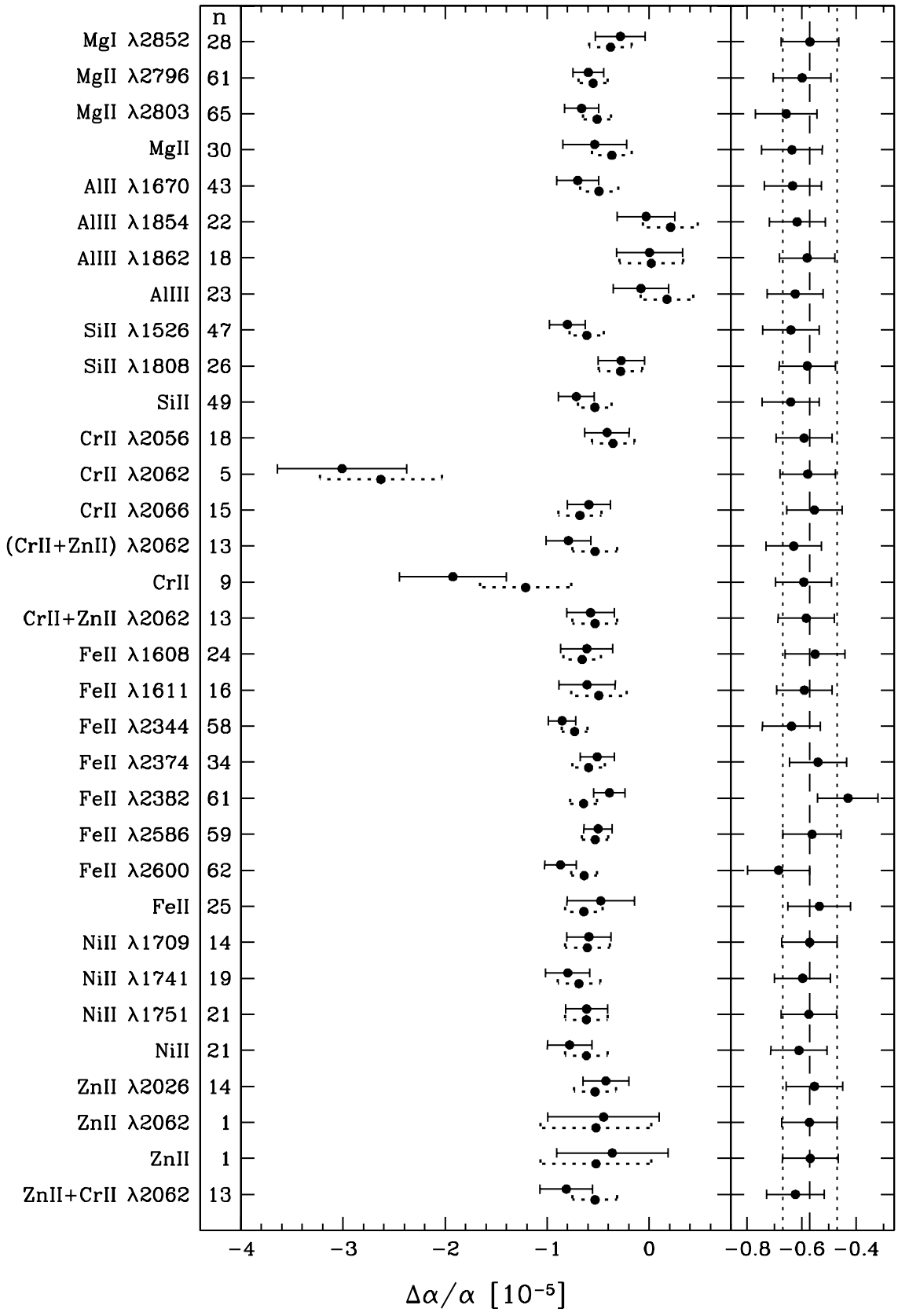

Figure 4.11. Single transition and species removal. See text for caption.

transitions has a negligible effect on $\Delta\alpha/\alpha$.

4-12.2 High-z compression test

As previously noted, the arrangement of the q coefficients for the low-z Mg/Fe II systems (see Fig. 3.3) implies that a compression of the wavelength scale will systematically lead to $\Delta\alpha/\alpha < 0$. The dependence of $\Delta\alpha/\alpha$ on the q coefficients is considerably more complicated for the high-z systems: a compression of the wavelength scale will have a different effect on each value of $\Delta\alpha/\alpha$ depending on which transitions are fitted. That is, compression is not degenerate with $\Delta\alpha/\alpha$ at high-z. If compression is responsible for our observed $\Delta\alpha/\alpha < 0$ at low-z, can we find evidence for it in the high-z absorption systems?

We search for compression in the high-z sample by fitting combinations of transitions for which the q coefficients are arranged in a similar way to those for the low-z Mg/Fe II systems. For example, consider a system where the following transitions are present in the QSO spectrum: Si II $\lambda\lambda$1526 & 1808, Fe II $\lambda\lambda$1608 & 1611 and Cr II $\lambda\lambda$2056 & 2066. The arrangement of q coefficients for such a system is shown in Fig. 4.12. Fitting the Si II λ1526 and Cr II transitions will yield $\Delta\alpha/\alpha < 0$ if a compression of the spectrum exists. Note that several different combinations could be used to the same effect, as indicated in Fig. 4.12 by solid diagonal lines. We treat such cases separately in our analysis since the lower wavelength transitions are of different q-type (see Fig. 3.3). The values of $\Delta\alpha/\alpha$ and the $1\,\sigma$ errors in these separate cases will not be independent. Note also that we can form combinations of transitions which mimic $\Delta\alpha/\alpha < 0$ for an *expansion* of the spectrum.

From the high-z sample, 47 systems contribute 76 different, but not independent, combinations to the compression sample. Similarly, 59 systems contribute 126 combinations to the expansion sample. In Table 4.3 we calculate the weighted and unweighted means for each sample both before and after removing transitions to form the compression and expansion combinations. Note that the number of compression combinations formed in a given absorption system is the number of times

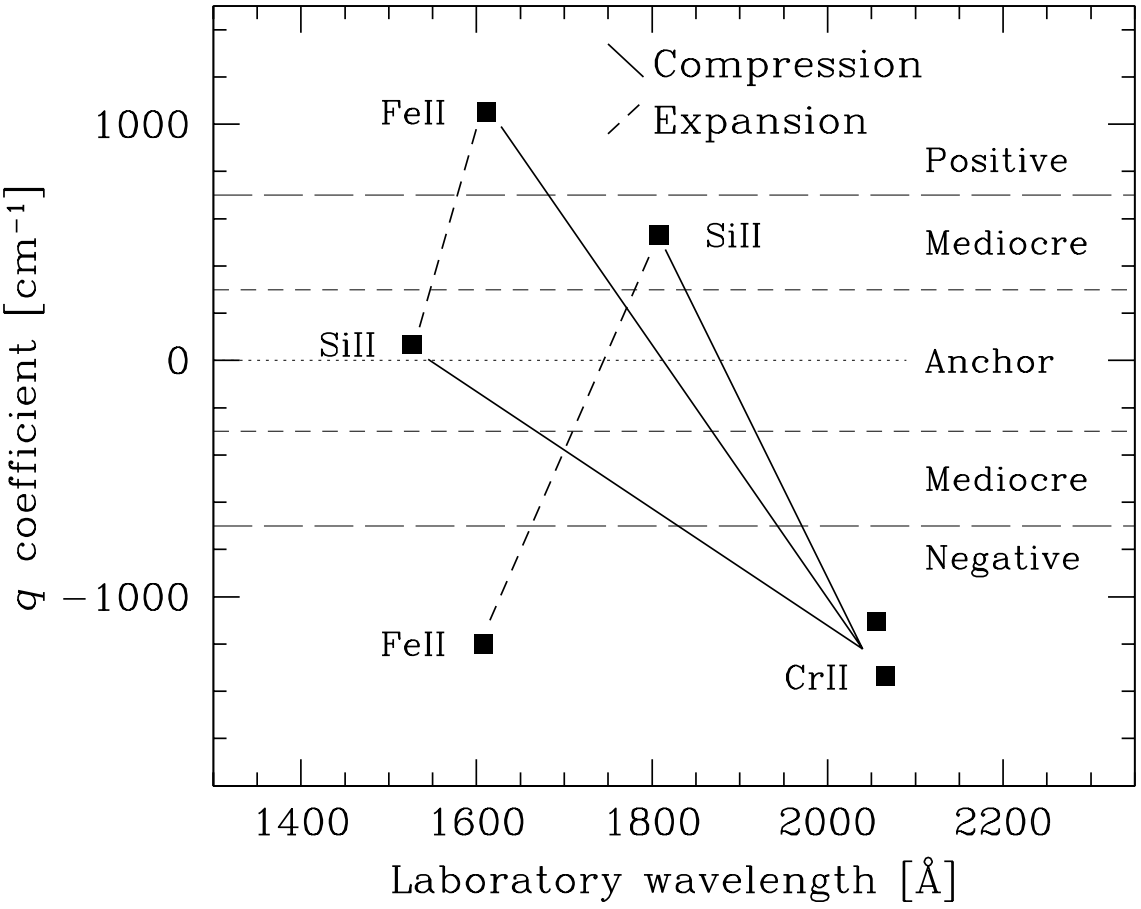

Figure 4.12. The high-z compression test. A compression of the spectrum will systematically produce $\Delta\alpha/\alpha < 0$ in a high-z absorption system if only certain combinations of transitions (solid diagonal lines) are fitted simultaneously. This mimics the situation for the low-z Mg/Fe II absorption systems and allows us to search for a compression-type systematic effect in the high-z systems. Combinations of transitions which will give $\Delta\alpha/\alpha < 0$ for an expansion of the spectrum can be selected in a similar way (dashed diagonal lines).

that system contributes to the pre-removal value. Table 4.3 shows no clear evidence for compression (or expansion) in the high-z sample. However, the weighted and unweighted means are not adequate statistics because each absorption system can contain many combinations. Also the pre- and post-removal values and their $1\,\sigma$ errors are not independent of each other.

To properly interpret results from the compression test, a comparison must be

Table 4.3. Results of the high-z compression test. Columns 2 and 3 show the weighted and unweighted mean value of $\Delta\alpha/\alpha$ (in units of 10^{-5}) for the relevant absorption systems before removing the transitions. Each absorption system may contribute many times to these values, depending on how many compression/expansion combinations can be formed from the fitted transitions. Columns 4 and 5 give the weighted and unweighted mean after transitions are removed to produce the compression/expansion combinations. Caveats of interpreting this table are given in the text.

Sample	Pre-removal		Post-removal	
	$\langle\Delta\alpha/\alpha\rangle_{\rm w}$	$\langle\Delta\alpha/\alpha\rangle$	$\langle\Delta\alpha/\alpha\rangle_{\rm w}$	$\langle\Delta\alpha/\alpha\rangle$
Compression	-0.74 ± 0.16	-0.88 ± 0.34	-1.56 ± 0.31	-0.82 ± 0.86
Expansion	-0.38 ± 0.17	-0.93 ± 0.72	-0.52 ± 0.10	-0.34 ± 0.26

made with detailed simulations of the QSO data. We synthesized each absorption system from the Voigt profile fit to the real QSO data, adding Gaussian noise appropriate to the measured S/N. From each synthetic spectrum we constructed 3 different cases:

1. $\Delta\alpha/\alpha = 0$. No line shifts were introduced into the synthetic spectra.

2. $\Delta\alpha/\alpha = -0.6 \times 10^{-5}$. Each transition in the synthetic spectrum was shifted according to the approximate value of $\Delta\alpha/\alpha$ measured in the real QSO data.

3. Compression. The synthetic spectrum was compressed according to

$$\lambda' = \lambda - C(\lambda_c - \lambda)\,, \tag{4.5}$$

where λ is the initial wavelength of a given pixel, λ' is the new value obtained by compressing the spectrum about a central wavelength, λ_c, by a factor C. This mimics the compression effect of atmospheric dispersion, as described by equation 4.4. Thus, we chose $\lambda_c = 5500$ Å as a representative central wavelength. In order to produce $\Delta\alpha/\alpha \approx -0.6 \times 10^{-5}$ in the low-z simulated spectra, we used $C = 4 \times 10^{-6}$.

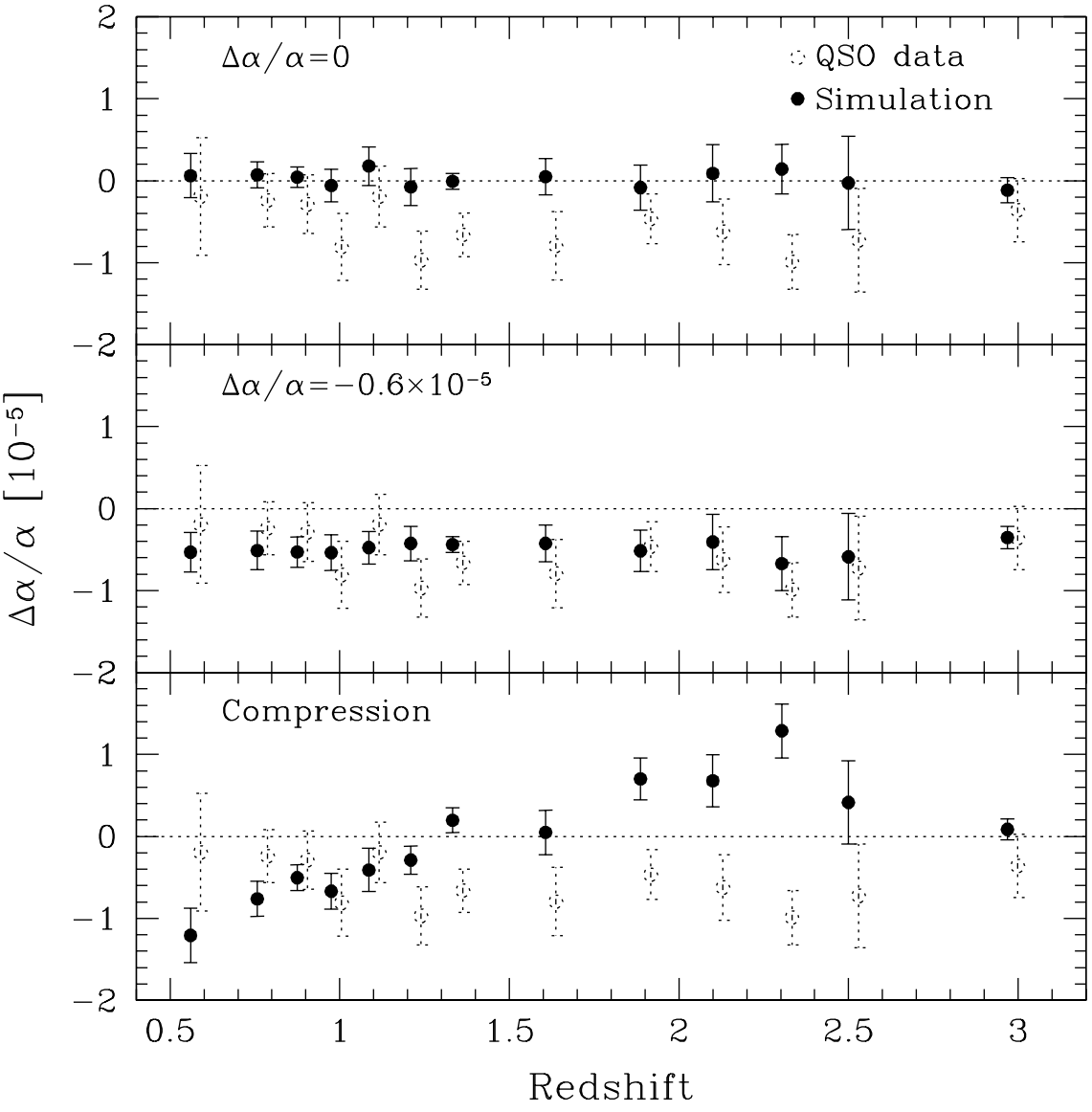

Figure 4.13. $\Delta\alpha/\alpha$ from simulations of the QSO spectra. The weighted mean from 20 simulations (solid circles) is compared with the real values (dotted circles, shifted for clarity) in each panel. The rms from the simulations is represented by the error bar. The upper panel has no input value of $\Delta\alpha/\alpha$ whereas $\Delta\alpha/\alpha = -0.6 \times 10^{-5}$ was introduced into the spectra for the middle panel. Note that we recover the input values and that the rms error bars match the $1\,\sigma$ errors in the real data. A compression was introduced into the spectra for the lower panel (equation 4.5) to allow interpretation of the high-z compression and q-type removal test results.

We ran 20 simulations of each absorption system, obtaining values of $\Delta\alpha/\alpha$ for each of the 3 cases above. The results are compared with the real values of $\Delta\alpha/\alpha$ in Fig. 4.13. Note that (i) we recover the input values of $\Delta\alpha/\alpha$ for the $\Delta\alpha/\alpha = 0$ and $\Delta\alpha/\alpha = -0.6 \times 10^{-5}$ cases and (ii) the compression simulation shows a similar behaviour to that of the atmospheric dispersion calculation in Fig. 4.9, confirming that simple distortions of the wavelength scale should have had an opposite overall effect on the high-z systems compared to the low-z systems.

We have applied the high-z compression test to the simulations for each of the above 3 cases. Figs. 4.14 and 4.15 compare the results with those from the real QSO spectra. The compression sample (Fig. 4.14) may contain some evidence of a compression of the real high-z spectra since the post-removal values are, in general, more negative than the pre-removal ones. However, the results from the compression simulation [case (iii) above] show a much stronger deviation and the pre-removal values, being predominantly positive, also reveal the compression of the data. This is not observed in the real data. Therefore, if a compression exists in the high-z QSO data, it is not sufficient to explain our low- or high-z results. The expansion sample (Fig. 4.15) shows no deviations from the pre-removal values. However, the compression simulation (lower panel) reveals this sample to be surprisingly insensitive to the artificial compression of the spectra.

Of particular note in Figs. 4.14 and 4.15 is the larger scatter observed in the QSO results compared to the rms errors for the 3 simulations. As discussed in Section 3-5.2, this extra scatter is expected in the high-z data. We also expect the scatter to be more apparent as more transitions are removed from each absorption system. Note that we do not see such a strong scatter in the pre-removal values, highlighting the strength of the MM method at high-z.

To summarize this section, the high-z compression test is a potentially powerful test for simple systematics. If we identified a compression effect in the high-z sample, this could explain (or weaken our confidence in) the measured $\Delta\alpha/\alpha < 0$ for the real low-z spectra. However, simulations demonstrate that such a compression effect can not explain the measured $\Delta\alpha/\alpha < 0$ for the high-z sample. Applying the high-z

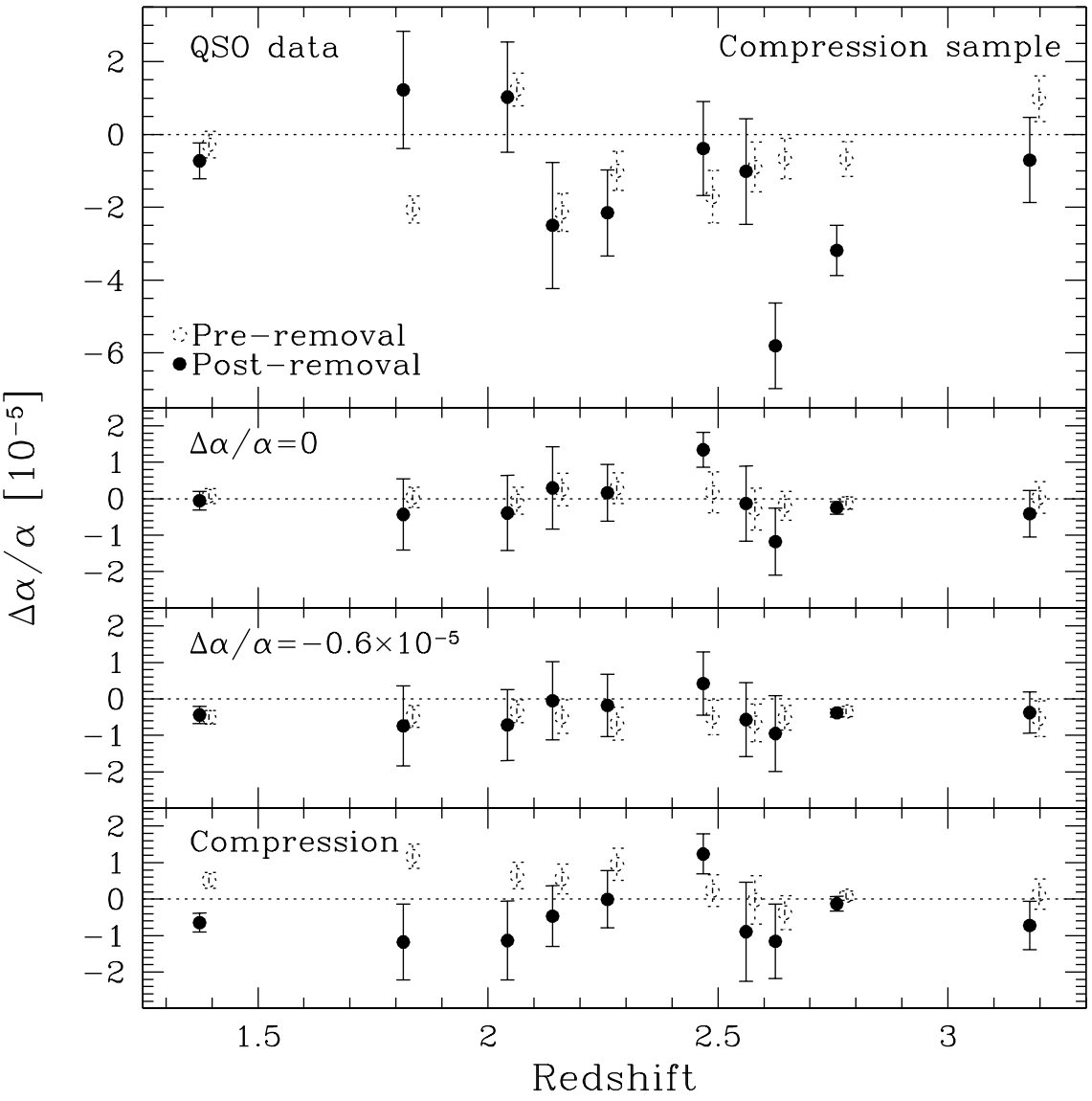

Figure 4.14. Detailed results of the high-z compression test in the compression sample for the QSO data (upper panel) and simulations (lower 3 panels). The error bars for the simulations represent the rms from 20 synthetic spectra. Each panel shows binned values of $\Delta\alpha/\alpha$ before and after transitions are removed to form the 76 compression combinations. Although the values of $\Delta\alpha/\alpha$ for the QSO data generally shift towards more negative values after line removal, the simulations with artificially compressed spectra (lower panel) show a larger shift. The pre-removal values for the data and this simulation also markedly disagree. See text for discussion.

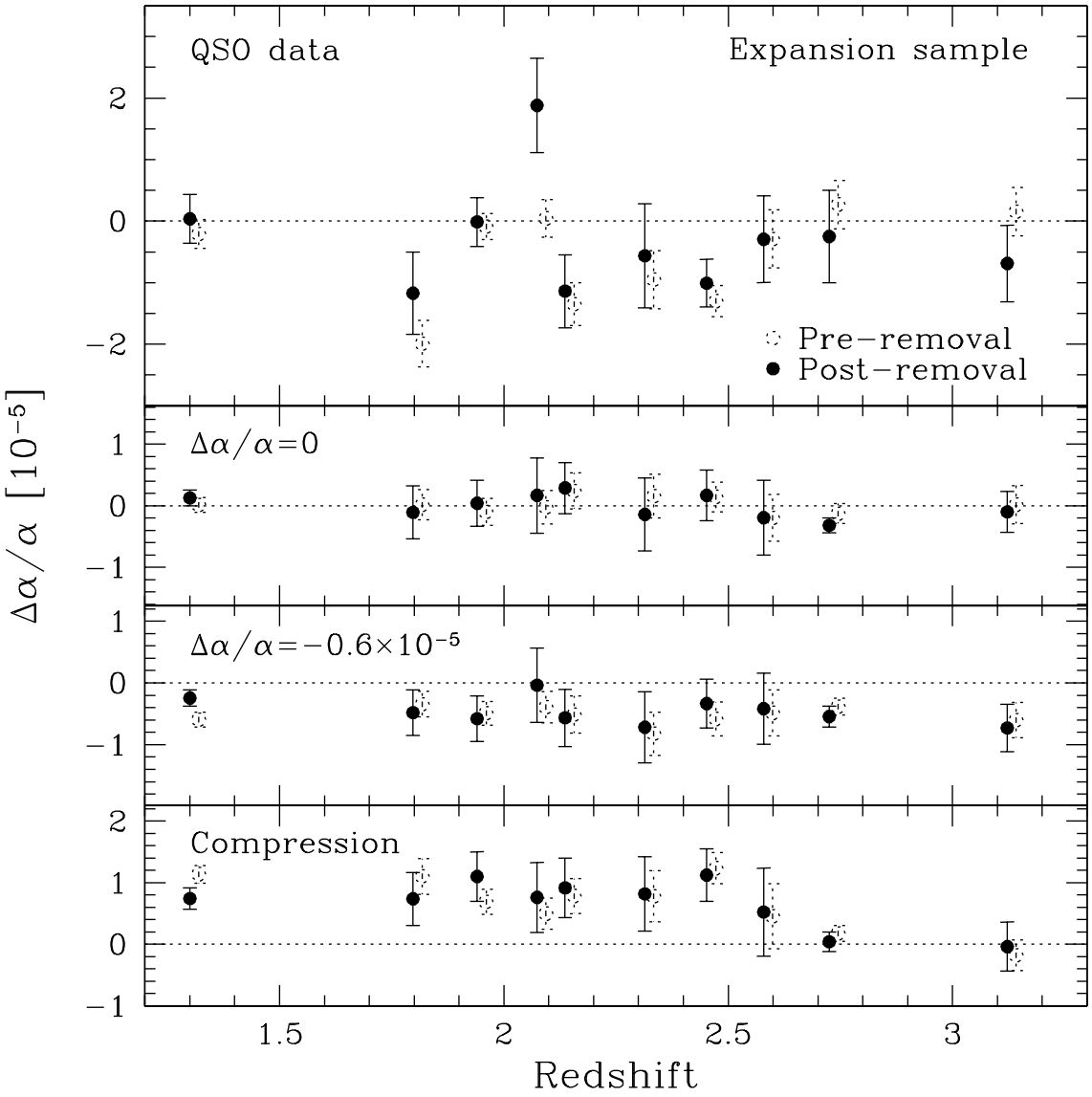

Figure 4.15. Same as Fig. 4.14 but for the expansion sample. 126 combinations contribute to the binned values of $\Delta\alpha/\alpha$ shown. No significant difference is observed between the pre- and post- removal values in the QSO data or in any of the simulations. The lower panel implies that the expansion sample is surprisingly insensitive to simple systematic errors.

compression test to the QSO data may reveal some evidence for a compression effect. However, applying the same test to artificially compressed synthetic spectra yields a much clearer and stronger effect on $\Delta\alpha/\alpha$. The interpretation is also complicated by the extra scatter in the real QSO results.

4-12.3 High-z q-type removal

If simple systematic errors are responsible for our measured non-zero $\Delta\alpha/\alpha$, it is surprising that $\Delta\alpha/\alpha$ is so consistent between the low- and high-z samples. The lower panel of Fig. 4.13 explicitly demonstrates this. It would be even more surprising if we were to take subsets of the QSO absorption lines, grouped according to the sign and magnitude of q, and found consistent values of $\Delta\alpha/\alpha$. We can apply such a test to the high-z sample only, since it contains transitions with several distinct types of q coefficient (see Fig. 3.3).

We have applied this high-z q-type removal test to 26 absorption systems. These contained at least one transition of each of the highly delineated q-types, i.e. anchors, positive- and negative-shifters. 21 of these systems also contain at least one mediocre-shifter. If a low-order distortion of the wavelength scale causes our observed non-zero $\Delta\alpha/\alpha$, removing all transitions of one q-type may result in a significant change in $\Delta\alpha/\alpha$. Table 4.4 compares the weighted and unweighted mean values of $\Delta\alpha/\alpha$ before and after q-type removal. Although removing the anchors, mediocre-shifters and negative-shifters produces only small changes in $\Delta\alpha/\alpha$, removing the positive-shifters may lead to a significant change. However, two important caveats should be noted: (i) the pre- and post- removal values of $\Delta\alpha/\alpha$ are not independent of each other. This also applies to the $1\,\sigma$ error bars. (ii) After removing the positive- and negative-shifters, the errors in the unweighted mean values are large, indicating a large scatter in $\Delta\alpha/\alpha$. Both these points make the results in Table 4.4 difficult to interpret.

As for the high-z compression test, comparison with simulations facilitates interpretation of the above results. We have applied the q-type removal test to the 3 simulations described in Section 4-12.2. Figs. 4.16–4.19 show a detailed comparison between these results and those from the real QSO spectra. Concentrating first on the simulations of compressed spectra (lower panels of Fig. 4.17–4.19), we see that removing the anchor transitions does not significantly affect the values of $\Delta\alpha/\alpha$. However, the effect is more significant when the positive- and negative-shifters are

Table 4.4. Results of the high-z q-type removal test. Column 2 and 3 show the weighted and unweighted mean value of $\Delta\alpha/\alpha$ (in units of 10^{-5}) for the 26 relevant absorption systems before removing the transitions (the first three rows necessarily have the same value). Columns 4 and 5 give the weighted and unweighted mean after transitions of the specified q-type are removed. Note that the pre- and post-removal values of $\Delta\alpha/\alpha$ and the $1\,\sigma$ errors are not independent of each other. A detailed comparison must refer to simulations of the QSO data (see Figs. 4.16–4.19).

q-type removed	Pre-removal		Post-removal	
	$\langle\Delta\alpha/\alpha\rangle_{\rm w}$	$\langle\Delta\alpha/\alpha\rangle$	$\langle\Delta\alpha/\alpha\rangle_{\rm w}$	$\langle\Delta\alpha/\alpha\rangle$
Anchors	-0.65 ± 0.18	-0.68 ± 0.55	-0.88 ± 0.21	-0.88 ± 0.46
Positive-shifters	-0.65 ± 0.18	-0.68 ± 0.55	1.21 ± 0.52	0.25 ± 1.39
Negative-shifters	-0.65 ± 0.18	-0.68 ± 0.55	-0.63 ± 0.34	-1.89 ± 1.28
Mediocre-shifters	-0.48 ± 0.22	-0.39 ± 0.59	-0.41 ± 0.22	-0.26 ± 0.72

removed. Overall, we see $\Delta\alpha/\alpha$ decrease when the positive-shifters are removed whereas removing the negative-shifters increases $\Delta\alpha/\alpha$.

However, we do not observe similar patterns in the real QSO data. Any effects that may be present are confused by the significant scatter in the post-removal QSO values of $\Delta\alpha/\alpha$. We even observe some extra scatter when removing the anchors from the real QSO data. As in the high-z compression test, this extra scatter is expected. We also expect it to be worse here than for the compression test since (i) removing the positive- or negative-shifters significantly reduces the sensitivity of the MM method to $\Delta\alpha/\alpha$, (ii) less absorption systems contain all three of the necessary q-types than systems contributing to either the compression or expansion samples and (iii) many combinations of transitions can be used for each absorption system in the compression test. Also, by selecting systems which contain anchors, positive- and negative shifters, we tend to select systems with transitions of very different line strengths (e.g. transitions of Al II, Cr II and Zn II; see Fig. 3.3). We explained how this leads to extra scatter in values of $\Delta\alpha/\alpha$ in Section 3-5.2. This effect can be seen in Fig. 4.16 which shows the unbinned pre-removal values of $\Delta\alpha/\alpha$ for the

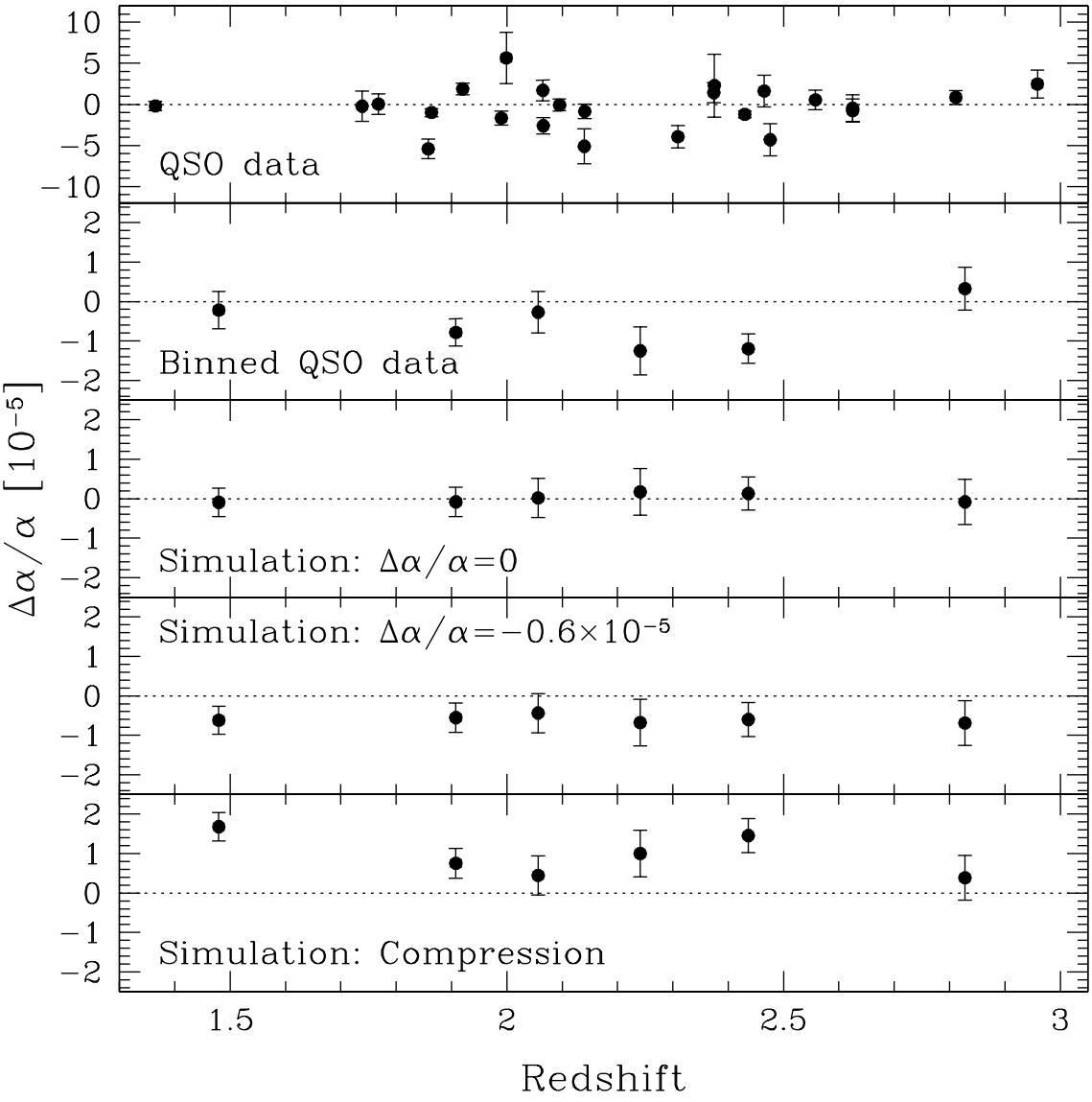

Figure 4.16. The sample of systems to which the high-z q-type removal test can be applied. The upper panel shows the values of $\Delta\alpha/\alpha$ for the 26 systems comprising the q-type sample, i.e. those with at least one anchor, positive- and negative-shifter. These data are binned in the next panel. The lower three panels show the weighted mean values of $\Delta\alpha/\alpha$ for the different simulations. These values and the binned QSO data are shown as dotted circles in Figs. 4.17–4.19.

26 systems we consider.

To summarize this section, simulations indicate that removing transitions, grouped according to the magnitude and sign of q, is a potentially powerful test

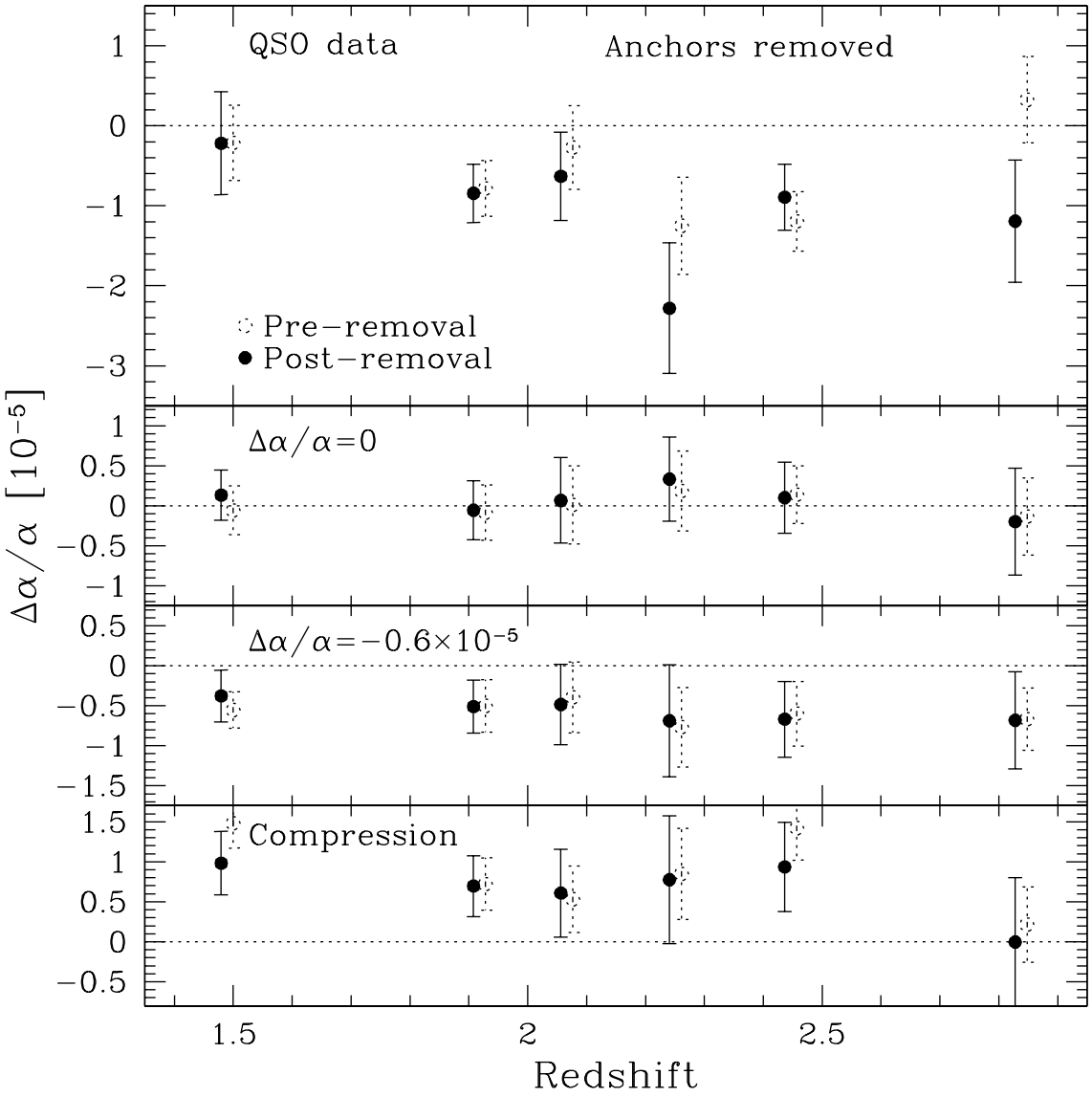

Figure 4.17. Detailed anchor removal results for the QSO data and simulations (lower 3 panels). The error bars for the simulations represent the rms from 20 synthetic spectra. The synthetic spectra with artificial compression (lower panel) indicate that removing the anchors should not affect $\Delta\alpha/\alpha$ significantly, even when distortions of the wavelength scale are present. The QSO values also show little deviation after line removal but some extra scatter may exist.

for simple systematic errors in the high-z data. However, the extra scatter in the values of $\Delta\alpha/\alpha$ for the relevant 26 absorption systems prevents any firm conclusion about the magnitude of such systematic effects.

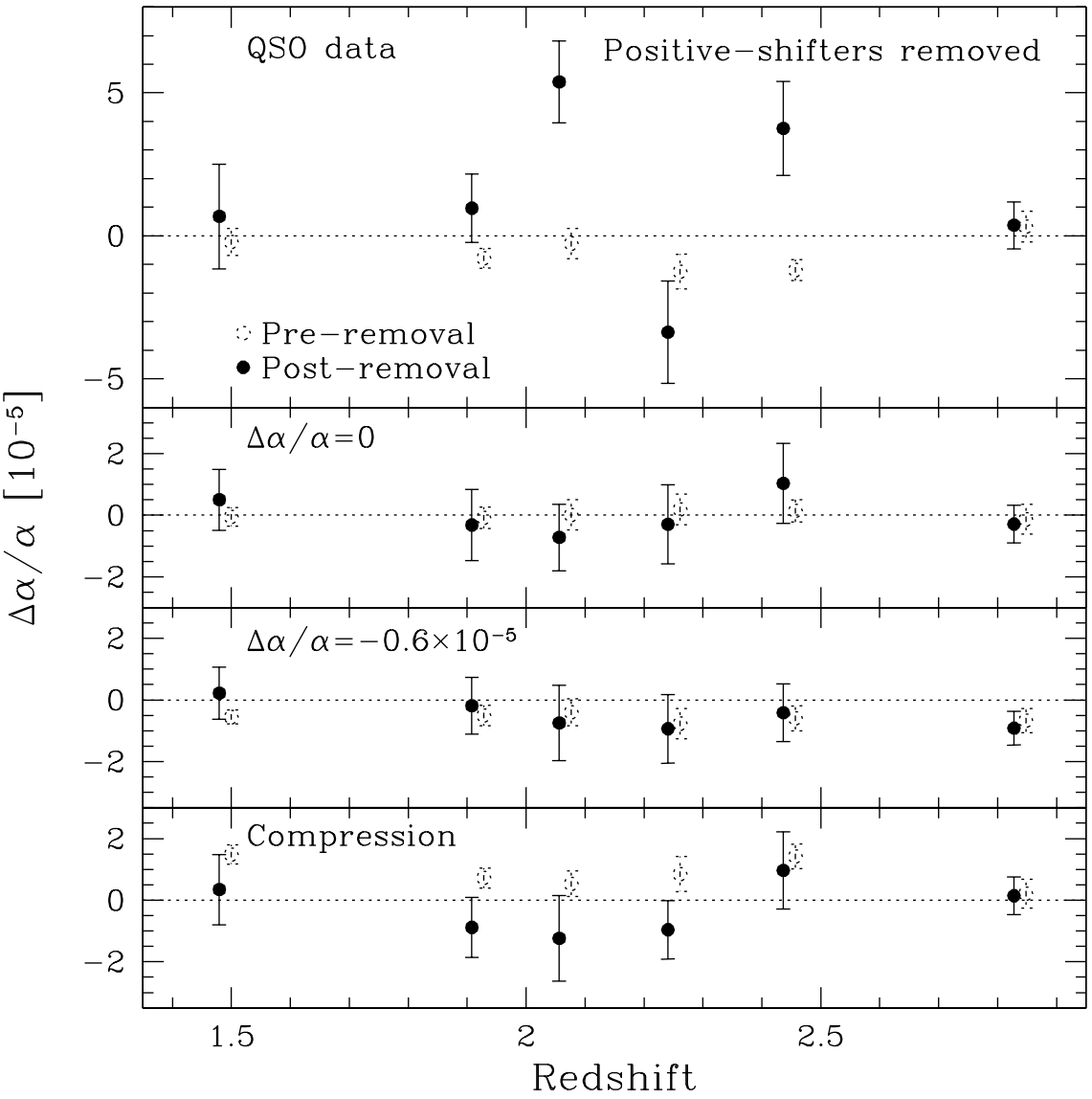

Figure 4.18. Detailed positive-shifter removal results for the QSO data and simulations (lower 3 panels). The error bars for the simulations represent the rms from 20 synthetic spectra. Although the compression simulation reveals a significant change in $\Delta\alpha/\alpha$ upon line-removal, the extra scatter in the post-removal QSO data precludes a firm conclusion about the presence of systematic effects (see text for discussion).

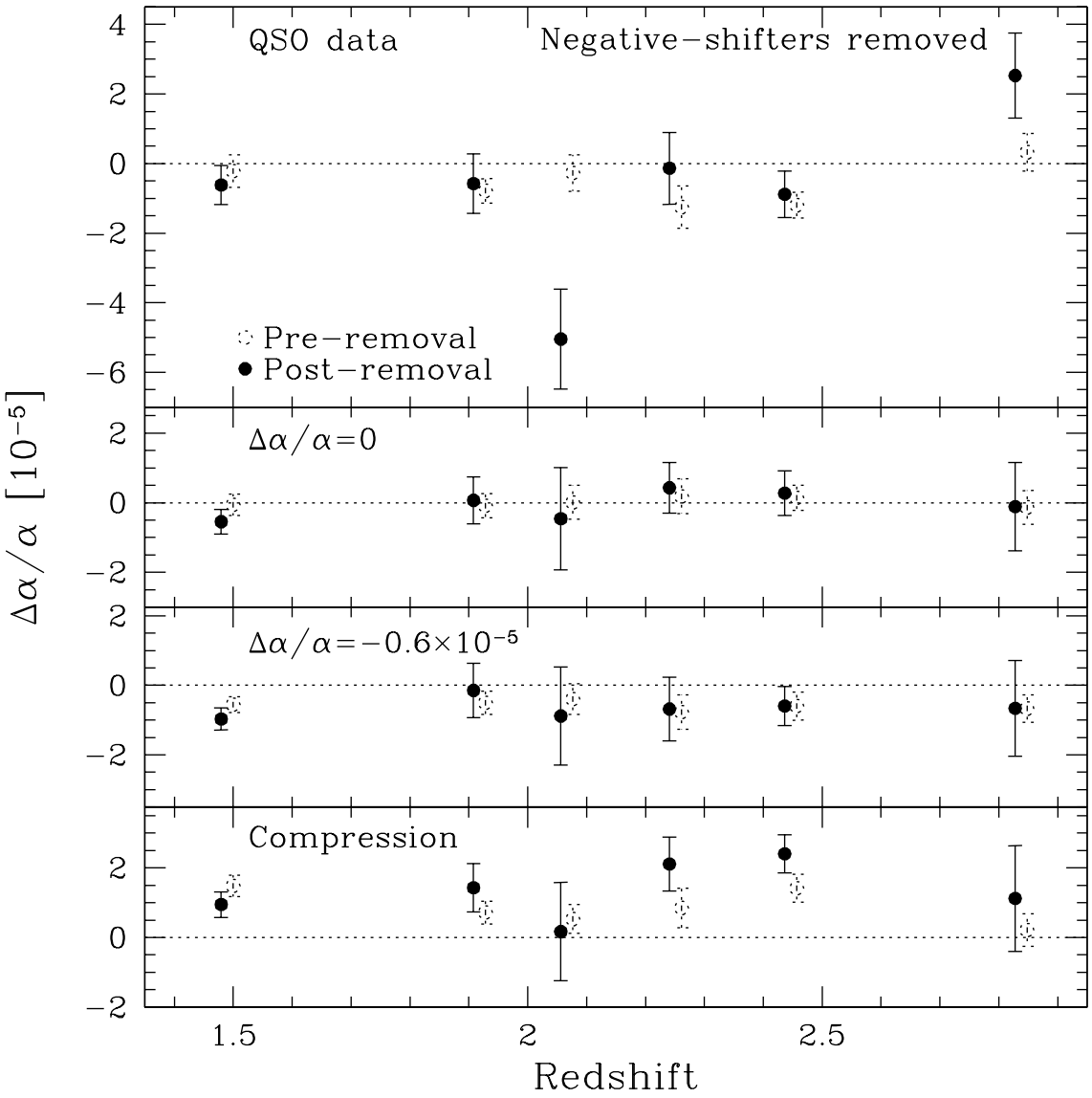

Figure 4.19. Detailed negative-shifter removal results for the QSO data and simulations (lower 3 panels). The error bars for the simulations represent the rms from 20 synthetic spectra. Although the compression simulation reveals a significant change in $\Delta\alpha/\alpha$ upon line-removal, the extra scatter in the post-removal QSO data precludes a firm conclusion about the presence of systematic effects (see text for discussion).

4-13 Summary of potential systematic errors in the MM method

We have searched for possible instrumental and astrophysical systematic effects which could mimic the evidence for varying α described in Chapter 3. The two most important systematic effects are those due to possible atmospheric dispersion effects and isotopic abundance variations. 60% of the absorption systems may be affected by the former. However, comparison of the affected and unaffected systems yields no evidence for these effects (Fig. 4.8). Also, modelling of the potential effects of atmospheric dispersion indicates that the low- and high-z values of $\Delta\alpha/\alpha$ should have been shifted in opposite senses (Fig. 4.9). Atmospheric dispersion effects clearly can not explain our results. The effect of possible variations in the isotopic abundances is more difficult to estimate. However, we obtained an upper limit on this effect by assuming strong abundance evolution of the Mg and Si isotopes. This systematic effect, if present, should have pushed $\Delta\alpha/\alpha$ to more positive values and so, when we incorporate our estimates into the analysis, $\Delta\alpha/\alpha$ becomes more negative (Fig. 4.5).

We corrected for these two systematic effects separately in Figs. 4.5 and 4.9. In Fig. 4.20 we correct for both effects simultaneously. We stress that there is no evidence for atmospheric dispersion effects and that the upper limit on the effect of isotopic abundance variations is from Galactic measurements and theoretical arguments only. Nevertheless, Figs. 4.5, 4.9 and 4.20 show that known systematic errors can not explain our results.

4-14 Systematic errors in the AD method

In light of the detailed analysis of systematic effects in the MM method above, we may now briefly summarize the important systematic effects for the AD method. Although the AD result in equation 2.6 is statistically insignificant, the precision obtained is approaching the level at which systematic errors begin to become im-

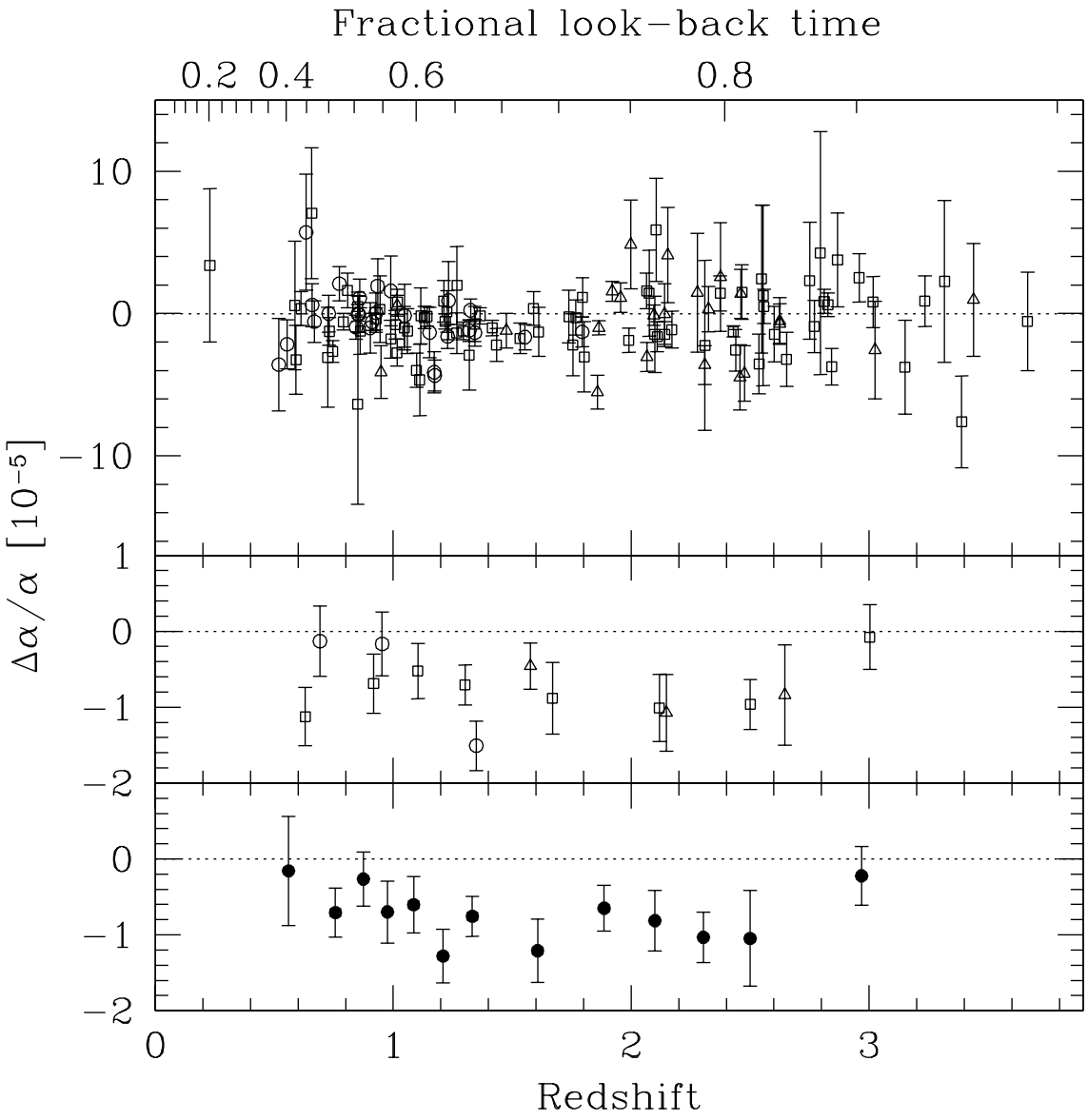

Figure 4.20. Same as Fig. 3.7 but corrected for both *potential* systematic errors, i.e. relevant systems are corrected for the atmospheric dispersion effects discussed in Section 4-11 and we assume zero abundance ratios of the weak isotopes ^{25,26}Mg and ^{29,30}Si in the absorption clouds (Section 4-10.3). The weighted mean of the corrected sample is $\Delta\alpha/\alpha = (-0.742 \pm 0.102) \times 10^{-5}$ (further statistics are given in Table 3.5). That is, correcting our data for possible systematic errors yields a more significant result.

portant. We have already discussed how the Varshalovich et al. (2000) result was severely affected by errors in the laboratory wavelengths of the Si IV $\lambda\lambda$1393 and 1402

transitions. We must therefore examine possible systematic errors in our results.

4-14.1 Wavelength miscalibration

We explained the potential for wavelength miscalibrations of the QSO data to affect values of $\Delta\alpha/\alpha$ in Section 4-6. We designed a direct test of the ThAr calibration spectra where the ThAr emission lines are treated with the same many-multiplet analysis as the QSO spectra. For each absorption system, this allows one to derive a value of $(\Delta\alpha/\alpha)_{\rm ThAr}$ from sections of ThAr spectra which correspond to sections of the QSO spectrum containing the Si IV doublet transitions.

The results are shown in Fig. 4.21 where we compare them with the results from the QSO data. It is clear that the QSO results have not been significantly affected in any systematic way. The weighted mean value of $(\Delta\alpha/\alpha)_{\rm ThAr} = (-6 \pm 9) \times 10^{-7}$. The scatter in the data is larger than what we expect on the basis of the individual $1\,\sigma$ error bars. As we discussed in Section 4-6.2, this is most likely due to blending of weak ThAr or contaminant emission lines with the ThAr lines of interest.

The results in Fig. 4.21 also limit possible variations in the Keck/HIRES instrumental profile (IP) asymmetry along and across echelle orders, as discussed in Section 4-7.

4-14.2 Systematic line blending with unknown species

There may have been weak, interloping, unresolved lines which, if the interloping species were in the same absorption cloud, could have produced a shift in the fitted line wavelengths of all velocity components of one or both Si IV transitions. As in Section 4-9, we distinguish between *random* blends and *systematic* blends. *Random* blends may occur if many absorption clouds at different redshifts intersect the line of sight to a single QSO. These will not affect the value of $\Delta\alpha/\alpha$ averaged over many absorption systems at different redshifts. A *systematic* blend will occur when two species are in the same cloud and have absorption lines with similar rest-wavelengths.

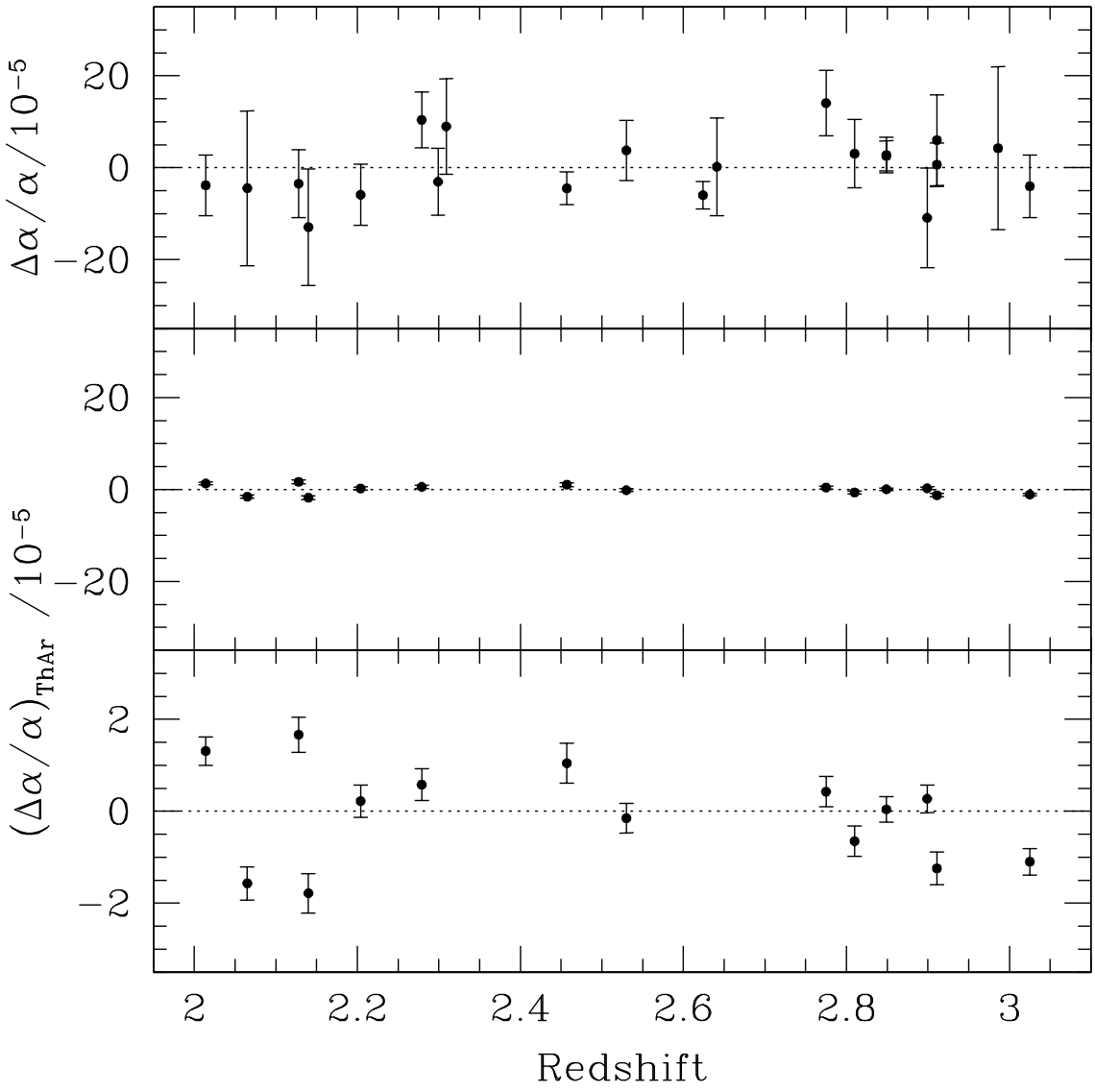

Figure 4.21. Comparison of QSO and ThAr results for the Si IV ADs. The top panel shows the QSO results and the middle panel shows the ThAr data on the same scale. The weighted mean is $(\Delta\alpha/\alpha)_{\rm ThAr} = (-6 \pm 9) \times 10^{-7}$. The lower panel is an expanded view of the ThAr results. Note that some ThAr data were not available. Clearly, this does not affect our conclusions.

Such an effect could mimic a systematic shift in α.

We have searched atomic line databases [Moore 1971; the Vienna Atomic Line Database (VALD), Piskunov et al. 1995; Kupka et al. 1999] for transitions of any species which may blend with Si IV $\lambda\lambda$1393 or 1402. The search was restricted to

transitions from the ground state with rest wavelengths λ such that $|\lambda - \lambda_0| \leq 0.2\,\text{Å}$ ($|\Delta v| \approx 12\,\text{kms}^{-1}$). This is a conservative upper limit adopted from simulations of typical blends. We did not identify any potential blends with Si IV λ1402 satisfying this criteria. For Si IV λ1393 we found one potential interloper: Be I λ1393 at $\lambda = 1393.804\,\text{Å}$ (VALD). This transition has an oscillator strength of $f = 2.080 \times 10^{-3}$. The Be I λ2349 transition is nearly three orders of magnitude stronger than this ($f = 1.698$) and, to our knowledge, has never been detected in QSO absorption spectra. This safely rules out Be I λ1393 as a candidate interloper.

In summary, we have found no known atomic transitions which may blend with either of the Si IV doublet lines. We have not considered molecular transitions as potential interlopers but consider this possibility to be unlikely due to the very low abundances of molecules in QSO absorbers (e.g. Black et al. 1987; Curran et al. 2002a, 2003a,b; Murphy et al. 2003b).

4-14.3 Differential isotopic saturation

Si has three naturally occurring isotopes, ^{28}Si, ^{29}Si and ^{30}Si, with terrestrial abundances in the ratio 92.23 : 4.68 : 3.09 (Rosman & Taylor 1998). Thus, each absorption line will be a composite of absorption lines from all three isotopes. We are not aware of any experimental determinations of the spectral separations between the isotopic components. Thus, the values of ω_0 in Table 2.1 (Griesmann & Kling 2000) are *composite* wavenumbers only. These wavenumbers will only strictly be applicable in the optically thin regime (linear part of the curve of growth). As the column density increases, the strongest isotopic component begins to saturate and the line centroid will shift according to the natural abundances (cf. Section 4-14.4) of the other isotopes.

Estimates of the isotopic separations for the Si IV doublet have been made by Safronova & Johnson (2001) and these are summarized in Table 4.5. From these separations we have estimated the absolute isotopic wavenumbers (ω_0 in Table 4.5) such that the abundance-weighted mean of the isotopic wavenumbers equals the

composite values in Table 2.1. The error in these results is $\lesssim 10\%$.

If we consider a Si IV doublet with a single velocity component then, as the λ1393 line begins to saturate, the line centroid will shift bluewards. The effective doublet separation will continue to increase but this increase will eventually slow and reverse as the λ1402 transition begins to saturate. It is clear that this is a potentially important systematic effect. Therefore, we have used the values of ω_0 in Table 4.5 to re-calculate $\Delta\alpha/\alpha$ for the sample of Si IV absorbers. Only 5 systems clearly contain saturated components and $\Delta\alpha/\alpha$ in these systems displays the expected behaviour: $\Delta\alpha/\alpha$ becomes more negative when the isotopic structures are included. Overall, the weighted mean for our sample becomes $\Delta\alpha/\alpha = (-0.8 \pm 1.3) \times 10^{-5}$.

4-14.4 Isotopic abundance variation

Timmes & Clayton (1996) suggest that the abundance of ^{29}Si and ^{30}Si should decrease with decreasing metallicity. In general, damped Lyman-α systems (DLAs), which some of the Si IV doublets are associated with, are thought to have metallicities $Z \lesssim -0.6$ at high redshift (e.g. Prochaska & Wolfe 2000). If the isotopic abundances of Si at redshifts $z = 2$–3 differ substantially from their terrestrial values then this may mimic a shift in α.

The dominant component of the isotopic shift is the mass shift (equation 3.7). For a single ion, the mass shift is degenerate with the redshift parameter fitted to the velocity components of an absorption system. That is, it will have no effect on the AD values of $\Delta\alpha/\alpha$. The specific isotopic shifts for the Si IV doublet have been calculated by Safronova & Johnson (2001) and are given in Table 4.5. We also show the volume isotopic shift for ^{30}Si IV as calculated by V. A. Dzuba (private communication) and these are clearly negligible. The specific shift is not degenerate with redshift but only at a negligible level. Thus, even if the isotopic ratios of ^{29}Si and ^{30}Si are much smaller in the Si IV absorbers, this will have a negligible effect on $\Delta\alpha/\alpha$.

Table 4.5. The isotopic structures of Si IV $\lambda\lambda$1393 and 1402 calculated by Safronova & Johnson (2001). We show the total isotopic separation, $\Delta\omega_0^{\rm tot}$, and the contribution from the specific ($\Delta\omega_0^{\rm spec}$) and volume ($\Delta\omega_0^{\rm vol}$) isotopic shifts. The final wavenumber, ω_0, is such that the abundance-weighted mean equals the corresponding composite value in Table 2.1. The last column shows the relative abundance of each isotope (Rosman & Taylor 1998).

Transition	A	$\Delta\omega_0^{\rm tot}$ (cm^{-1})	$\Delta\omega_0^{\rm spec}$ (cm^{-1})	$\Delta\omega_0^{\rm vol}$ (10^{-3} cm^{-1})	ω_0 (cm^{-1})	λ_0 (Å)	%
Si IV λ1393	28	–	–	–	71748.344	1393.76039	92.23
	29	0.1044	0.0585	–	71748.478	1393.75779	4.68
	30	0.2017	0.1130	4.413	71748.545	1393.75649	3.09
Si IV λ1402	28	–	–	–	71287.365	1402.77313	92.23
	29	0.1042	0.0583	–	71287.499	1402.77049	4.68
	30	0.2013	0.1126	4.418	71287.566	1402.76917	3.09

4-14.5 Hyperfine structure effects

Hyperfine splitting can lead to saturation effects similar to the isotopic saturation effects discussed in Section 4-14.3. The transitions of the ^{29}Si isotope will experience hyperfine splitting since the neutron number is odd. As with the isotopic structure, the magnitude of hyperfine splitting has not been measured. However, V. A. Dzuba (private communication) has estimated the splitting and finds it to be a factor of $\sim$2 times smaller than the isotopic splitting. This may also be estimated by comparison with the hyperfine structure of ^{25}Mg since the Si IV and Mg II doublets have similar ground and excited state wavefunctions and the magnetic moments of Mg and Si are similar (see Table 4.1). Drullinger et al. (1980) have measured the hyperfine splitting of the ^{25}Mg II λ2796 transition: the hyperfine splitting is $\sim$2 times smaller than the isotopic separations. It is therefore clear that saturation effects will be negligible.

4-14.6 Atmospheric dispersion effects

Five of the Si IV absorption systems were observed without the use of an image rotator (i.e. they were observed before August 1996 when a rotator was installed on Keck/HIRES). As discussed in Section 4-11.3, the QSO light is dispersed across the spectrograph slit by the atmosphere and, if the slit is not maintained perpendicular to the horizon by an image rotator, light of different wavelengths will enter the spectrograph at slightly different angles. This leads to two effects: (i) a compression of the spectra relative to the ThAr calibration frames and (ii) a distortion of the IP due to truncation of the dispersed seeing discs on either side of the slit jaws.

In Section 4-11.3 we modelled these two effects and their effect on the values of $\Delta\alpha/\alpha$. For the Si IV doublet, a typical value for the angular separation between $\lambda\lambda$1393 and 1402 due to atmospheric dispersion is only $\Delta\psi \approx 0\farcs007$ (using $z_{\rm abs} = 2.6$ and using the same atmospheric conditions used when applying equation 4.4). This implies a shift in $\Delta\alpha/\alpha \approx -0.2 \times 10^{-5}$. We confirmed this value using simulations similar to those described in Section 4-11.3 (see Fig. 4.9). The sign of this correction

is such that removing the compression implied by equation 4.4 from the data will result in a more positive $\Delta\alpha/\alpha$. The correction is substantial for an individual system so we have applied it to the 5 affected systems to obtain an upper limit on the overall effect on $\Delta\alpha/\alpha$. Our weighted mean value of $\Delta\alpha/\alpha$ for the entire sample becomes $\Delta\alpha/\alpha = (-0.4 \pm 1.3) \times 10^{-5}$.

Chapter 5

Other QSO absorption line methods

In Chapter 3 we demonstrated how the MM method provides an order of magnitude increase in precision over the AD method described in Chapter 2. Even tighter constraints can be placed on variations in *combinations* of dimensionless constants using radio QSO absorption spectra. In this chapter we describe constraints on variations in $y \equiv \alpha^2 g_p$, $\mu \equiv m_e/m_p$ and $x \equiv \alpha^2 g_p/\mu$. We first give a detailed discussion of the former and use two absorption systems to significantly improve on previous limits. We discuss the literature constraints on possible variations of x in Section 5-5 and of μ in Section 5-6. Comparison between $\Delta\alpha/\alpha$, $\Delta y/y$, $\Delta x/x$ and $\Delta\mu/\mu$ comes with several important caveats. We discuss these in Section 5-7.

5-1 $\Delta y/y$: Introduction

Comparison of H I 21-cm and molecular rotational spectra of QSO absorption systems with laboratory spectra is a particularly useful probe of fundamental physics at high redshift. The H I 21-cm hyperfine transition frequency is proportional to $\mu_p\mu_B/\hbar a^3$ where $\mu_p = g_p e\hbar/4m_p c$ and $\mu_B = e\hbar/2m_e c$ is the Bohr magneton. Here, g_p is the proton g-factor, m_p and m_e are the masses of the proton and electron

respectively and $a = \hbar^2/m_e e^2$ is the Bohr radius. The rotational transition frequencies of diatomic molecules, such as CO, are proportional to $\hbar/Ma^2$ where M is the reduced mass. Therefore, the ratio of the hyperfine and molecular rotational frequencies is proportional to $\alpha^2 g_p M/m_p$. Variations in this quantity will be dominated by variations in $y \equiv \alpha^2 g_p$ since variations in M/m_p are suppressed by a factor $m_p/U \sim 100$ where U is the binding energy of nucleons in nuclei. If any variation in y occurs, it will be observed as a difference in redshift between the H I 21-cm ($z_{\rm H}$), and molecular ($z_{\rm mol}$) absorption lines (Drinkwater et al. 1998, hereafter D98):

$$\frac{\Delta y}{y} \equiv \frac{y_z - y_0}{y_0} \approx \frac{\Delta z}{1+z} \equiv \frac{z_{\rm mol} - z_{\rm H}}{1+z_{\rm mol}} \tag{5.1}$$

where y_z and y_0 are the values of y at the absorption redshift z and in the laboratory respectively.

The first comparison of H I 21-cm and molecular absorption was made by Varshalovich & Potekhin (1996, hereafter VP96). They compared the published redshifts of the CO absorption (reported in Wiklind & Combes 1994) and H I 21-cm absorption (reported in Carilli et al. 1992) towards PKS 1413+135. They interpreted any shift as a change in the molecular mass, M. Wiklind & Combes (1997) carried out a similar analysis. D98 pointed out that such a shift actually constrains $\Delta y/y$ rather than $\Delta M/M$ with a similar argument to that above. VP96's value of $\Delta M/M$ translates to $\Delta y/y = (-4 \pm 6) \times 10^{-5}$.

Like VP96, D98 used the published redshifts for the CO(0–1) lines towards PKS 1413+135[1]. However, D98 improved the precision of $\Delta y/y$ by fitting Voigt profiles to the H I 21-cm data rather than using the published redshifts. The errors on the redshift of each velocity component in the H I data were reduced by an order of magnitude compared to the estimates of VP96. D98 also applied this analysis to another absorber towards TXS 0218+357 at $z_{\rm abs} = 0.685$. They derived an *upper limit* on any variation in y for both absorbers: $|\Delta y/y| < 0.5 \times 10^{-5}$.

[1]The CO data of Wiklind & Combes (1994), used by VP96, showed a $-11\,{\rm km s^{-1}}$ offset from the H I 21-cm velocity. We used a new, corrected CO dataset reported in Wiklind & Combes (1997) which shows no such offset.

The present work aims at turning the upper limit on $\Delta y/y$ in D98 into a measurement of $\Delta y/y$ by fitting simultaneously the H I 21-cm data *and* the rotational lines of several molecular species. We describe the available data in Section 5-2 and describe our analysis and results in Section 5-3. We discuss our new results in Section 5-4, comparing them with other constraints on y variability.

5-2 $\Delta y/y$: Available data

Only 4 QSOs have had mm-band rotational molecular absorption detected along their lines-of-sight: TXS 0218+357, PKS 1413+135, B3 1504+377 and PKS 1830−211. Below we describe the molecular and H I data available for the first two of these QSOs. We do not have sufficient data to consider PKS 1830−211. The molecular absorption profile is very broad (FWHM $\sim 40\,\mathrm{kms}^{-1}$, Wiklind & Combes 1998) and so constraints on $\Delta y/y$ would be weak. We do not consider B3 1504+377 any further due to a $15\,\mathrm{kms}^{-1}$ offset between the H I 21-cm (Carilli et al. 1997, 1998) and HCO^+ (Wiklind & Combes 1996) velocity scales, as noted in D98. Checks on the origin of this difference have not revealed any instrumental or human error and so it may well be that the molecular and H I absorption occurs in different clouds. However, as noted in D98, this seems unlikely because the molecular and H I velocity structures are very similar. Further data is required to clarify this problem.

5-2.1 TXS 0218+357

TXS 0218+357 is a gravitationally lensed QSO (Patnaik et al. 1993), probably at a redshift $z_{\rm em} \approx 0.94$ (Wiklind & Combes 1995), showing absorption in the lensing galaxy at $z_{\rm abs} = 0.6847$ (Carilli et al. 1993; Browne et al. 1993). VLBI observations (Patnaik et al. 1993; Biggs et al. 2001) show two, compact, flat-spectrum components (A to the south-west and B to the north-east) and a steep-spectrum Einstein ring. The background QSO shows intensity variability on intraday (Biggs et al. 2001) and longer (∼monthly) time-scales (O'Dea et al. 1992; Patnaik et al. 1993).

We use the spectrum of this QSO despite the fact that it is lensed since the A component provides the dominant absorption in both the molecular (Menten & Reid 1996) and 21-cm (Carilli et al. 2000, hereafter C00) bands. Thus, the profile of the $z = 0.6847$ absorber should not vary significantly over the time between molecular and H I 21-cm observations.

In this work we use the H I 21-cm spectrum of the $z_{\rm abs} = 0.6847$ absorption system published by Carilli et al. (1993) (FWHM $= 6.9\,{\rm kms}^{-1}$). Spectra of the CO(1–2), ^{13}CO(1–2), C^{18}O(1–2) and CO(2–3) molecules are taken from Combes & Wiklind (1995) (FWHM $\sim 30\,{\rm ms}^{-1}$) and spectra of HCO$^+$(1–2) and HCN(1–2) are from Wiklind & Combes (1995) (FWHM $\sim 2\,{\rm kms}^{-1}$). These data are presented in Fig. 5.1.

5-2.2 PKS 1413+135

PKS 1413+135 is at the centre of an on-edge spiral galaxy at $z_{\rm em} = 0.24671$ and the absorption occurs in the disk of this galaxy (Wiklind & Combes 1997). VLBI observations (C00) show that the 21-cm continuum flux is dominated by a jet extending from an inverted-spectrum nucleus. The nucleus dominates the mm continuum emission (Perlman et al. 1996). Thus, the H I 21-cm and molecular absorption lie along different sight lines separated by $\sim 0\farcs03$ (C00). We address this problem and its effect on our results in Section 5-4.

Here we use the H I 21-cm spectrum of the $z = 0.2467$ absorption system observed by Carilli et al. (1992) (FWHM $\approx 1.3\,{\rm kms}^{-1}$). The molecular absorption lines of CO(0–1), HCO$^+$(1–2) and HCO$^+$(2–3) were observed with the narrow band autocorrelator at the IRAM 30 m telescope on Pico Veleta, Spain, by Wiklind & Combes (1997) (FWHM $\sim 40\,{\rm ms}^{-1}$). These data are presented in Fig. 5.2.

5-3 $\Delta y/y$: Analysis, results and errors

We used VPFIT (see Section A-2) to fit multi-velocity component Voigt profiles to both the H I 21-cm and molecular absorption lines. The laboratory values for the

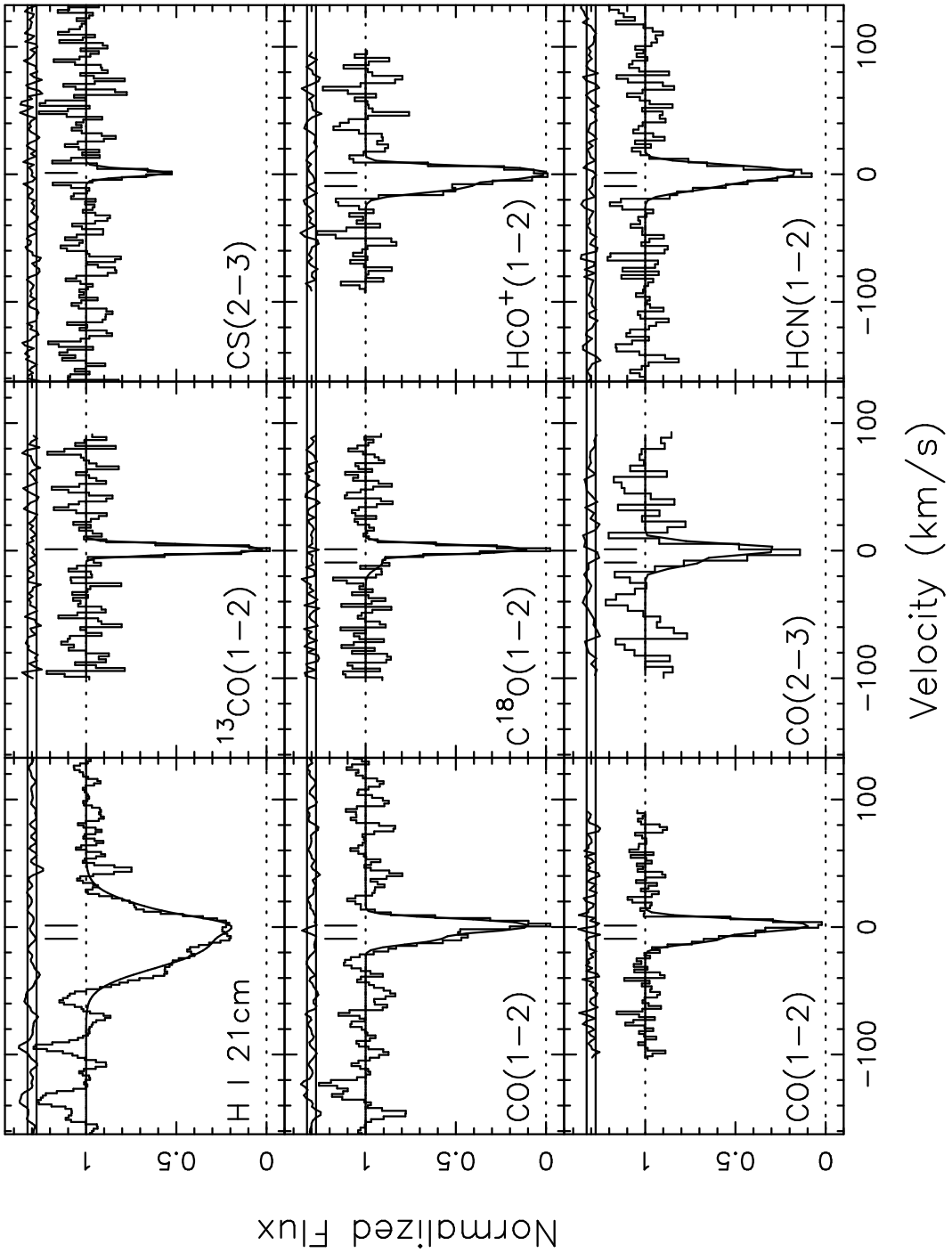

Figure 5.1. Spectra of the $z_{\rm abs} = 0.6847$ absorption system towards TXS 0218+357. The data are plotted as a histogram and the solid line represents our Voigt profile fit. The tick-marks above the data show the position of the fitted velocity components. The residuals (i.e. [data]−[fit]), normalized to a constant $1\,\sigma$ error (defined by the S/N in the continuum), are shown above each spectrum. Note that two independent spectra of CO(1–2) have been included.

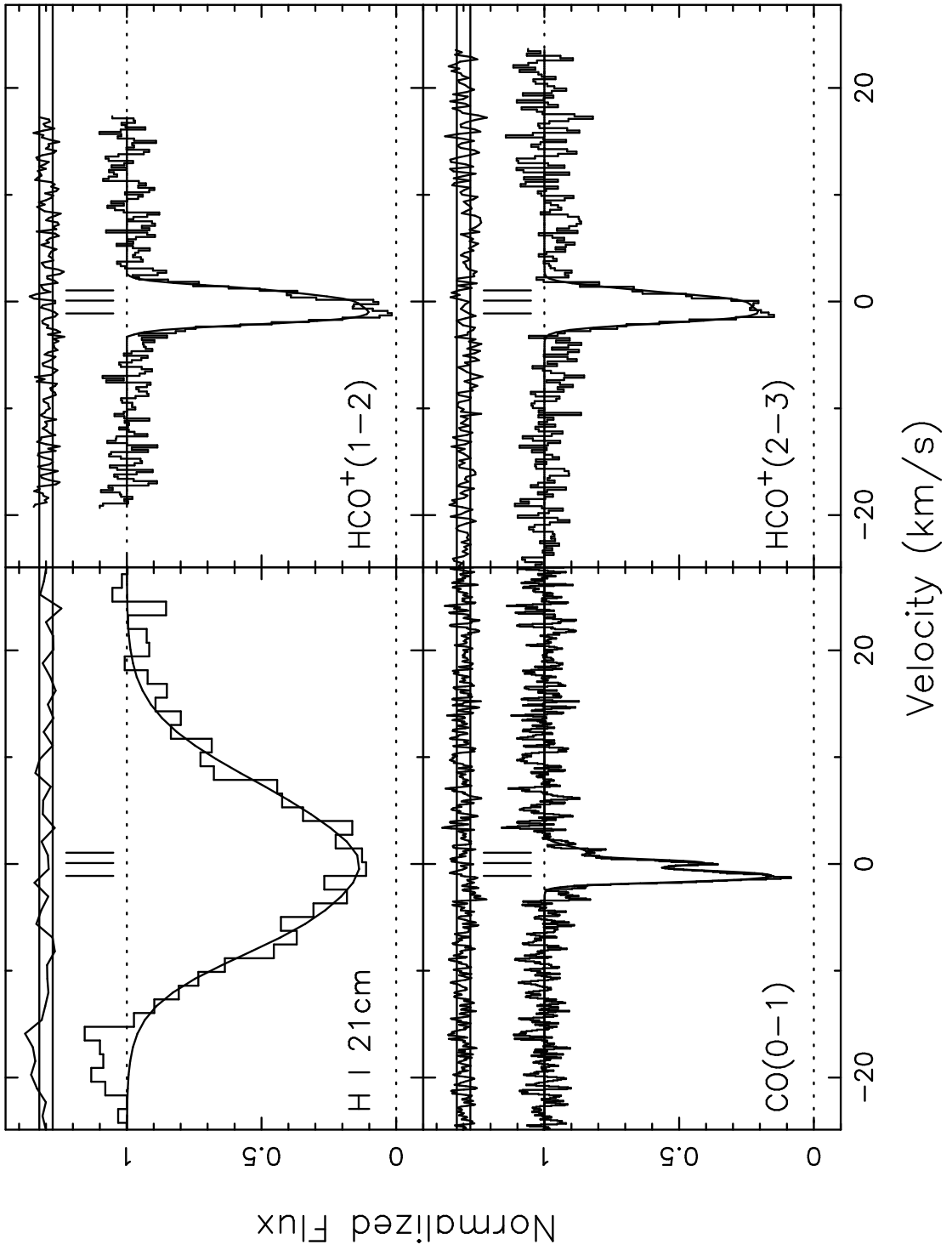

Figure 5.2. Spectra of the $z_{\rm abs} = 0.2467$ absorption system towards PKS 1413+135. The data are plotted as a histogram and the solid line represents our Voigt profile fit. The tick-marks above the data show the position of the fitted velocity components. The residuals (i.e. [data]−[fit]), normalized to a constant $1\,\sigma$ error (defined by the S/N in the continuum), are shown above each spectrum.

Table 5.1. Laboratory frequencies of transitions used in our analysis. Molecular frequencies are taken from Pickett et al. (1998) and the H I 21-cm frequency is from Essen et al. (1971).

Molecule	Transition	Frequency/GHz
CO	0–1	115.2712018(5)
	1–2	230.5380000(5)
	2–3	345.7959899(5)
^{13}CO	1–2	220.3986765(53)
C^{18}O	1–2	219.5603568(81)
CS	2–3	146.969033(50)
HCO$^+$	1–2	178.375065(50)
	2–3	267.557619(10)
HCN	1–2	177.261110(2)
H I	21-cm	1.420405751766(1)

transition frequencies were taken from Pickett et al. (1998)[2] and Essen et al. (1971) and are listed in Table 5.1. By simultaneously fitting several molecular transitions of differing strengths in the same absorber, we get the best possible estimate of the velocity structure. We determine the number of velocity components to be fitted to each system by requiring that $\chi^2_\nu \sim 1$ for the fit.

An iterative technique is used to find the best fitting value of $\Delta y/y$. We vary $\Delta y/y$ outside VPFIT (i.e. we vary the ratio of the hyperfine and molecular frequencies) and fit all lines simultaneously. During the fit we force the redshift parameters for corresponding velocity components to be the same for all transitions, thereby reducing the number of free parameters. We change $\Delta y/y$ at each iteration of the routine, i, to find χ^2_i as a function of $\Delta y/y$. The best fitting value of $\Delta y/y$ is that which gives the minimum χ^2, $\chi^2_{\rm min}$, and the $1\,\sigma$ error in $\Delta y/y$ is found using $\chi^2_{\rm min}+1$.

For the $z_{\rm abs} = 0.6847$ absorption system towards TXS 0218+357 we find the best

[2]Data available at http://spec.jpl.nasa.gov

fitting value of

$$\Delta y/y = (-0.16 \pm 0.36) \times 10^{-5} \tag{5.2}$$

and for the $z_{\rm abs} = 0.2467$ absorption system towards PKS 1413+135 we find

$$\Delta y/y = (-0.20 \pm 0.20) \times 10^{-5}\,. \tag{5.3}$$

To check internal consistency, we have investigated the effect of removing individual transitions from the analysis of each absorption system. Our values of $\Delta y/y$ showed no significant change upon removal of any molecular transition. In particular, we found no change when we removed either or both the CS(2–3) and ^{13}CO(0–1) transitions from our analysis of TXS 0218+357. The low velocity component does not seem to be present in these transitions and was not fitted (see Fig. 5.1). The fact that the results are insensitive to removal of these lines indicates the robustness of our line fitting method and highlights the advantage of using many different molecular transitions.

The $1\,\sigma$ errors quoted in equations 5.2 and 5.3 are statistical only. However, as noted in Section 5-2.2, the fact that we probe slightly different sight lines with the molecular and H I 21-cm observations may result in an additional random error. D98 investigated this problem empirically by fitting several QSO spectra exhibiting Galactic absorption and comparing the fitted redshifts of the HCO^+ and H I velocity components. D98 find a close correspondence between the velocity components of HCO^+ and H I with a Gaussian dispersion of only $1.2\,{\rm km s}^{-1}$. This corresponds to an error $\Delta y/y = 0.4 \times 10^{-5}$. Our two results, being of similar value and so close to zero, suggest that this error estimate may be too large. However, it is clear that such a conclusion can only be reached with a larger sample of absorption systems. We have added this error in quadrature to obtain our final results:

$$\begin{aligned} \Delta y/y &= (-0.20 \pm 0.44) \times 10^{-5} \quad \text{at } z = 0.2467 \quad \text{and} \\ \Delta y/y &= (-0.16 \pm 0.54) \times 10^{-5} \quad \text{at } z = 0.6847 \end{aligned} \tag{5.4}$$

or

$$\begin{aligned} \Delta \alpha/\alpha &= (-0.10 \pm 0.22) \times 10^{-5} \quad \text{at } z = 0.2467 \quad \text{and} \\ \Delta \alpha/\alpha &= (-0.08 \pm 0.27) \times 10^{-5} \quad \text{at } z = 0.6847 \end{aligned} \tag{5.5}$$

assuming (perhaps incorrectly, see Section 5-7) a constant g_p.

5-4 $\Delta y/y$: Discussion

C00 have recently reported *upper limits* on $\Delta y/y$ using the same two absorption systems we analyse above. They obtained new H I 21-cm spectra of each absorber and compared the measured redshift with the published molecular redshifts. C00 find $\Delta y/y = (+1.0 \pm 0.3) \times 10^{-5}$ for TXS 0218+357 ($z_{\rm abs} = 0.6847$) and $\Delta y/y = (+1.29 \pm 0.08) \times 10^{-5}$ for PKS 1413+135 ($z_{\rm abs} = 0.2467$) where the errors are statistical only. They add to this an additional error of $\pm 1 \times 10^{-5}$, which is derived from other measurement uncertainties in the H I data (e.g. frequency calibration errors).

However, C00 also argue that the line-of-sight problem above could lead to errors as large as $10\,{\rm kms}^{-1}$ on the basis of typical sub-kiloparsec ISM motions. They therefore conclude with an upper limit of $|\dot{\alpha}/\alpha| < 3.5 \times 10^{-15}\,{\rm yr}^{-1}$ (assuming constant g_p) for a look-back time (within their assumed cosmology) of 4.8 Gyr to $z = 0.6847$. This corresponds to $|\Delta y/y| < 1.7 \times 10^{-5}$. This final dominant error term of $10\,{\rm kms}^{-1}$ is much greater than the $1.2\,{\rm kms}^{-1}$ error we apply in equations 5.4 and 5.5 but we stress that our value has been obtained empirically (by D98) and so should be more reliable.

5-5 $\Delta x/x$: Current limits and systematic errors

Wolfe et al. (1976) was the first to constrain variations in fundamental parameters with a comparison of H I 21-cm and optical resonance transitions. The ratio of the hydrogen hyperfine frequency and the Rydberg energy is proportional to $x \equiv \alpha^2 g_p/\mu$. Therefore, a variation in x would manifest itself as a difference between the absorption redshifts of H I 21-cm ($z_{\rm H}$) and a resonance transition in an alkali-like ion ($z_{\rm opt}$):

$$\frac{\Delta x}{x} \equiv \frac{x_z - x_0}{x_0} \approx \frac{\Delta z}{1+z} \equiv \frac{z_{\rm opt} - z_{\rm H}}{1 + z_{\rm opt}}\,. \qquad (5.6)$$

Wolfe et al. (1976) compared the H I 21-cm and Mg II absorption redshifts in the BL Lac QSO 0235+164 at $z_{\rm abs} = 0.524$ and obtained the limit, $|\Delta x/x| < 1.4 \times 10^{-4}$.

Tubbs & Wolfe (1980) marginally improved this limit to $|\Delta x/x| < 1.1 \times 10^{-4}$ using H I 21-cm and various optical resonance lines in absorption at $z_{\rm abs} = 1.776$ towards Q1331+170. Less restrictive limits were obtained for these two absorption systems by Wolfe & Davis (1979). The optical redshifts were relatively imprecise ($\delta z_{\rm opt} \sim 1 \times 10^{-4}$ compared with $\delta z_{\rm H} \sim 1 \times 10^{-5}$) and so limited the precision of these measurements.

Cowie & Songaila (1995) addressed this precision imbalance between the radio and optical data by using the higher resolution, higher S/N observations of Q1331+170 in Songaila et al. (1994). The C I absorption redshift was used to obtain

$$\Delta x/x = (0.70 \pm 0.55) \times 10^{-5}\,, \tag{5.7}$$

at $z_{\rm abs} = 1.776$ where the $1\,\sigma$ error has equal contributions from the H I 21-cm (Wolfe & Davis 1979) and optical redshifts, i.e. $\delta z_{\rm opt} \approx \delta z_{\rm H} \approx 1 \times 10^{-5}$.

A crucial systematic error in the above result is potential line-of-sight velocity differences between the H I 21-cm and C I absorption clouds. The QSO will emit optical light from a region close to the central black hole in comparison to the radio continuum emission which will be dominated by the radio lobes. Thus, the optical and radio absorption will occur along different lines of sight with potentially different kinematics. This effect should be of similar magnitude to that estimated for the mm/H I comparison in D98 (i.e. $\Delta v = 1.2\,{\rm km s^{-1}}$) and so an additional error of $\delta x \approx 0.4 \times 10^{-5}$ may need to be added in quadrature to equation 5.7. However, we stress that the real magnitude of this systematic error has not yet been properly quantified. Just as in the case of $\Delta y/y$, obtaining reliable constraints on $\Delta x/x$ is clearly a statistical problem and, currently, the number of known H I 21-cm absorption systems with corresponding optical absorption is small (e.g. Curran et al. 2002b).

5-6 $\Delta\mu/\mu$: Current limits and systematic errors

Pagel (1977) first addressed the constancy of $\mu \equiv m_p/m_e$ at high redshift by com-

paring the absorption redshifts of the H I Lyman series and various resonance lines of metal ions. This method, first suggested by Thompson (1975), relies on the larger mass shift for the H I lines than for the metal lines. Pagel obtained $|\Delta\mu/\mu| < 0.13$ using several QSO spectra with $1.7 < z_{\rm abs} < 2.7$.

A far more sensitive method is to compare the redshifts of the Lyman and Werner transitions of H_2 molecules which are redshifted above the atmospheric cutoff when $z_{\rm abs} \gtrsim 1.8$. Even if $z_{\rm abs} \approx z_{\rm em}$, the H_2 lines all fall in the Lyman-α forest and so one major draw-back of this method is significant random blending. Foltz et al. (1988) first pointed out that the vibrational component of the transition energy increases with increasing excited state vibrational quantum number. They obtained $|\Delta\mu/\mu| < 2\times10^{-4}$ using the $z_{\rm abs} = 2.8114$ absorption system towards Q 0528−2505. However, Varshalovich & Levshakov (1993) pointed out that different electronic-ro-vibrational transitions have a different dependence on the reduced mass of the molecule in question. They introduced the sensitivity coefficients, K_i, to describe the shift in rest wavelength, $\Delta\lambda_i$, for each transition, i, due to a non-zero $\Delta\mu/\mu \ll 1$,

$$\Delta\mu/\mu = K_i \frac{\Delta\lambda_i}{\lambda_i} \,. \tag{5.8}$$

They calculated the K_i coefficients for the Lyman and Werner bands of H_2 using the Born-Oppenheimer approximation, finding that they differ in magnitude and sign from transition to transition. This breaks the degeneracy between the redshift of the fitted absorption lines and the value of $\Delta\mu/\mu$. This is similar to the MM method (Chapter 3) where the diversity of q coefficients allows robust constraints on $\Delta\alpha/\alpha$.

Varshalovich & Levshakov (1993) analysed the spectrum of Foltz et al. (1988) to obtain the limit $|\Delta\mu/\mu| < 0.005$. Varshalovich & Potekhin (1995) compared the transition wavelengths of H_2, D_2, T_2 and HD molecules to obtain an alternative estimate of K_i. These values were consistent with those found previously. Again, they analysed the spectrum of Foltz et al. (1988) and obtained $|\Delta\mu/\mu| < 0.002$. Potekhin et al. (1998) used a new spectrum of the same absorption system, with a much higher resolution (i.e. $R \approx 14000$ compared to $R \approx 5000$), to obtain

$$\Delta\mu/\mu \equiv \frac{\mu_z - \mu_0}{\mu_0} = (-10 \pm 8)\times10^{-5} \,. \tag{5.9}$$

They used the laboratory wavelengths of Abgrall et al. (1993a,b) for the H_2 transitions. A consistent value was found using those of Morton & Dinerstein (1976).

Recently, Ivanchik et al. (2002) have analysed $R \approx 43000$, S/N $\approx$ 10–40 VLT/UVES spectra of 2 absorption systems: $z_{\rm abs} = 3.0249$ towards Q0347−3819 and $z_{\rm abs} = 2.3377$ towards Q 1232+0815. From the two systems, they identified 30 apparently unblended H_2 transitions and used a regression analysis of the measured redshifts and K_i coefficients (from Varshalovich & Potekhin 1995) to obtain

$$\begin{aligned} \Delta\mu/\mu &= (5.8 \pm 3.4) \times 10^{-5} \quad \text{and} \\ \Delta\mu/\mu &= (14.4 \pm 11.4) \times 10^{-5}\,, \end{aligned} \tag{5.10}$$

for $z_{\rm abs} = 3.0249$ and $z_{\rm abs} = 2.3377$ respectively. Analysing the fitted H_2 line positions for both absorbers simultaneously gives

$$\begin{aligned} \Delta\mu/\mu &= (5.7 \pm 3.8) \times 10^{-5} \quad \text{or} \\ \Delta\mu/\mu &= (12.5 \pm 4.5) \times 10^{-5}\,, \end{aligned} \tag{5.11}$$

where the first value was obtained using the laboratory wavelengths of Abgrall et al. (1993a,b) and the second was obtained with those of Morton & Dinerstein (1976). A refined analysis of Q0347−3819 has yielded $\Delta\mu/\mu = (5.0 \pm 1.8) \times 10^{-5}$ (Ivanchik et al. 2003). Levshakov et al. (2002a) have also analysed the UVES spectrum of Q 0347−3819 and find $\Delta\mu/\mu = (5.0 \pm 3.2) \times 10^{-5}$, in agreement with equation 5.10. Therefore, some evidence exists for a larger $\mu \equiv m_p/m_e$ in these H_2 absorption systems.

However, two potential systematic errors could significantly affect the above results:

1. Laboratory wavelength errors. The most recent laboratory measurements of H_2 Lyman and Werner transition wavelengths are those of Abgrall et al. (1993a,b). Ivanchik et al. (2002) quote the measurement errors in these wavelengths to be $\sim 1.5\,$mÅ, leading to a potential systematic error of $\Delta\mu/\mu \sim 2 \times 10^{-5}$. However, no clear statement of the wavelength accuracy or precision is made by Abgrall et al.. Indeed, the difference between the two values of $\Delta\mu/\mu$ in equation 5.11 indicate a larger systematic error (cf. statements in Ivanchik et al. 2002).

Potential errors in the laboratory H_2 wavelengths are therefore a major source of systematic uncertainty.

2. Kinematic effects. Levshakov et al. (2002a) claim to observe a gradual shift in $z_{\rm abs}$ for absorption lines arising from progressively higher (excited state) rotational levels, J. They point out that small absorption line velocity shifts with increasing J are claimed to have been observed towards ζ Orionis A by Jenkins & Peimbert (1997). The observed velocities of $J = 0$ and $J = 3$ transitions appear to differ by $\Delta v \approx 0.8\,{\rm kms}^{-1}$. This effect is not observed towards other Orion belt stars (Jenkins et al. 2000). Jenkins & Peimbert (1997) propose that the absorption lines of different J states are formed in different zones of post-shock gas to explain their observation. Similar velocity shifts in DLAs could lead to a systematic error of magnitude $\Delta\mu/\mu \sim 4 \times 10^{-5}$.

The above measurements of $\Delta\mu/\mu$ in high-z H_2 absorption systems can be significantly improved with improved laboratory H_2 wavelengths and by significantly increasing the number of absorption systems analysed. The latter is problematic because only 5 (plus 2 tentative) such absorption systems are currently known (Table 5.2). Also, all current works have fitted all H_2 lines independently and derived $\Delta\mu/\mu$ from a linear regression analysis. Clearly, a more robust technique would be to fit all lines simultaneously, thereby reducing the number of free parameters. $\Delta\mu/\mu$ could then be introduced as a free parameter in the fit, just as for $\Delta\alpha/\alpha$ in Chapter 3.

5-7 Comparing $\Delta\alpha/\alpha$, $\Delta y/y$, $\Delta x/x$ and $\Delta\mu/\mu$

The above constraints on $\Delta y/y$ and $\Delta x/x$ can only be compared with our MM constraints on $\Delta\alpha/\alpha$ if one assumes the constancy of g_p and g_p/μ respectively. If one suspects variation in α then it seems wholly unjustified to assume the constancy of other fundamental parameters like g_p and μ. In Fig. 5.3 we plot all the current constraints on $\Delta\alpha/\alpha$, $\Delta y/y$ and $\Delta x/x$ on the same vertical scale. Note that we do

Table 5.2. Summary of H_2 absorption detections. We list the QSO B1950 name, the absorption redshift, $z_{\rm abs}$, the measured H_2 column density, $N(H_2)$, the H I column density, the iron-hydrogen abundance ratio (compared to solar values), [Fe/H], and the metallicity, Z, of the absorber[a]. Detections for 0841+1256 and 0000−2613 are tentative because few H_2 lines are detected, primarily due to heavy blending of other lines with Ly-α forest absorption. Note that these 2 systems will not be useful for measuring $\Delta\mu/\mu$.

QSO	$z^b_{\rm abs}$	$\log N(H_2)$	$\log N(\mathrm{H\,I})$	[Fe/H]	Z[a]	Notes
0551−366	1.9622[c]	17.41 ± 0.70[1]	20.50 ± 0.08[1]	-0.96 ± 0.09[1]	-0.13 ± 0.09[1]	
0013−004	1.9731[d]	18.9 ± 1.1[2]	20.83 ± 0.05[2]	-1.52 ± 0.07[2]	-0.74 ± 0.07[2]	
1232+0815	2.3377[e]	16.78 ± 0.10[3]	20.90 ± 0.10[3]	-1.90 ± 0.13[3]	-1.20 ± 0.20[3]	
0841+1256	2.3742[f]	14.56 ± 0.10[4]	20.95 ± 0.09[5]	-1.777 ± 0.092[5]	-1.51 ± 0.10[5]	Only 2 H_2 lines
0528+2505	2.8114[g]	16.77 ± 0.09[6]	21.35 ± 0.10[4]	-1.41 ± 0.13[6]	-0.91 ± 0.12[7]	
0347−3819	3.0249[h]	14.61 ± 0.02[8]	20.626 ± 0.005[5]	-1.623 ± 0.008[5]	-1.17 ± 0.027[5]	
0000−2613	3.3901[i]	13.94 ± 0.06[9]	21.41 ± 0.08[7]	-2.160 ± 0.086[10,5]	-2.07 ± 0.10[11]	Only 1 H_2 line

[a][Si/H] for 1232+0815 and 0347−3819, [Zn/H] otherwise; [b]References c–i are to the first H_2 discovery papers; [c]Ledoux et al. (2002); [d]Ge & Bechtold (1997); [e]Ge & Bechtold (1999); Ge et al. (2001); [f]Petitjean et al. (2000); [g]Foltz et al. (1988); [h]Levshakov et al. (2002b); [i]Levshakov et al. (2000); [1]Ledoux et al. (2002); [2]Petitjean et al. (2002); [3]Srianand et al. (2000); [4]Petitjean et al. (2000); [5]Prochaska et al. (2001, values from online database, 9th Oct. 2002); [6]Srianand & Petitjean (1998); [7]Lu et al. (1996); [8]Levshakov et al. (2002b); [9]Levshakov et al. (2000); [10]Molaro et al. (2001); [11]Molaro et al. (2000);

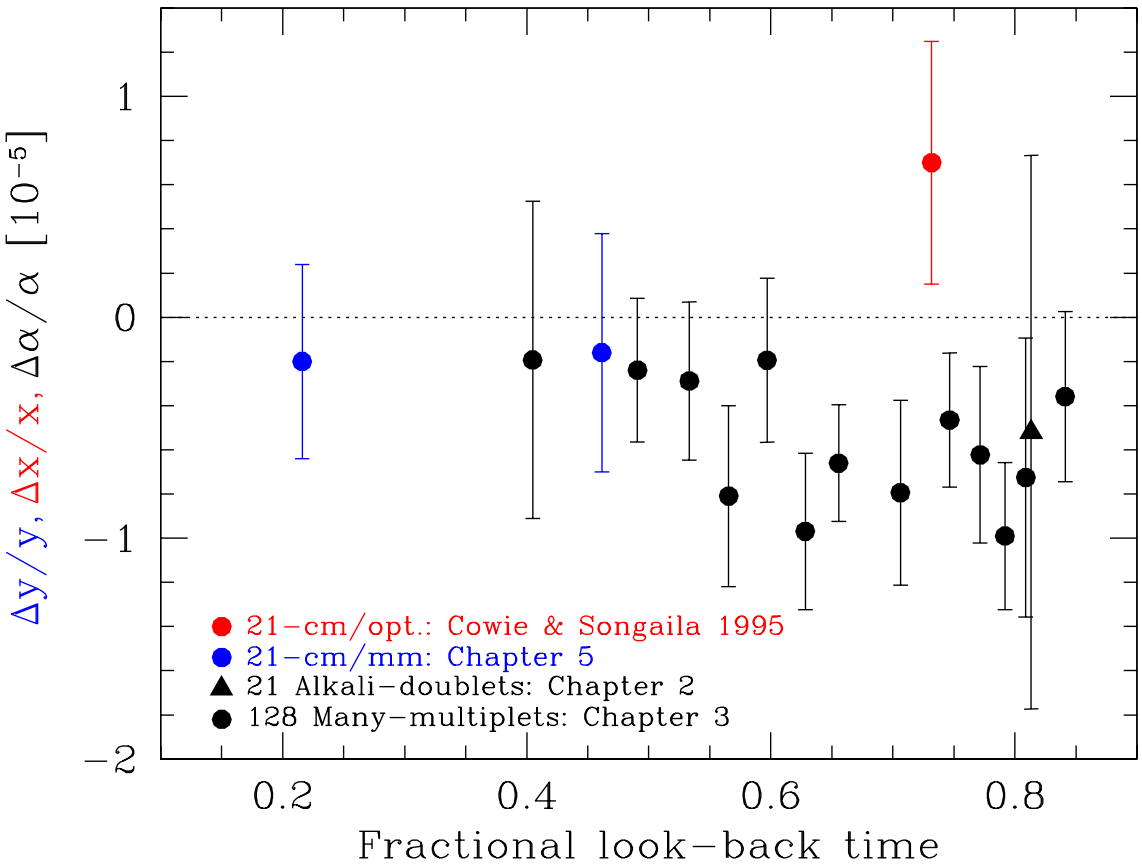

Figure 5.3. Summary of absorption line constraints on $\Delta\alpha/\alpha$, $\Delta y/y$ and $\Delta x/x$. Note that we do not convert the constraints on $\Delta y/y$ and $\Delta x/x$ to constraints on $\Delta\alpha/\alpha$ by assuming constant g_p and g_p/μ. All points are plotted with $1\,\sigma$ error bars.

not convert the constraints on $\Delta y/y$ and $\Delta x/x$ to constraints on $\Delta\alpha/\alpha$ by assuming constant g_p and μ.

Also, as described above, the current measurements of $\Delta y/y$ and $\Delta x/x$ may be strongly influenced by line-of-sight velocity differences between the mm/optical and H I 21-cm absorption lines. Systematic errors of this sort are currently poorly constrained. A significant increase in the sample sizes is clearly required. Also, using VLBI to select background QSOs with compact radio continuum emission (i.e. with the radio lobes oriented along the line-of-sight) will greatly reduce this systematic error.

Note that comparing the weighted mean $\Delta\alpha/\alpha$ from the MM results (equation 3.10) and the Cowie & Songaila (1995) estimate of $\Delta x/x$ allows us to constrain vari-

ations in $w \equiv g_p m_e/m_p = g_p/\mu$: $\Delta w/w = (1.8 \pm 0.6) \times 10^{-5}$ ($1\,\sigma$ error). Although this formally has a $3.2\,\sigma$ significance, the possibility of line-of-sight velocity differences between the optical and H I absorbing regions significantly reduces confidence in this result.

Some *model dependent* links between $\Delta\alpha/\alpha$, $\Delta x/x$, $\Delta y/y$ and $\Delta\mu/\mu$ have been studied recently. Within the paradigm of grand unification, one may expect variations in α to be a manifestation of variations in the strong coupling scale, $\Lambda_{\rm QCD}$, at high energies. This should in turn lead to variations in α_s (e.g. Dent & Fairbairn 2003), nucleon masses (e.g. Calmet & Fritzsch 2002), quark masses and the Higgs vacuum expectation value (e.g. Langacker et al. 2002). In particular, Langacker et al. (2002) claim that $\Delta x/x \sim -32\,\Delta\alpha/\alpha$ and $\Delta\mu/\mu \sim 34\,\Delta\alpha/\alpha$ and Calmet & Fritzsch (2002) claim that $\Delta y/y \sim -121\,\Delta\alpha/\alpha$ (but see discussion in Dent & Fairbairn 2003) should be expected. These relations are clearly not consistent with the values plotted in Fig. 5.3. Langacker et al. (2002) stresses that the observations should be used to constrain the theory and not *vice versa*.

One man's constant is another man's variable.

Alan J. Perlis (1922–1990)

Chapter 6

Conclusions

6-1 Summary

In this thesis we exploited QSO absorption lines to place stringent constraints on possible variations in several fundamental constants. We used the alkali doublet (AD) and many-multiplet (MM) methods to analyse a large number of high quality Keck/HIRES spectra, kindly provided in reduced form by C. W. Churchill, J. X. Prochaska & A. M. Wolfe and W. L. W. Sargent. These data led to our main result: possible evidence for a variable fine-structure constant, α. We have also constrained variations in $\alpha^2 g_p$ (for g_p the proton g-factor) by comparison of H I 21-cm (provided by C. L. Carilli) and rotational molecular (provided by F. Combes & T. Wiklind) absorption spectra of two absorption systems. Below we summarize the main results of these analyses.

1. In Chapter 2 we applied the AD technique to Keck/HIRES spectra of 8 QSOs which contained 21 Si IV $\lambda\lambda$1393/1402 doublet absorption systems over the redshift range $2.0 < z_{\rm abs} < 3.1$. We find a weighted mean value of $\Delta\alpha/\alpha \equiv (\alpha_z - \alpha_0)/\alpha_0 = (-0.5 \pm 1.3) \times 10^{-5}$ which is currently the tightest constraint on possible variations in α derived from the AD method. The factor of 3.3 increase in precision over the results of Varshalovich et al. (2000) is due to increased data

quality (i.e. spectral resolution and S/N).

2. Previous AD analyses were limited by uncertainties in the laboratory values of the Si IV transition wavelengths (Table 2.1). We used the new laboratory measurements of Griesmann & Kling (2000) which reduces this uncertainty by nearly two orders of magnitude to $\delta(\Delta\alpha/\alpha) \lesssim 0.2 \times 10^{-5}$. We thoroughly explored other possible systematic effects in the AD method (Section 4-14), finding that differential isotopic saturation is the main potential effect (Section 4-14.3). Five of the 21 absorption systems were significantly affected. We used theoretical estimates of the Si IV $\lambda\lambda$1393 and 1402 isotopic structures (Safronova & Johnson 2001) to quantify the effect on $\Delta\alpha/\alpha$ in these cases. Overall, $\Delta\alpha/\alpha$ decreases to $\Delta\alpha/\alpha = (-0.8 \pm 1.3) \times 10^{-5}$ once this effect is taken into account.

3. In Chapter 3 we applied the recently introduced MM method to three large, independent Keck/HIRES samples of QSO spectra. In total, 128 absorption systems covered the redshift range $0.2 < z_{\rm abs} < 3.7$. The first application of the MM method by Webb et al. (1999) concentrated on low-z (i.e. $z_{\rm abs} < 1.8$) Mg/Fe II absorption systems and our new analysis contains 74 such systems. However, we have extended the MM method to higher z where many different species (Al II, Al II, Si II, Cr II, Fe II, Ni II and Zn II) contribute transitions with a diverse range of q coefficients (Fig. 3.3). This diversity strengthens the MM method against systematic effects at high z.

4. The total sample of 128 absorption systems gives a weighted mean $\Delta\alpha/\alpha = (-0.574 \pm 0.102) \times 10^{-5}$. This represents $5.6\,\sigma$ statistical evidence for a smaller α in the QSO absorption clouds. All 3 samples separately yield consistent and significant non-zero values of $\Delta\alpha/\alpha$. The low- and high-z samples also give consistent values despite being based on very different transitions with a very different arrangement of q coefficients.

5. One advantage of studying QSO absorption lines is the large look-back times involved, allowing constraints on slow cosmological evolution of the constants. If one assumes that $\Delta\alpha/\alpha = 0$ at $z_{\rm abs} = 0$ then our new measurements of $\Delta\alpha/\alpha$

yield a best fitting value of $\dot{\alpha}/\alpha = (6.41 \pm 1.12) \times 10^{-16}\,\mathrm{yr}^{-1}$. Although the constant $\dot{\alpha}/\alpha$ model is preferred over the constant $\Delta\alpha/\alpha$ model, this is currently only at the 55% confidence level. A larger number of absorption systems is required to properly distinguish these two simple possibilities.

6. The distribution of QSO sight-lines over the sky also allows a search for angular variations. We find no evidence for significant dipolar variations in our values of $\Delta\alpha/\alpha$ (Section 3-5.4). However, all the absorption systems we study were observed on a northern telescope and so $\Delta\alpha/\alpha$ is unconstrained over a large portion of the sky. This significantly reduces our sensitivity to angular variations (Fig. 3.11). A large sample observed towards southern (i.e. DEC $< -20°$) QSOs would be desirable for reliable constraint on such variations.

7. The absorption systems studied are distributed over large cosmological distances and can be used to search for spatial correlations in the value of α (Section 3-5.5). The two-point correlation function for α (equation 3.13) reveals no evidence for significant correlations over comoving separations $\approx$0.2–13 Gpc (Fig. 3.12).

8. The above results are consistent with a varying α. Such an astounding conclusion requires a thorough investigation of possible systematic effects which could mimic a significantly non-zero $\Delta\alpha/\alpha$. In Chapter 4 we examined a wide range of possibilities of both instrumental and astrophysical origin. Using general arguments and/or simple analyses, we ruled out the following potential sources of systematic effects: laboratory wavelength errors, heliocentric velocity variations and errors, kinematic effects, magnetic fields, air-vacuum wavelength conversion errors, line blending, spectrograph temperature variations and hyperfine structure effects.

9. Possible wavelength calibration errors need more careful consideration. We designed a test of the thorium–argon (ThAr) calibration spectra: for each QSO absorption system, we selected several sets of ThAr emission lines corresponding to the observed wavelengths of the relevant MM transitions. The ThAr lines were then analysed with the MM method by assigning to each ThAr line the q

coefficient of the corresponding MM transition (Fig. 4.2). The weighted mean value of $(\Delta\alpha/\alpha)_{\rm ThAr} = (0.4 \pm 0.8) \times 10^{-7}$ and the distribution of $(\Delta\alpha/\alpha)_{\rm ThAr}$ (Fig. 4.3) explicitly demonstrate the reliability of the wavelength scale to a precision two orders of magnitude below our observed effect. This result also rules out large errors due to instrumental profile (IP) variations and asymmetries.

10. Detailed modelling reveals the potential importance of atmospheric dispersion effects, particularly for the low-z Mg/Fe II systems. In total, 77 systems were observed before an image rotator was installed on Keck/HIRES and so may be affected. However, comparison between the affected and unaffected systems (Fig. 4.8) reveals no evidence for such effects. Furthermore, our models predict a strong correlation between $\Delta\alpha/\alpha$ and the zenith angle of the QSO observations (Fig. 4.10) and this correlation is not observed in the QSO data (Fig. 4.7). This confirms the lack of evidence for atmospheric dispersion effects.

11. The isotopic structures of the MM transitions could also lead to systematic effects. The most important effect is due to possible isotopic abundance variations. We included in our Voigt profile fits the measured Mg isotopic structures and our estimates for those of the Si transitions. Measurements of Mg and theoretical estimates for Si in stars strongly suggest an under-abundance of the weak ^{25,26}Mg and ^{29,30}Si isotopes in QSO absorption systems which have sub-solar metallicity. We found that fitting only the strong isotopes of Mg and Si leads to *more negative* values of $\Delta\alpha/\alpha$, predominantly in the low-z systems where Mg is important (Fig. 4.5). We also found that differential isotopic saturation in the Mg and Si transitions could only lead to small shifts in $\Delta\alpha/\alpha$. Although the isotopic structures for transitions of other species are not known, the above results place an upper limit on similar effects in those species since the total isotopic shifts should be smaller than those in Mg and Si.

12. One advantage of the MM method is that, in most absorption systems, one may remove single transitions or species from the Voigt profile fits and still obtain well-constrained values of $\Delta\alpha/\alpha$. Removing lines in this way directly constrains

systematic errors, possibly with unknown origin, associated with single transitions or species. We conducted such a line-removal test in Section 4-12.1, identifying no 'suspect' transitions or species in our analysis. This rules out large laboratory wavelength errors and effects due to the unknown isotopic and hyperfine structures for species other than Mg and Si.

13. Two other line-removal tests were designed to search for simple distortions of the wavelength scale (e.g. an overall compression) in the high-z systems. The first uses several different combinations of transitions in each absorption system, selected to give a systematically negative $\Delta\alpha/\alpha$ if a compression exists (Section 4-12.2). The second test groups transitions according to the sign and magnitude of q. Simulations of the absorption systems in our sample demonstrate the potential of these tests for identifying simple systematics in the QSO spectra (Figs. 4.14–4.15 & 4.17–4.19). However, the high-z values of $\Delta\alpha/\alpha$ are possibly prone to additional scatter (Section 3-5.2) and this may preclude firm conclusions from these tests.

14. In Chapter 5 we obtained constraints on $y \equiv \alpha^2 g_p$ in two low redshift absorbers, $z_{\rm abs} = 0.2467$ towards PKS 1413+135 (Fig. 5.2) and $z_{\rm abs} = 0.6847$ towards TXS 0218+357 (Fig. 5.1). We improved previous analyses by fitting Voigt profiles to the H I 21-cm *and* the mm-band molecular rotational transitions, yielding the most stringent absorption line constraints on $\Delta y/y \equiv (y_z - y_0)/y_0$ to date: $\Delta y/y = (-0.20 \pm 0.44) \times 10^{-5}$ at $z_{\rm abs} = 0.2467$ and $\Delta y/y = (-0.16 \pm 0.54) \times 10^{-5}$ at $z_{\rm abs} = 0.6847$. The $1\,\sigma$ errors are dominated by the Drinkwater et al. (1998) estimate of potential line-of-sight velocity differences between the H I 21-cm and mm absorbing regions, $|\Delta v| \approx 1.2\,{\rm kms}^{-1}$. A larger sample of mm/H I 21-cm comparisons is required to properly quantify this uncertainty and to provide an important cross-check on the optical MM results.

6-2 Comparing local and QSO absorption line constraints on $\Delta\alpha/\alpha$

The optical MM results above provide strong statistical evidence for a varying α. We have found no systematic errors that can explain this result. It is clearly desirable to find independent constraints on α-variation.

In Section 5-7 we commented on the difficulty in reliably comparing the MM constraints on $\Delta\alpha/\alpha$ with our two constraints on $\Delta y/y$ and the single strong constraint on $\Delta x/x$ from Cowie & Songaila (1995). Several very strong 'local' constraints on $\Delta\alpha/\alpha$ were described in Section 1-4.1 and we compare these with the QSO absorption line constraints in Fig. 6.1. Note that only the AD and MM QSO absorption line methods constrain $\Delta\alpha/\alpha$ directly. In contrast to Fig. 5.3, we convert the absorption line constraints on $\Delta y/y$ and $\Delta x/x$ to constraints on $\Delta\alpha/\alpha$ by assuming constant g_p and g_p/μ respectively. The Sortais et al. (2001) atomic clock constraint (see Section 1-4.1.1) also assumes a constant g_p. Finally, as discussed in Sections 1-4.1.3 and 1-4.1.2, the meteoritic β-decay (Olive et al. 2002) and Oklo neutron capture (Fujii et al. 2000) constraints have an unexplored dependence on several fundamental parameters besides α. Thus, drawing comparisons between our AD and MM constraints on $\Delta\alpha/\alpha$ and other constraints is very difficult.

Interpreting Fig. 6.1 is further complicated by the possibility of spatial variations in α. Although we find no evidence of spatial correlations in our MM values of α, significant correlations may still exist on scales as large as galaxy clusters (i.e. $\lesssim 200\,\mathrm{Mpc}$). Bekenstein (1979) and Barrow & O'Toole (2001) also caution that comparing values of $\Delta\alpha/\alpha$ in areas of different gravitational potential is dangerous without a detailed theory of both time *and* space variations of α. Therefore, the local and QSO absorption line constraints can not be reliably compared.

In Summary, the MM evidence for varying α is not ruled out by other known constraints.

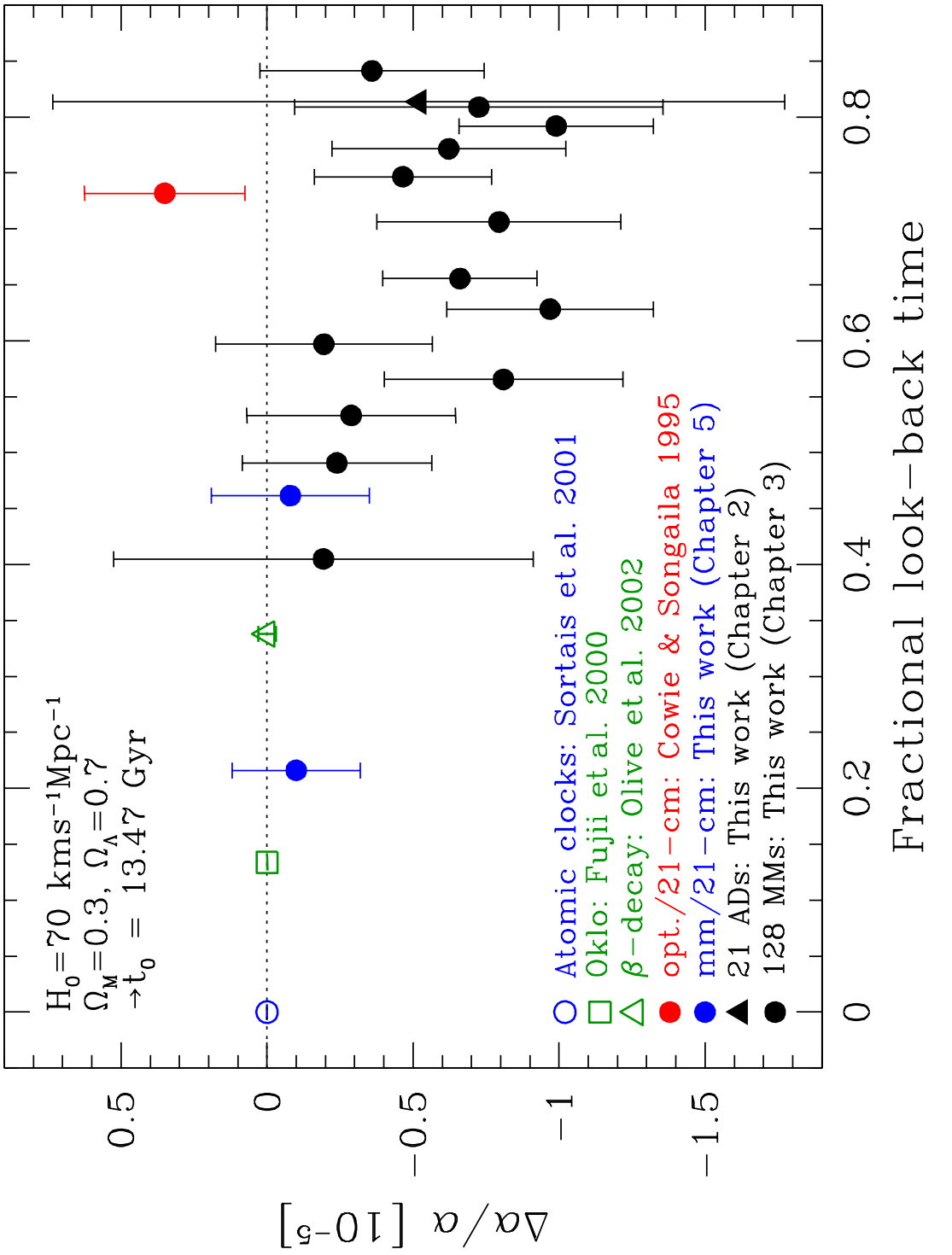

Figure 6.1. Comparing local (open symbols) and QSO absorption (solid symbols) constraints on $\Delta\alpha/\alpha$. Only the black symbols (AD and MM QSO absorption line methods) constrain $\Delta\alpha/\alpha$ directly. Blue symbols assume a constant g_p, the red optical/H I constraint assumes constant g_p/μ and the green symbols have a complicated and unexplored dependence on several other fundamental parameters.

6-3 Future work

Considering the above summary, the only current avenue for confidently ruling out the present evidence for varying α is to obtain *independent MM constraints from QSO spectra*. All the optical QSO spectra contributing to our possible detection of varying-α were observed with the one telescope and spectrograph. The present work has shown that no known systematic errors can mimic the effect of varying α in the Keck/HIRES spectra. However, if subtle, unknown instrumental effects cause the line-shifts we observe, the high quality spectra now available from the VLT/UVES and soon-to-be available from Subaru/HDS will bear this out. If the present results are confirmed, iodine cell calibration techniques, similar to those used to identify extra-solar planets (e.g. Marcy & Butler 1992), could be applied to selected absorption systems to confidently rule out instrumental effects.

If the MM results are correct and α really does vary, obtaining a statistical sample of mm/H I measurements of $\Delta y/y$ may provide a more precise probe. Currently, the paucity of mm absorbers (see Section 5-2) limits progress in this direction. This motivates a systematic search for new mm absorbers (Curran et al. 2002a,b, 2003a; Murphy et al. 2003b). A statistical sample of optical/H I constraints on $\Delta x/x$ would also be crucial and, by comparison with MM constraints on $\Delta\alpha/\alpha$, may lead to stringent constraints on $\Delta\mu/\mu$, independent of those obtained from H_2 absorption (e.g. Ivanchik et al. 2002, 2003, see Section 5-6).

Appendix A

Voigt profile fitting

A-1 The Voigt profile

Consider a single absorption cloud occulting a background QSO which presents an unabsorbed continuum intensity, $I_0(\nu)$, to the cloud. If the absorbed continuum, $I(\nu)$, is observed with a spectrograph which has an instrumental profile (IP) defined by $\Phi(\delta\nu)$ then the measured spectrum is the convolution of the intrinsic spectrum and the IP,

$$I(\nu) = \Phi(\delta\nu) \otimes I_0(\nu) \exp\left[-\tau(\nu)\right] , \tag{A.1}$$

where $\tau(\nu)$ is the optical depth of absorption due to the intervening gas. The optical depth is related to the line-of-sight integrated column density of absorbing particles, $N = \int n(l)\, dl\, \mathrm{cm}^{-2}$, and the atomic absorption co-efficient, $\kappa(\nu)$, by

$$\tau(\nu) = N\kappa(\nu) . \tag{A.2}$$

If we consider absorption due to a transition of frequency ν_0 in the rest frame of the cloud then, under the assumption that the absorption coefficient does not depend on the position in the cloud, we may write

$$\kappa(\nu) = \frac{\sqrt{\pi}\, e^2}{m_e c} \frac{f H(a,u)}{\Delta\nu_b} , \tag{A.3}$$

where f is the oscillator strength of the transition and $\Delta\nu_b$ is the Doppler width which is related to the velocity dispersion parameter of the absorbing particles by

$$b = c\,\frac{\Delta\nu_b}{\nu_0}\,. \tag{A.4}$$

The b-parameter may have both thermal and turbulent contributions (Struve & Elvey 1934), as discussed in Section 3-4 (see equation 3.9).

$H(a,u)$ is the Voigt function evaluated at $a = \Gamma/4\pi\Delta\nu_b$ and $u = (\nu - \nu_0)/\Delta\nu_b$ where Γ is the transition damping constant[1]. The Voigt function is the convolution of Lorentzian and Gaussian profiles. The former represents the natural line profile of an electronic transition. The Gaussian part of the Voigt profile assumes that the absorbing particles follow a Maxwellian velocity distribution. The Voigt function is defined as

$$H(a,u) = \frac{a}{\pi}\int_{-\infty}^{+\infty}\frac{\exp(-y^2)}{a^2+(u-y)^2}\,dy \tag{A.5}$$

which is the real part of the Faddeeva (or complex probability) function, $F(w)$, of the complex variable $w = u + ia$,

$$F(w) = \frac{i}{\pi}\int_{-\infty}^{+\infty}\frac{\exp(-t^2)}{w-t}\,dt = \exp(-w^2)\,\mathrm{erfc}(-iw) = H(a,u) + iJ(a,u)\,. \tag{A.6}$$

Computing the Voigt function is non-trivial and an extensive literature focuses both on the accuracy and speed of various numerical algorithms and computer codes. See Wells (1999) for a short review. See also the tabulations of Finn & Mugglestone (1965) and Hummer (1965). The fastest approximations use look-up tables for the Taylor series expansion coefficients of $H(a,u)$ (Harris 1948):

$$\begin{aligned} H(a,u) &= H_0(u) + aH_1(u) + a^2H_2(u) + a^3H_3(u) + a^4H_4(u) + \ldots \text{ for} \quad \text{(A.7)}\\ H_0(u) &= \exp(-u^2)\,,\\ H_1(u) &= -\frac{2}{\sqrt{\pi}}\left[1 - 2uE(u)\right]\,,\\ H_2(u) &= (1-2u^2)\exp(-u^2)\,, \end{aligned} \tag{A.8}$$

[1]If the transition is from the ground electronic state, $\Gamma = \sum_{j=1}^{k} A_{kj}$, where k refers to the upper level and A_{kj} is the Einstein coefficient for spontaneous emission. If the lower level is also an excited state, $\Gamma = \sum_{i=1}^{l}\Gamma_{li} + \sum_{i=1}^{u}\Gamma_{ui}$.

$$
\begin{aligned}
H_3(u) &= -\frac{2}{\sqrt{\pi}}\left[\frac{2}{3}(1-u^2) - 2u(1-\frac{2}{3}u^2)E(u)\right] \quad \text{and,} \\
H_4(u) &= (\frac{1}{2} - 2u^2 + \frac{2}{3}u^4)\exp(-u^2)\,, \quad \text{where} \\
E(u) &= \exp(-u^2)\int_0^u \exp(t^2)\,dt\,. \qquad \text{(A.9)}
\end{aligned}
$$

Another algorithm popular in the astronomical literature (e.g. Churchill & Vogt 2001) is the Cpf12 code of Humlíček (1979)[2]. These series techniques are limited in precision and strong cancellations in the series require several guarding decimal places to be used. Monaghan (1971) advanced a slow algorithm based on differential equations which, in principle, allows calculation of $H(a,u)$ to arbitrary precision.

Fig. A.1 compares the precision of these various techniques for calculating $H(a,u)$. Two algorithms based on the series technique of Harris (1948) are plotted: the H1 curve (black) is calculated using only the H_0, H_1 and H_2 coefficients in equations A.8 whereas the higher order coefficients, H_3 and H_4, are included in the calculation for the H2 curve (red). The Humlíček (1979) Cpf12 algorithm is represented by the blue curve. We plot the fractional deviation from the fiducial value of $H(a,u)$, $|\delta H/H|$, as a function of u for several values of a. The fiducial values were produced using the Monaghan (1971) algorithm and should be correct to 16 significant figures[3].

Clearly, the H2 and Humlíček routines give vastly superior precision over the H1 routine. However, the H1 routine is faster than the other methods: the speeds for the different routines are in the ratio H1 : H2 : Humlíček : Monaghan = 1 : 2.2 : 3.8 : 35.5. VPFIT uses the H1 algorithm to generate the Voigt function. In the simulations in Section A-3 we use the Monaghan algorithm to produce synthetic spectra and fit these with VPFIT. We find no evidence for residual errors in $\Delta\alpha/\alpha$ due to errors in the Voigt function calculation. Of course, the Voigt function is symmetric and so errors in $H(a,u)$ should only lead to errors in column densities and b-parameters rather than line positions.

[2] Humlíček (1982) later advanced the W4 algorithm, which had improved accuracy but was slower, particularly when a was not constant (e.g. in cases where several different transitions are considered).

[3] Poppe & Wijers (1990) have produced high precision calculations of $H(a,u)$ which allows one to check the accuracy of other algorithms. Some values are even quoted to 25 significant figures.

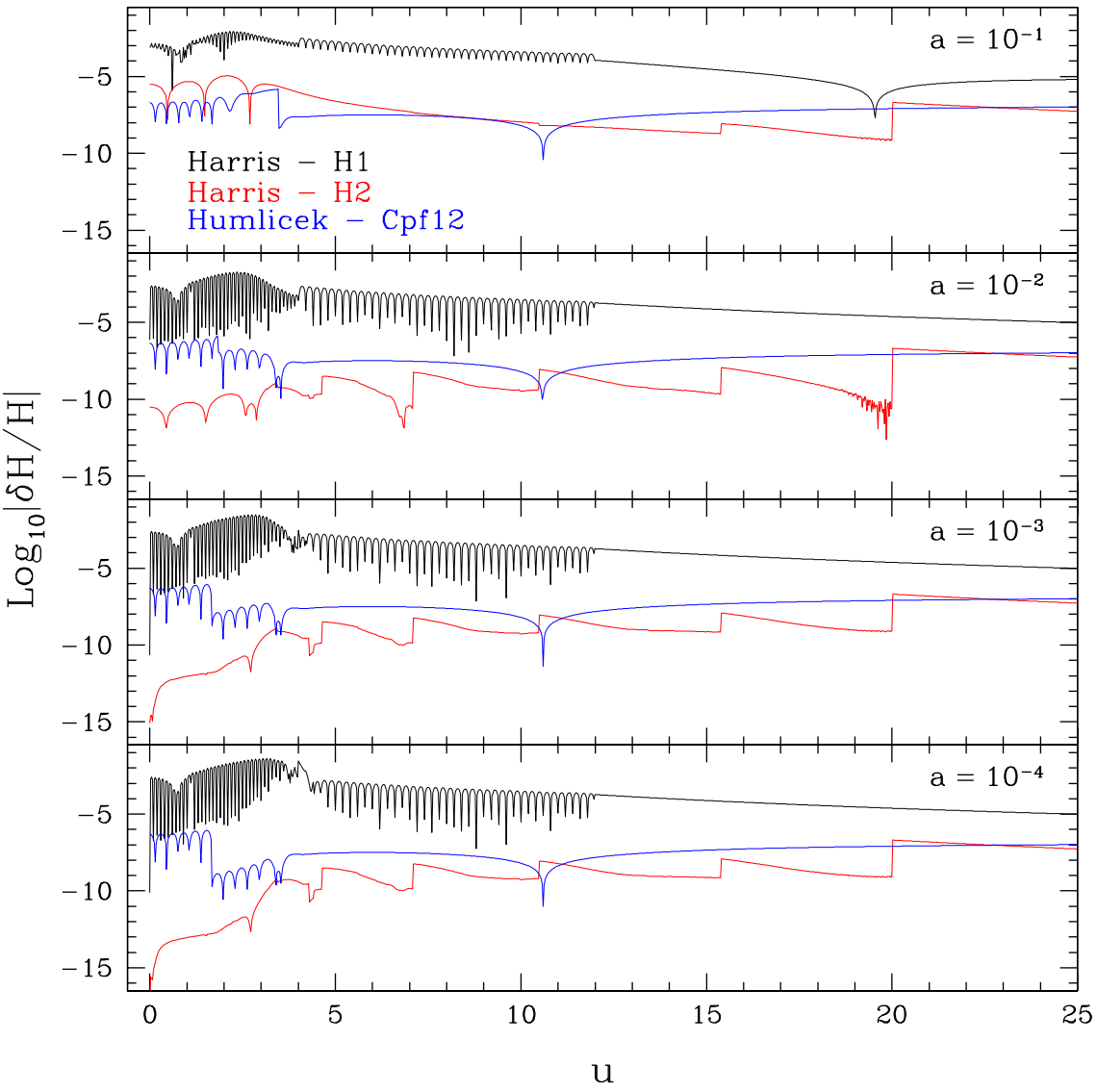

Figure A.1. Comparison of the relative precision, $|\delta H/H|$, for various algorithms commonly used to calculate the Voigt function, $H(a, u)$. The H1 algorithm is that of Harris (1948) using only the H_0, H_1 and H_2 expansion coefficients in equations A.8 whereas the H2 algorithm uses the H_3 and H_4 coefficients as well. The Cpf12 algorithm of Humlíček (1979) is also shown. The fiducial values of $H(a, u)$ were produced using the Monaghan (1971) algorithm and should be correct to 16 significant figures. The seemingly erratic structure of the Harris curves is due to the interpolation techniques employed when considering values of u not explicitly given in the look-up tables. Several different regimes of approximation are used in the Humlíček code, again leading to a rather erratic curve.

A-2 Theory behind VPFIT

VPFIT minimizes χ^2 in an iterative procedure using Gauss–Newton type (i.e. equation A.14) parameter updates. The genral theory of such techniques is set out in Gill et al. (1981). Using a general notation, we wish to minimize a 'goodness-of-fit' function $F(\mathbf{x})$ of the set of parameters $\mathbf{x}$ (in our case $\mathbf{x} = (N, b, z, \Delta\alpha/\alpha)^{\mathrm{T}}$),

$$F(\mathbf{x}) = \frac{1}{2}\sum_i \frac{[I(\mathbf{x})_i - d_i]^2}{\sigma_i^2} \tag{A.10}$$

$$\equiv \frac{1}{2}\sum_i f(\mathbf{x})_i^2 \tag{A.11}$$

where d_i, σ_i and $I(\mathbf{x})_i$ are the values of the data, $1\,\sigma$ error and model fit respectively at the i^{th} data point. If we are near the solution, $\mathbf{x} = \mathbf{x}^*$, then we may write a Taylor series expansion about the current point k in parameter space,

$$F(\mathbf{x}_k + \mathbf{p}) \simeq F(\mathbf{x}_k) + \mathbf{g}^{\mathrm{T}}(\mathbf{x}_k)\mathbf{p} + \frac{1}{2}\mathbf{p}^{\mathrm{T}}\mathbf{G}(\mathbf{x}_k)\mathbf{p} \tag{A.12}$$

where $\mathbf{p}$ is the predicted parameter unit vector update to minimize $F(\mathbf{x}_k+\mathbf{p})$, $\mathbf{g}(\mathbf{x})$ is the matrix of partial derivatives of F with respect to the parameters $\mathbf{x}$ (the gradient vector) and $\mathbf{G}(\mathbf{x})$ is the matrix of partial second derivatives (the Hessian matrix). To minimize equation A.10 we must estimate $\mathbf{p}$ so as to minimize the function

$$\Phi_k = \mathbf{g}^{\mathrm{T}}(\mathbf{x}_k)\mathbf{p} + \frac{1}{2}\mathbf{p}^{\mathrm{T}}\mathbf{G}(\mathbf{x}_k)\mathbf{p}\,. \tag{A.13}$$

To find a stationary point $\mathbf{p}_k$ of equation A.13 we must solve the system of linear equations given by

$$\gamma\mathbf{G}(\mathbf{x}_k)\mathbf{p}_k = -\mathbf{g}(\mathbf{x}_k) \tag{A.14}$$

for $\gamma = 1$. The factor γ is introduced here since the quadratic model is unlikely to be perfect. Provided that we can find the gradient vector and the Hessian matrix then we can use equation A.14 iteratively to find the best fitting values of the parameters, $\mathbf{x}^*$.

In the context of fitting Voigt profiles to absorption lines, the gradient vector can be calculated most accurately using finite difference first derivatives. It then only remains to find an estimate of the Hessian matrix. We may express the mn^{th}

component of the Hessian matrix as the partial second derivative of $F(\mathbf{x})$ with respect to the $m^{\rm th}$ and $n^{\rm th}$ components of $\mathbf{x}$ (i.e. the $m^{\rm th}$ and $n^{\rm th}$ parameters),

$$\mathbf{G}^{mn}(\mathbf{x}) \equiv \frac{\partial^2 F(\mathbf{x})}{\partial \mathbf{x}^m \partial \mathbf{x}^n} \tag{A.15}$$

$$= \sum_{i=1}^{M} \frac{\partial^2 I(\mathbf{x})_i}{\partial \mathbf{x}^m \partial \mathbf{x}^n} \frac{I(\mathbf{x})_i - d_i}{\sigma_i^2} + \sum_{i=1}^{M} \frac{\partial I(\mathbf{x})_i}{\partial \mathbf{x}^m} \frac{\partial I(\mathbf{x})_i}{\partial \mathbf{x}^n} \frac{1}{\sigma_i^2} \tag{A.16}$$

$$= \mathbf{Q}^{mn}(\mathbf{x}) + \mathbf{R}^{mn}(\mathbf{x}) \,, \tag{A.17}$$

where M is the number of data points and $\mathbf{R}(\mathbf{x}) \equiv \mathbf{J}^{\rm T}(\mathbf{x})\mathbf{J}(\mathbf{x})$ for $\mathbf{J}(\mathbf{x})$ the Jacobian matrix of $f(\mathbf{x})$. If we are close to the solution $\mathbf{x}^*$ then we expect $\sum_i f(\mathbf{x})_i \to 0$ as $M \to \infty$. Also, each $f(\mathbf{x})_i$ can be considered as an independent random variable with $\langle f(\mathbf{x})_i \rangle = 0$. Thus, we expect that $G(\mathbf{x})$ will be dominated by the second order term in equation A.16 (and equation A.17):

$$\mathbf{G}^{mn}(\mathbf{x}) \approx \mathbf{R}^{mn}(\mathbf{x}) \,, \tag{A.18}$$

which is positive definite and so we are guaranteed that $F(\mathbf{x}_k + \mathbf{p}) < F(\mathbf{x})$. Equation A.18 can be evaluated directly from the finite difference first derivatives already used to calculate $\mathbf{g}(\mathbf{x})$.

We have therefore set up an iterative algorithm to minimize $F(\mathbf{x})$ through equation A.14 if we can determine the factor γ. For an exact quadratic model in equation A.12, $\gamma = 1$. However, to find the most suitable value at each iteration k of the algorithm, a univariate minimization of $F(\mathbf{x}_k + \gamma\mathbf{p})$ with respect to γ can be performed. The algorithm can be concluded when $F(\mathbf{x}_k + \gamma\mathbf{p}) - F(\mathbf{x}_k) \leq \Delta$ for some set tolerance Δ. The parameter errors can then be found by inverting the Hessian matrix at the solution (Fisher 1958).

A-3 Testing VPFIT with Monte Carlo simulations

We have used Monte Carlo simulations to confirm that the line-shifts observed in the Keck/HIRES QSO spectra in Chapter 3 are not due to errors/bugs in the line-fitting software, VPFIT. Using a Voigt profile generation code, independent of and

different to that used in VPFIT, we constructed synthetic absorption systems at a range of redshifts and with varying degrees of complexity (i.e. different numbers of velocity components). As a simple example, Figs. A.2 and A.3 show the distribution of $\Delta\alpha/\alpha$ values determined from several simulations containing just a single velocity component. We used an instrumental resolution and velocity dispersion per pixel typical of the Keck/HIRES (i.e. FWHM $= 6.6\,\mathrm{kms}^{-1}$ and $\Delta v = 2.0\,\mathrm{kms}^{-1}$) and assumed a turbulent broadening regime with $b = 5\,\mathrm{kms}^{-1}$. The column densities of the different species we chosen to be typical of those found in the real QSO spectra. In all cases we introduced noise into the synthetic spectra such that S/N = 100. The figures show the input value of $\Delta\alpha/\alpha$, the input absorption redshift and the different transitions fitted (identified by the ID letters defined in Table 3.1).

Two very important features should be noted in Figs. A.2 and A.3: (i) the input value of $\Delta\alpha/\alpha$ was reliably extracted from each simulation [i.e. $\langle\Delta(\Delta\alpha/\alpha)\rangle = 0$] and (ii) the rms and mean $1\,\sigma$ error for $\Delta\alpha/\alpha$, $\langle\delta(\Delta\alpha/\alpha)\rangle$, agree. This was also the case for more complex velocity structures and for all combinations of transitions that were tested. Simulations were also conducted using the velocity structures derived from the QSO absorption systems themselves. The results are presented in Fig. 4.13 and it is clear that points (i) and (ii) above apply.

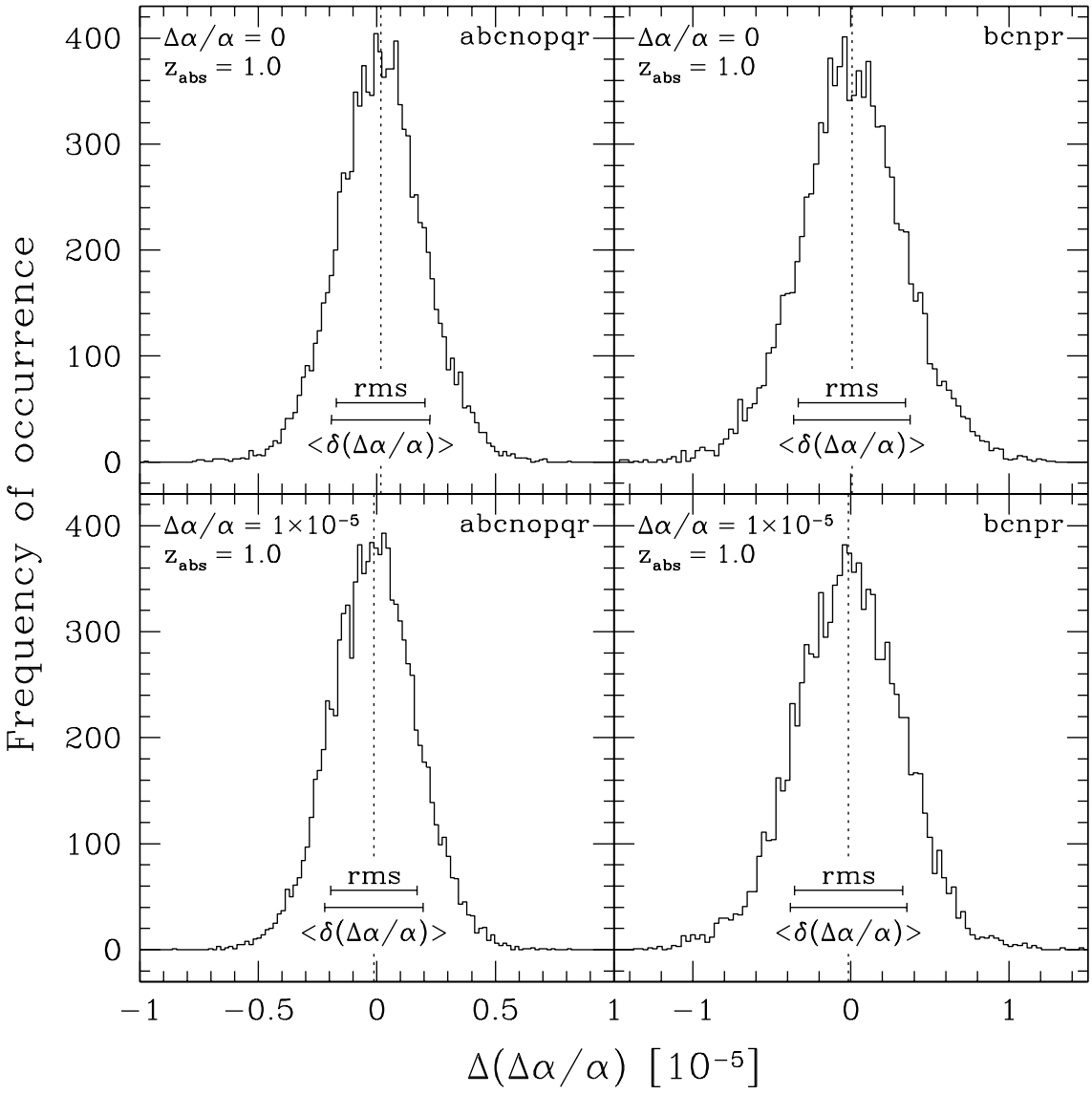

Figure A.2. 10000 Monte Carlo simulations of a single velocity component low-z Mg/Fe II absorption system. The input values of $\Delta\alpha/\alpha$ were $\Delta\alpha/\alpha = 0$ in the upper panels and $\Delta\alpha/\alpha = 1\times10^{-5}$ in the lower panels. The transitions fitted are indicated by the ID letters in the upper right-hand corner of each panel (see Table 3.1). All Mg and Fe II transitions with $\lambda_0 > 2000$ Å were fitted in the left panels whereas only the strong Fe II transitions and the Mg II doublet were used in the right panels. The absorption redshift was $z_{\rm abs} = 1.0$ in all cases. The rms and mean $1\,\sigma$ error for $\Delta\alpha/\alpha$ are indicated by the horizontal error bars.

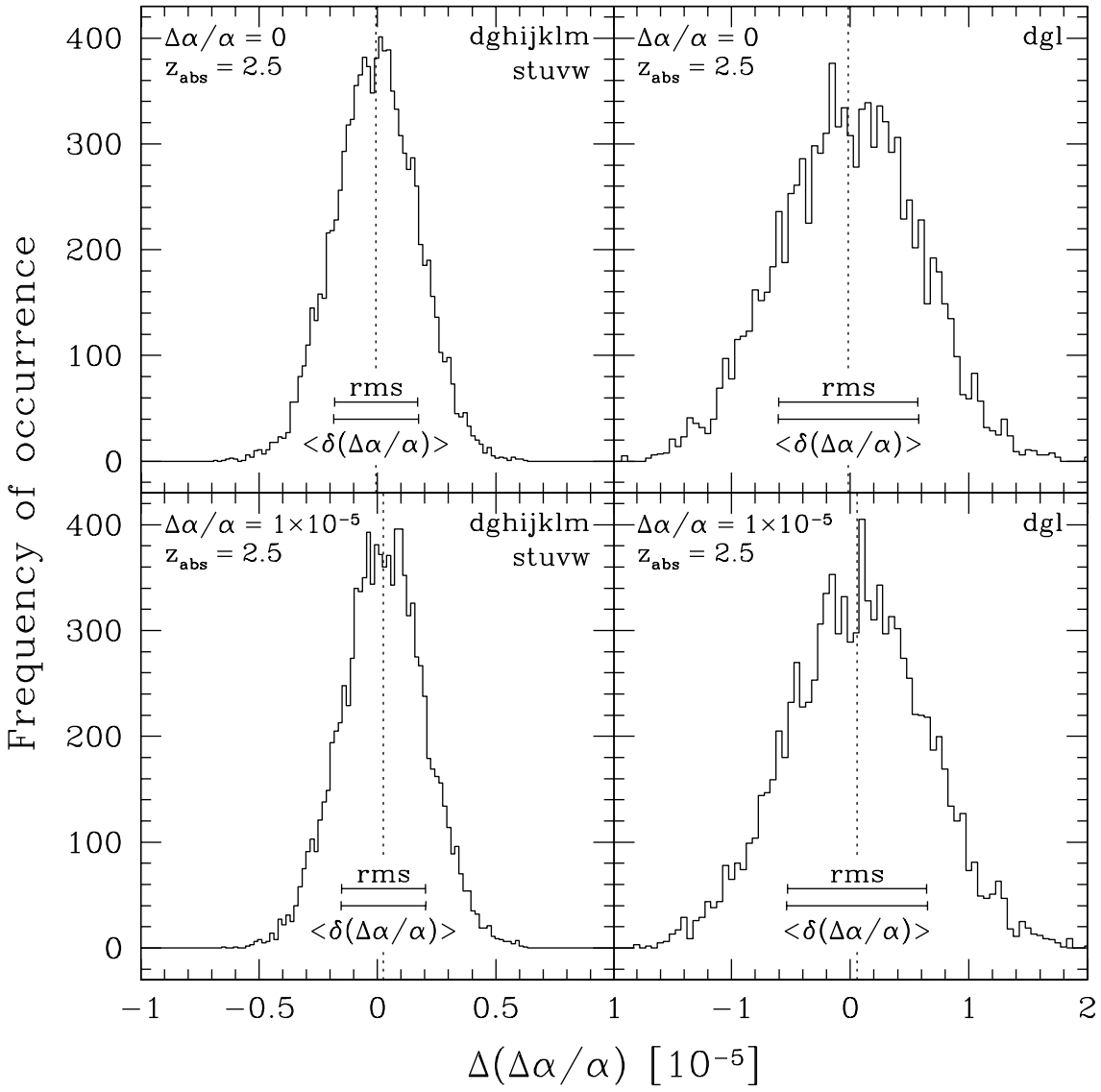

Figure A.3. 10000 Monte Carlo simulations of a single velocity component high-z absorption system. The input values of $\Delta\alpha/\alpha$ were $\Delta\alpha/\alpha = 0$ in the upper panels and $\Delta\alpha/\alpha = 1 \times 10^{-5}$ in the lower panels. The transitions fitted are indicated by the ID letters in the upper right-hand corner of each panel (see Table 3.1). The left panels simulate a DLA and so many different transitions are fitted. The right panels use a lower column density for each species and so we only fit the strong transitions. The absorption redshift was $z_{\rm abs} = 2.5$ in all cases. The rms and mean $1\,\sigma$ error for $\Delta\alpha/\alpha$ are indicated by the horizontal error bars.

Appendix B

Si IV alkali doublet Voigt profile fits

In Figs. B.1–B.23 we plot all 21 Si IV doublet absorption systems used to obtain constraints on $\Delta\alpha/\alpha$ in Chapter 2. For each absorption system we give the B1950 name of the QSO and nominal absorption redshift, $z_{\rm abs}$. We plot the flux, normalized by a fit to the continuum, as a histogram, our Voigt profile fit (solid curve) and the residuals (i.e. [data]−[fit]). The latter are normalized by the $1\,\sigma$ errors (horizontal solid lines). The tick-marks above the continuum indicate the position of individual velocity components. We plot all transitions on a common velocity scale centred at the specified arbitrary redshift. We discuss our methods for fitting random blends in Section 4-9.1 but, for brevity, we do not identify strong random blends here.

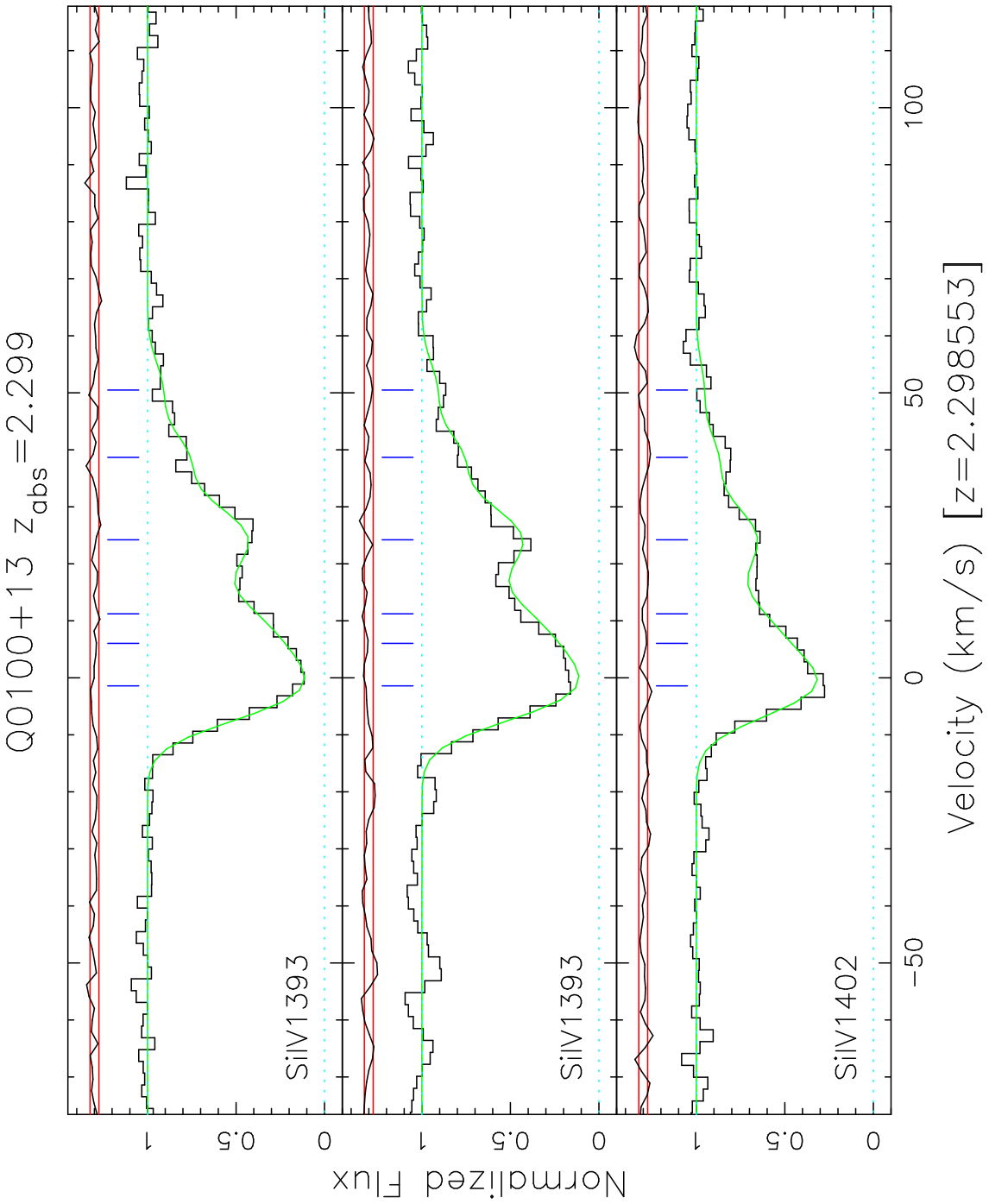

Figure B.1. Q0100+1300, $z_{\rm em} = 2.68$, $z_{\rm abs} = 2.299$.

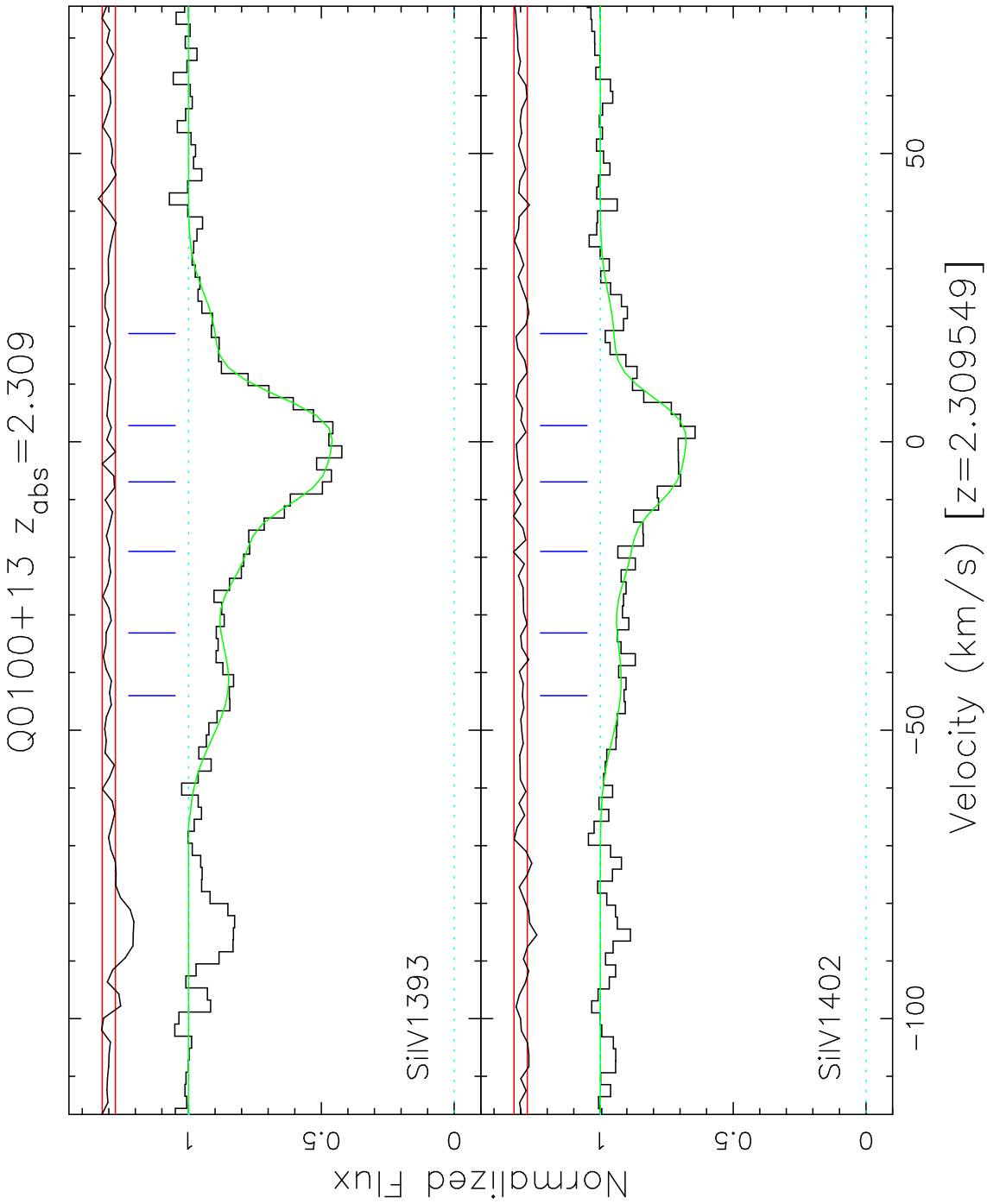

Figure B.2. Q0100+1300, $z_{\rm em} = 2.68$, $z_{\rm abs} = 2.309$.

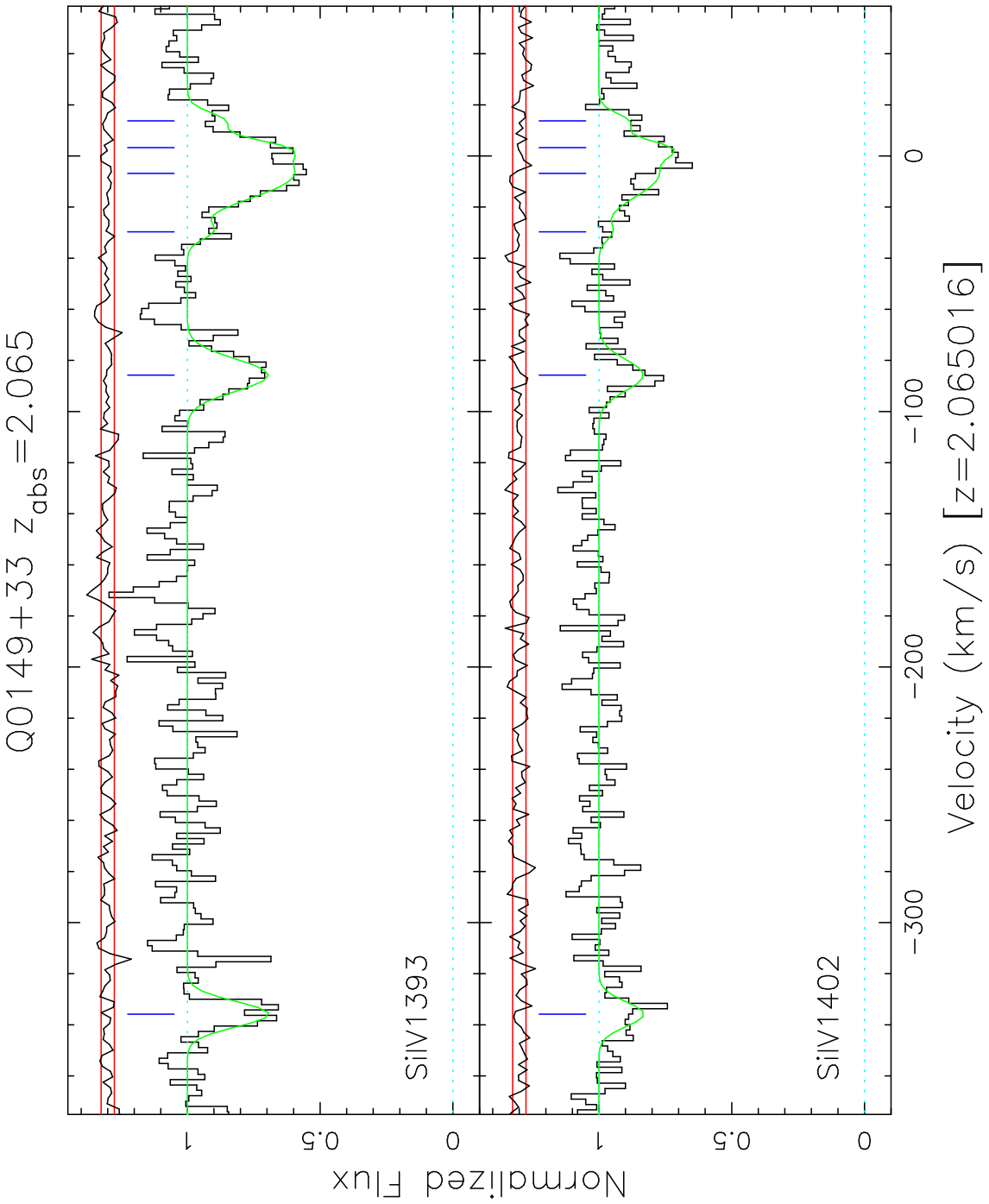

Figure B.3. Q0149+3335, $z_{\rm em} = 2.43$, $z_{\rm abs} = 2.065$.

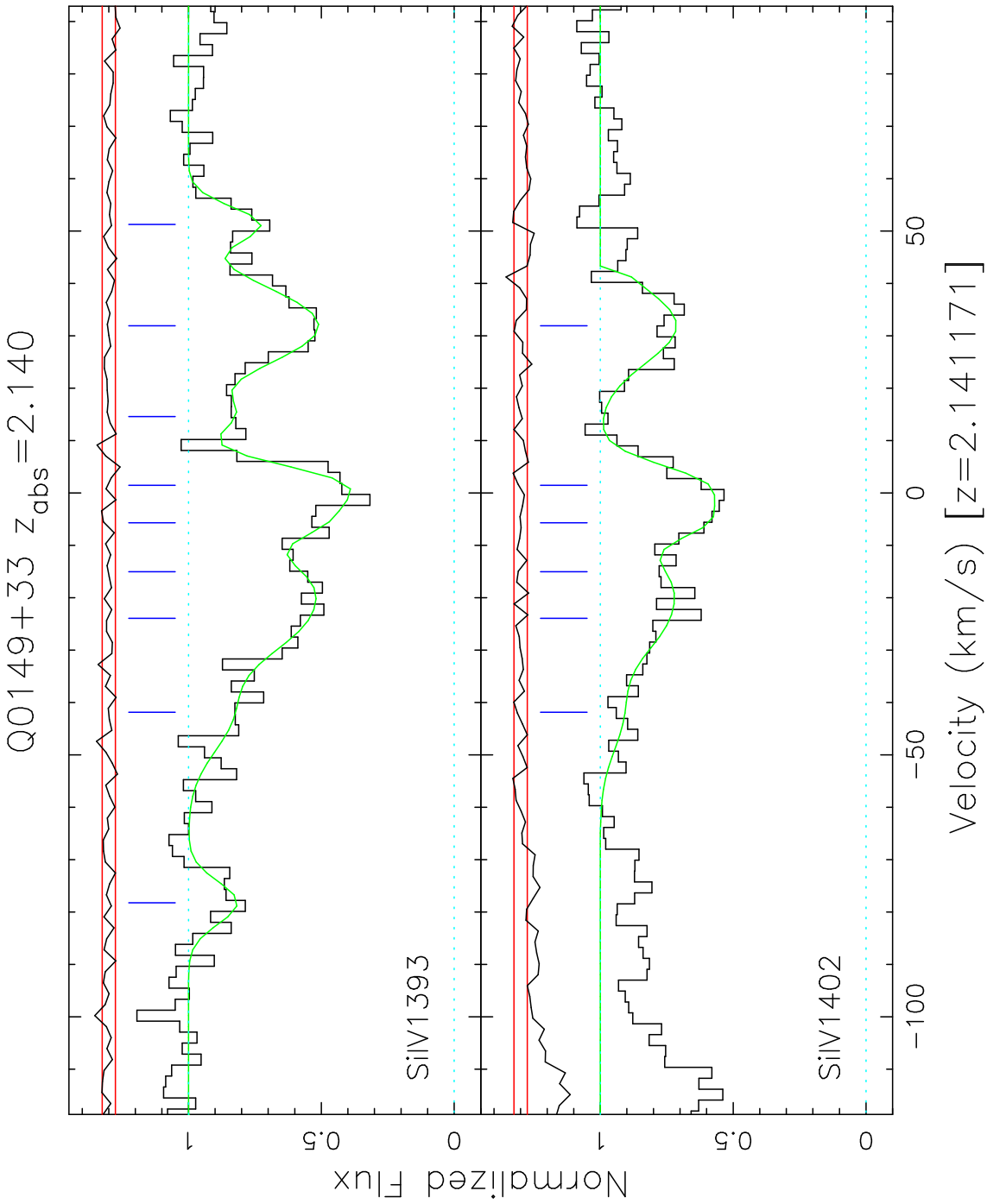

Figure B.4. Q0149+3335, $z_{\rm em} = 2.43$, $z_{\rm abs} = 2.140$.

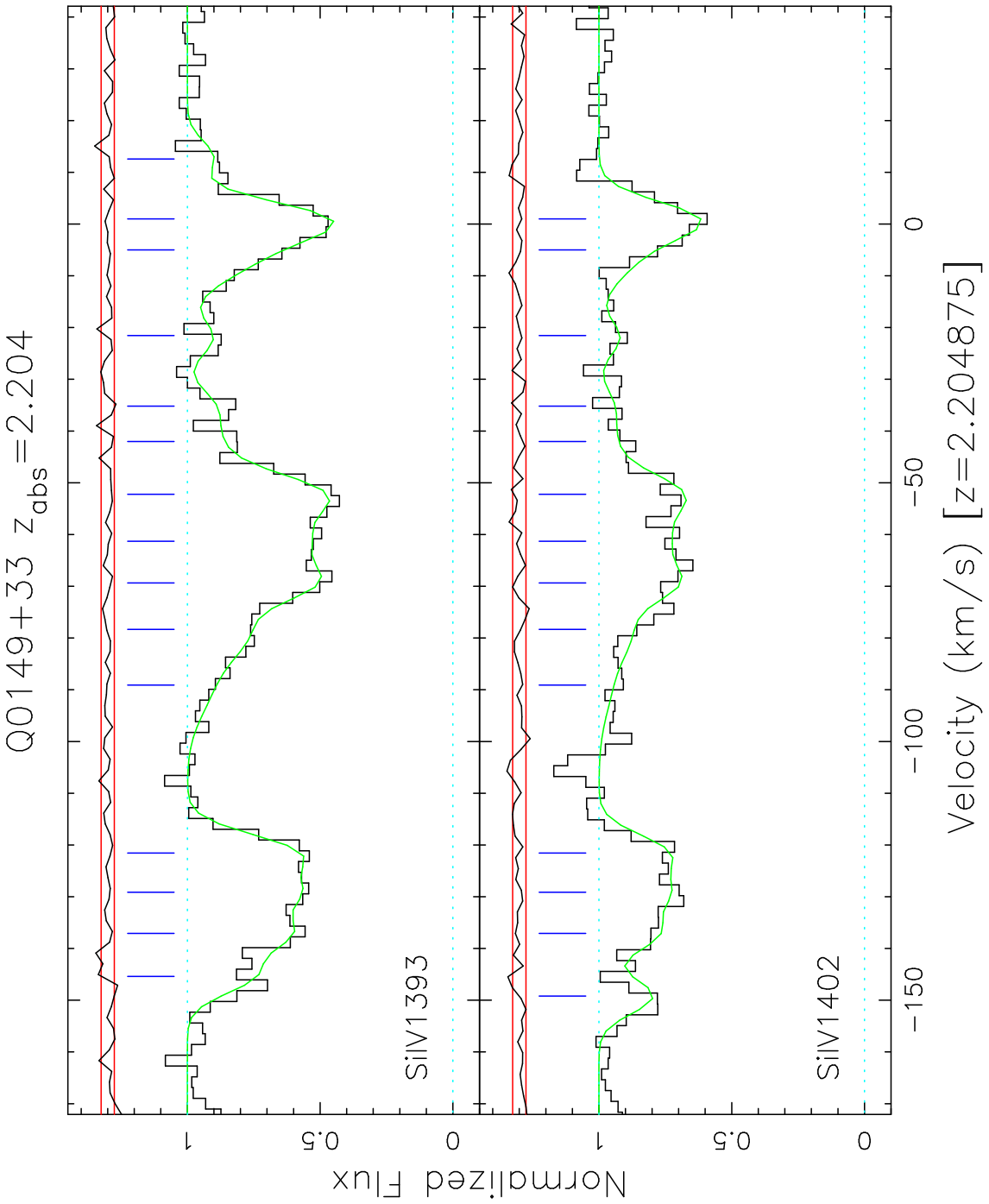

Figure B.5. Q0149+3335, $z_{\rm em} = 2.43$, $z_{\rm abs} = 2.204$.

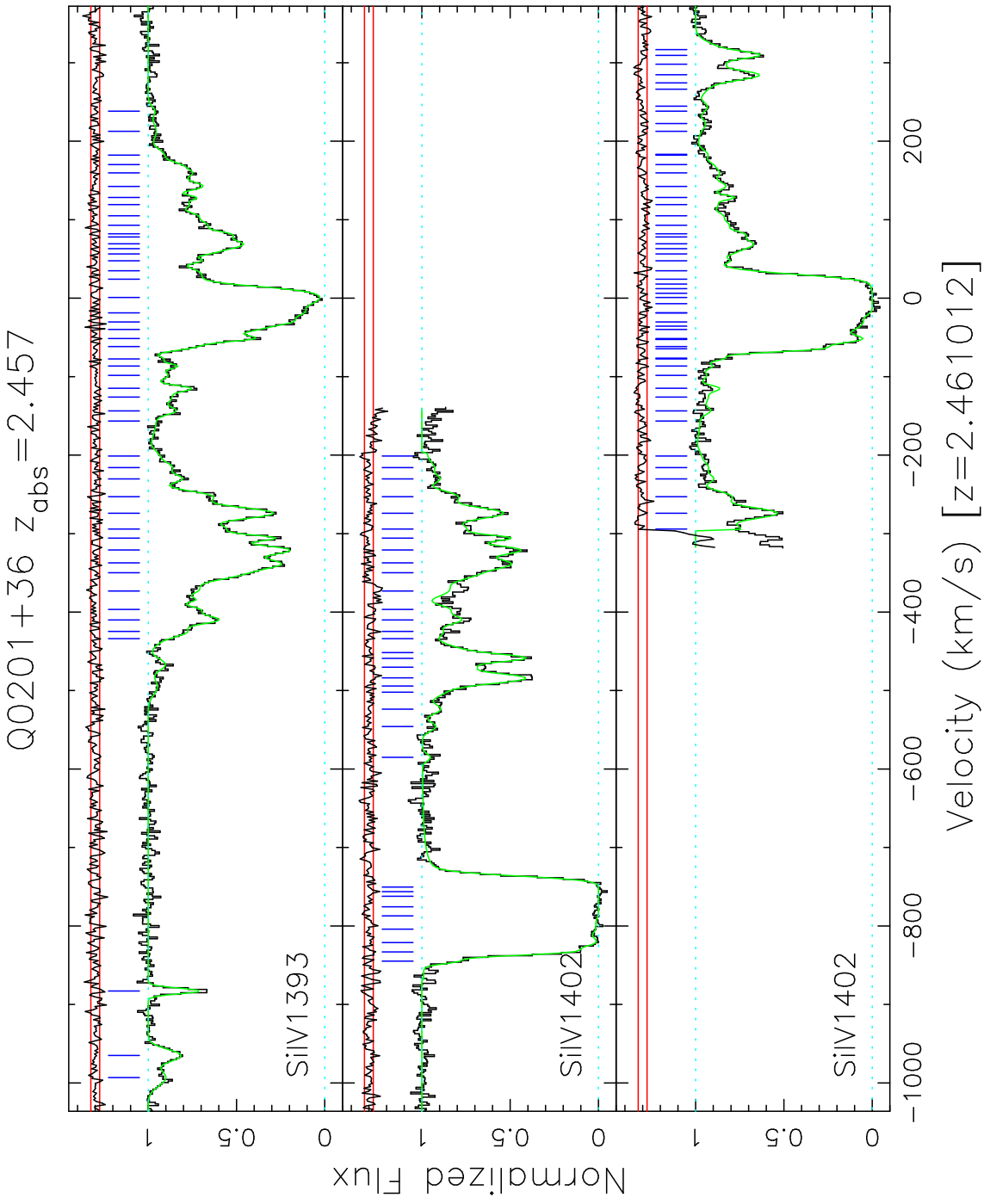

Figure B.6. Q0201+3634, $z_{\rm em} = 2.49$, $z_{\rm abs} = 2.457$.

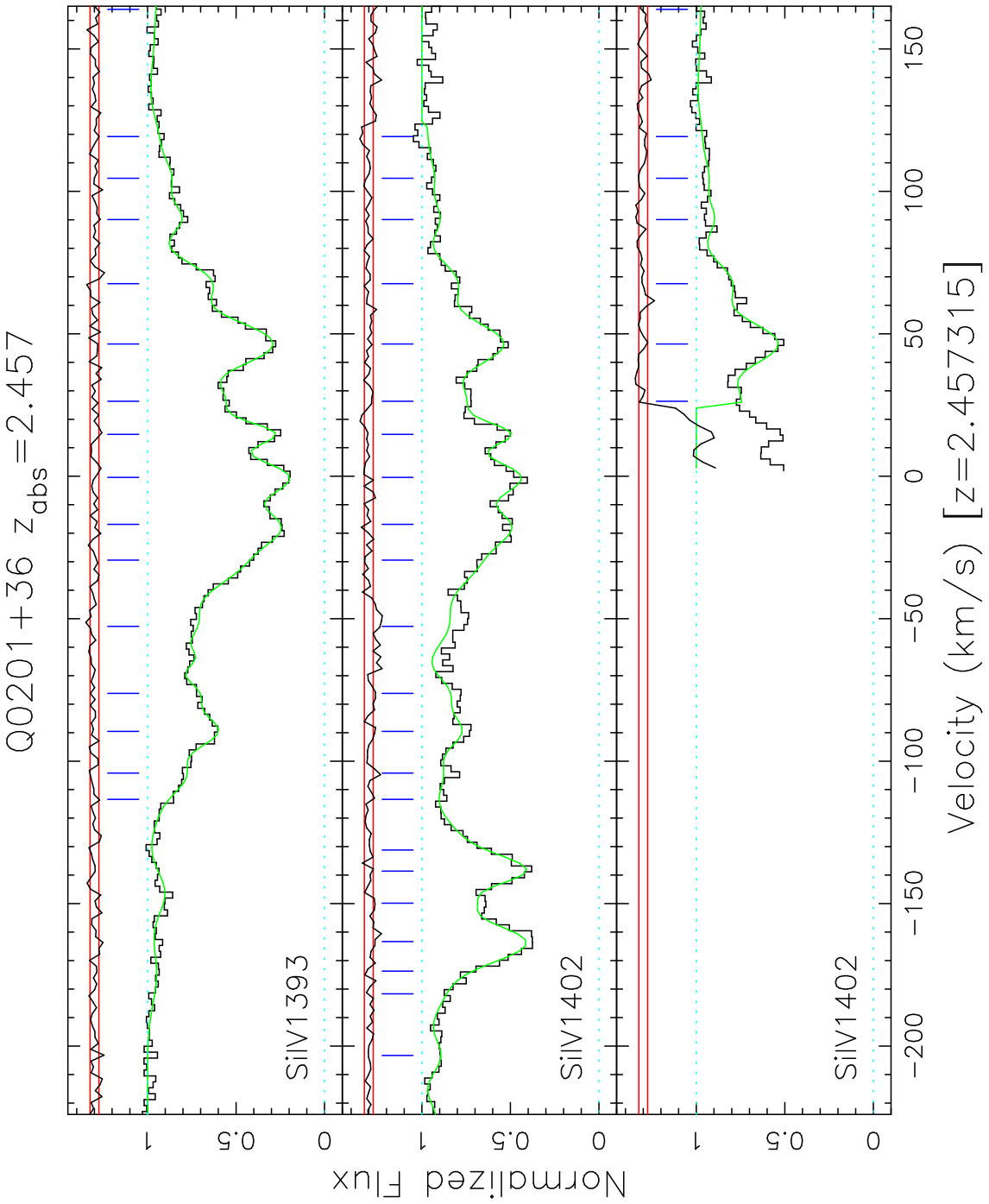

Figure B.7. Q0201+3634, $z_{\rm em} = 2.49$, $z_{\rm abs} = 2.457$. Detail of low-velocity portion.

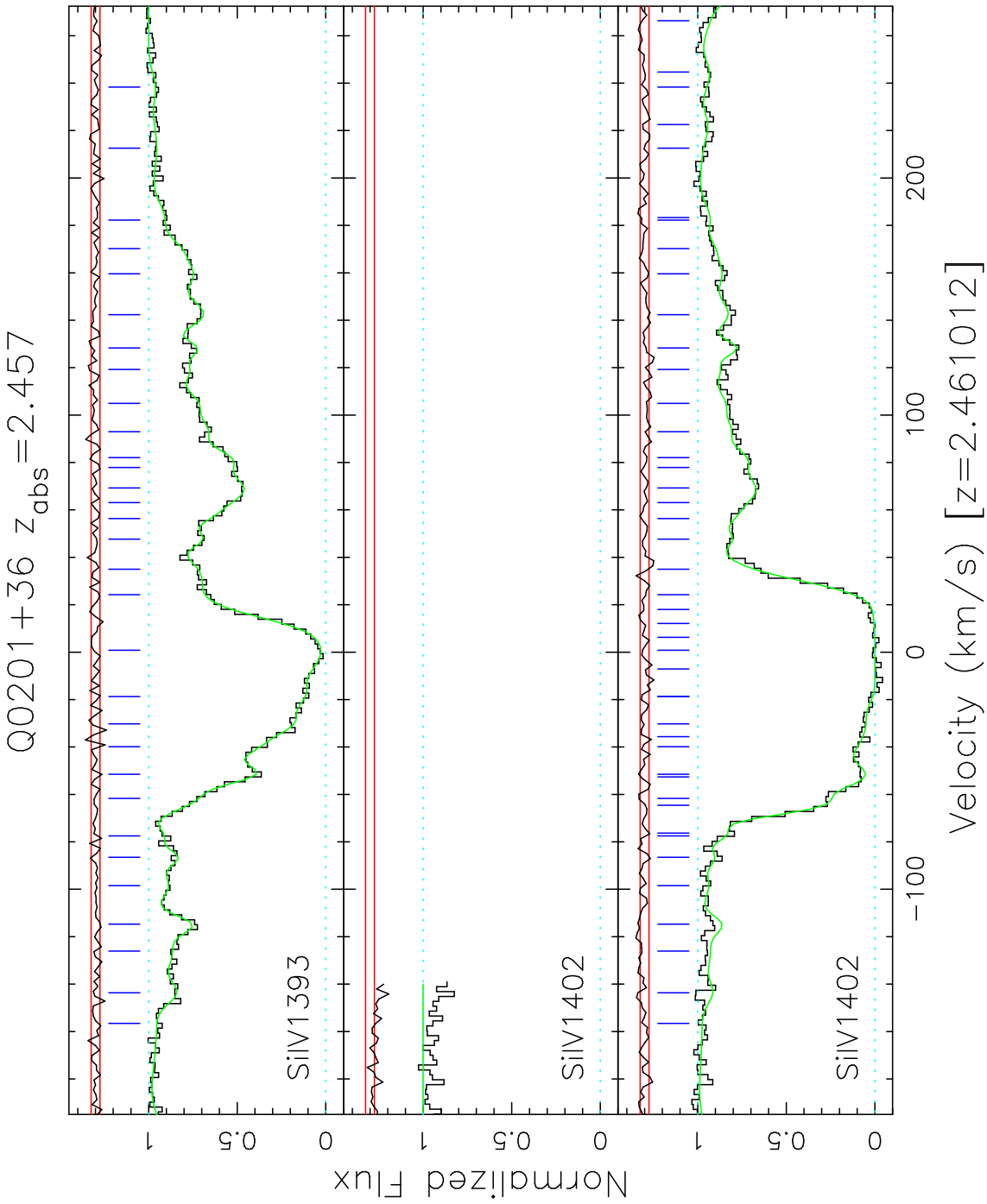

Figure B.8. Q0201+3634, $z_{\rm em} = 2.49$, $z_{\rm abs} = 2.457$. Detail of high-velocity portion.

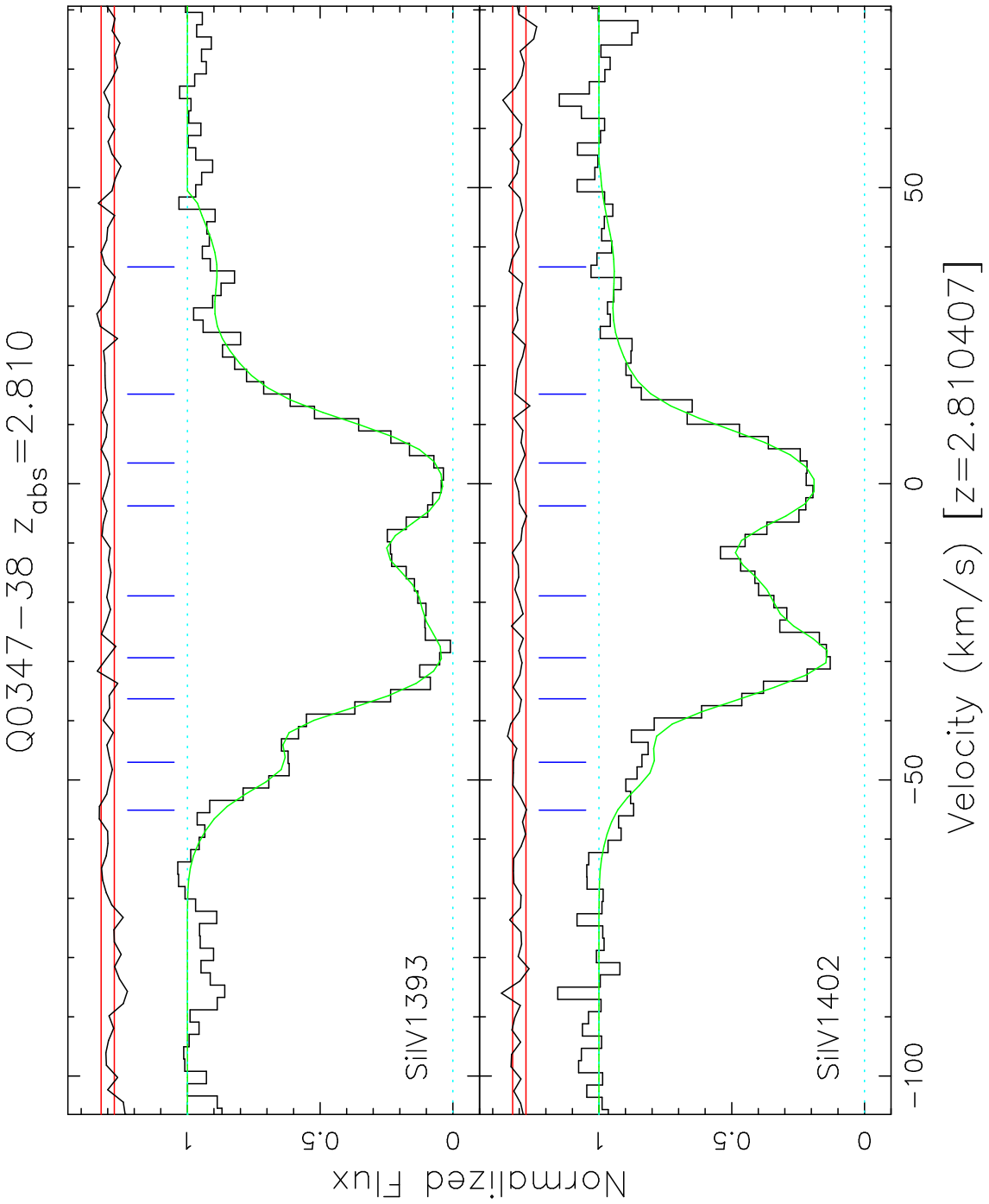

Figure B.9. Q0347−3819, $z_{\rm em} = 3.23$, $z_{\rm abs} = 2.810$.

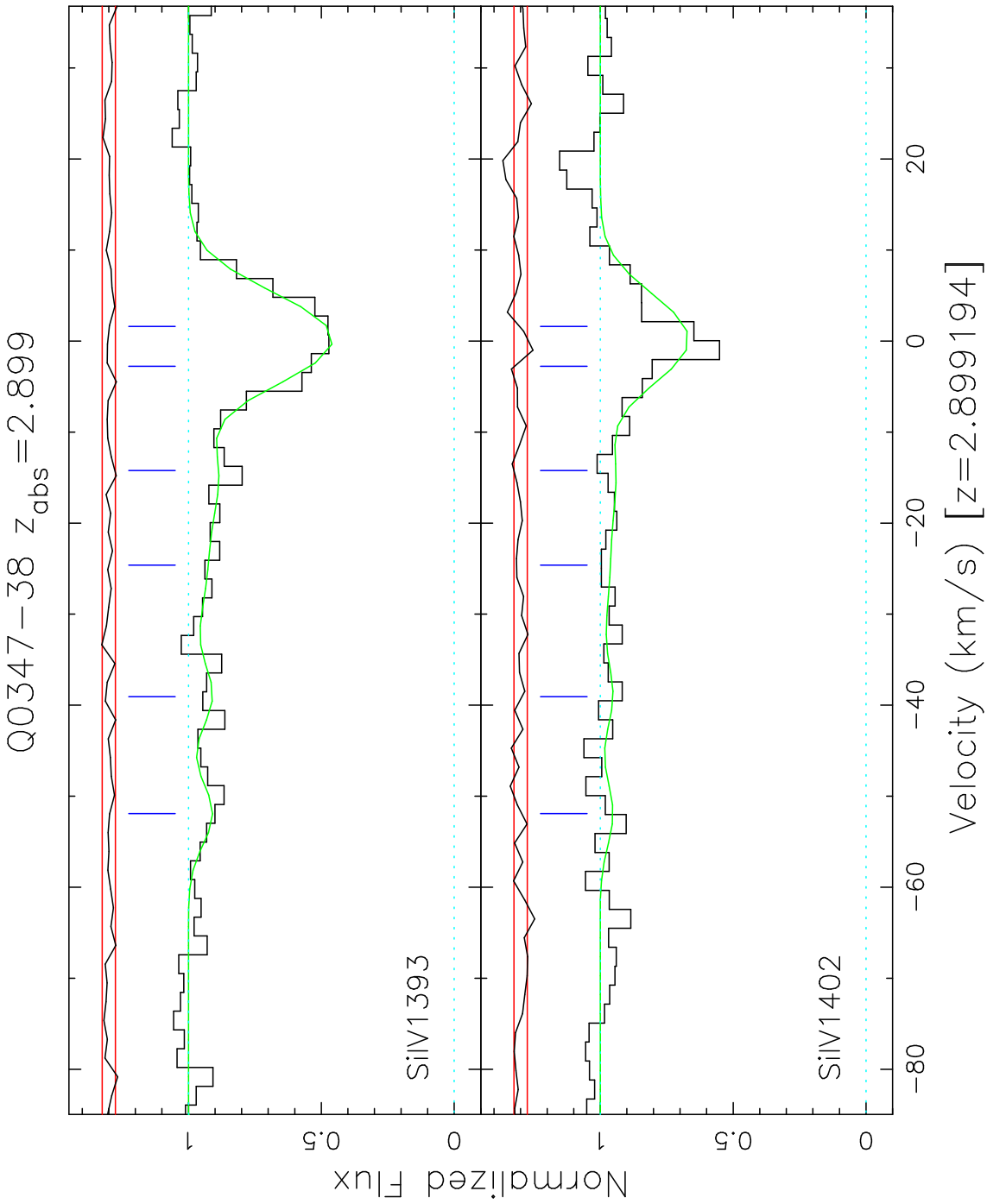

Figure B.10. Q0347−3819, $z_{\rm em} = 3.23$, $z_{\rm abs} = 2.899$.

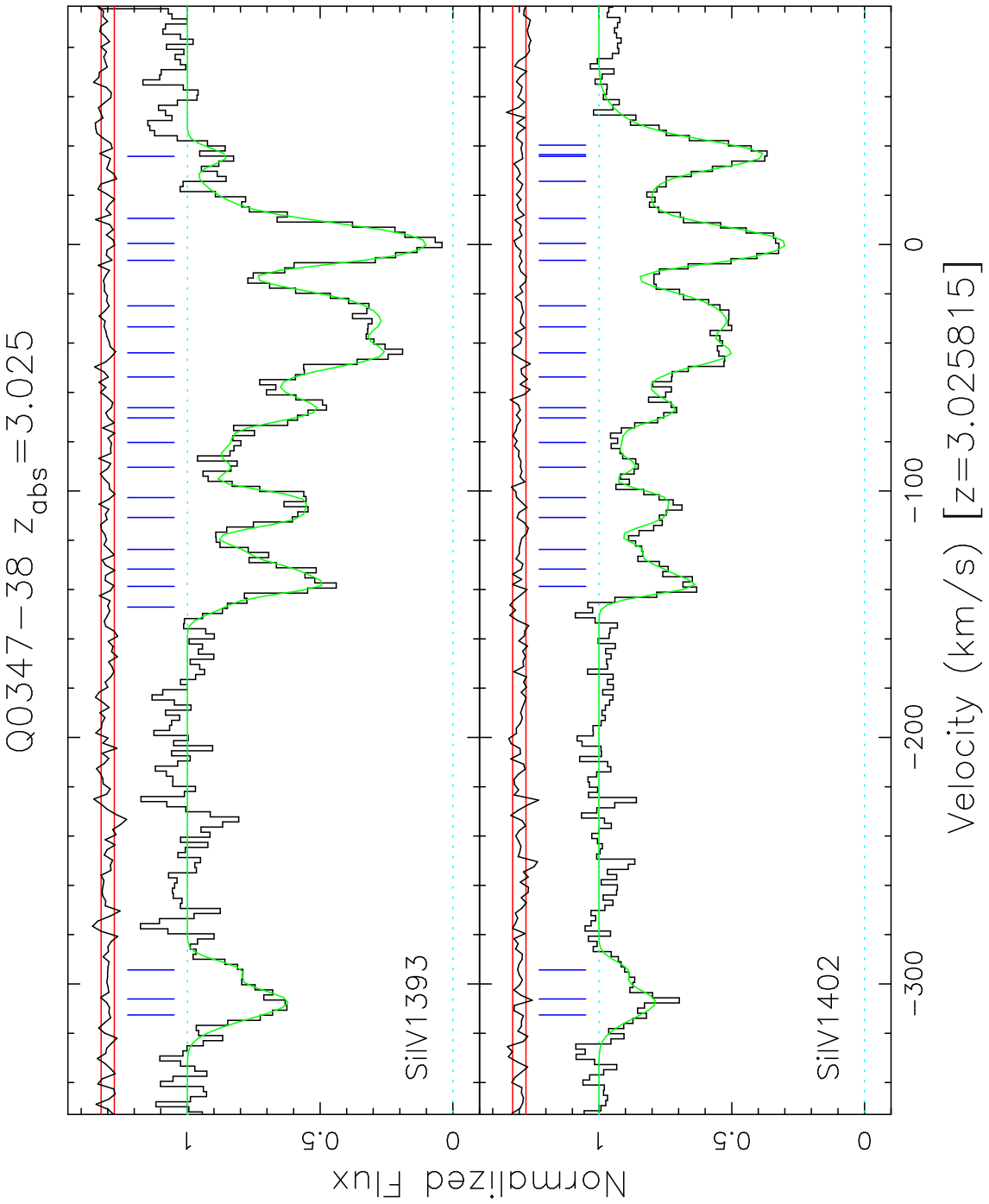

Figure B.11. Q0347−3819, $z_{\rm em} = 3.23$, $z_{\rm abs} = 3.025$.

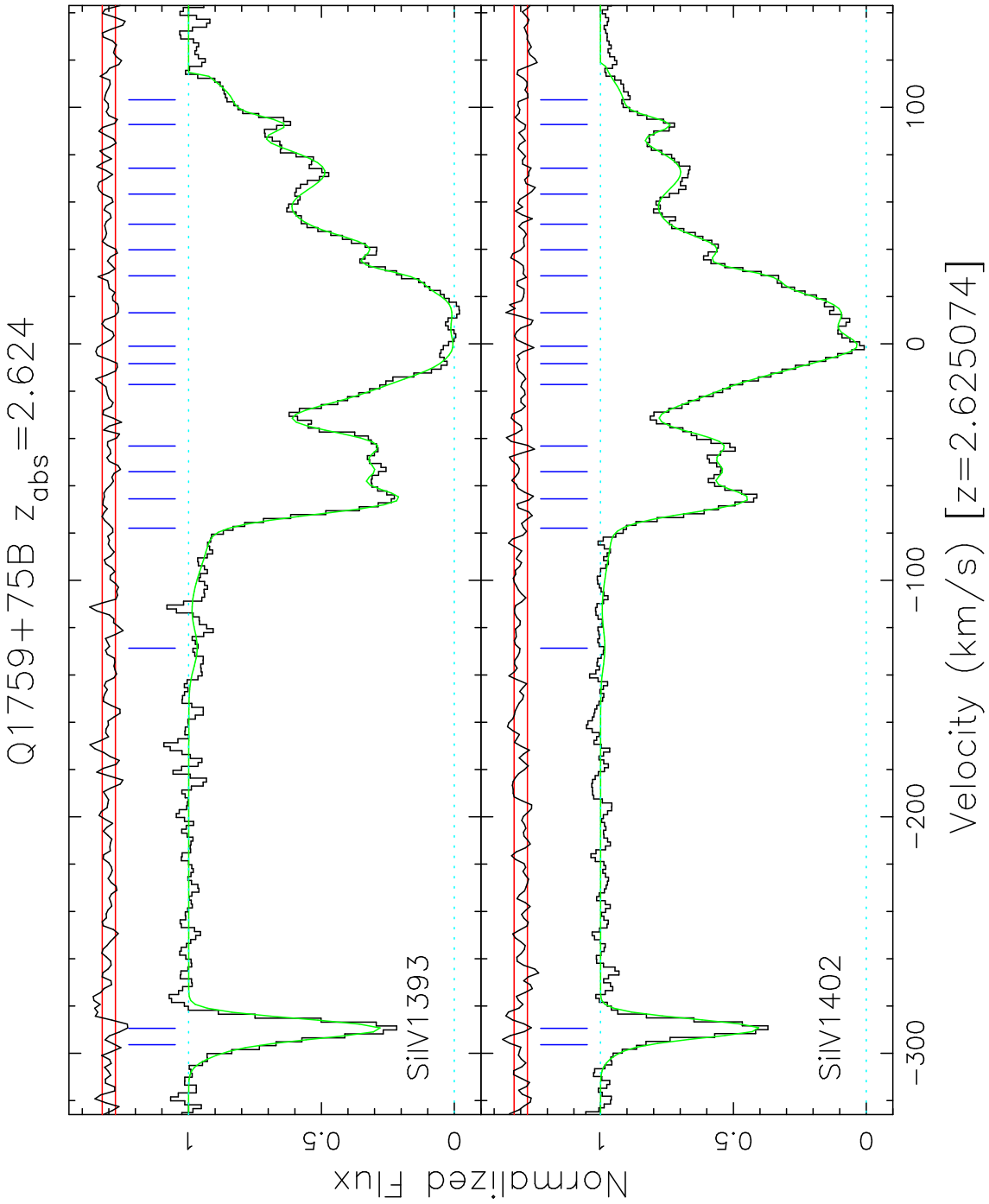

Figure B.12. Q1759+7539, $z_{\rm em} = 3.05$, $z_{\rm abs} = 2.624$. This system constributed by Outram et al. (1999).

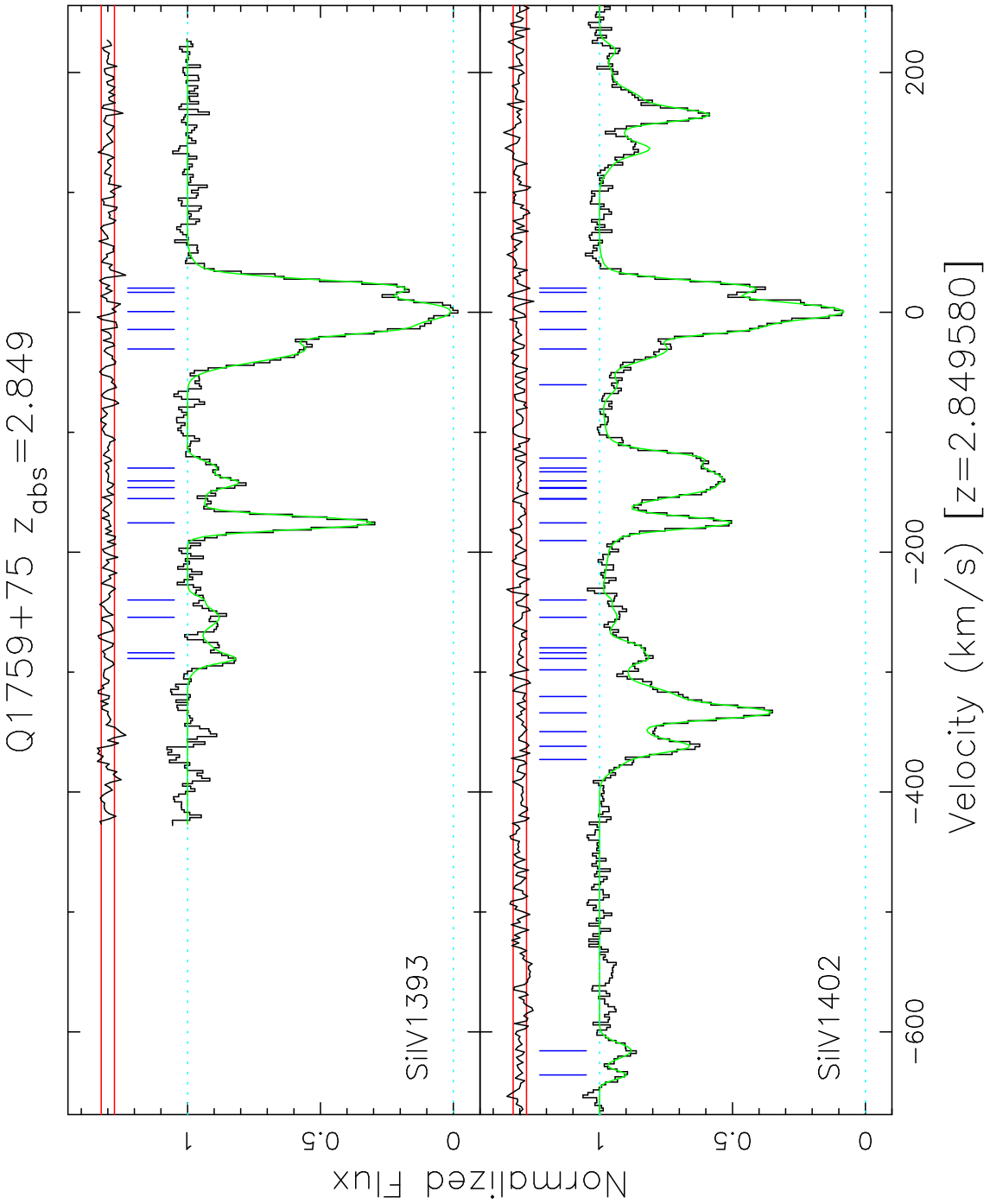

Figure B.13. Q1759+7539, $z_{em} = 3.05$, $z_{abs} = 2.849$. This system constributed by Outram et al. (1999).

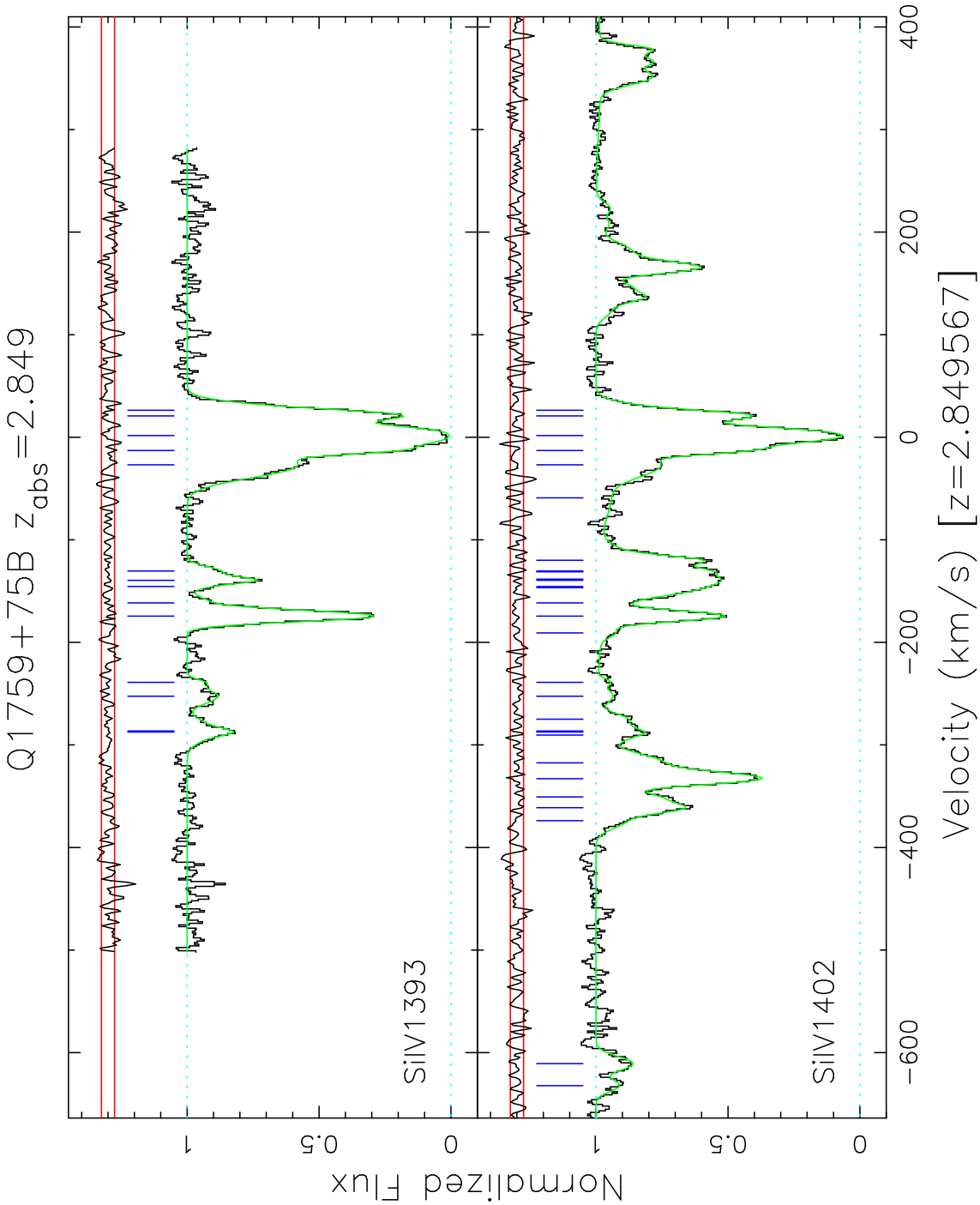

Figure B.14. Q1759+7539, $z_{\rm em} = 3.05$, $z_{\rm abs} = 2.849$.

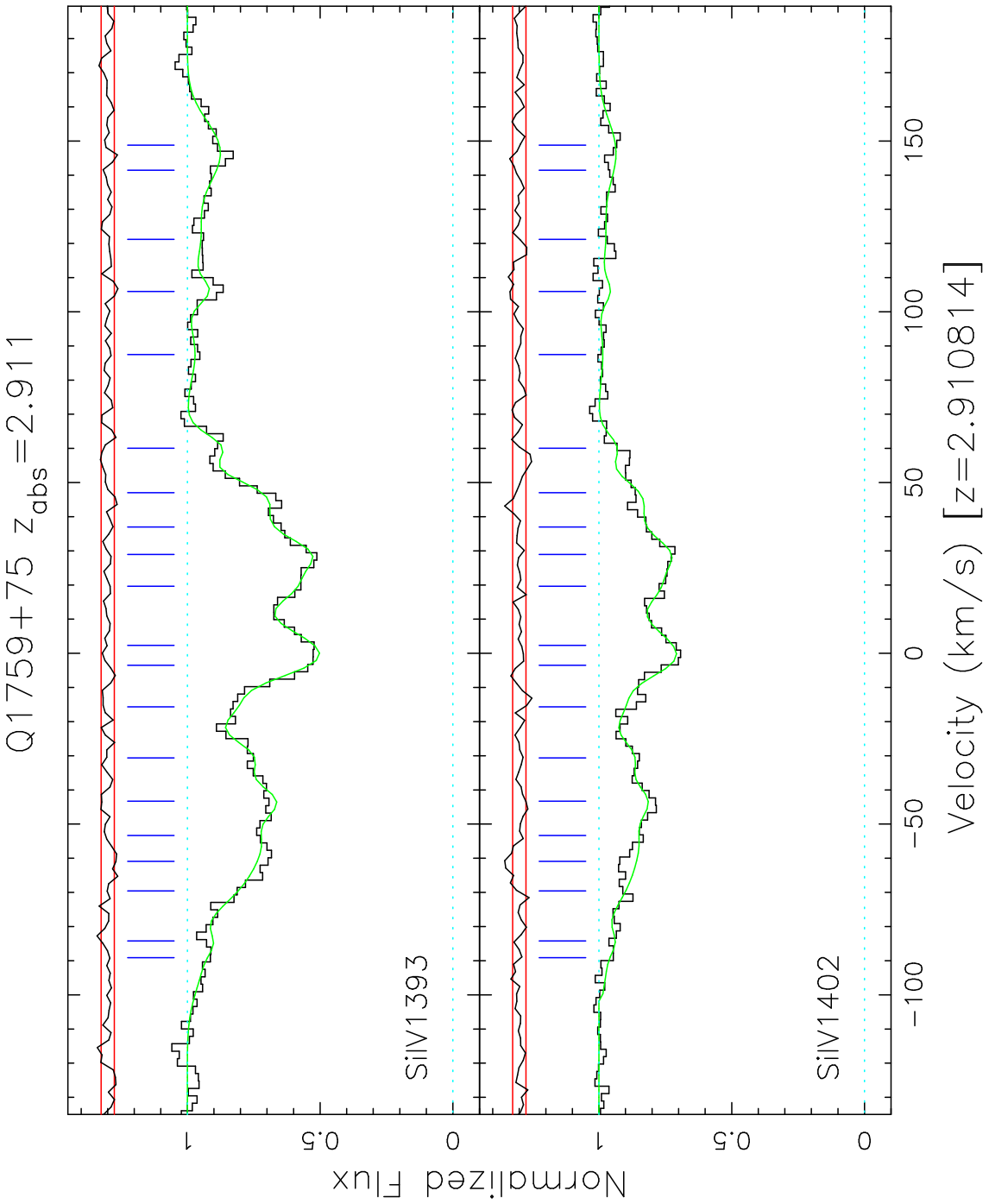

Figure B.15. Q1759+7539, $z_{\rm em} = 3.05$, $z_{\rm abs} = 2.911$.

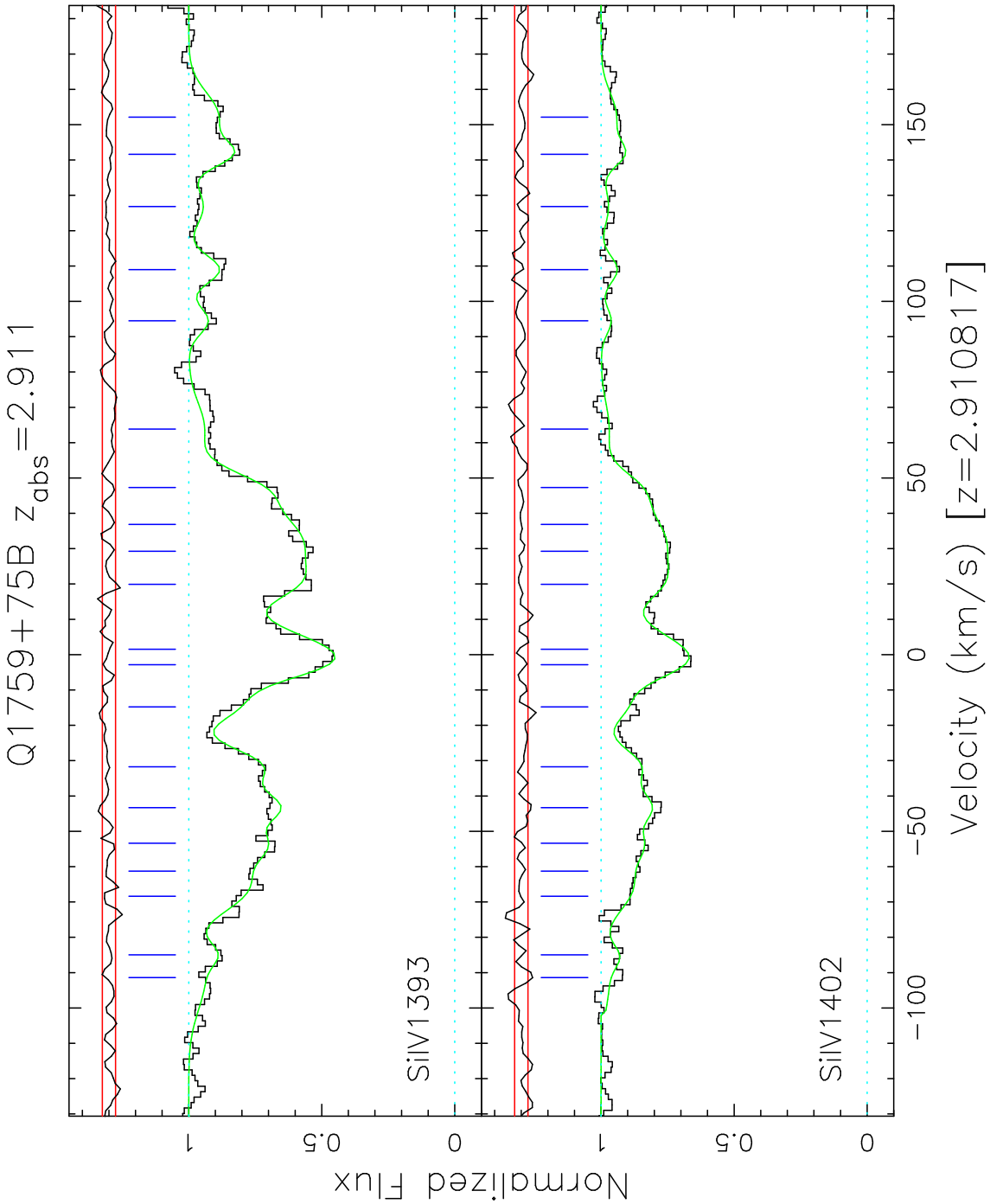

Figure B.16. Q1759+7539, $z_{\rm em} = 3.05$, $z_{\rm abs} = 2.911$. This system constributed by Outram et al. (1999).

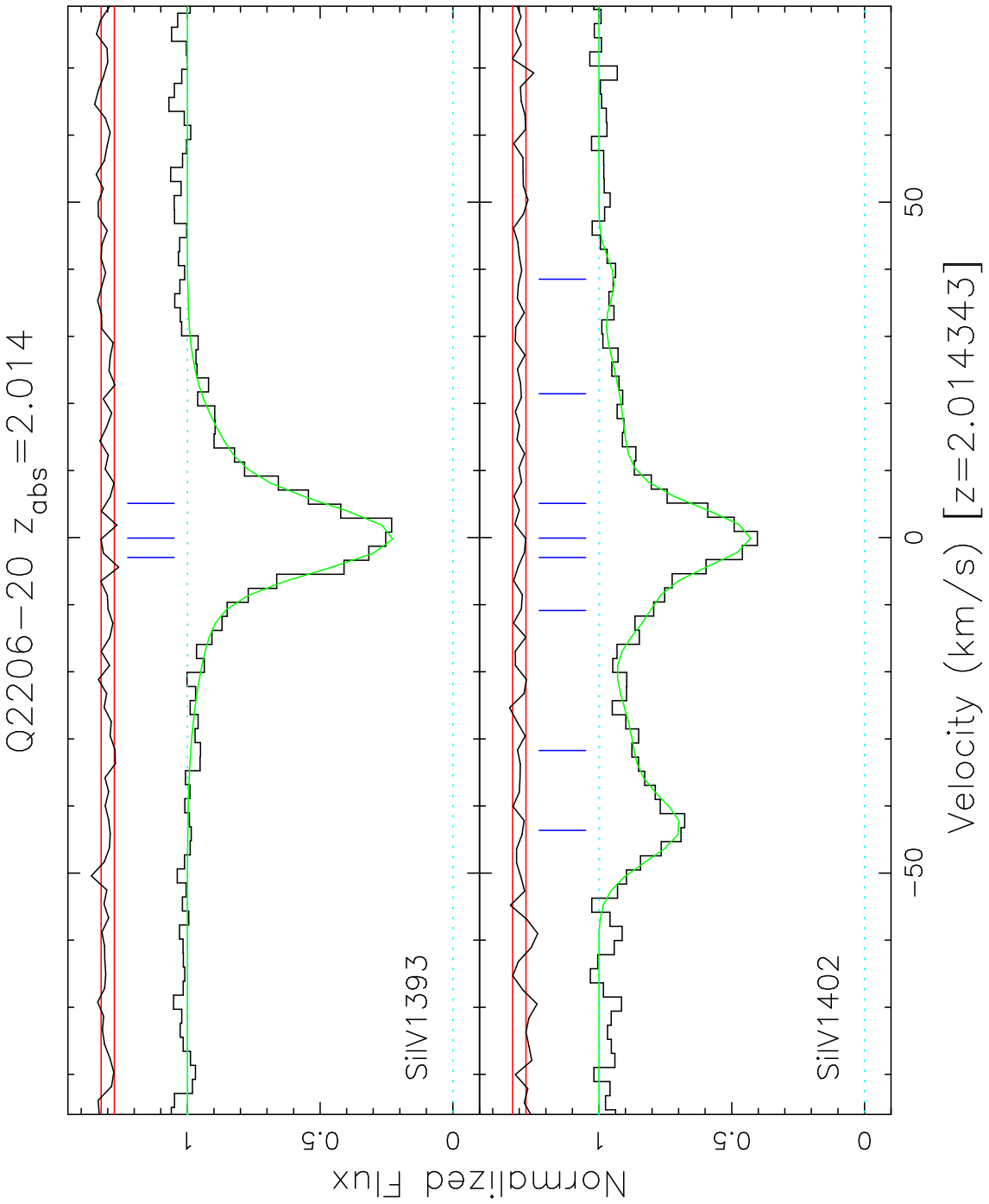

Figure B.17. Q2206−1958, $z_{\rm em} = 2.56$, $z_{\rm abs} = 2.014$.

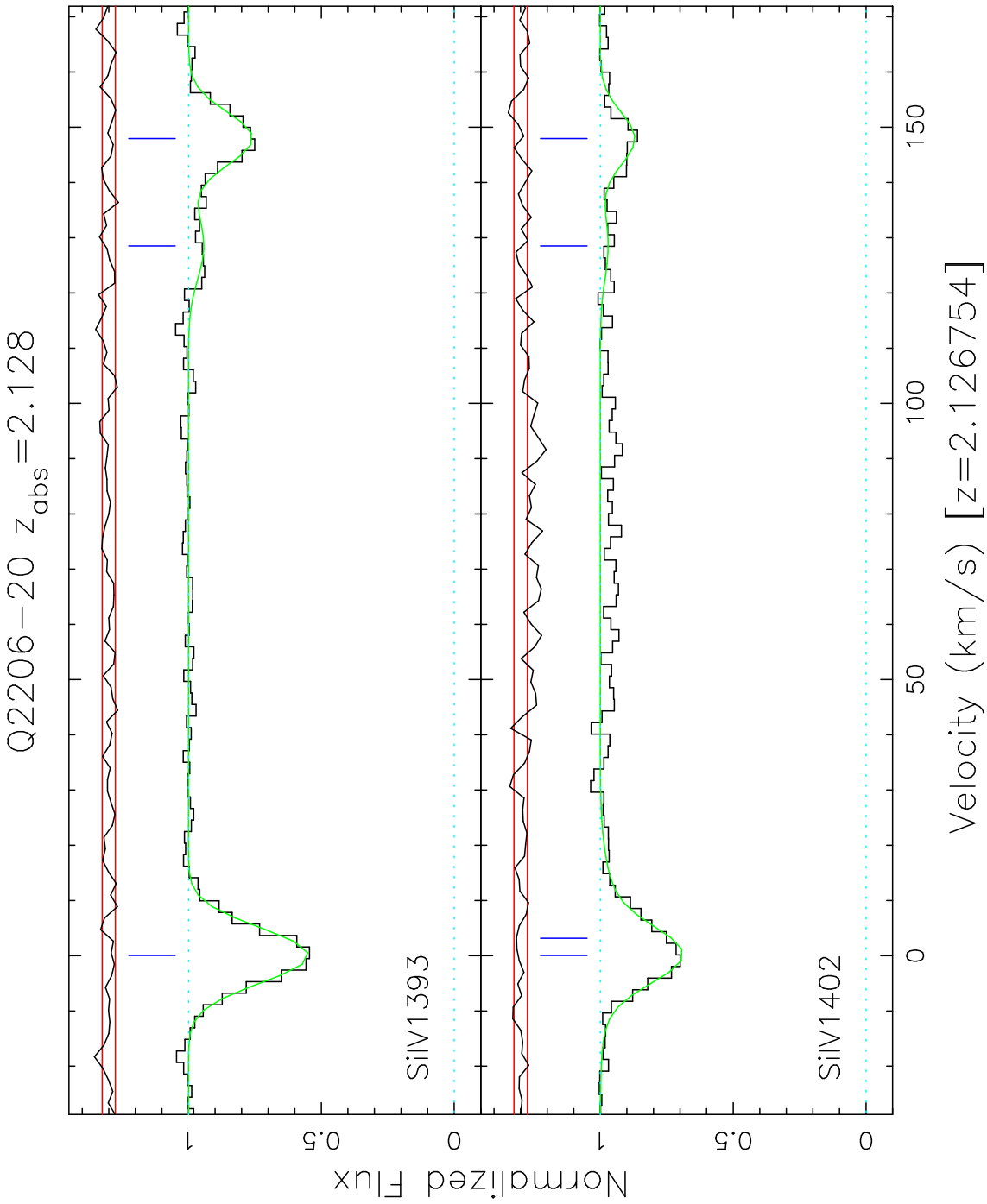

Figure B.18. Q2206−1958, $z_{\rm em} = 2.56$, $z_{\rm abs} = 2.128$.

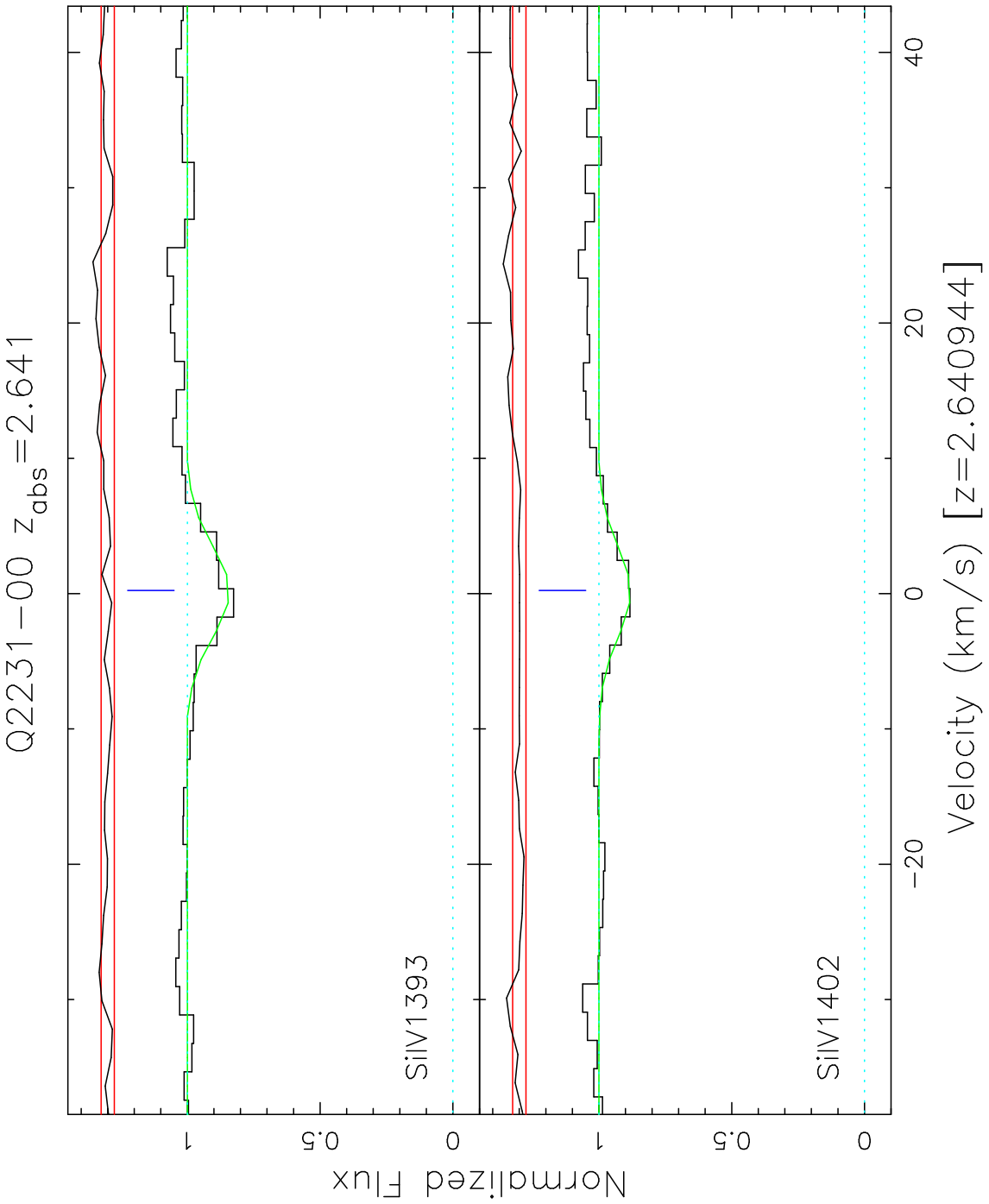

Figure B.19. Q2231−0015, $z_{\rm em} = 3.02$, $z_{\rm abs} = 2.641$.

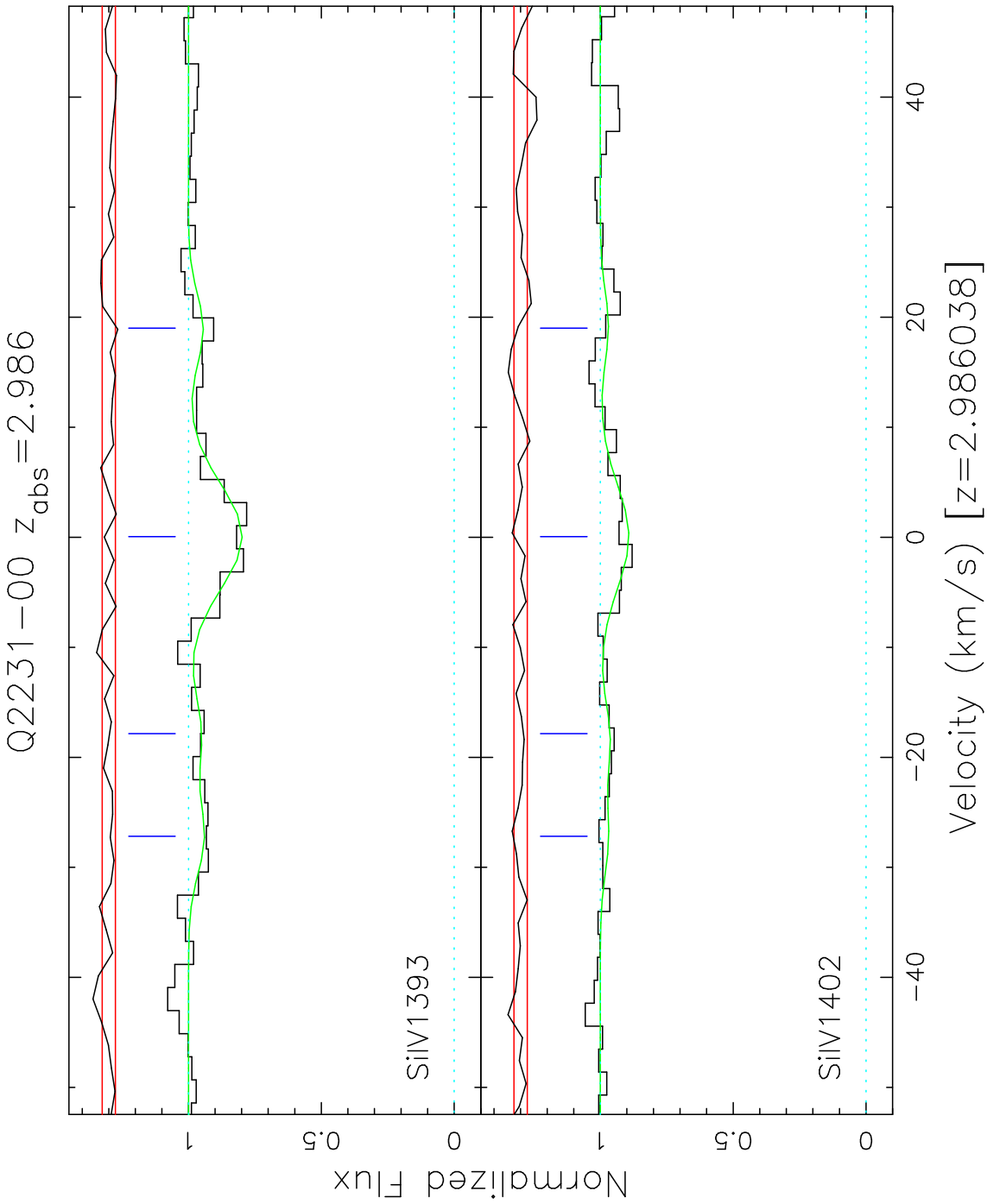

Figure B.20. Q2231−0015, $z_{\rm em} = 3.02$, $z_{\rm abs} = 2.986$.

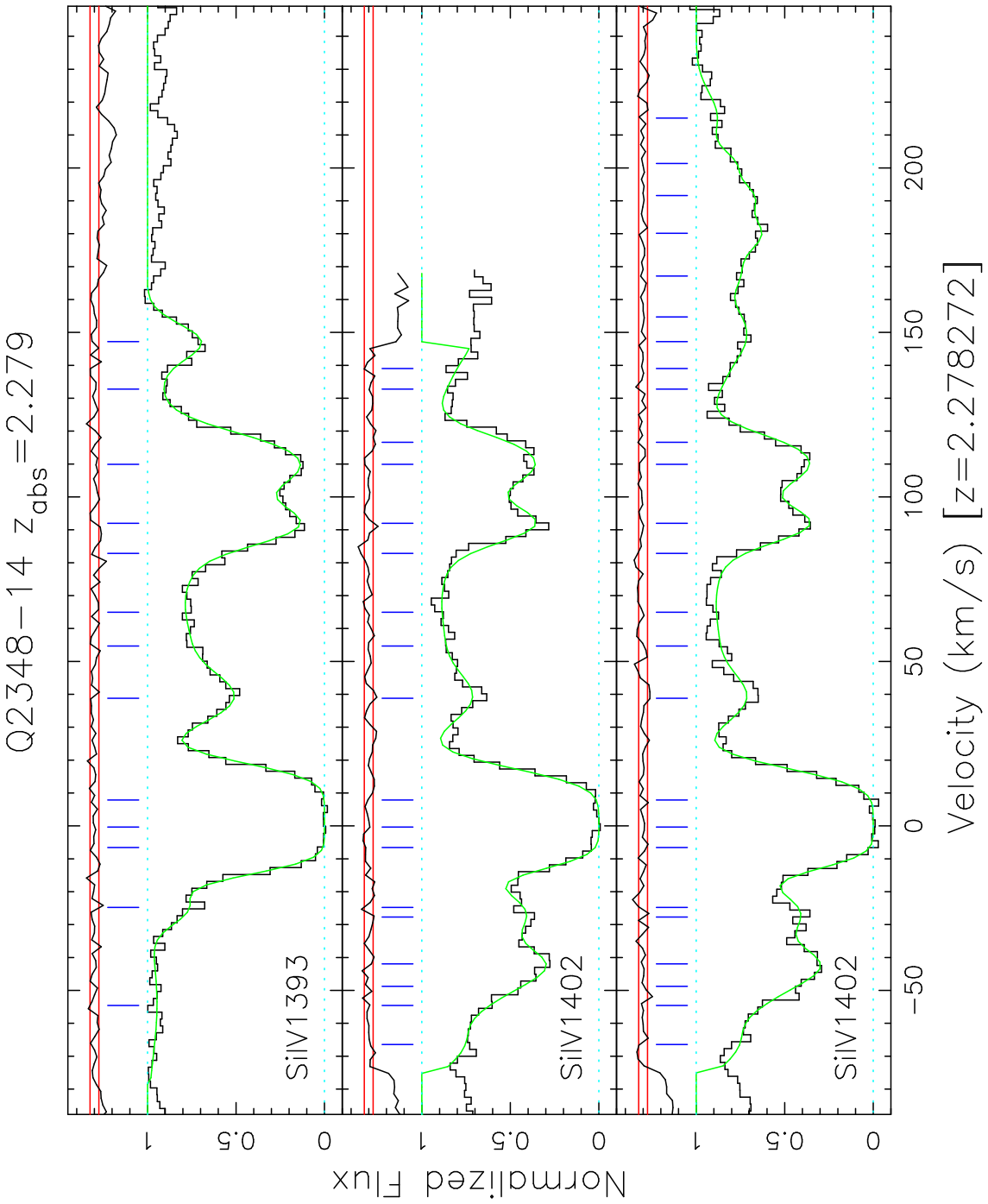

Figure B.21. Q2348−1444, $z_{\rm em} = 2.94$, $z_{\rm abs} = 2.279$.

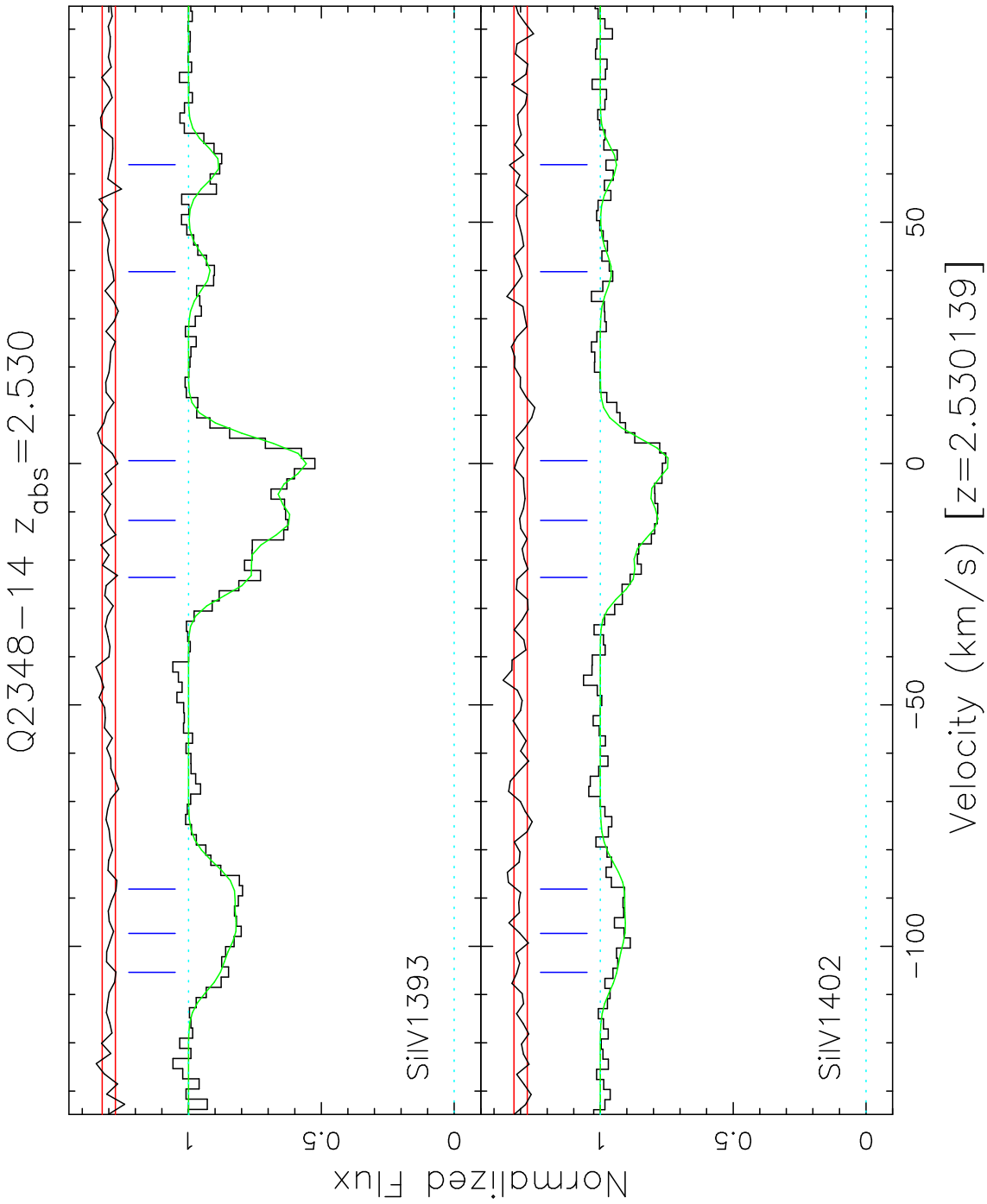

Figure B.22. Q2348−1444, $z_{\rm em} = 2.94$, $z_{\rm abs} = 2.530$.

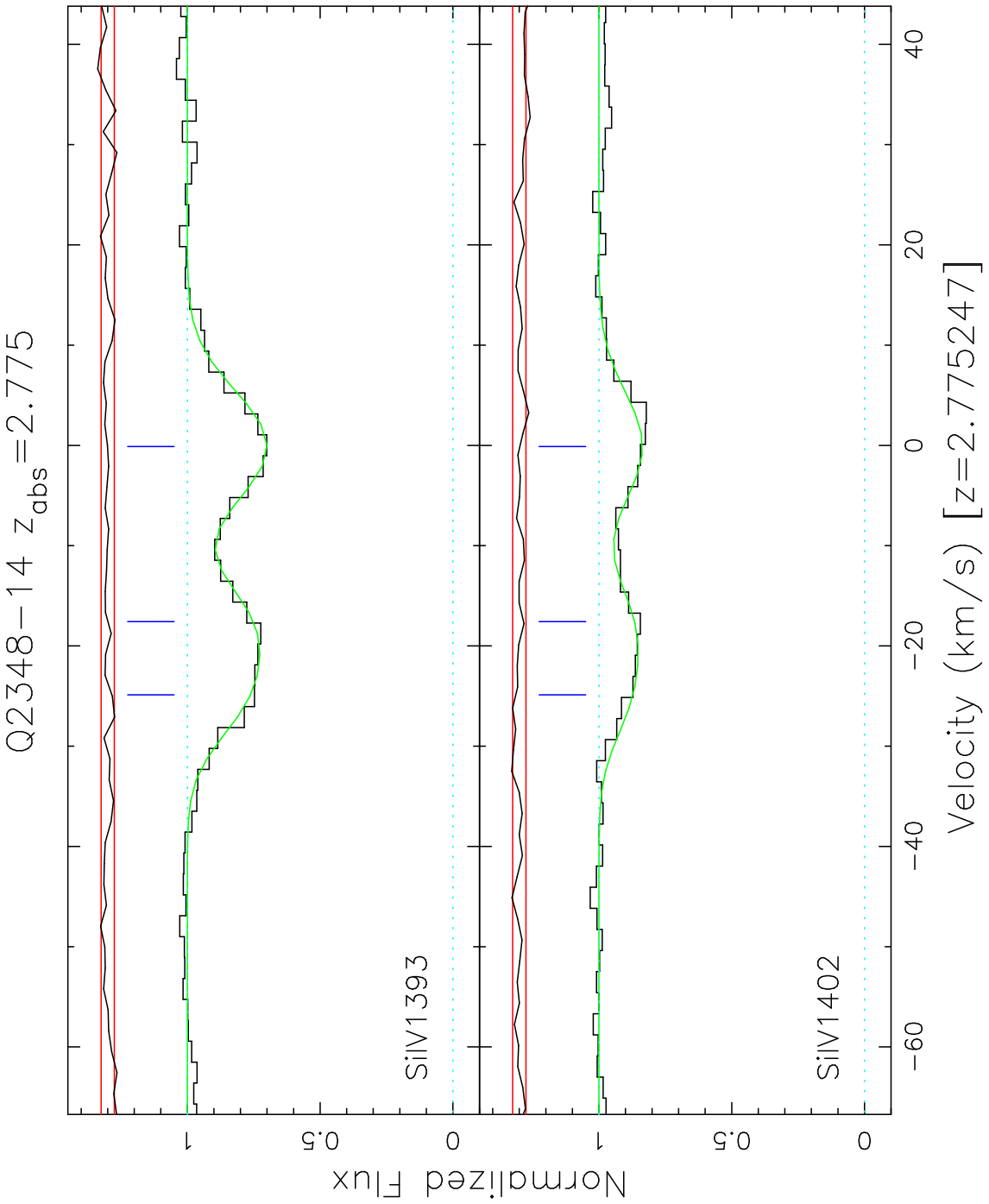

Figure B.23. Q2348−1444, $z_{\rm em} = 2.94$, $z_{\rm abs} = 2.775$.

Appendix C

Many multiplet Voigt profile fits

Here we plot all the many-multiplet absorption systems in all three independent Keck/HIRES samples used to obtain constraints on $\Delta\alpha/\alpha$ in Chapter 3. For each system we give the QSO's B1950 name, its emission redshift, $z_{\rm em}$, as given in the NED[1] and the nominal absorption redshift, $z_{\rm abs}$, which can be used to identify the system in Table 3.4. We plot the flux, normalized by a fit to the continuum, as a histogram, our Voigt profile fit (solid curve) and the residuals (i.e. [data]−[fit]). The latter are normalized by the $1\,\sigma$ errors (horizontal solid lines). The tick-marks above the continuum indicate the position of individual velocity components. For transitions where several isotopic (e.g. Mg I λ2852) and/or hyperfine components (e.g. Al III λ1854) were fitted, the tick-mark corresponds to the composite wavelength in Table 3.1. All transitions appear on a common velocity scale centred at the specified arbitrary redshift. Our methods for fitting random blends are discussed in Section 4-9.1 but we do not identify the strong blends here. Most of these features are identified in Churchill (1997) and Churchill et al. (1999) for sample 1 and Prochaska & Wolfe (1996, 1997, 1999) and Prochaska et al. (2001) for sample 2. Transitions lying in the Lyman-α forest are indicated with an 'F' in the bottom right-hand corner of the relevant spectral region. However, we generally avoided fitting such transitions due to potential blends with forest lines.

[1]The NASA/IPAC Extragalactic Database is available at http://nedwww.ipac.caltech.edu.

C-1 Sample 1

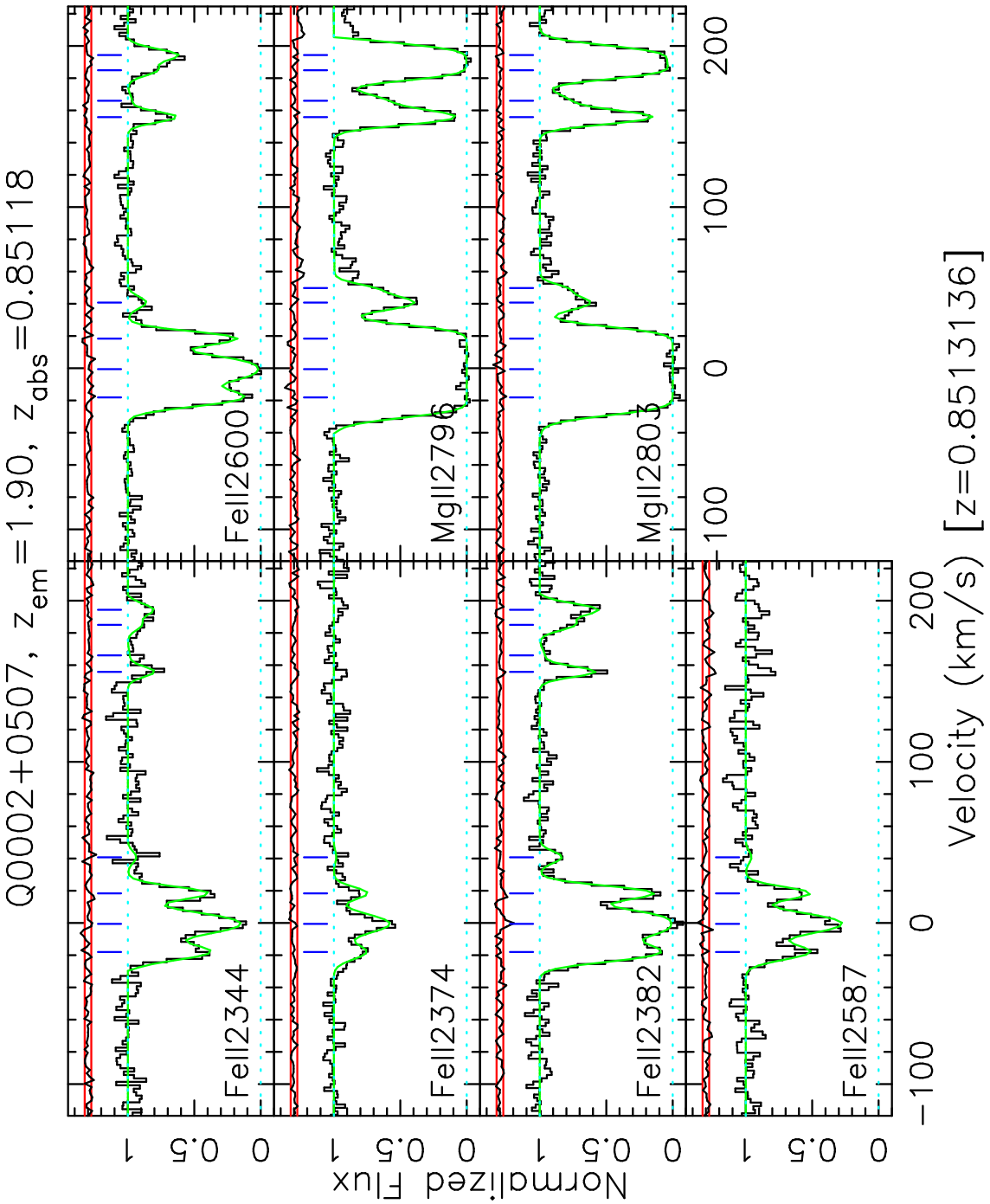

Figure C.1. Q0002+0507, $z_{\rm em} = 1.90$, $z_{\rm abs} = 0.85118$.

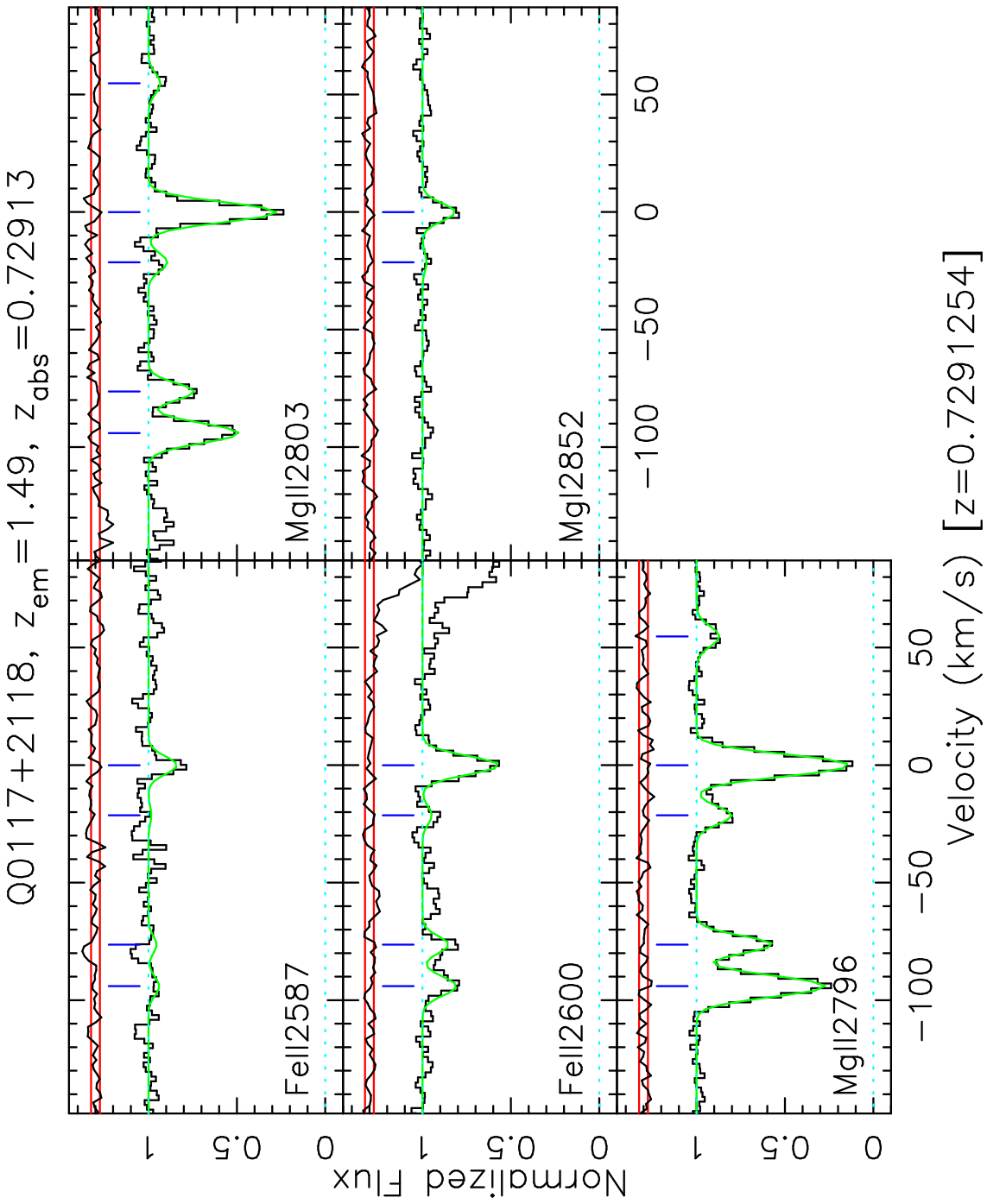

Figure C.2. Q0117+2118, $z_{\rm em} = 1.49$, $z_{\rm abs} = 0.72913$.

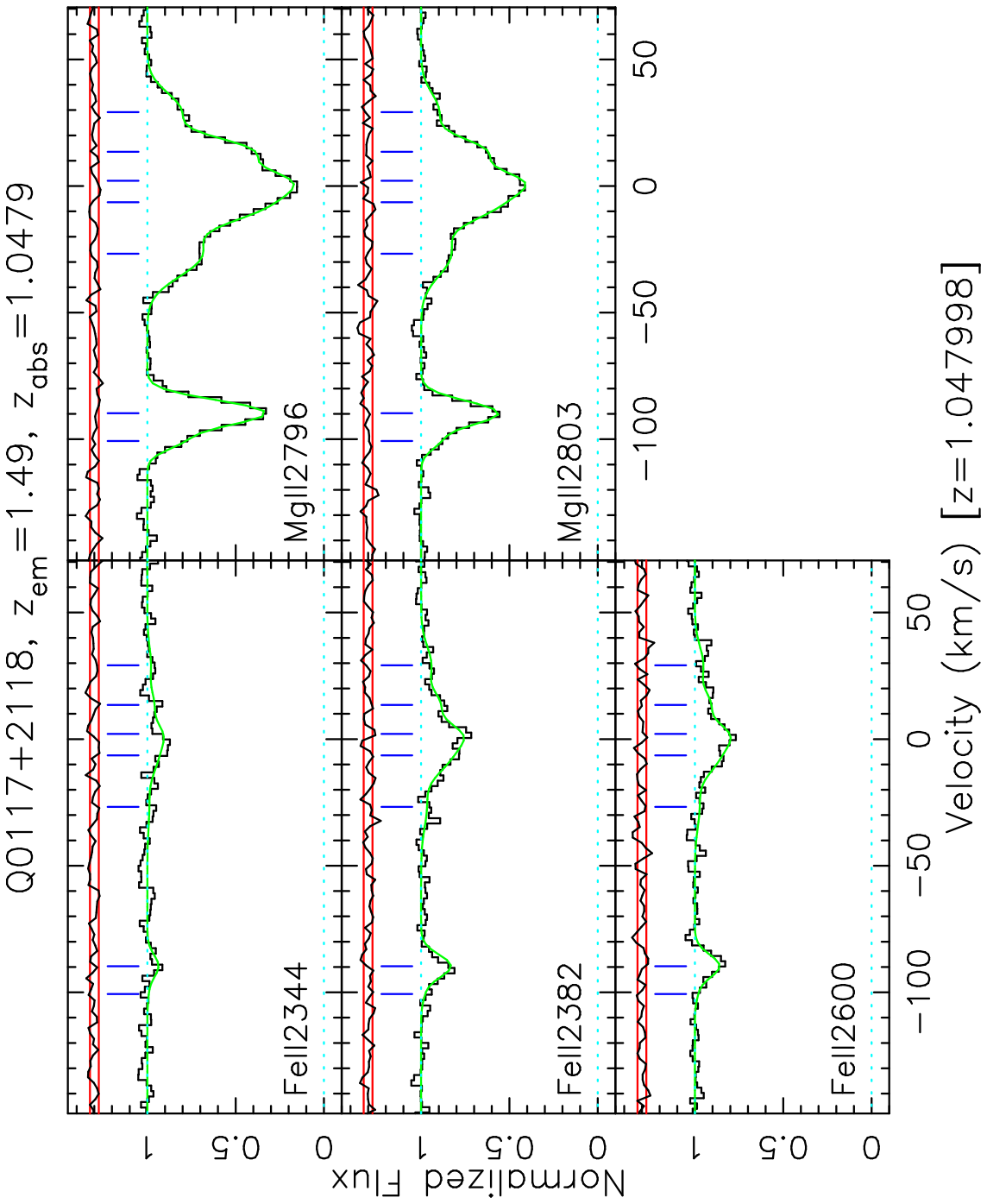

Figure C.3. Q0117+2118, $z_{\rm em} = 1.49$, $z_{\rm abs} = 1.0479$.

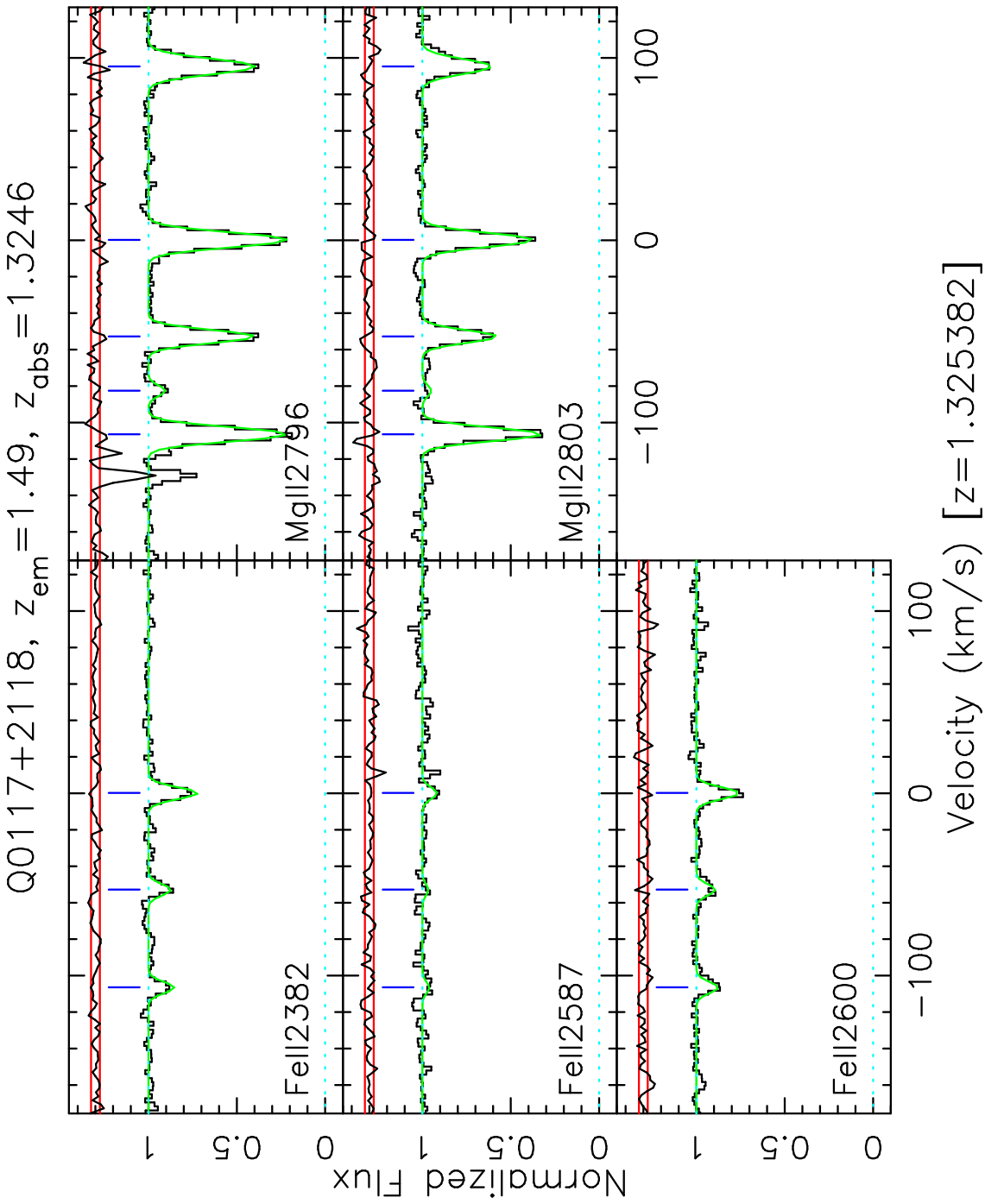

Figure C.4. Q0117+2118, $z_{\rm em} = 1.49$, $z_{\rm abs} = 1.3246$.

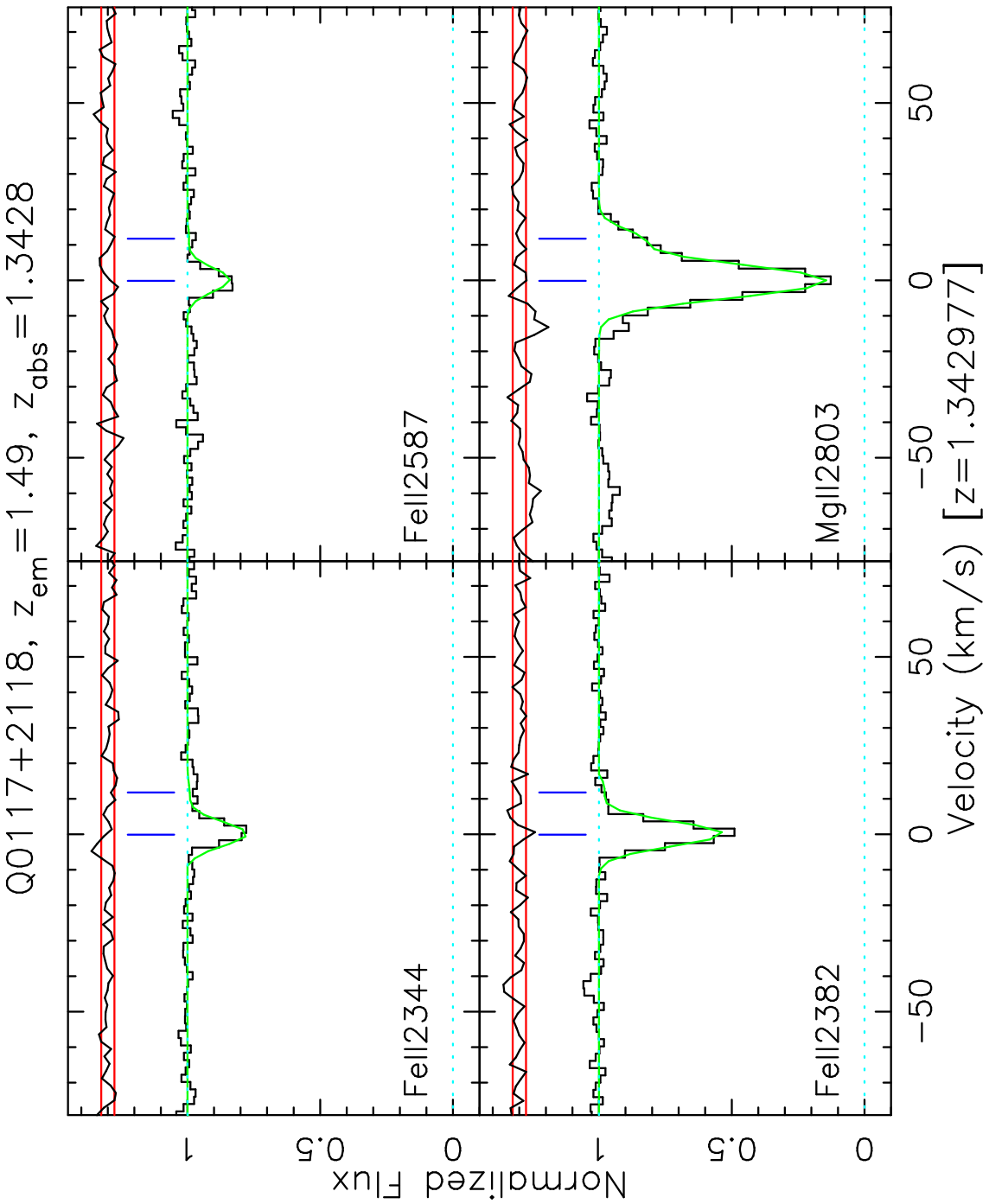

Figure C.5. Q0117+2118, $z_{\rm em} = 1.49$, $z_{\rm abs} = 1.3428$.

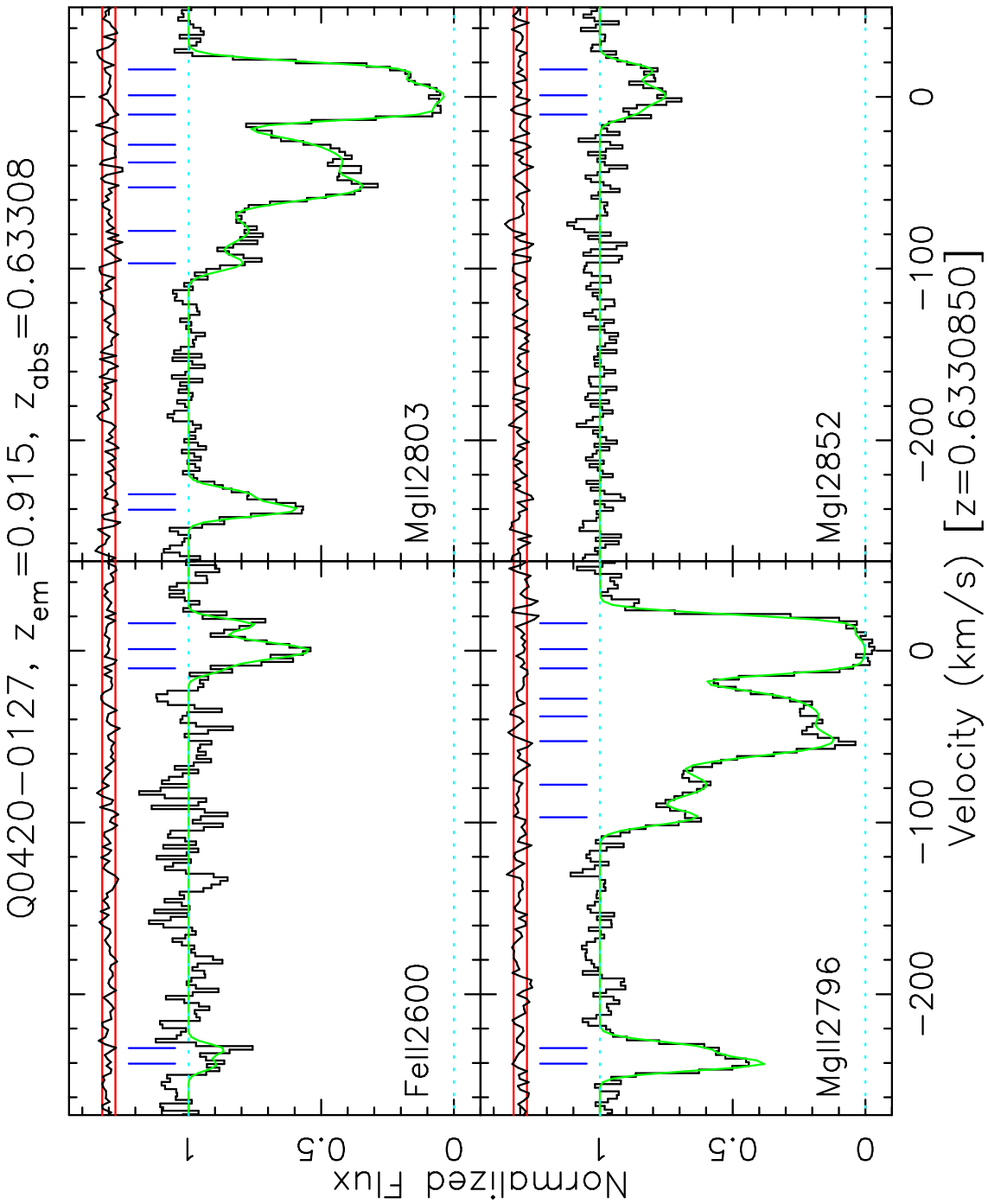

Figure C.6. Q0420−0127, $z_{\rm em} = 0.915$, $z_{\rm abs} = 0.63308$.

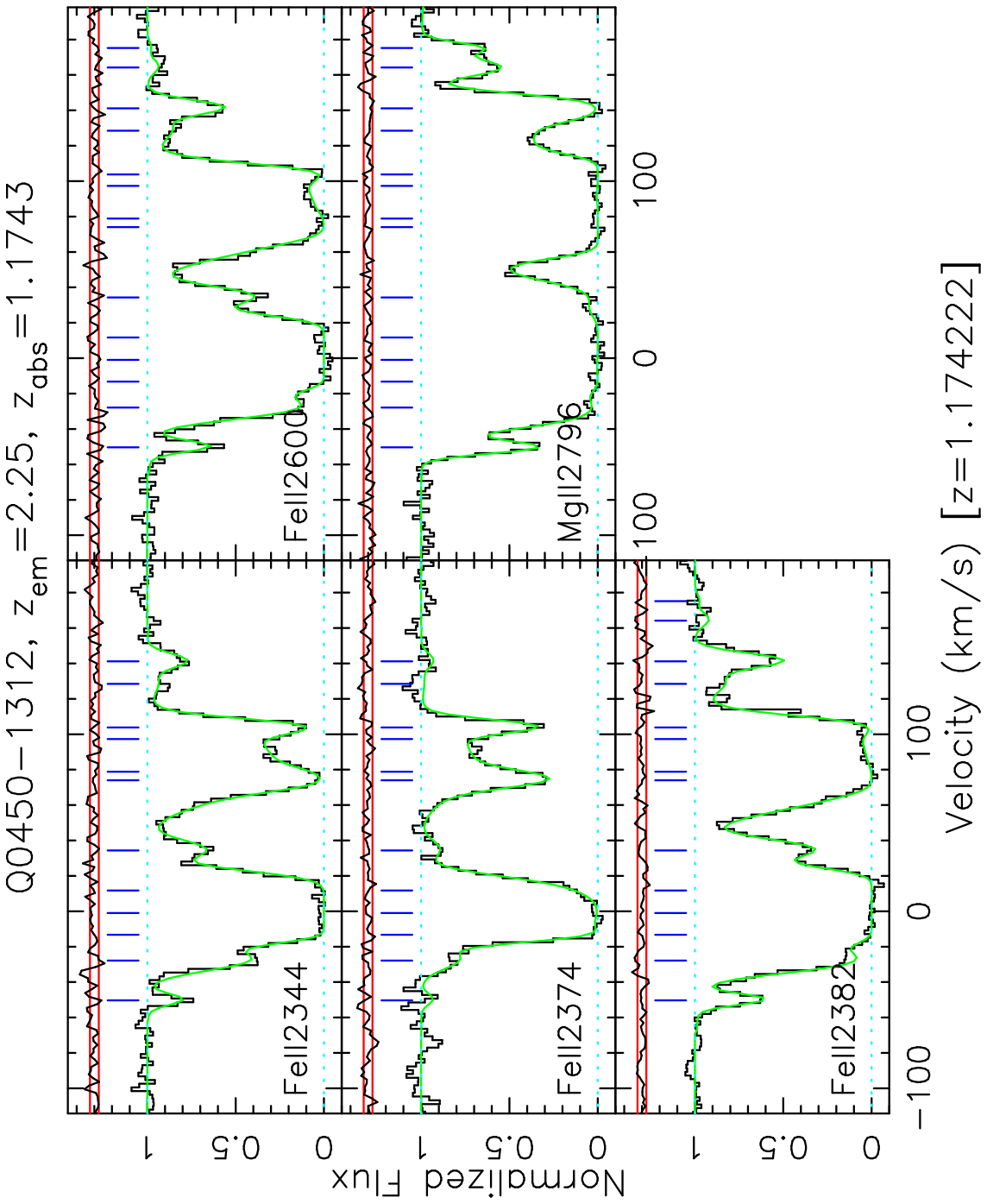

Figure C.7. Q0450−1312, $z_{\rm em} = 2.25$, $z_{\rm abs} = 1.1743$.

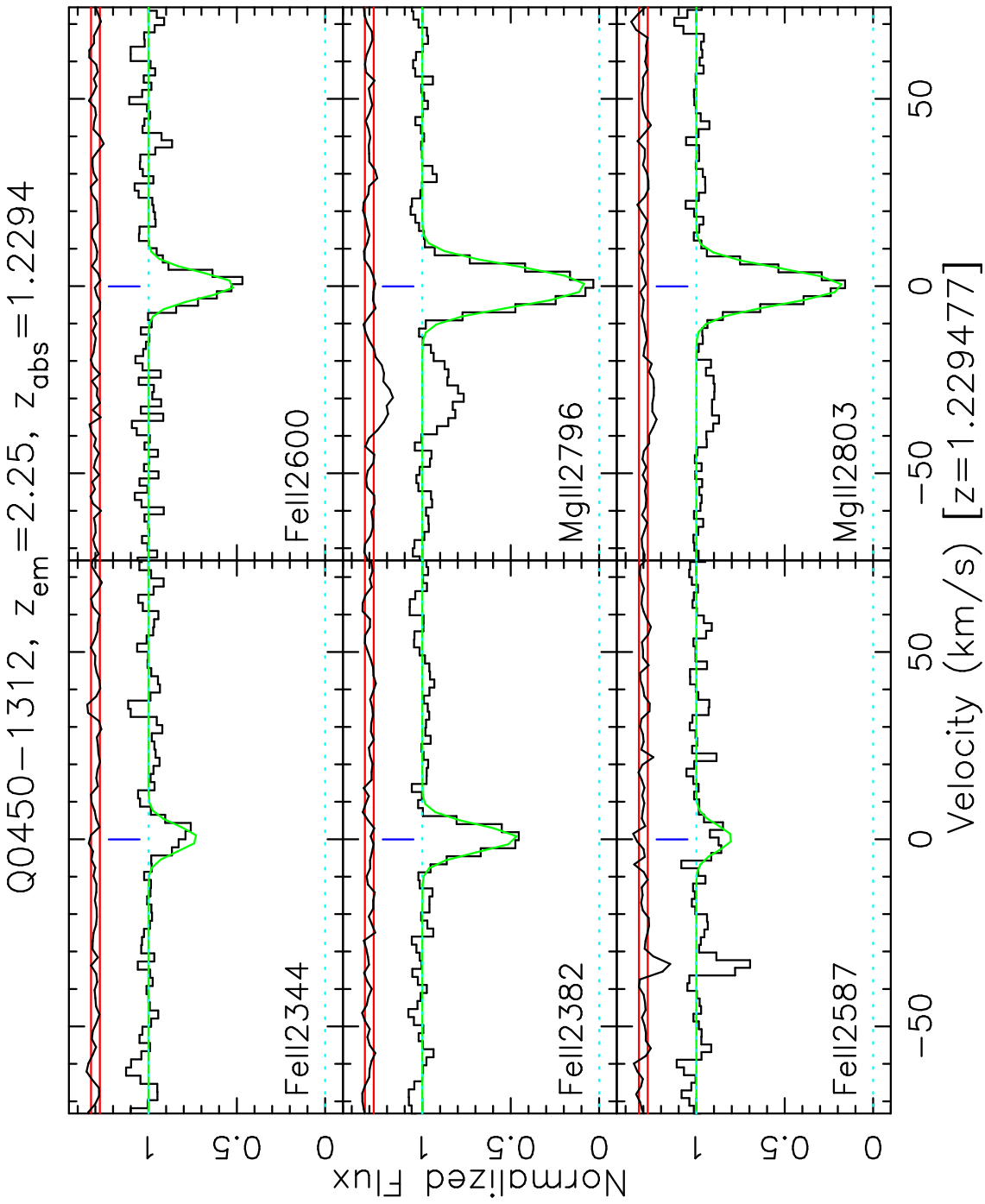

Figure C.8. Q0450−1312, $z_{\rm em} = 2.25$, $z_{\rm abs} = 1.2294$.

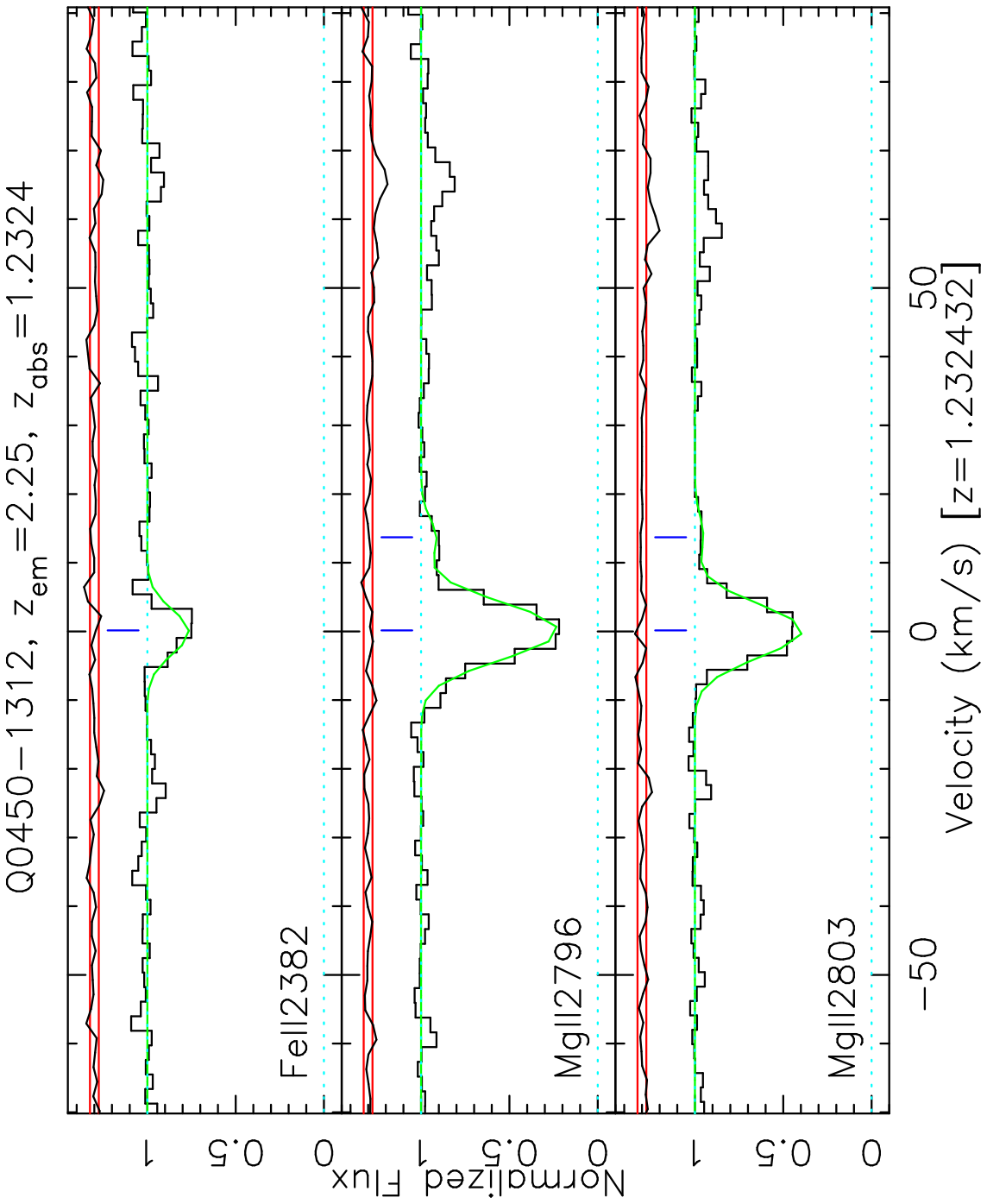

Figure C.9. Q0450−1312, $z_{\rm em} = 2.25$, $z_{\rm abs} = 1.2324$.

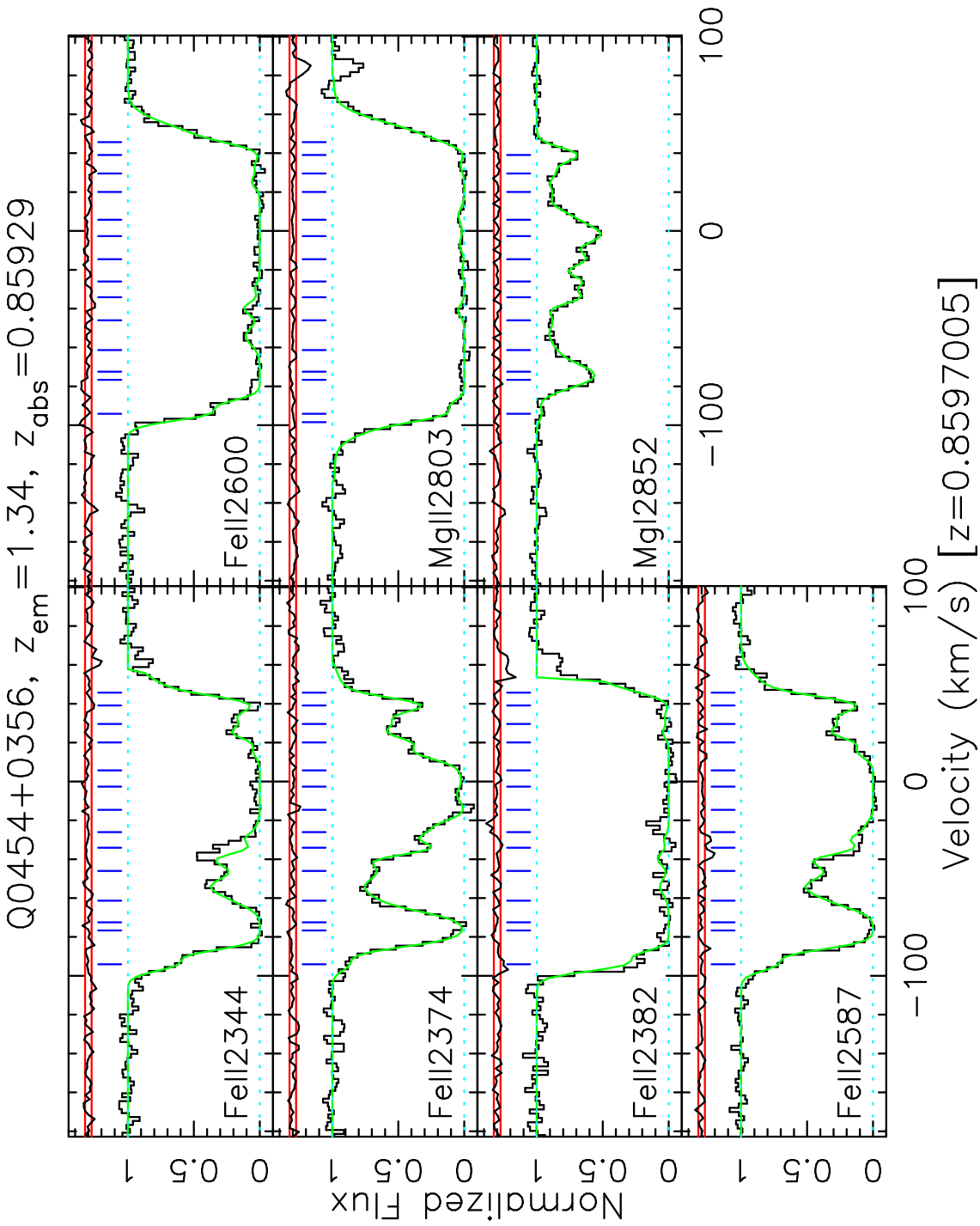

Figure C.10. Q0454+0356, $z_{\rm em} = 1.34$, $z_{\rm abs} = 0.85929$.

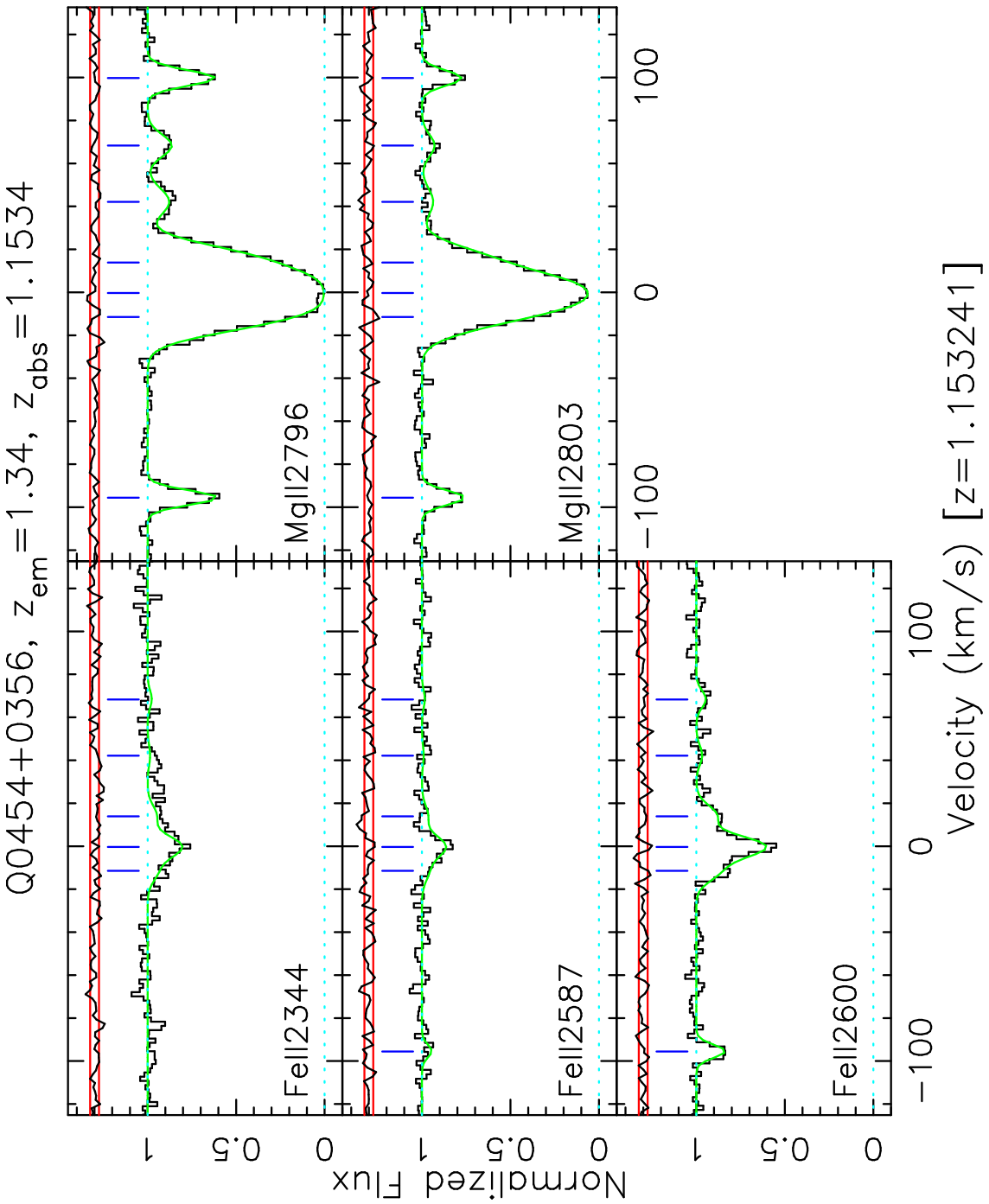

Figure C.11. Q0454+0356, $z_{\rm em} = 1.34$, $z_{\rm abs} = 1.1534$.

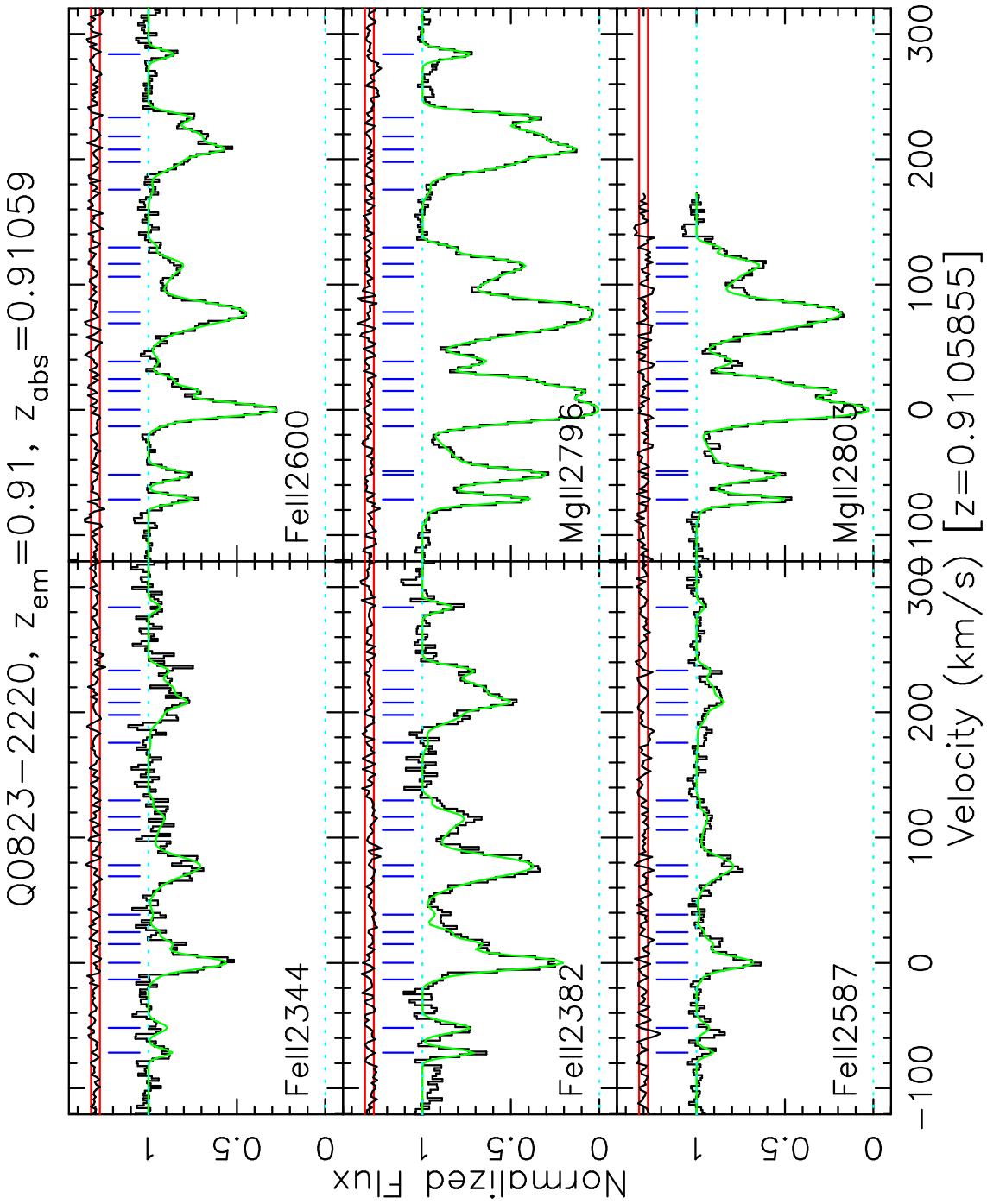

Figure C.12. Q0823−2220, $z_{\rm em} = 0.91$, $z_{\rm abs} = 0.91059$.

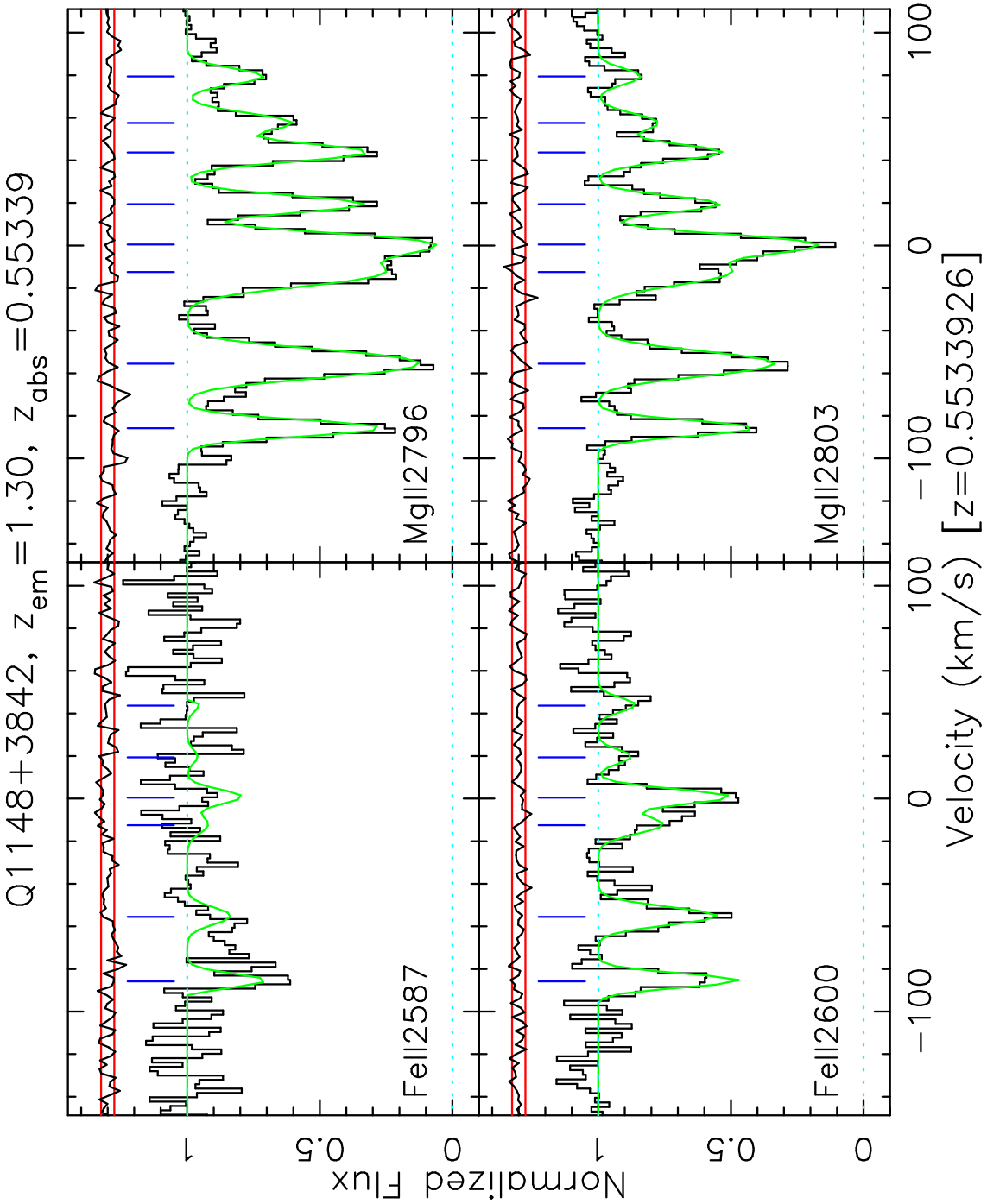

Figure C.13. Q1148+3842, $z_{\rm em} = 1.30$, $z_{\rm abs} = 0.55339$.

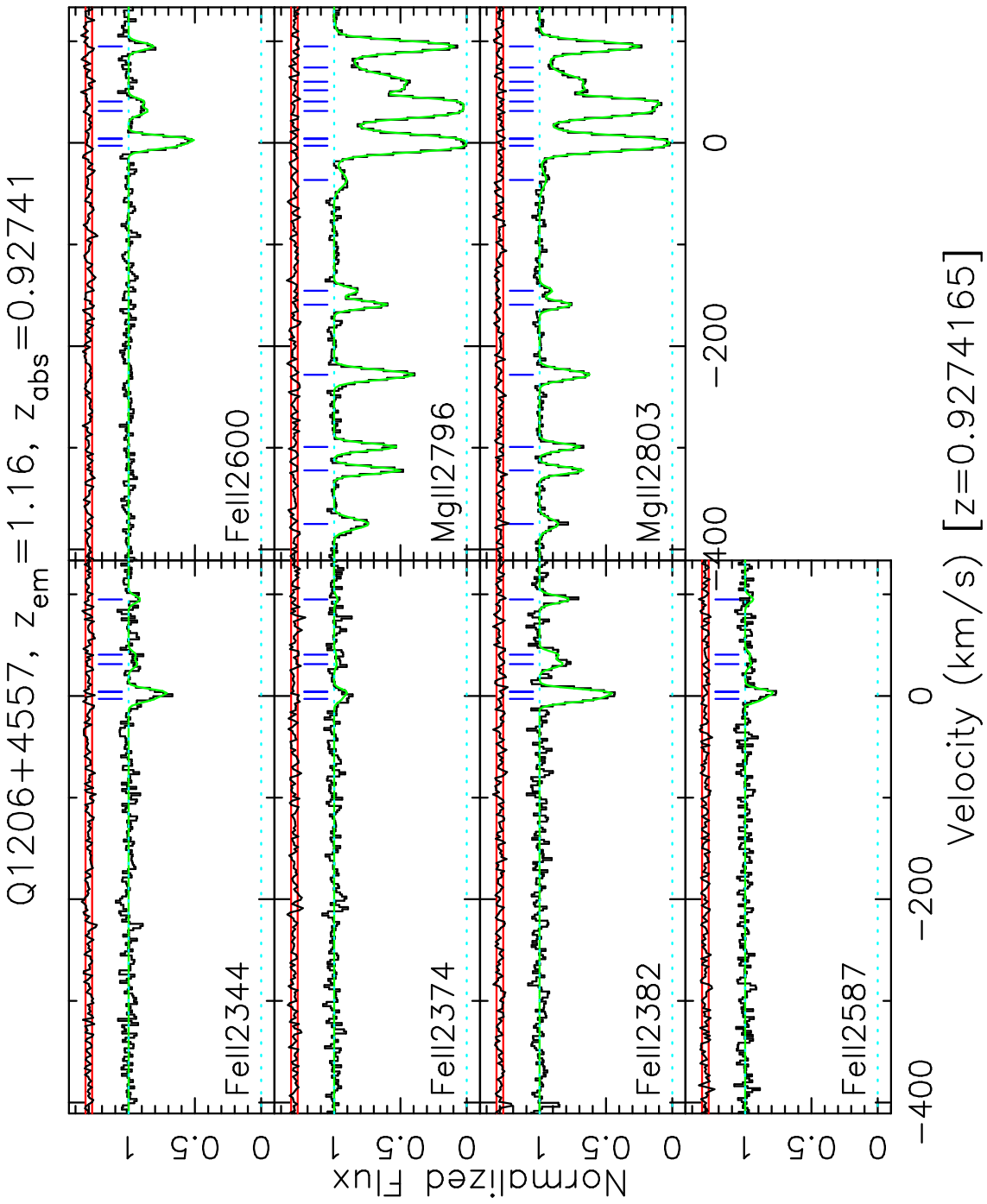

Figure C.14. Q1206+4557, $z_{\rm em} = 1.16$, $z_{\rm abs} = 0.92741$.

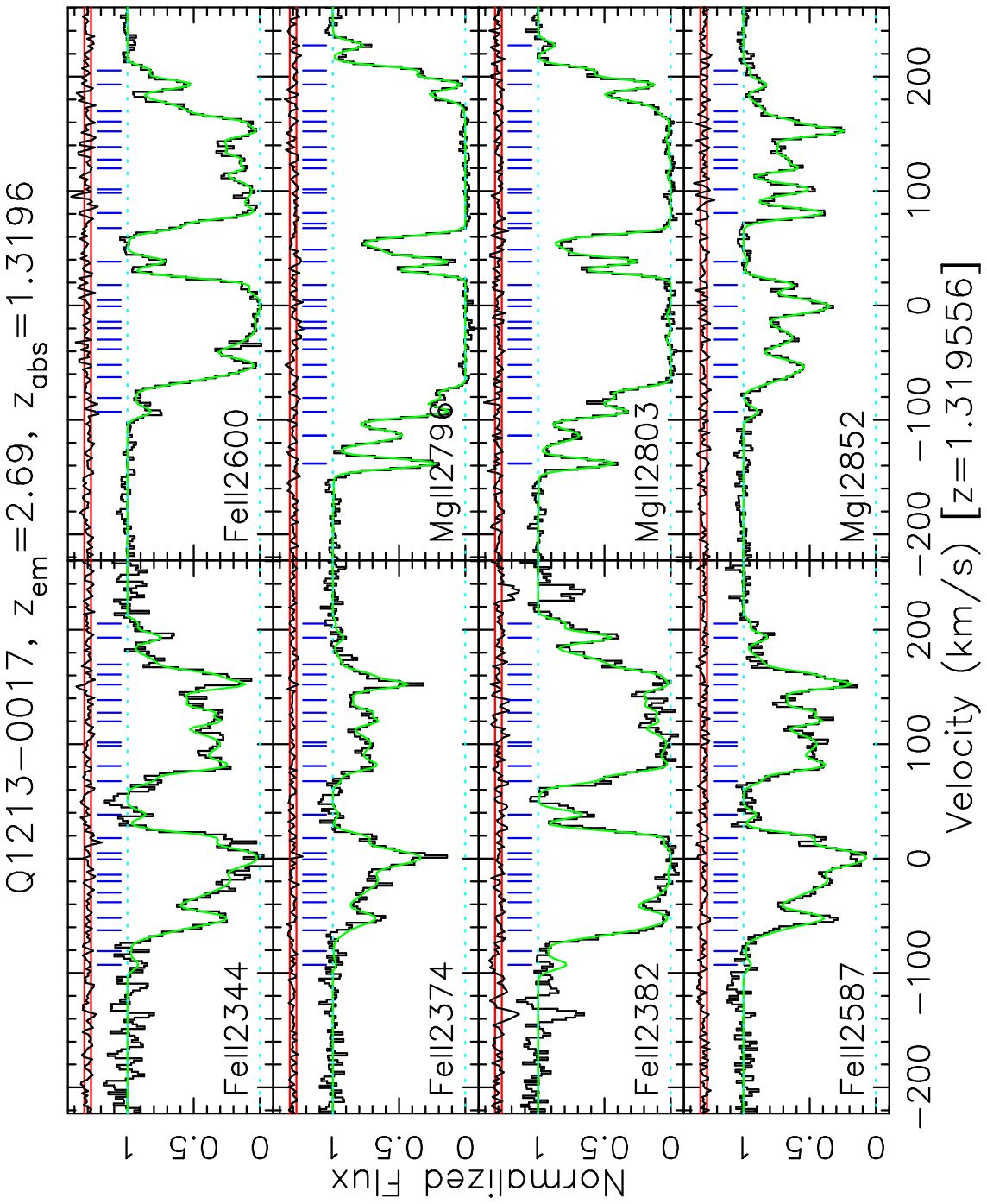

Figure C.15. Q1213−0017, $z_{\rm em} = 2.69$, $z_{\rm abs} = 1.3196$.

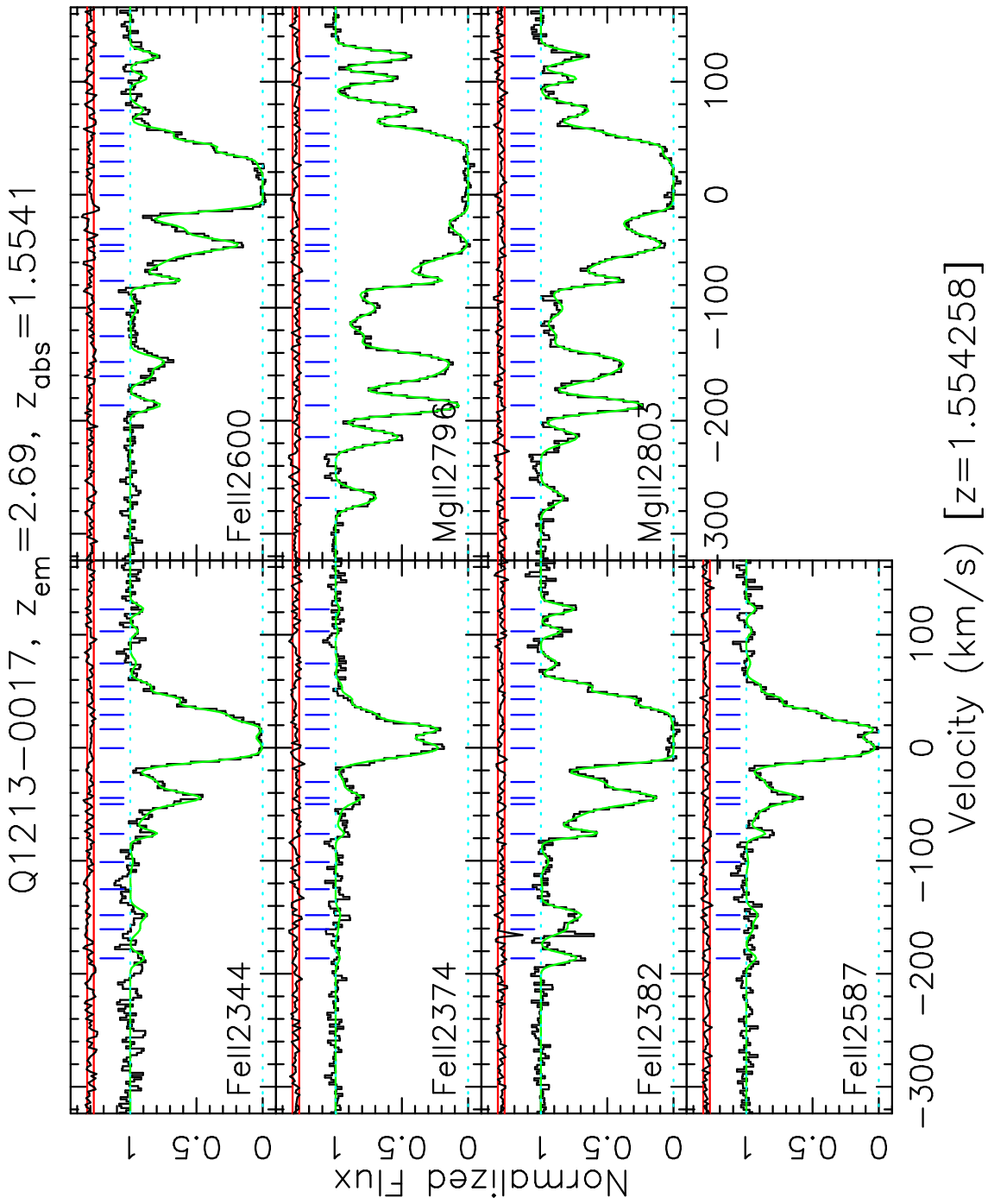

Figure C.16. Q1213−0017, $z_{\rm em} = 2.69$, $z_{\rm abs} = 1.5541$.

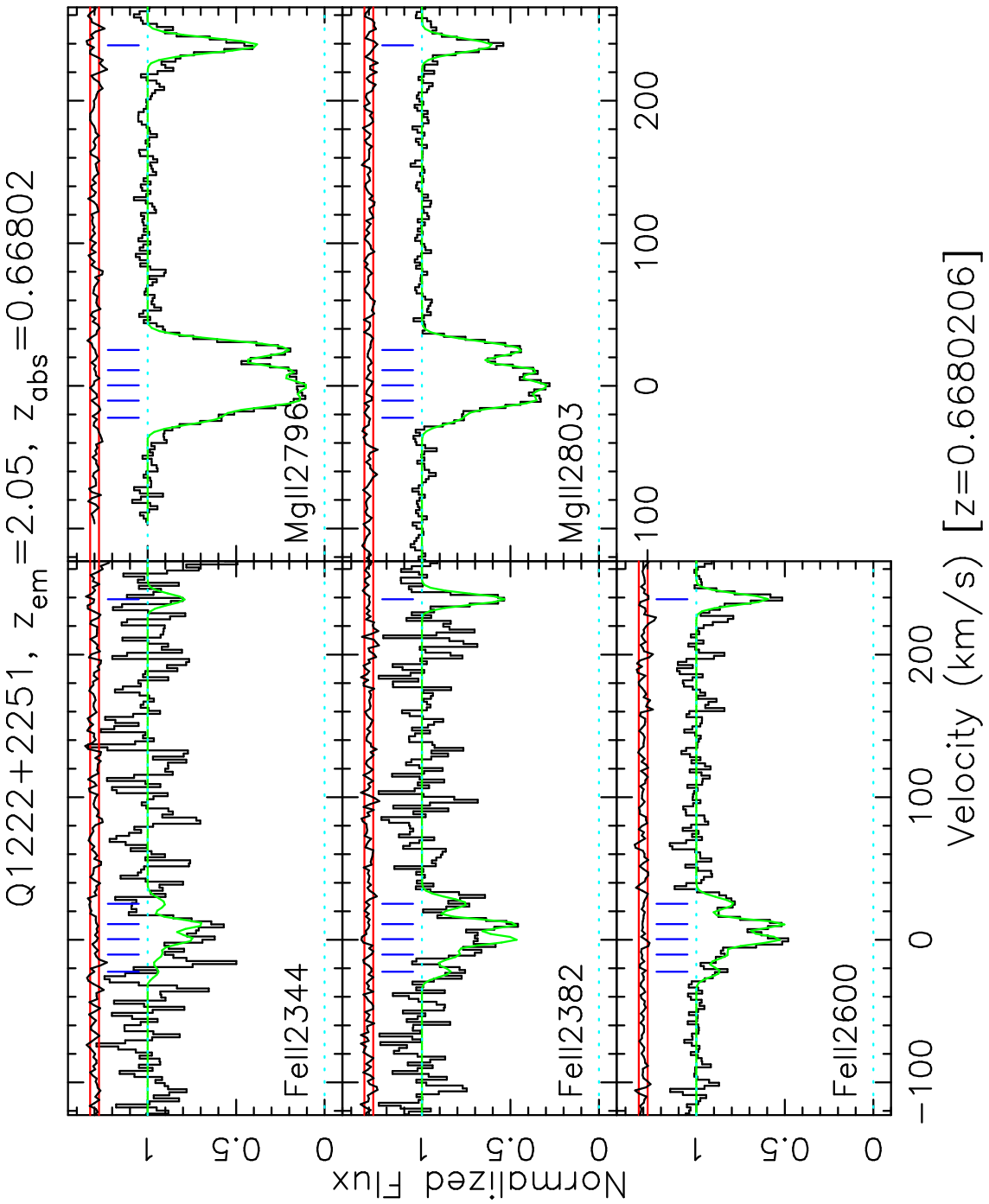

Figure C.17. Q1222+2251, $z_{\rm em} = 2.05$, $z_{\rm abs} = 0.66802$.

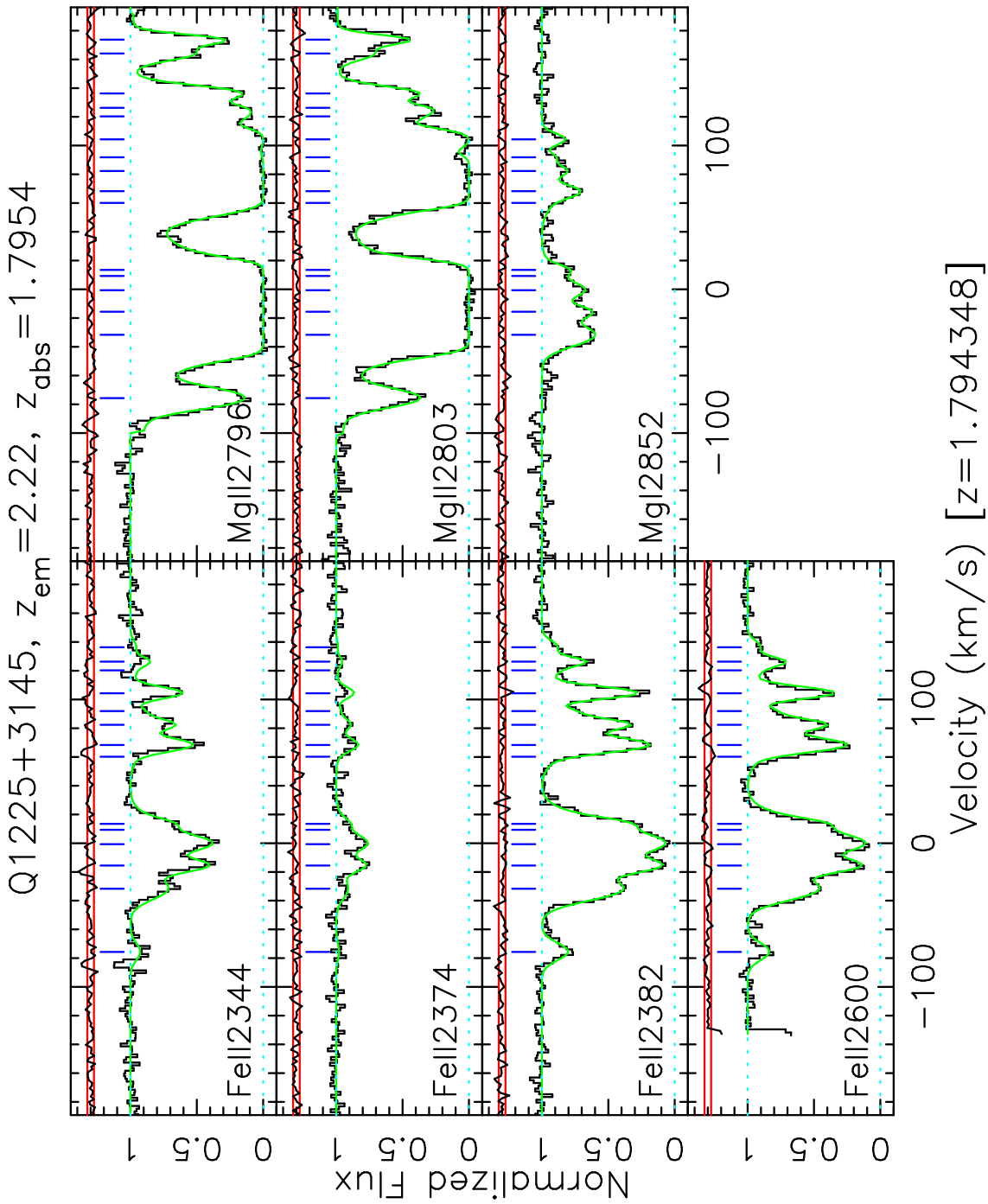

Figure C.18. Q1225+3145, $z_{\rm em} = 2.22$, $z_{\rm abs} = 1.7954$.

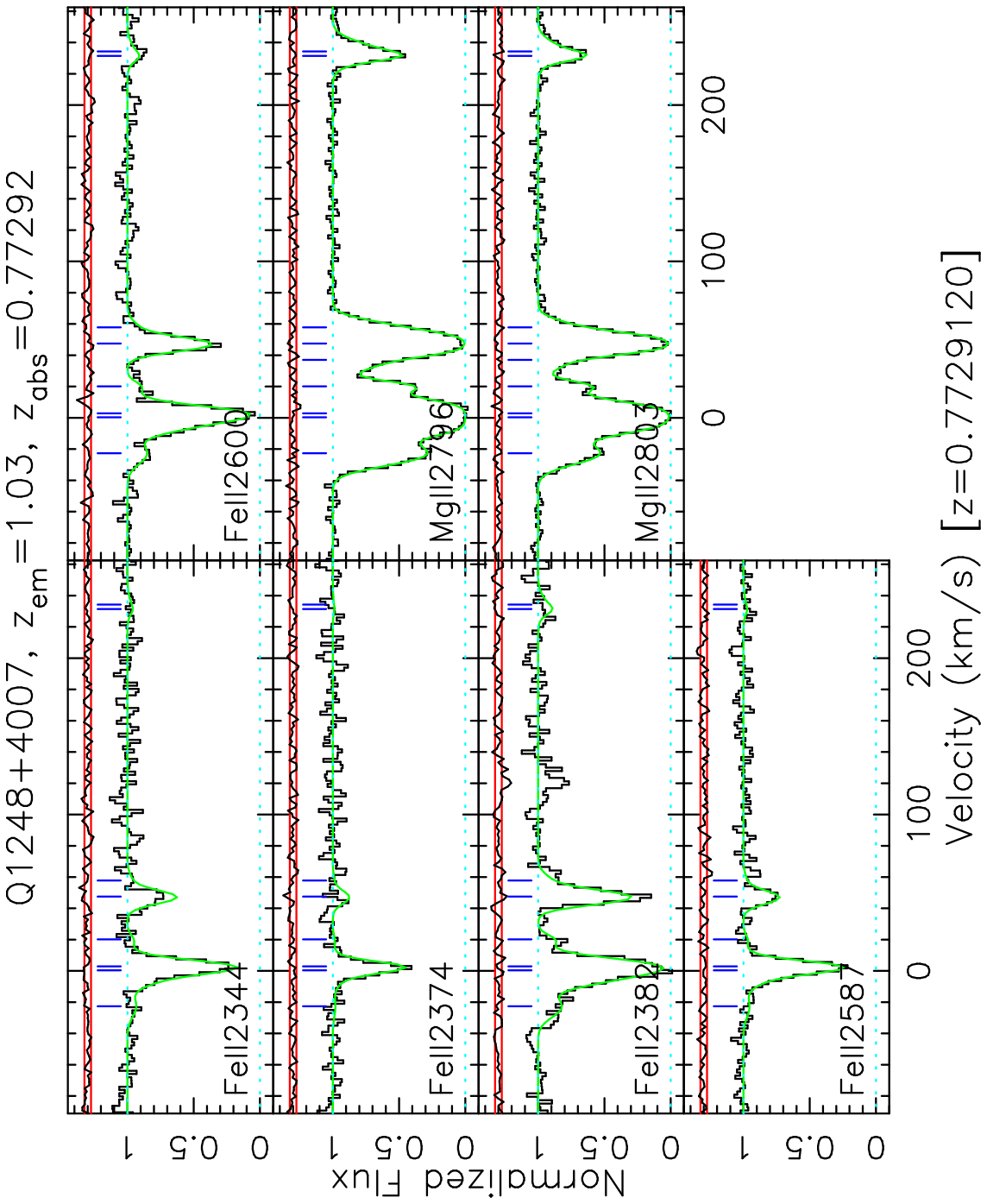

Figure C.19. Q1248+4007, $z_{\rm em} = 1.03$, $z_{\rm abs} = 0.77292$.

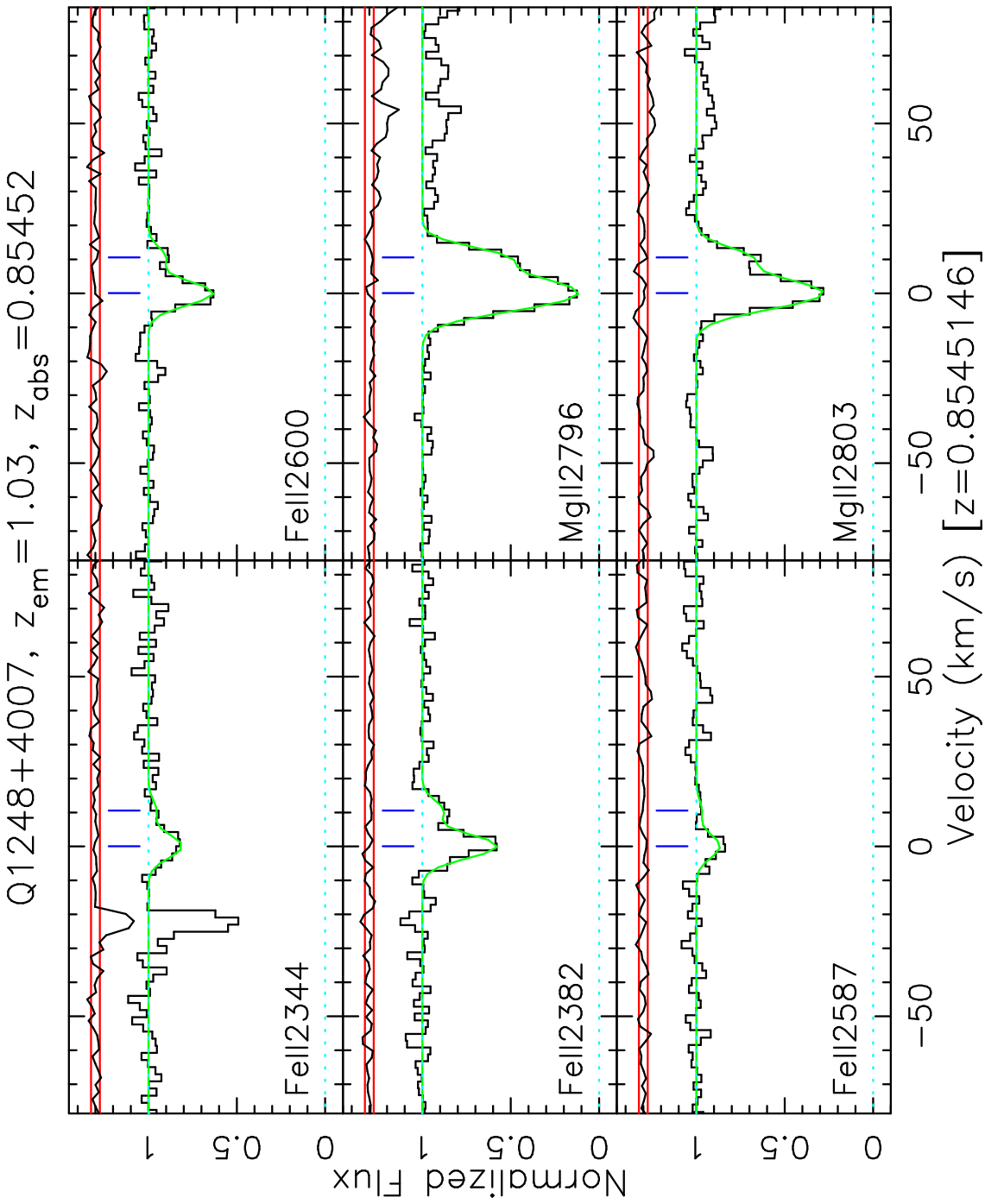

Figure C.20. Q1248+4007, $z_{\rm em} = 1.03$, $z_{\rm abs} = 0.85452$.

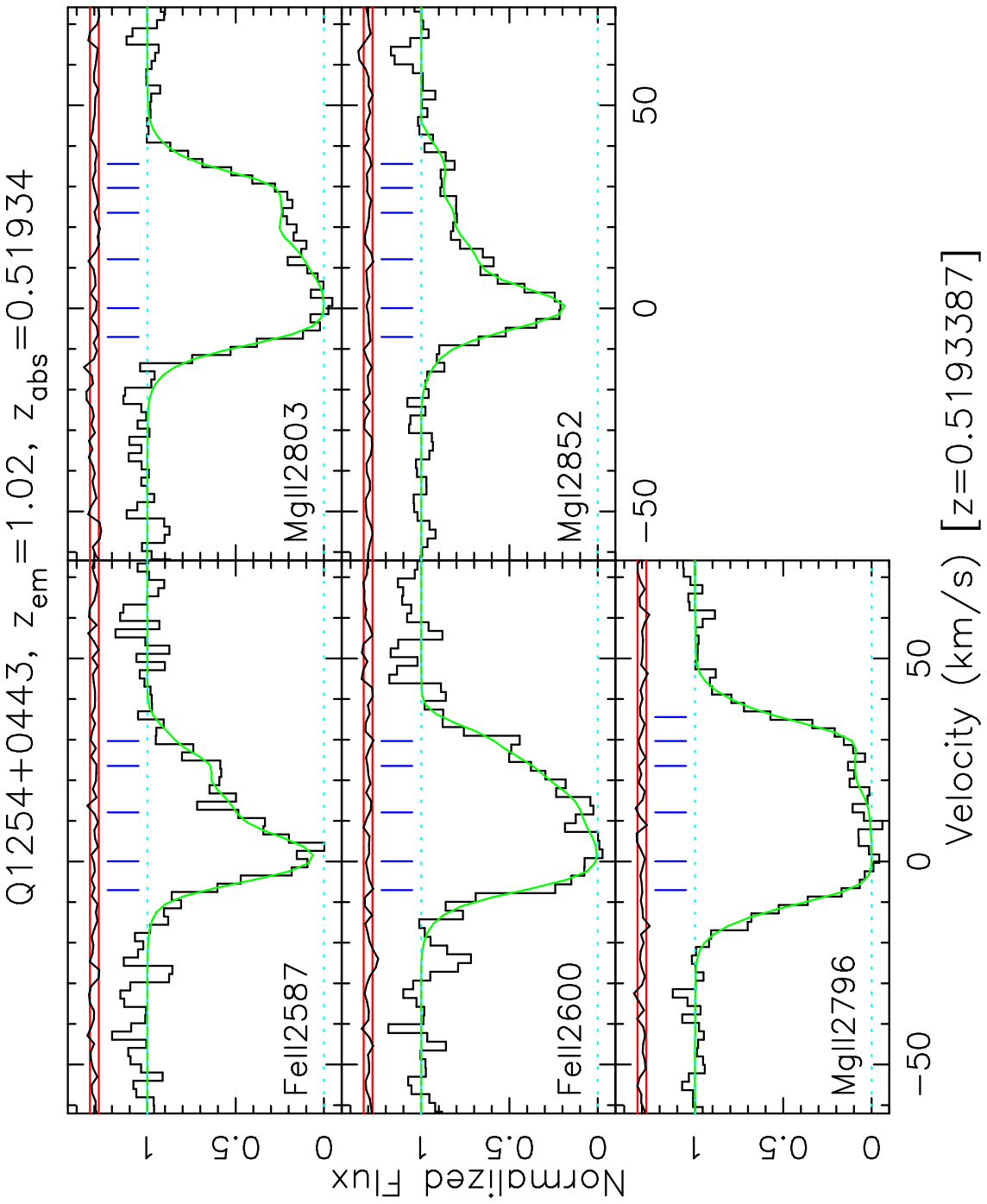

Figure C.21. Q1254+0443, $z_{\rm em} = 1.02$, $z_{\rm abs} = 0.51934$.

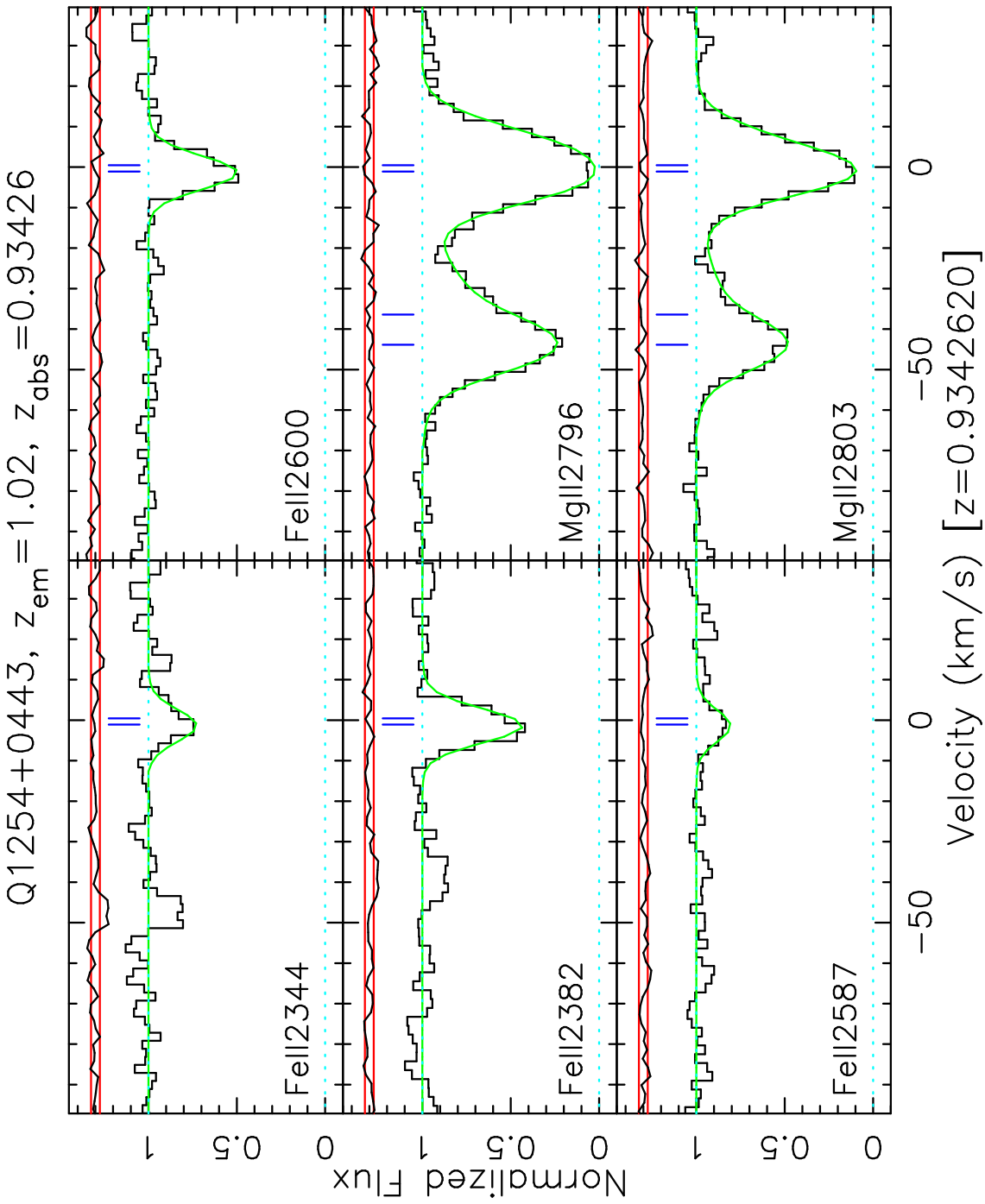

Figure C.22. Q1254+0443, $z_{\rm em} = 1.02$, $z_{\rm abs} = 0.93426$.

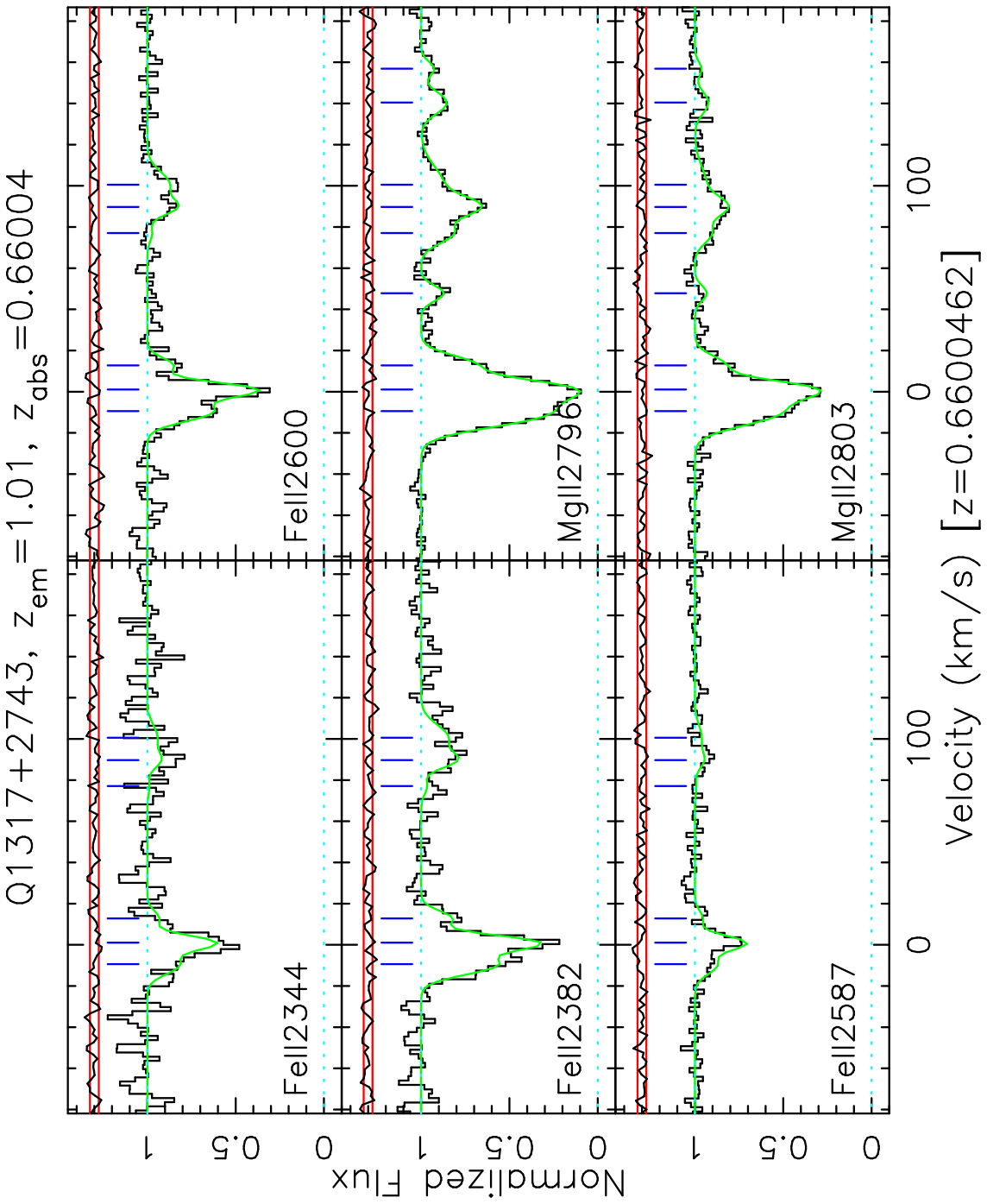

Figure C.23. Q1317+2743, $z_{\rm em} = 1.01$, $z_{\rm abs} = 0.66004$.

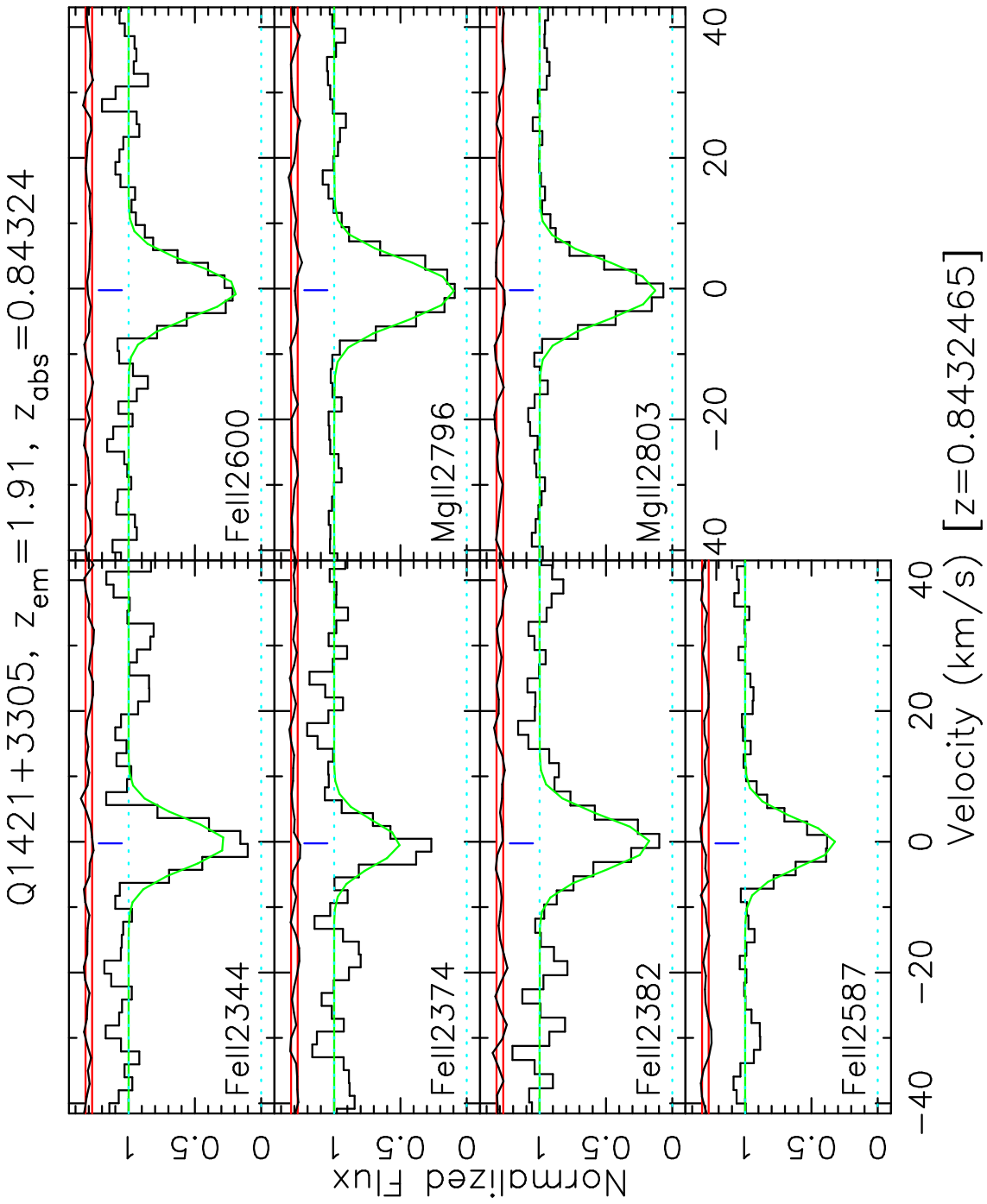

Figure C.24. Q1421+3305, $z_{\rm em} = 1.91$, $z_{\rm abs} = 0.84324$.

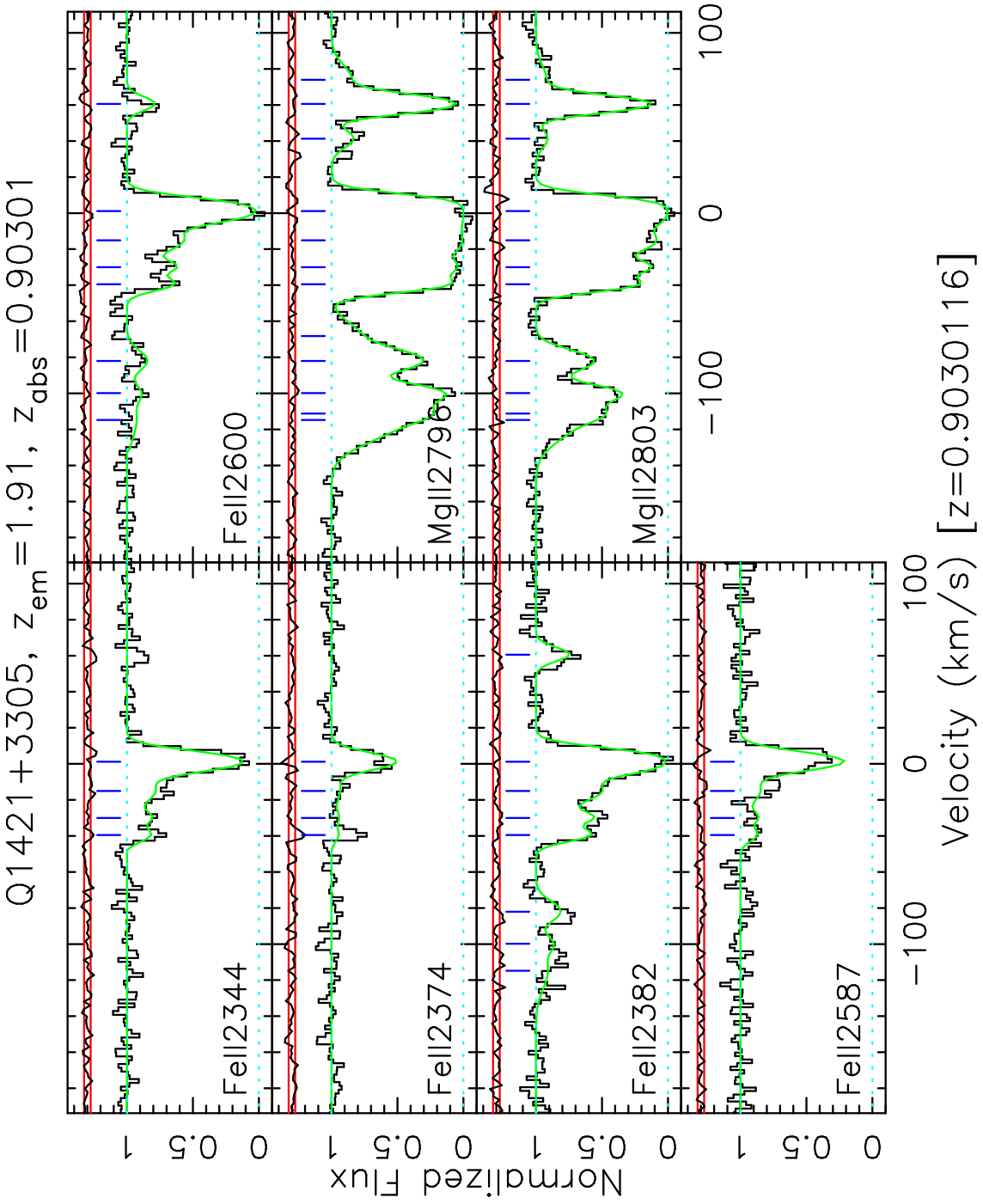

Figure C.25. Q1421+3305, $z_{\rm em} = 1.91$, $z_{\rm abs} = 0.90301$.

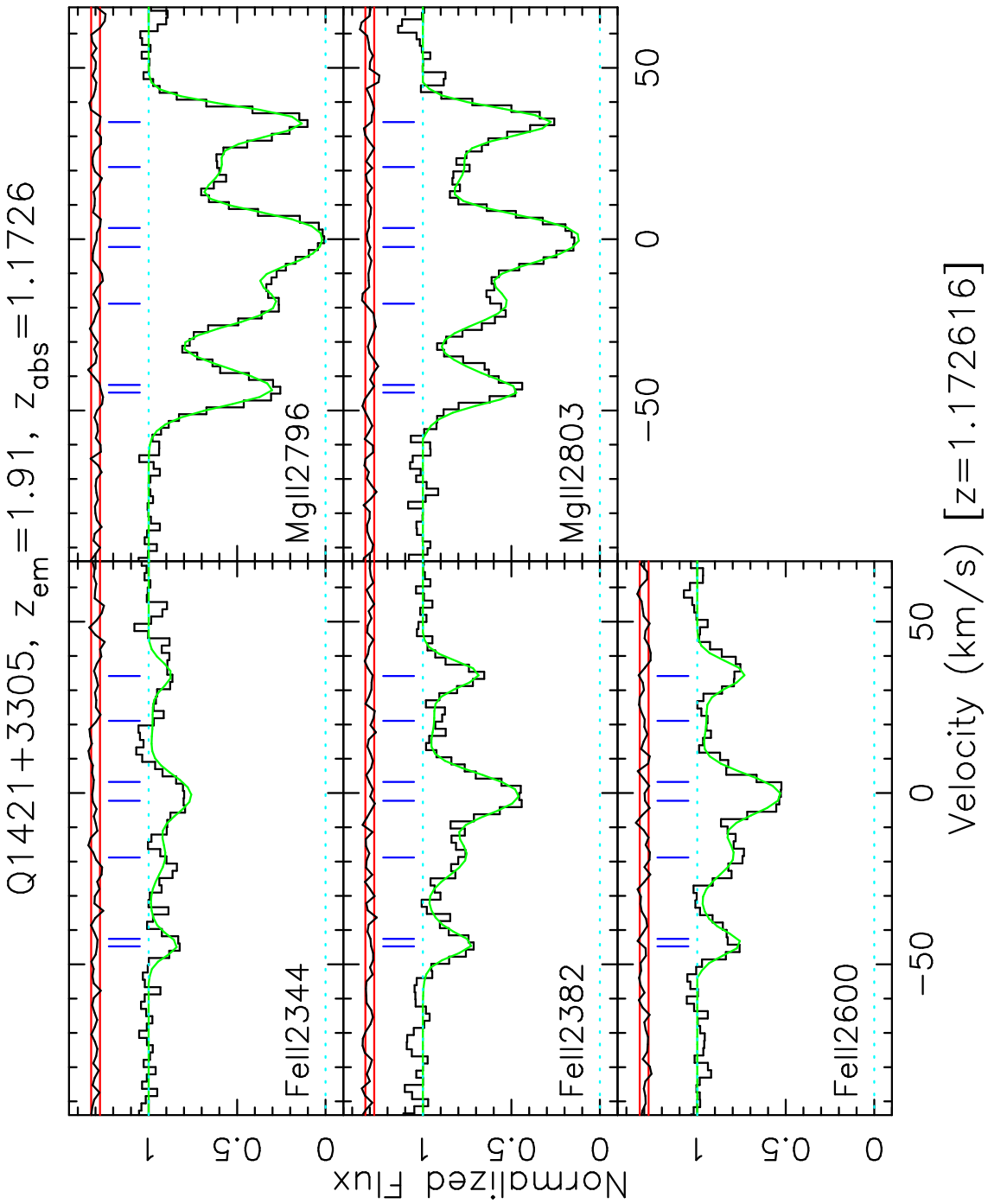

Figure C.26. Q1421+3305, $z_{\rm em} = 1.91$, $z_{\rm abs} = 1.1726$.

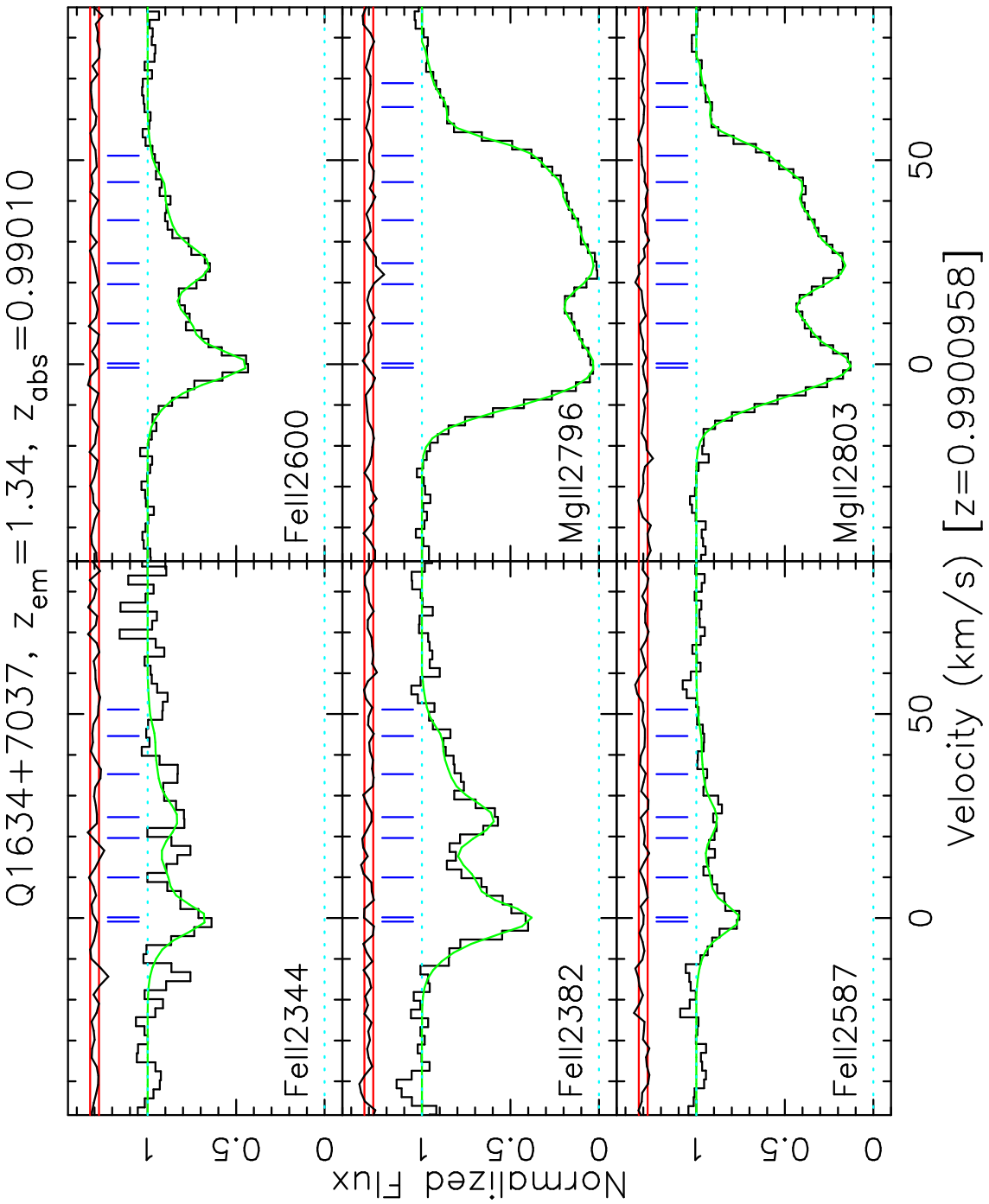

Figure C.27. Q1634+7037, $z_{\rm em} = 1.34$, $z_{\rm abs} = 0.99010$.

C-2 Sample 2

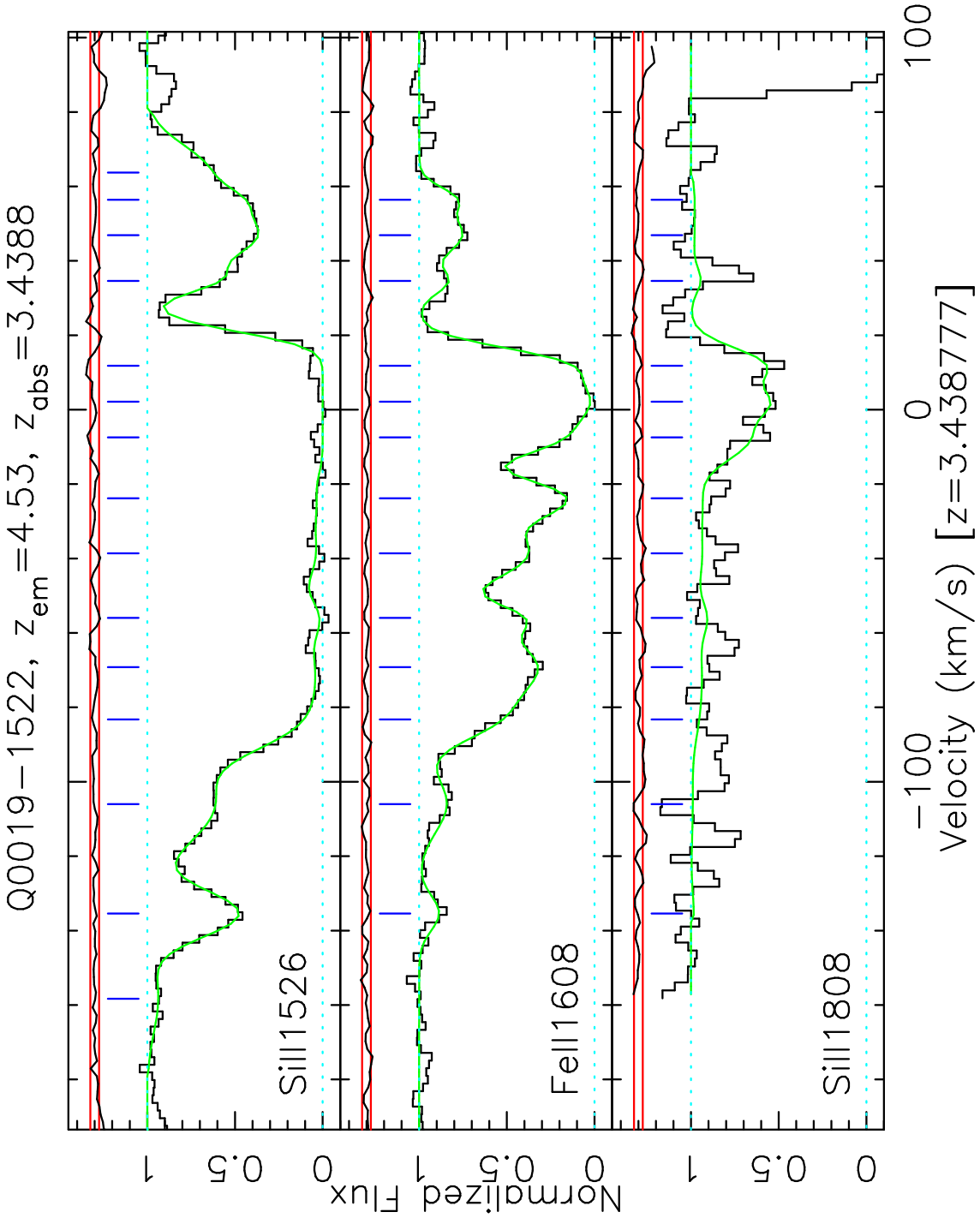

Figure C.28. Q0019−1522, $z_{\rm em} = 4.53$, $z_{\rm abs} = 3.4388$.

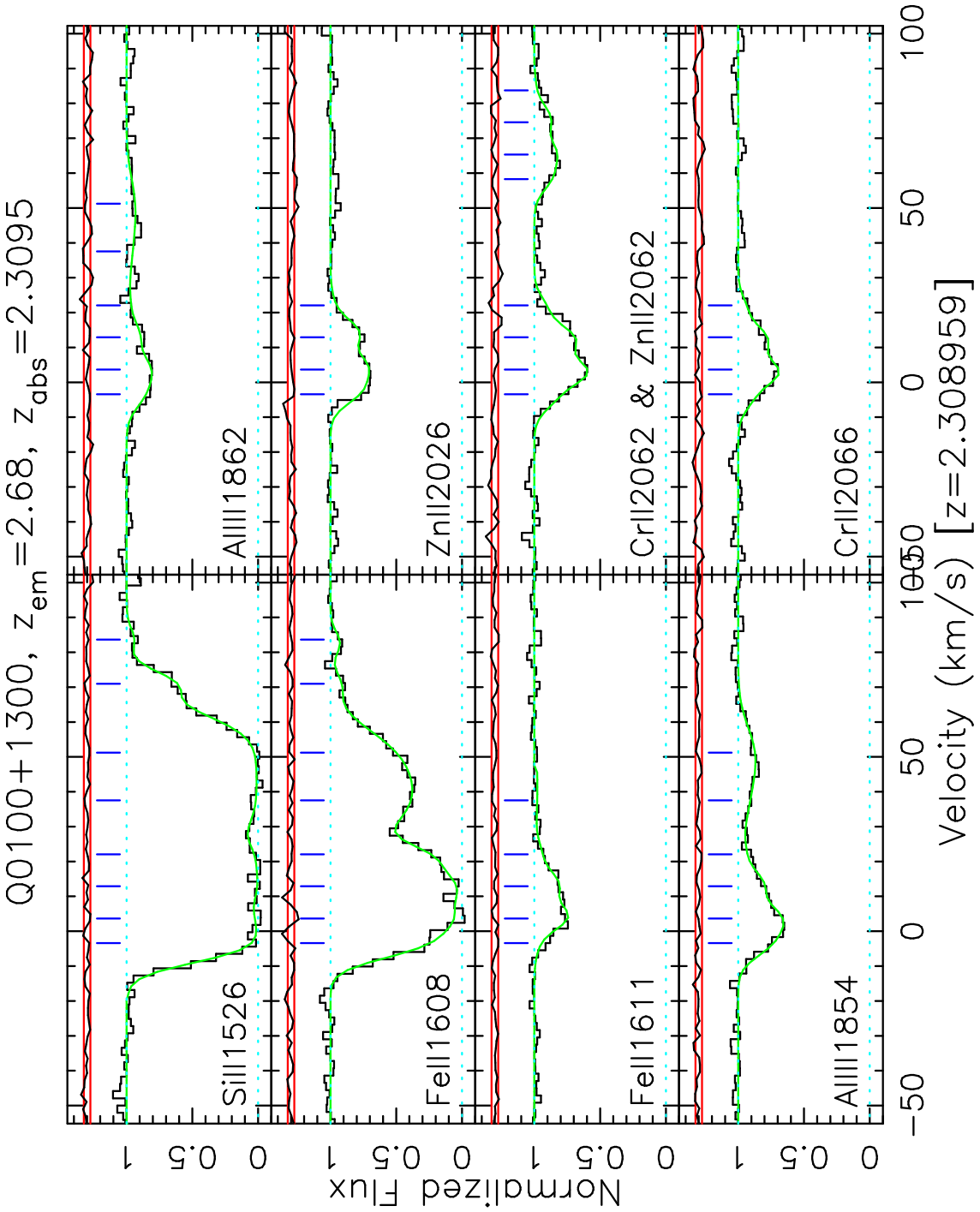

Figure C.29. Q0100+1300, $z_{\rm em} = 2.68$, $z_{\rm abs} = 2.3095$.

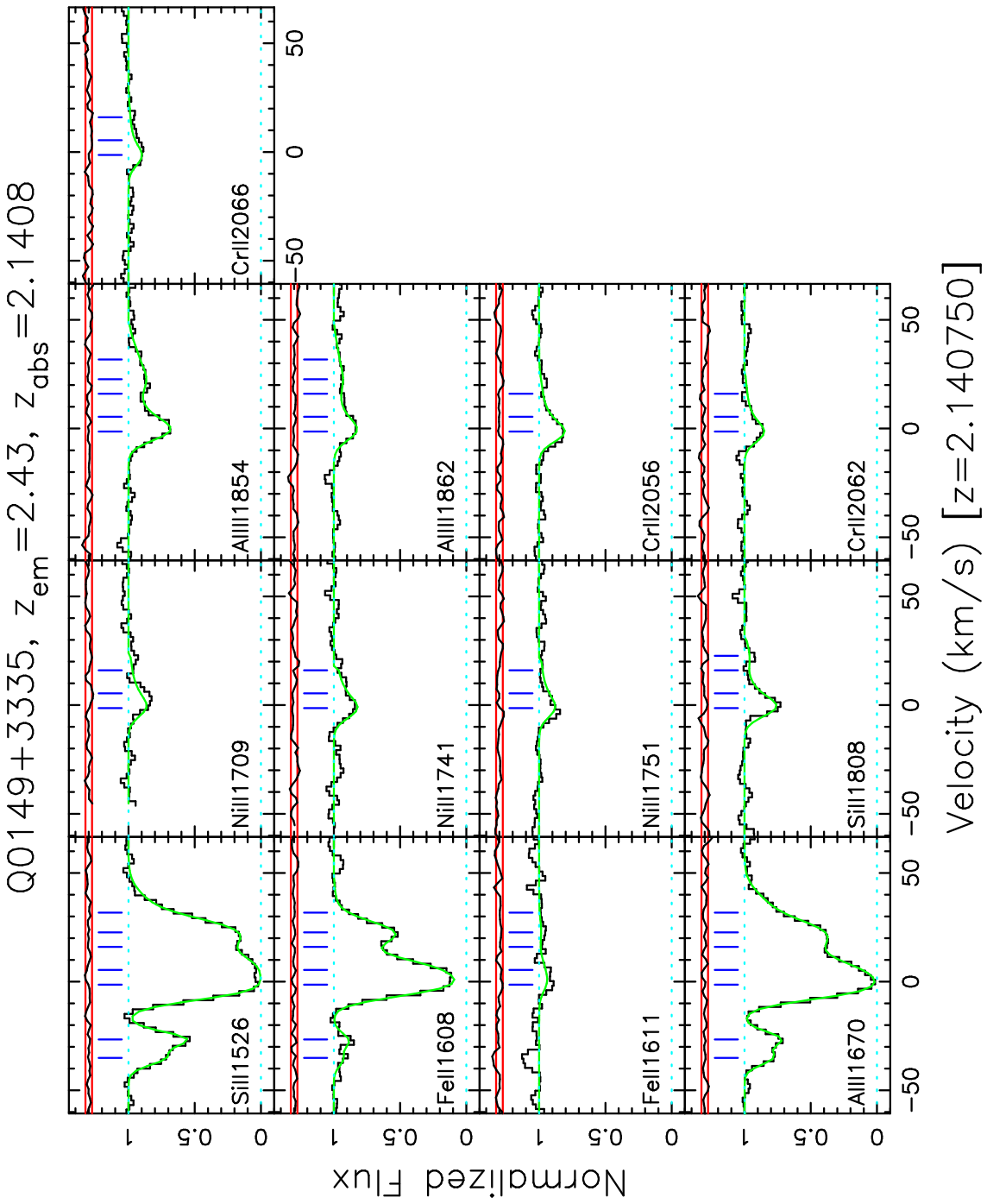

Figure C.30. Q0149+3335, $z_{\rm em} = 2.43$, $z_{\rm abs} = 2.1408$.

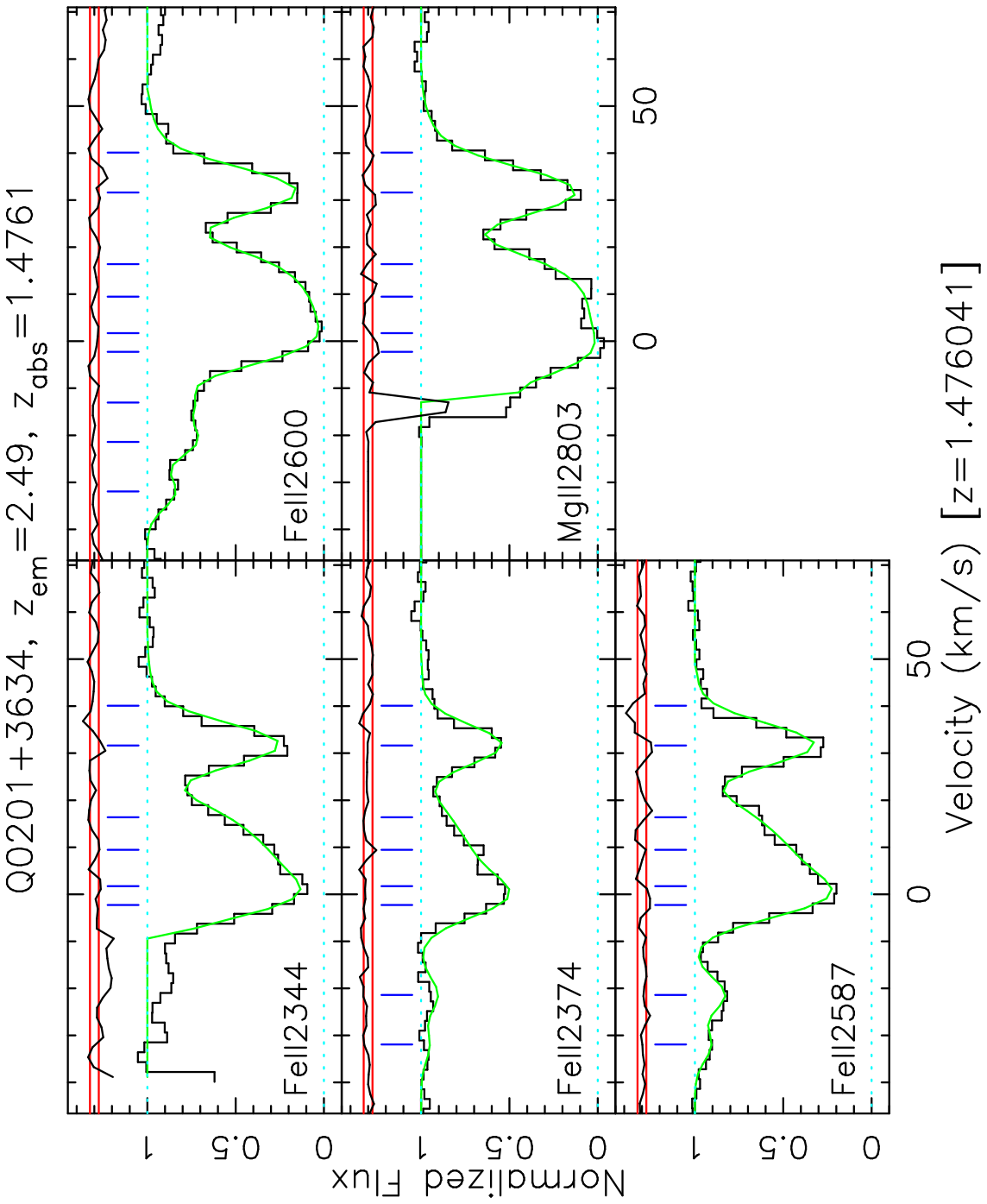

Figure C.31. Q0201+3634, $z_{\rm em} = 2.49$, $z_{\rm abs} = 1.4761$.

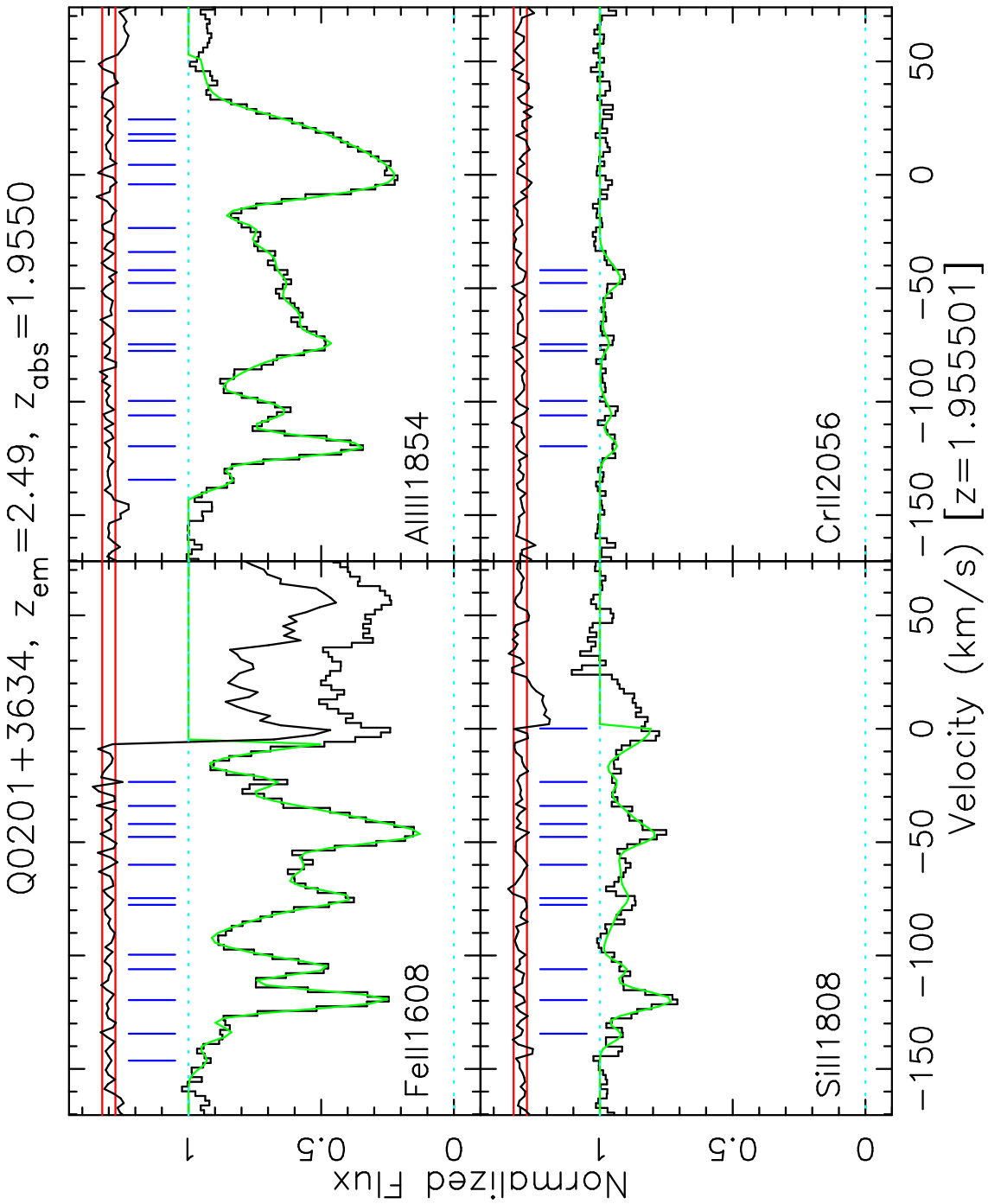

Figure C.32. Q0201+3634, $z_{\rm em} = 2.49$, $z_{\rm abs} = 1.9550$.

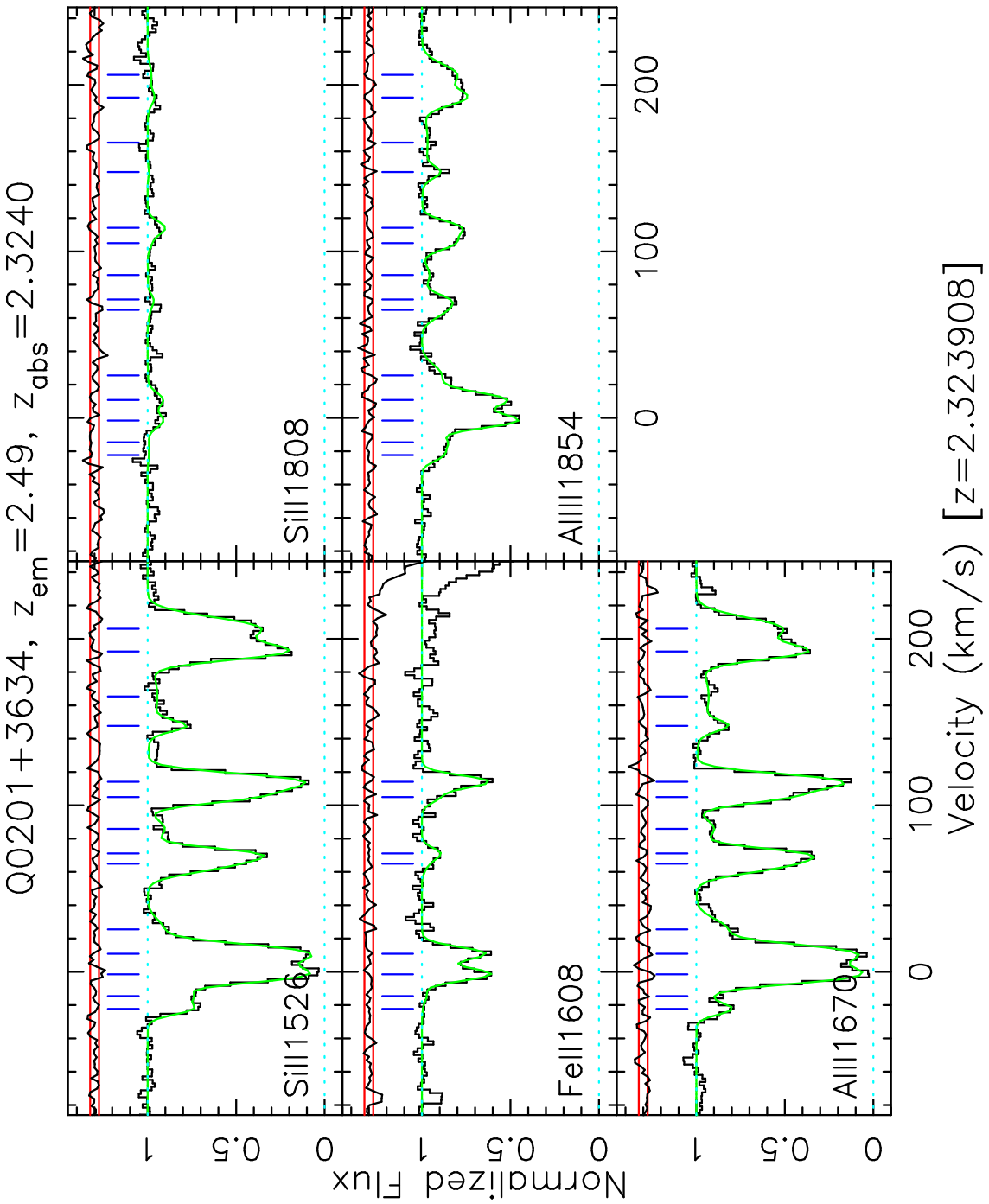

Figure C.33. Q0201+3634, $z_{\rm em} = 2.49$, $z_{\rm abs} = 2.3240$.

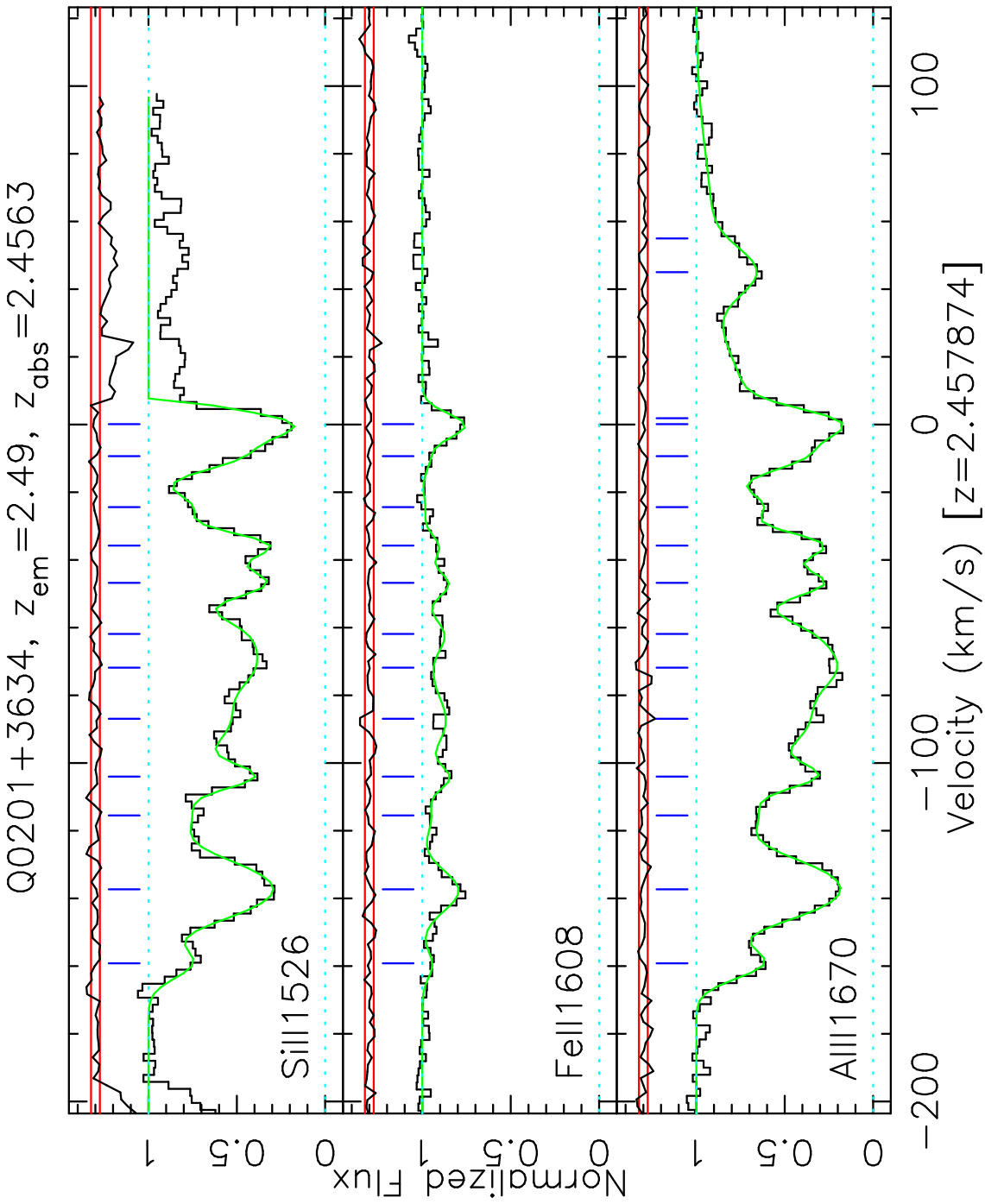

Figure C.34. Q0201+3634, $z_{\rm em} = 2.49$, $z_{\rm abs} = 2.4563$.

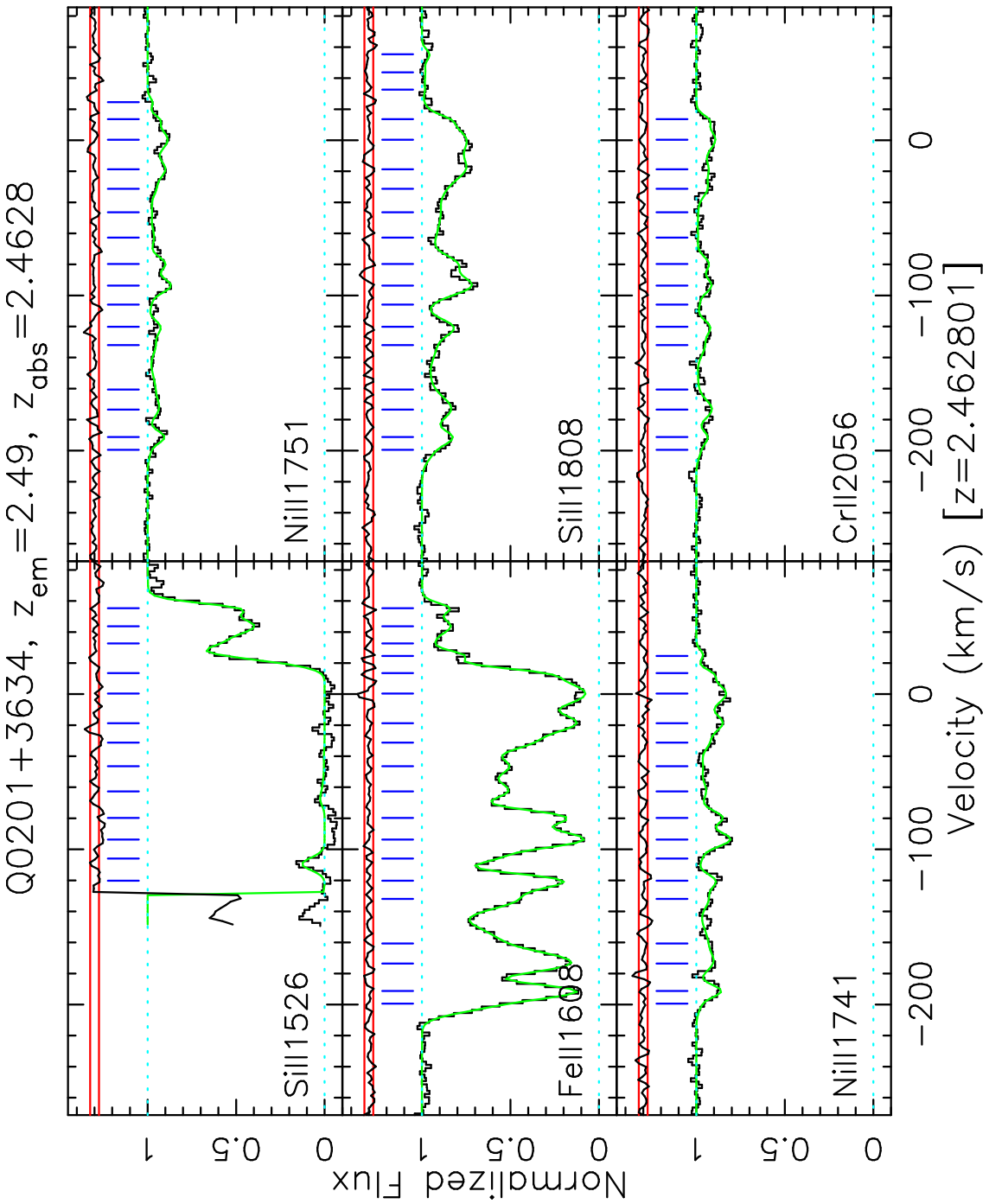

Figure C.35. Q0201+3634, $z_{\rm em} = 2.49$, $z_{\rm abs} = 2.4628$.

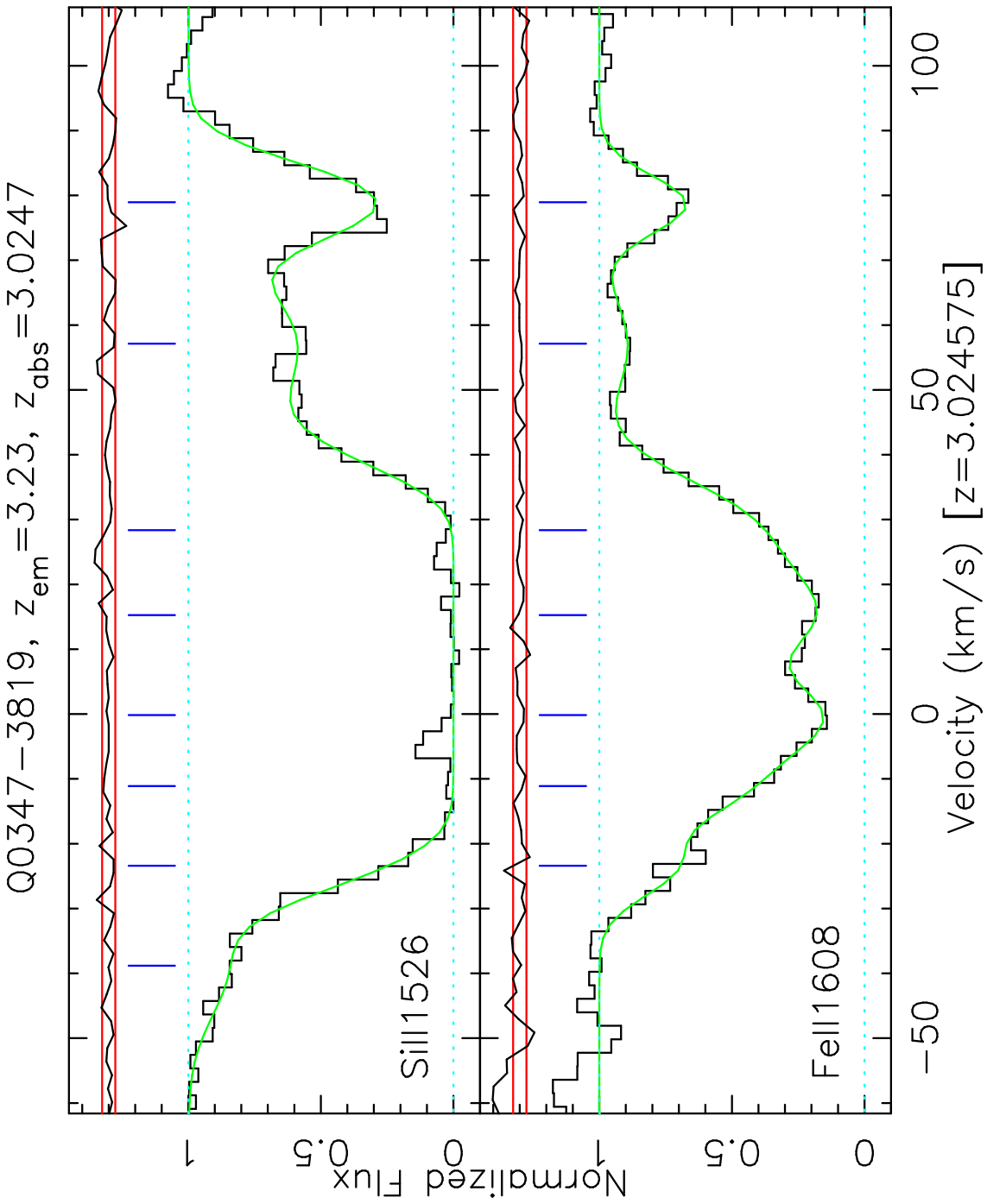

Figure C.36. Q0347−3819, $z_{\rm em} = 3.23$, $z_{\rm abs} = 3.0247$.

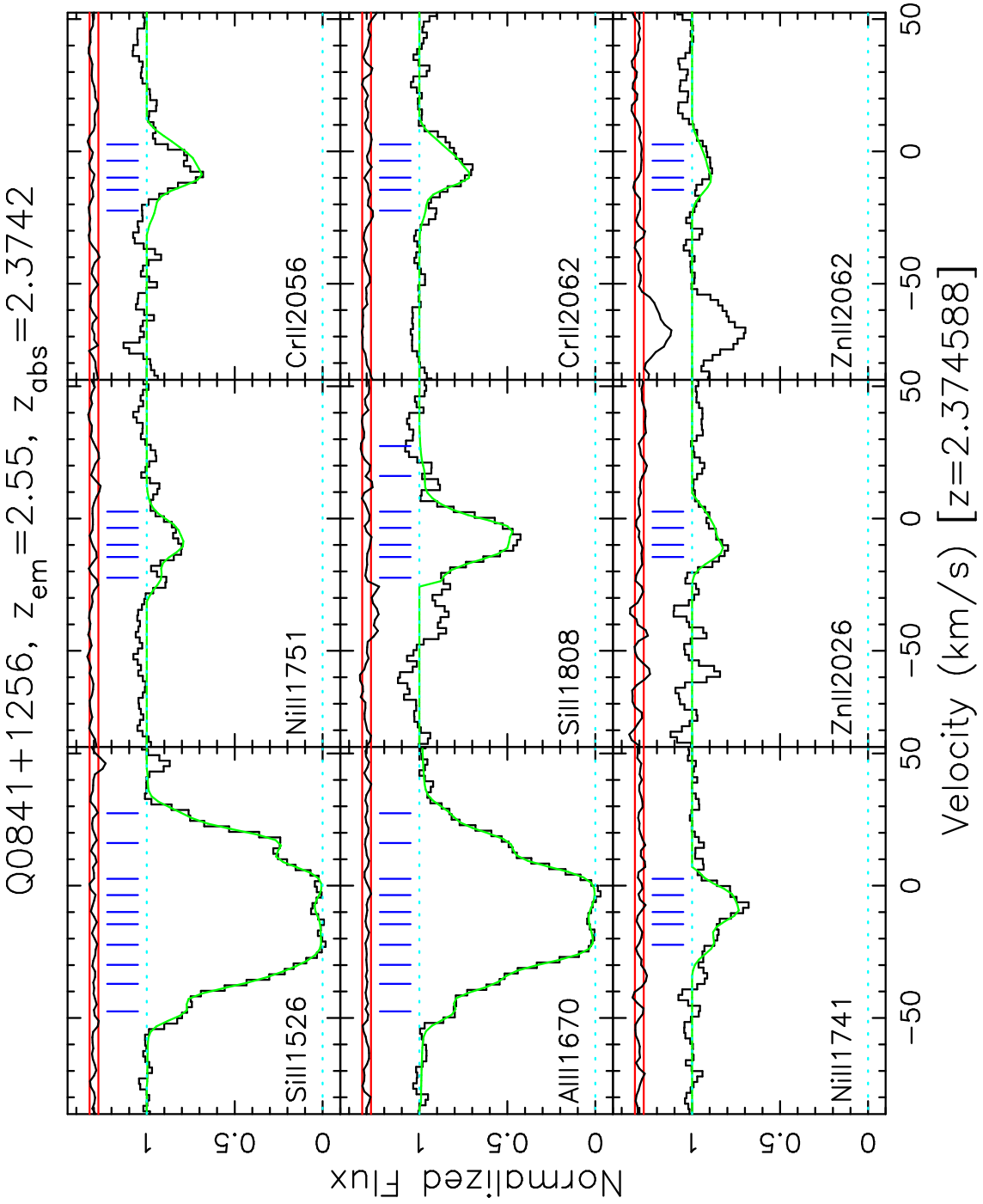

Figure C.37. Q0841+1256, $z_{\rm em} = 2.55$, $z_{\rm abs} = 2.3742$.

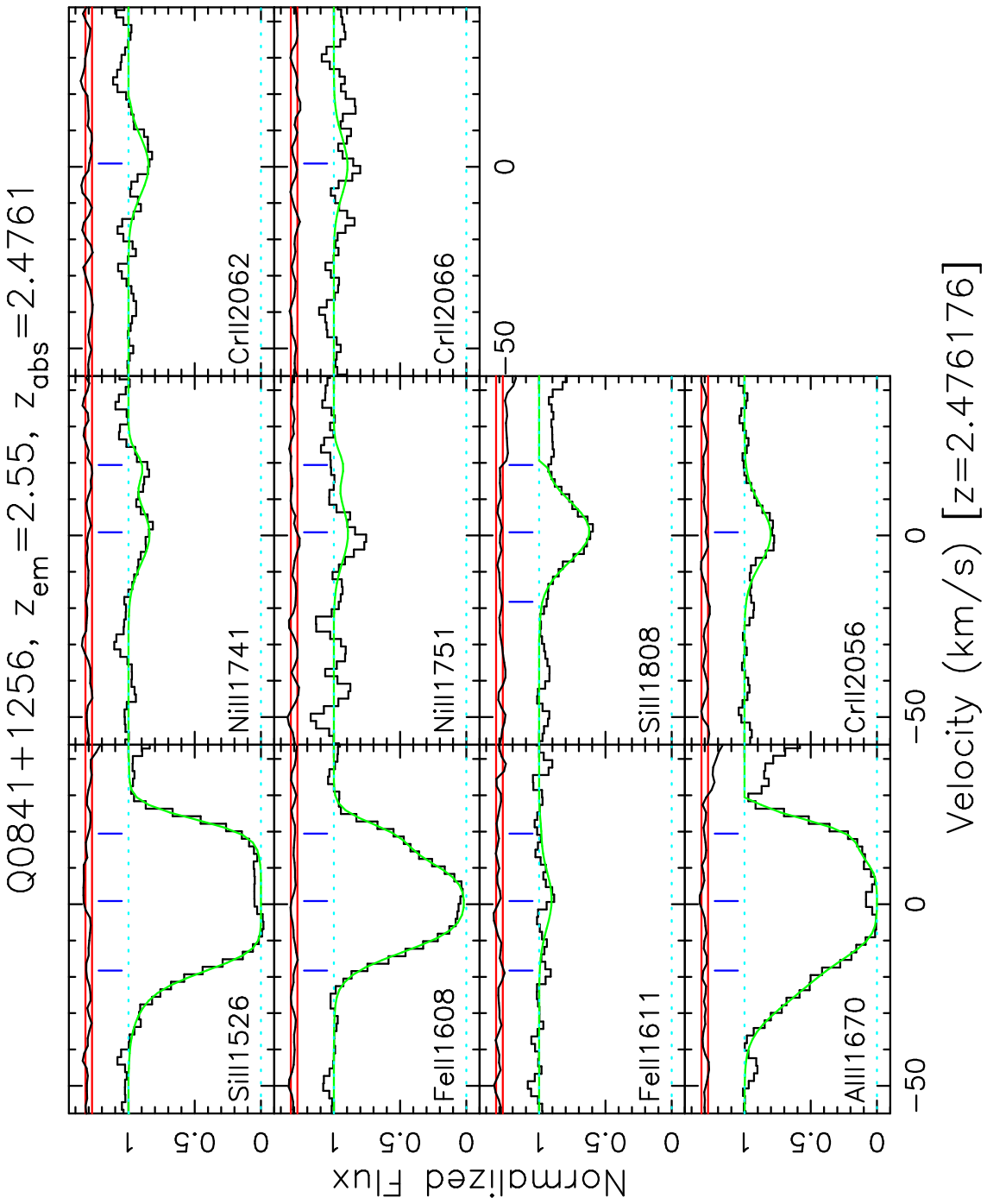

Figure C.38. Q0841+1256, $z_{\rm em} = 2.55$, $z_{\rm abs} = 2.4761$.

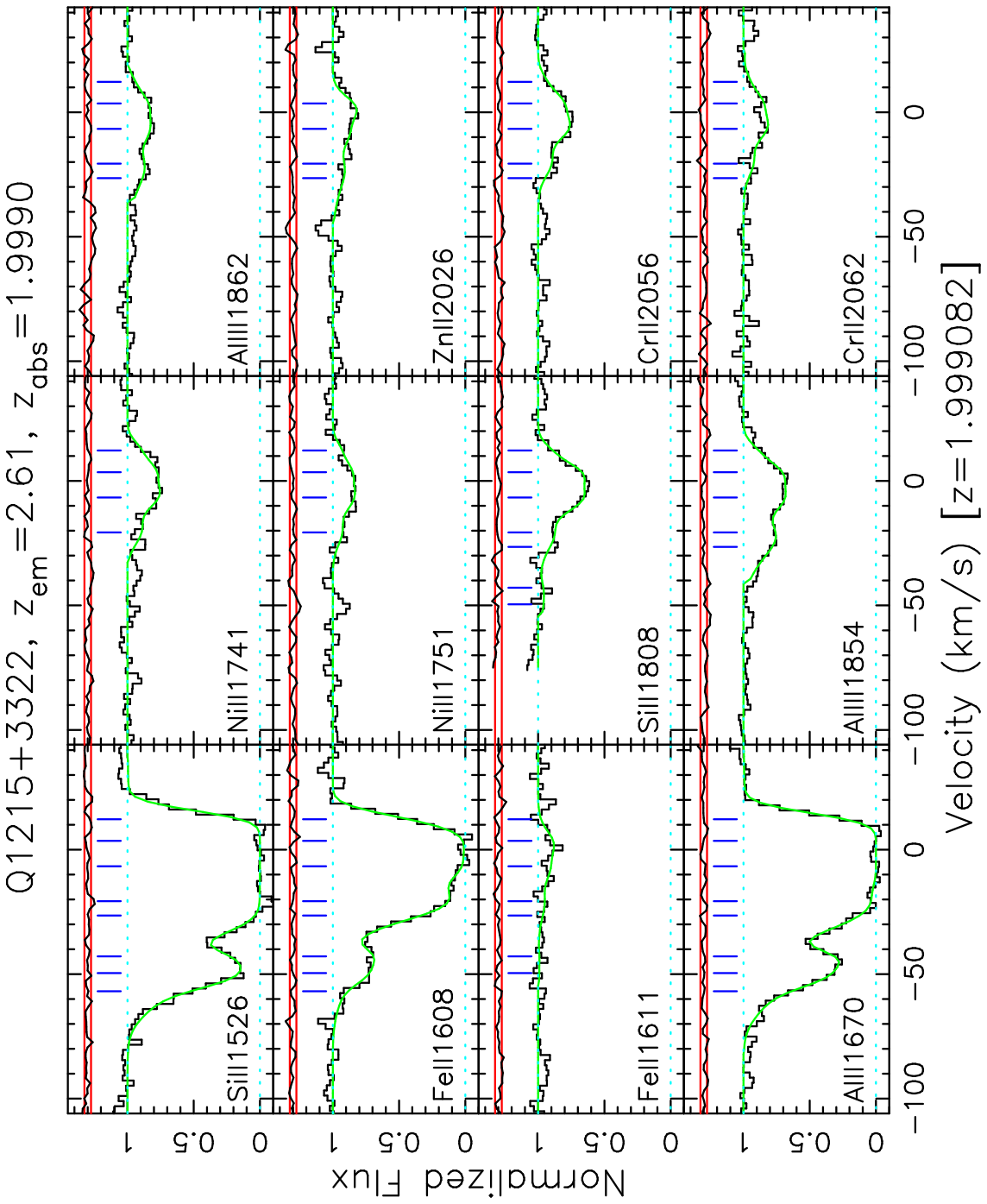

Figure C.39. Q1215+3322, $z_{\rm em} = 2.61$, $z_{\rm abs} = 1.9990$.

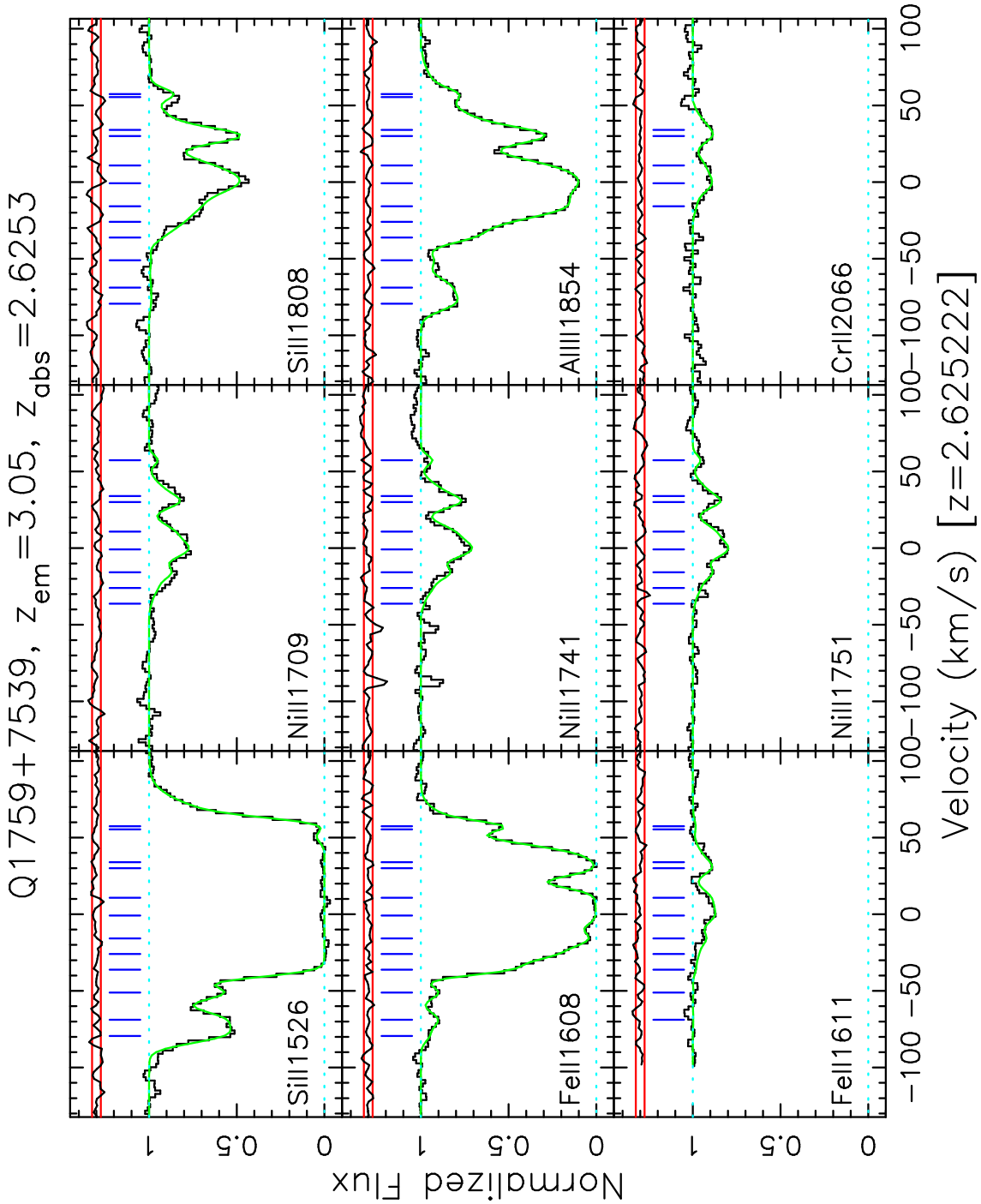

Figure C.40. Q1759+7539, $z_{\rm em} = 3.05$, $z_{\rm abs} = 2.6253$.

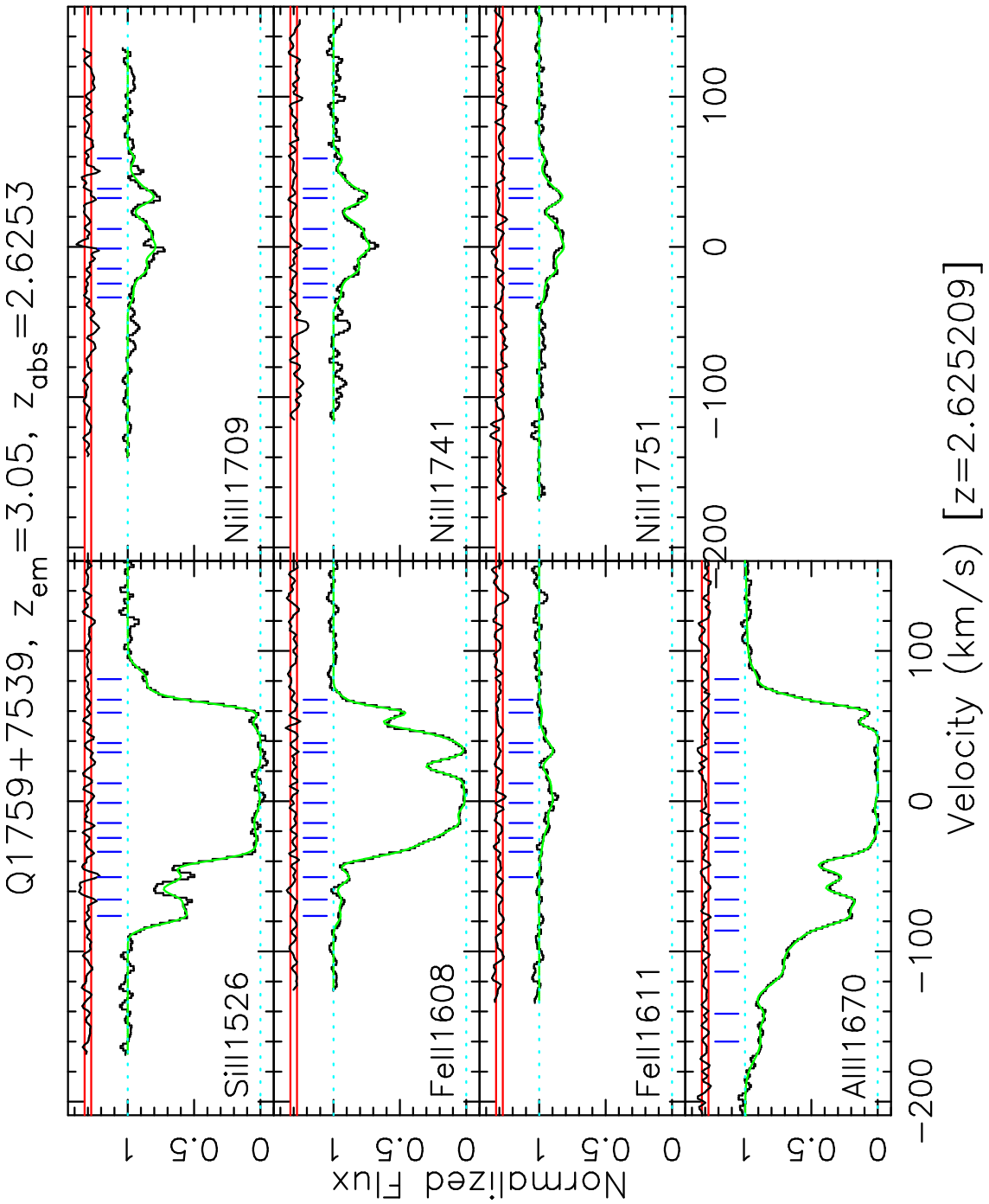

Figure C.41. Q1759+7539, $z_{\rm em} = 3.05$, $z_{\rm abs} = 2.6253$. This spectrum contributed by Outram et al. (1999).

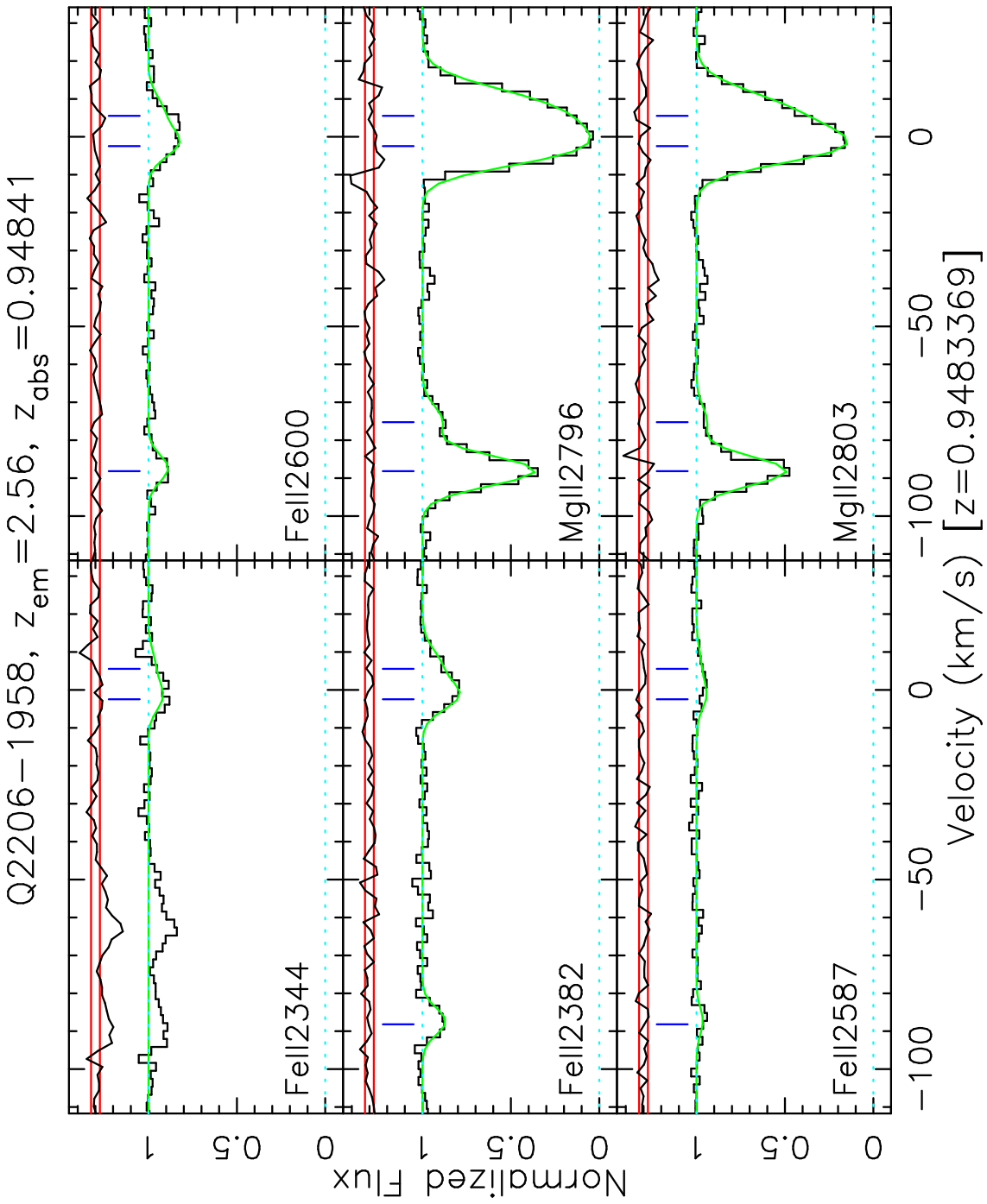

Figure C.42. Q2206−1958, $z_{\rm em} = 2.56$, $z_{\rm abs} = 0.94841$.

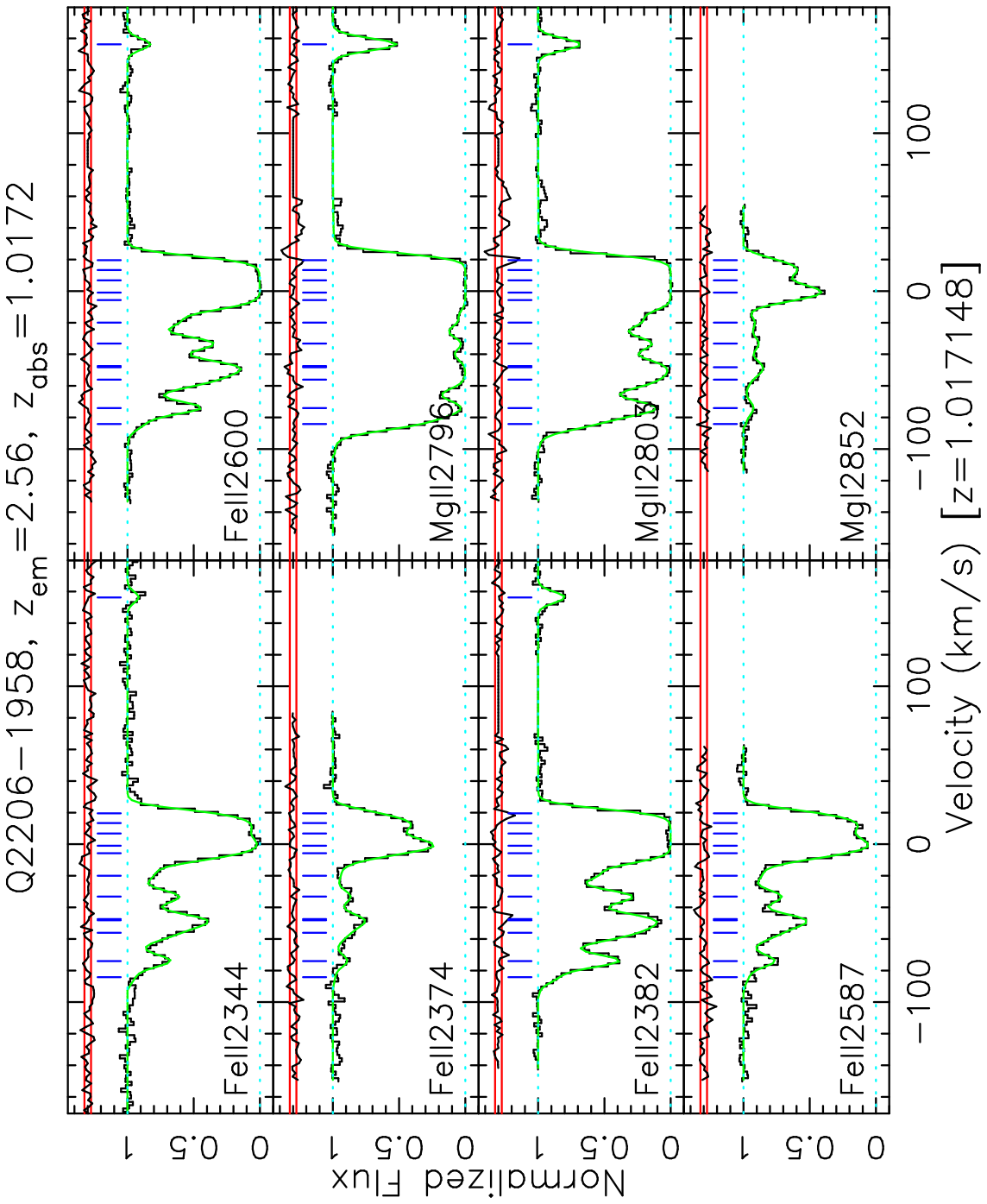

Figure C.43. Q2206−1958, $z_{\rm em} = 2.56$, $z_{\rm abs} = 1.0172$.

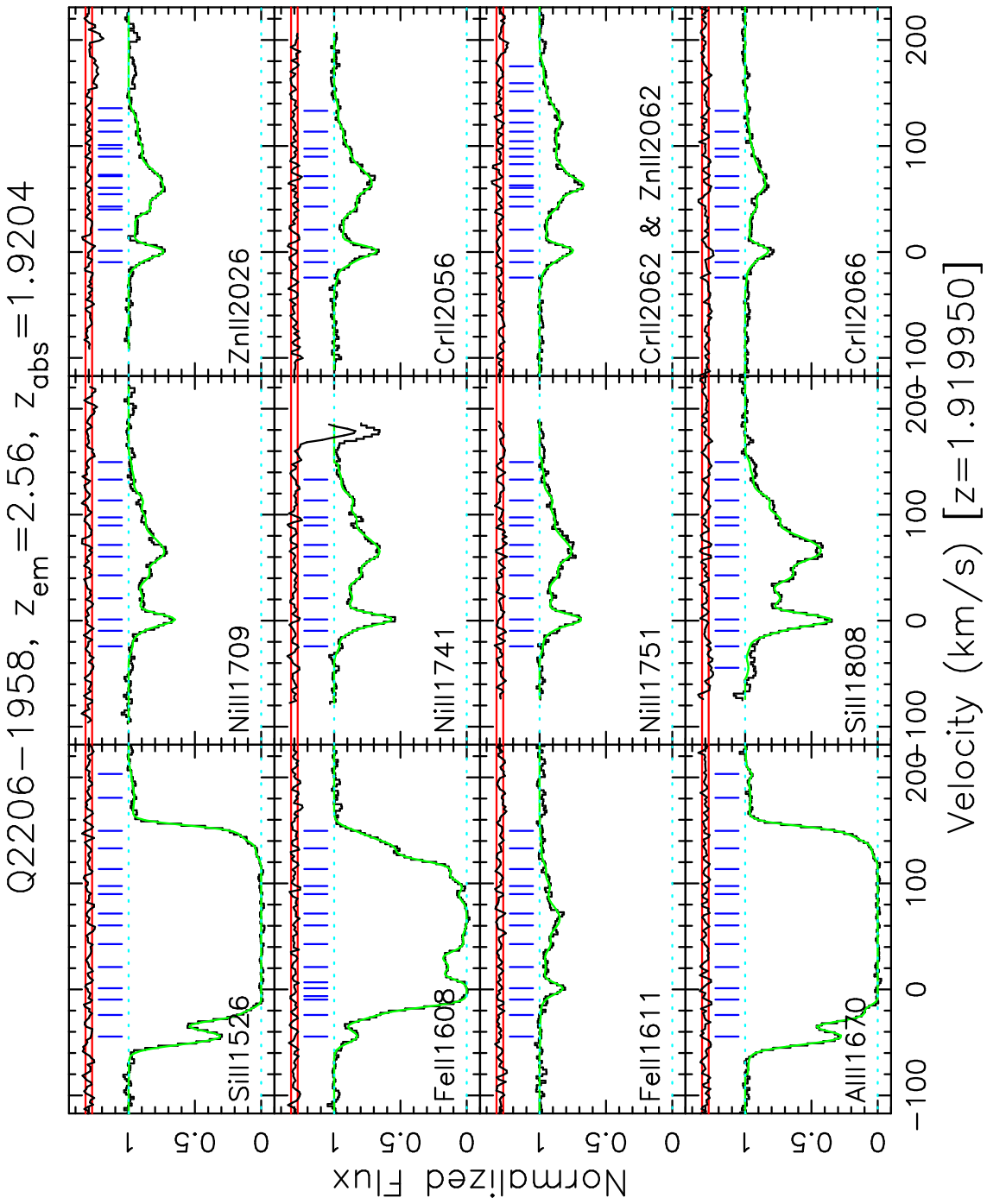

Figure C.44. Q2206−1958, $z_{\rm em} = 2.56$, $z_{\rm abs} = 1.9204$.

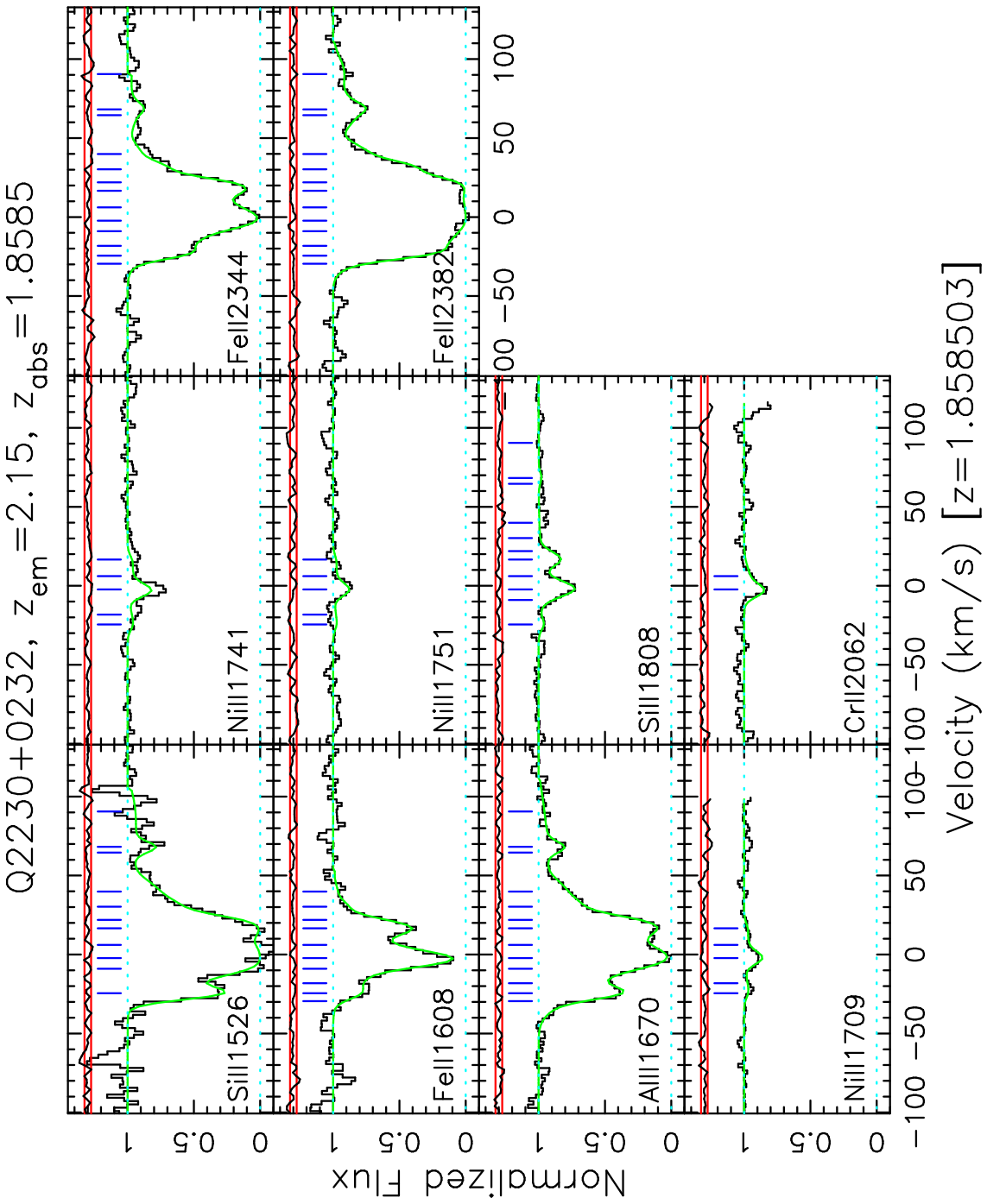

Figure C.45. Q2230+0232, $z_{\rm em} = 2.15$, $z_{\rm abs} = 1.8585$.

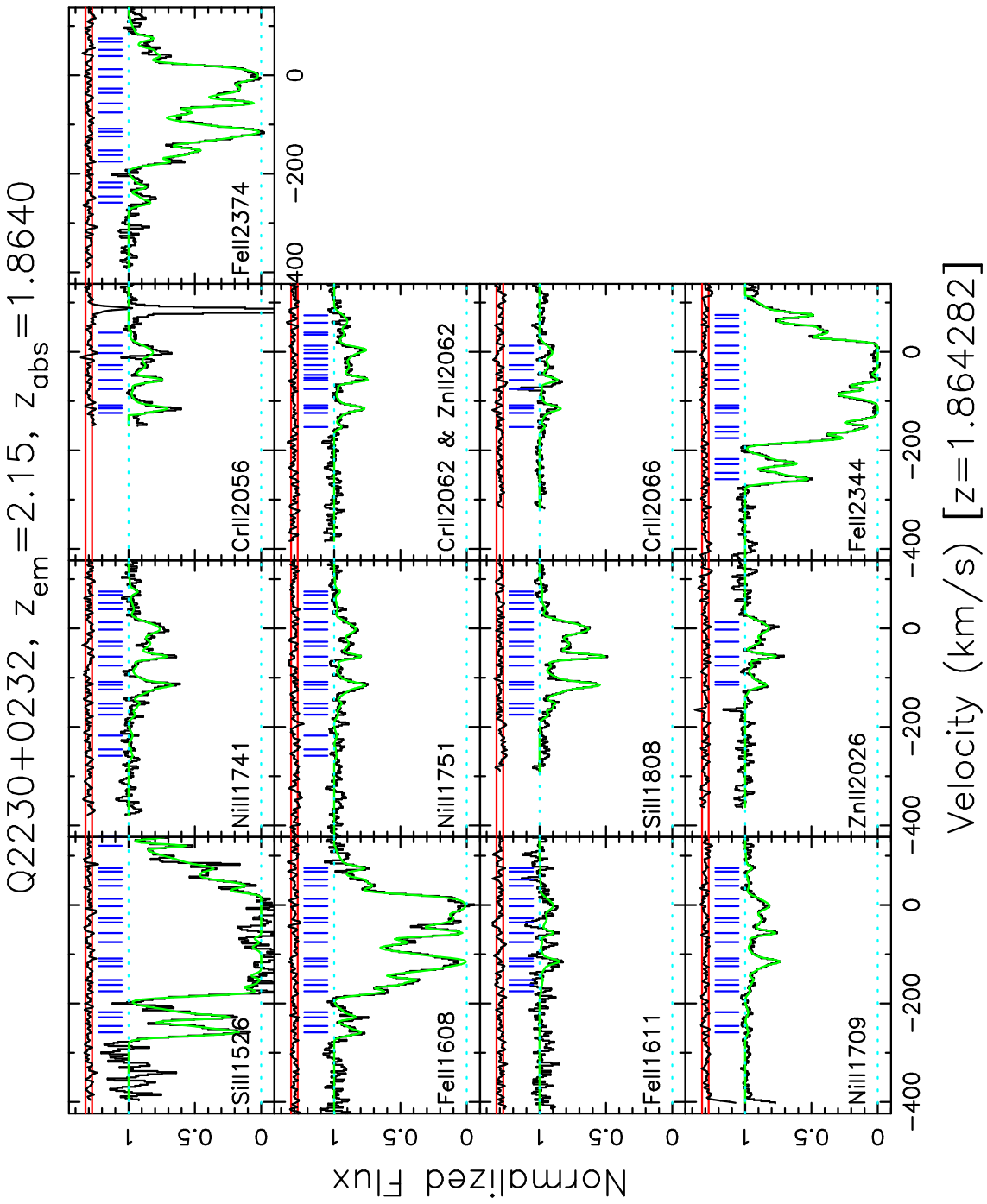

Figure C.46. Q2230+0232, $z_{\rm em} = 2.15$, $z_{\rm abs} = 1.8640$.

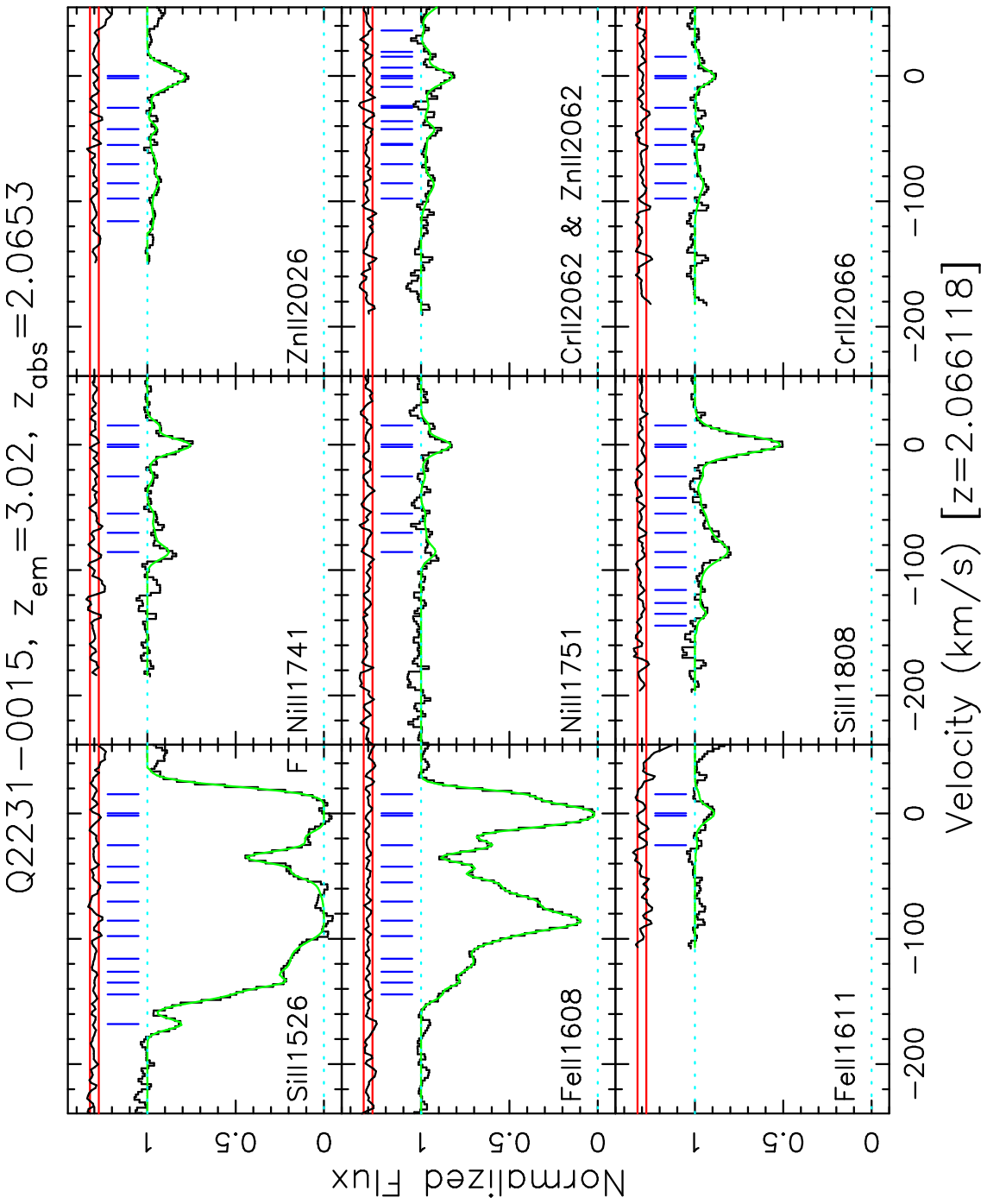

Figure C.47. Q2231−0015, $z_{\rm em} = 3.02$, $z_{\rm abs} = 2.0653$.

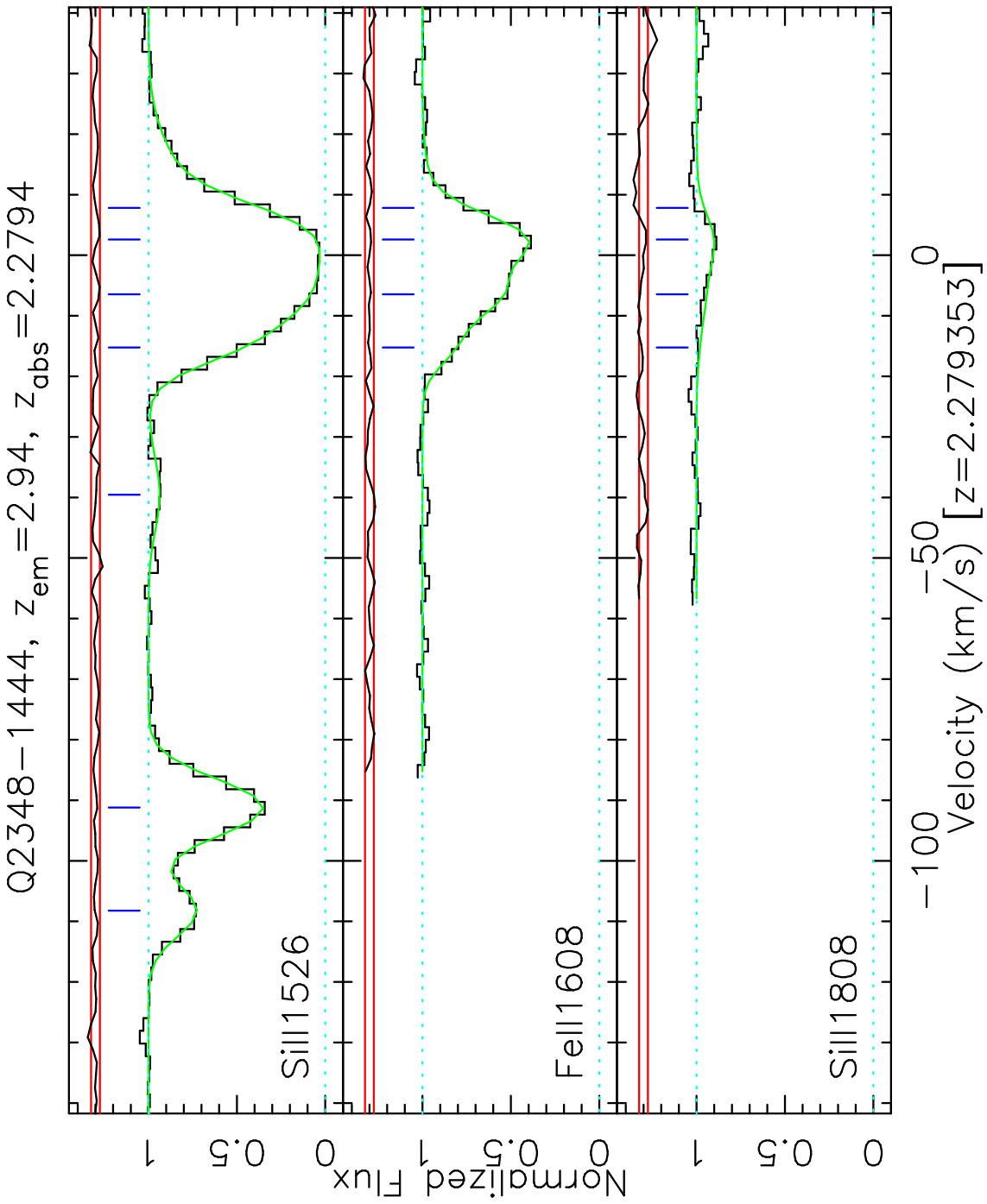

Figure C.48. Q2348−1444, $z_{\rm em} = 2.94$, $z_{\rm abs} = 2.2794$.

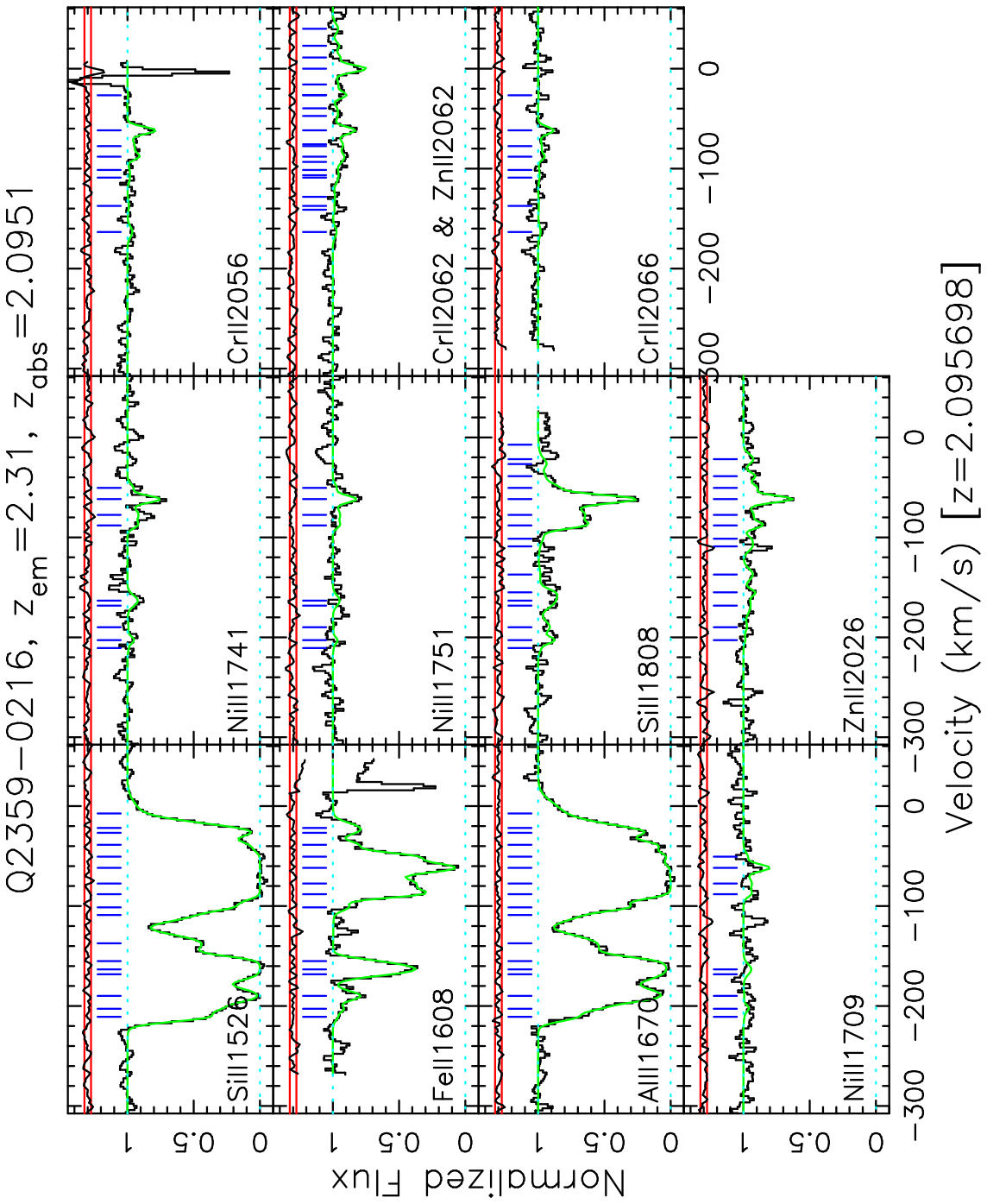

Figure C.49. Q2359−0216, $z_{\rm em} = 2.31$, $z_{\rm abs} = 2.0951$.

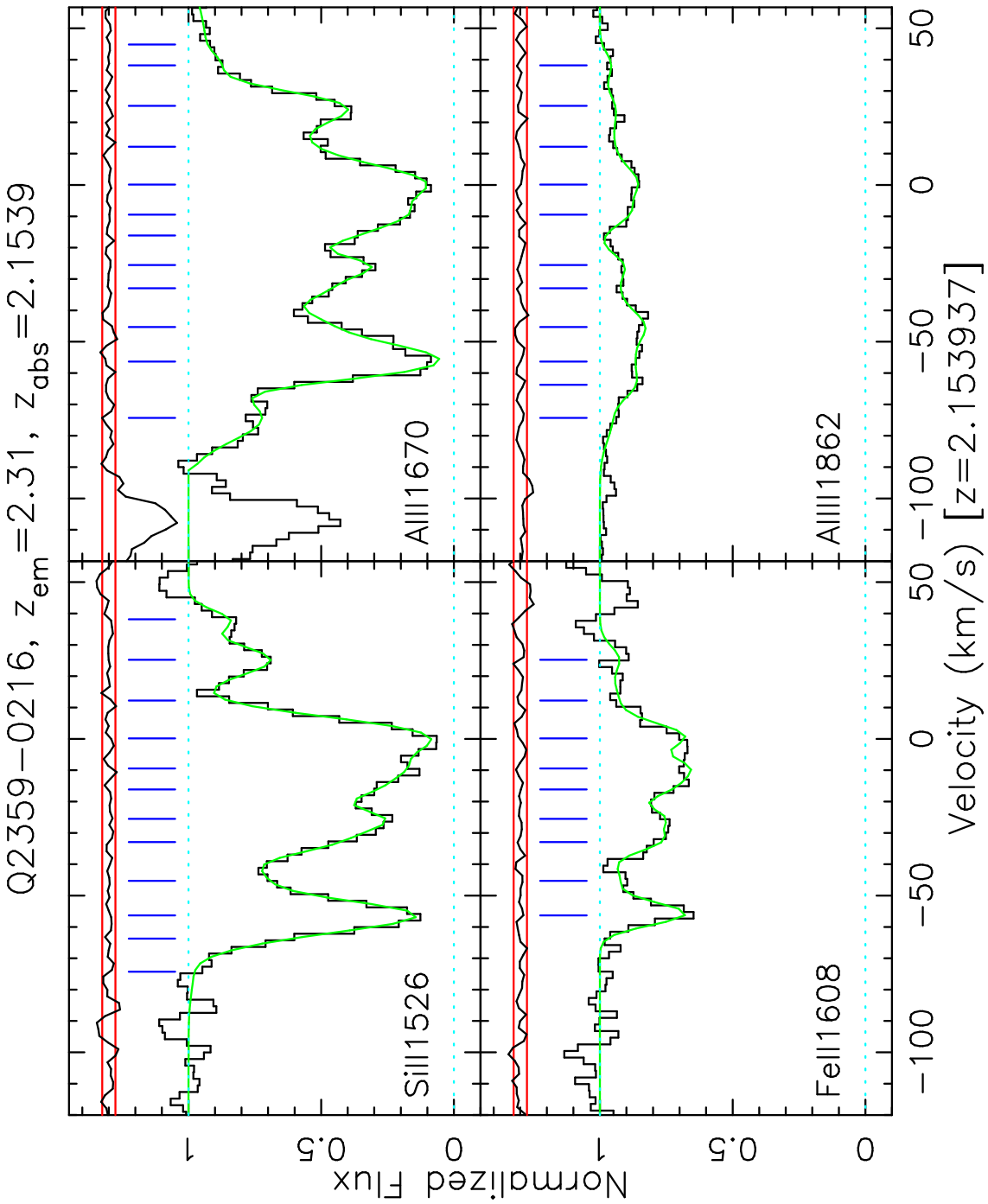

Figure C.50. Q2359−0216, $z_{\rm em} = 2.31$, $z_{\rm abs} = 2.1539$.

C-3 Sample 3

NOTE: *Plots of the absorption systems in Sample 3 are omitted in this version of the thesis since these data are yet to be published by W. L. W. Sargent and co-workers.*

References

Abgrall H., Roueff E., Launay F., Roncin J. Y., Subtil J. L., 1993a, A&AS, 101, 273

Abgrall H., Roueff E., Launay F., Roncin J. Y., Subtil J. L., 1993b, A&AS, 101, 323

Albrecht A., Magueijo J., 1999, Phys. Rev. D, 59, 043516

Andrews S. M., Meyer D. M., Lauroesch J. T., 2001, ApJ, 552, L73

Antoniadis I., Arkani-Hamed N., Dimopoulos S., Dvali G., 1998, Phys. Lett. B, 436, 257

Arkani-Hamed N., Dimopoulos S., Dvali G., 1998, Phys. Lett. B, 429, 263

Avelino P. P. et al., 2001, Phys. Rev. D, 64, 103505

Bahcall J. N., Salpeter E. E., 1965, ApJ, 142, 1677

Bahcall J. N., Sargent W. L. W., Schmidt M., 1967, ApJ, 149, L11

Barrow J. D., 1987, Phys. Rev. D, 35, 1805

Barrow J. D., 1990, in Bertotti B., Balbinot R., Bergia S., Messina A., eds, Modern Cosmology in Retrospect. Cambridge Univ. Press, Cambridge, UK, p. 67

Barrow J. D., 1996, MNRAS, 282, 1397

Barrow J. D., 1999, Phys. Rev. D, 59, 043515

Barrow J. D., 2002, From Alpha to Omega: The Constants of Nature. Jonathan Cape, London, UK

Barrow J. D., Magueijo J., 1998, Phys. Lett. B, 443, 104

Barrow J. D., Magueijo J., 1999a, Phys. Lett. B, 447, 246

Barrow J. D., Magueijo J., 1999b, Classical Quantum Gravity, 16, 1435

Barrow J. D., Magueijo J., 2000, ApJ, 532, L87

Barrow J. D., O'Toole C., 2001, MNRAS, 322, 585

Barrow J. D., Tipler F. J., 1986, The anthropic cosmological principle. Clarendon Press, Oxford, UK

Battye R. A., Crittenden R., Weller J., 2001, Phys. Rev. D, 63, 043505

Bekenstein J. D., 1979, Comments on Astrophys., 8, 89

Bekenstein J. D., 1982, Phys. Rev. D, 25, 1527

Bennett C. L. et al. 1996, ApJ, 464, L1

Bergström L., Iguri S., Rubinstein H., 1999, Phys. Rev. D, 60, 045005

Bethe H. A., Salpeter E. E., 1977, Quantum mechanics of one- and two-electron atoms. Plenum, New York, NY, USA

Biggs A. D., Browne I. W. A., Wilkinson P. N., 2001, MNRAS, 323, 995

Black J. H., Chaffee F. H., Foltz C. B., 1987, ApJ, 317, 442

Brans C., Dicke R. H., 1961, Phys. Rev., 124, 924

Briggs F. H., Wolfe A. M., Turnshek D. A., Schaeffer J., 1985, ApJ, 293, 387

Browne I. W. A., Patnaik A. R., Walsh D., Wilkinson P. N., 1993, MNRAS, 263, L32

Burbidge E. M., Lynds C. R., Burbidge G. R., 1966, ApJ, 144, 447

Cahn R. N., 1996, Rev. Mod. Phys., 68, 951

Calmet X., Fritzsch H., 2002, Euro. Phys. J. C, 24, 639

Campbell B. A., Olive K. A., 1995, Phys. Lett. B, 345, 429

Carilli C. L., Menten K. M., Reid M. J., Rupen M. P., 1997, ApJ, 474, L89

Carilli C. L., Menten K. M., Reid M. J., Rupen M. P., Yun M. S., 1998, ApJ, 494, 175

Carilli C. L. et al., 2000, Phys. Rev. Lett., 85, 5511 (C00)

Carilli C. L., Perlman E. S., Stocke J. T., 1992, ApJ, 400, L13

Carilli C. L., Rupen M. P., Yanny B., 1993, ApJ, 412, L59

Chamoun N., Landau S. J., Vucetich H., 2001, Phys. Lett. B, 504, 1

Chandrasekhar S., 1939, Nat, 139, 757

Chen H., Lanzetta K. M., Webb J. K., Barcons X., 1998, ApJ, 498, 77

Chodos A., Detweiler S., 1980, Phys. Rev. D, 21, 2167

Churchill C. W., 1997, PhD thesis, Univ. California, Santa Cruz

Churchill C. W., Le Brun V., 1998, ApJ, 499, 677

Churchill C. W., Mellon R. R., Charlton J. C., Jannuzi B. T., Kirhakos S., Steidel C. C., Schneider D. P., 2000a, ApJS, 130, 91

Churchill C. W., Mellon R. R., Charlton J. C., Jannuzi B. T., Kirhakos S., Steidel C. C., Schneider D. P., 2000b, ApJ, 543, 577

Churchill C. W. et al., 2003a, in preparation

Churchill C. W., Mellon R. R., Charlton J. C., Vogt S. S., 2003b, ApJ, submitted, preprint (astro-ph/0212120)

Churchill C. W., Rigby J. R., Charlton J. C., Vogt S. S., 1999, ApJS, 120, 51

Churchill C. W., Vogt S. S., 2001, AJ, 122, 679

Clayton M. A., Moffat J. W., 1999, Phys. Lett. B, 460, 263

Clayton M. A., Moffat J. W., 2000, Phys. Lett. B, 477, 269

Clayton M. A., Moffat J. W., 2001, Phys. Lett. B, 506, 177

Combes F., Wiklind T., 1995, A&A, 303, L61

Cowie L. L., Songaila A., 1995, ApJ, 453, 596

Cowie L. L., Songaila A., Kim T., Hu E. M., 1995, AJ, 109, 1522

Crawford I. A., Howarth I. D., Ryder S. D., Stathakis R. A., 2000, MNRAS, 319, L1

Curran S. J., Murphy M. T., Webb J. K., Pihlström Y. M., 2003, MNRAS, 340, 139

Curran S. J., Murphy M. T., Webb J. K., Rantakyrö F., Johansson L. E. B., Nikolić S., 2002a, A&A, 394, 763

Curran S. J., Webb J. K., Murphy M. T., Bandiera R., Corbelli E., Flambaum V. V., 2002b, Publ. Astron. Soc. Austral., 19, 455

Curran S. J., Webb J. K., Murphy M. T., Carswell R. F., 2003b, in preparation

Damour T., Dyson F., 1996, Nucl. Phys. B, 480, 37

Damour T., Polyakov A. M., 1994, Nucl. Phys. B, 423, 532

Davé R., Hernquist L., Katz N., Weinberg D. H., 1999, ApJ, 511, 521

Dent T., Fairbairn M., 2003, Nucl. Phys. B, 653, 256

Dicke R. H., 1957, Rev. Mod. Phys., 29, 355

Dicke R. H., 1961, Nat, 192, 440

Dicke R. H., 1962, Phys. Rev., 125, 2163

Dirac P. A. M., 1937, Nat, 139, 323

Drinkwater M. J., Webb J. K., Barrow J. D., Flambaum V. V., 1998, MNRAS, 295, 457 (D98)

Drullinger R. E., Wineland D. J., Bergquist J. C., 1980, Appl. Phys., 22, 365

Duff M. J., Okun L. B., Veneziano G., 2002, J. High Energy Phys., 2002, 023

Dyson F. J., 1967, Phys. Rev. Lett., 19, 1291

Dyson F. J., 1972, in Salam A., Wigner E. P., eds, Aspects of Quantum Theory. Cambridge Univ. Press, Cambridge, UK, p. 213

Dzuba V. A., Flambaum V. V., Kozlov M. G., Marchenko M., 2002, Phys. Rev. A, 66, 022501

Dzuba V. A., Flambaum V. V., Murphy M. T., Webb J. K., 2001a, in Karshenboim S. G., Pavone F. S., Bassani G. F., Inguscio M., Hänsch T. W., eds, Lecture Notes in Physics Vol. 570, The Hydrogen Atom: Precision Physics of Simple Atomic Systems. Springer-Verlag, Berlin, Germany, p. 564

Dzuba V. A., Flambaum V. V., Murphy M. T., Webb J. K., 2001b, Phys. Rev. A, 63, 42509

Dzuba V. A., Flambaum V. V., Webb J. K., 1999a, Phys. Rev. A, 59, 230

Dzuba V. A., Flambaum V. V., Webb J. K., 1999b, Phys. Rev. Lett., 82, 888

Edlen B., 1953, J. Opt. Soc. Am., 43, 339

Edlen B., 1966, Metrologia, 2, 71

Essen L., Donaldson R. W., Bangham M. J., Hope E. G., 1971, Nat, 229, 110

Feretti L., Dallacasa D., Govoni F., Giovannini G., Taylor G. B., Klein U., 1999, A&A, 344, 472

Fernandez-Soto A., Lanzetta K. M., Barcons X., Carswell R. F., Webb J. K., Yahil A., 1996, ApJ, 460, L85

Filippenko A. V., 1982, PASP, 94, 715

Finn G. D., Mugglestone D., 1965, MNRAS, 129, 221

Fisher R. A., 1958, Statistical Methods for Research Workers. Harper, New York, NY, USA

Flambaum V. V., Shuryak E. V., 2002, Phys. Rev. D, 65, 103503

Flowers J. L., Petley B. W., 2001, Rep. Prog. Phys., 64, 1191

Foltz C. B., Chaffee F. H., Black J. H., 1988, ApJ, 324, 267

Forgács P., Horváth Z., 1979, Gen. Relativ. Gravitation, 11, 205

Freund P. G. O., 1982, Nucl. Phys. B, 209, 146

Fujii Y., Iwamoto A., Fukahori T., Ohnuki T., Nakagawa M., Hidaka H., Oura Y., Möller P., 2000, Nucl. Phys. B, 573, 377

Gaillard M. K., Grannis P. D., Sciulli F. J., 1999, Rev. Mod. Phys., 71, 96

Gamow G., 1967, Phys. Rev. Lett., 19, 913

Gay P. L., Lambert D. L., 2000, ApJ, 533, 260

Ge J., Bechtold J., 1997, ApJ, 477, L73

Ge J., Bechtold J., 1999, in Carilli C. L., Radford S. J. E., Menten K. M., Langstom G. I., eds, ASP Conf. Ser. Vol. 156, Highly Redshifted Radio Lines. Astron. Soc. Pac., San Francisco, CA, U.S.A, p. 121

Ge J., Bechtold J., Kulkarni V. P., 2001, ApJ, 547, L1

Gill P. E., Murray W., Wright M. H., 1981, Practical optimization. Academic Press, London, UK

Griesmann U., Kling R., 2000, ApJ, 536, L113

Gunn J. E., Peterson B. A., 1965, ApJ, 142, 1633

Haehnelt M. G., Steinmetz M., Rauch M., 1998, ApJ, 495, 647

Haldane J. B. S., 1937a, Nat, 139, 1002

Haldane J. B. S., 1937b, Nat, 158, 555

Hallstadius L., 1979, Z. Phys. A, 291, 203

Hannestad S., 1999, Phys. Rev. D, 60, 023515

Harris D. L., 1948, ApJ, 108, 112

Hazard C., 1963, MNRAS, 126, 489

Herbig G. H., 1975, ApJ, 196, 129

Hogan C. J., 2000, Rev. Mod. Phys., 72, 1149

Hořava P., 1996, Phys. Rev. D, 54, 7561

Hořava P., Witten E., 1996, Nucl. Phys. B, 475, 94

Humlíček J., 1979, J. Quant. Spectrosc. Radiat. Transfer, 21, 309

Humlíček J., 1982, J. Quant. Spectrosc. Radiat. Transfer, 27, 437

Hummer D. G., 1965, MNRAS, 70, 1

Ivanchik A. V., Potekhin A. Y., Varshalovich D. A., 1999, A&A, 343, 439

Ivanchik A. V., Rodriguez E., Petitjean P., Varshalovich D. A., 2002, Astron. Lett., 28, 423

Ivanchik A. V., Rodriguez E., Petitjean P., Varshalovich D. A., 2003, in Martins C. J. A. P., ed., The cosmology of extra dimensions and varying fundamental constants. Kluwer, Netherlands

Jenkins E. B., Peimbert A., 1997, ApJ, 477, 265

Jenkins E. B., Woźniak P. R., Sofia U. J., Sonneborn G., Tripp T. M., 2000, ApJ, 538, 275

Jenniskens P., Desert F.-X., 1994, A&AS, 106, 39

Jordan P., 1937, Naturwiss., 25, 513

Jordan P., 1939, Z. Phys., 113, 660

Kaluza T., 1921, Preuss. Akad. Wiss. K, 1, 966

Kaplinghat M., Scherrer R. J., Turner M. S., 1999, Phys. Rev. D, 60, 023516

Kelly R. L., 1987, J. Phys. Chem. Ref. Data Suppl., 16, 1

Klein O., 1926, Z. Phys., 37, 895

Kolb E. W., Perry M. J., Walker T. P., 1986, Phys. Rev. D, 33, 869

Kothari D. S., 1938, Nat, 142, 354

Kujat J., Scherrer R. J., 2000, Phys. Rev. D, 62, 023510

Kupka F., Piskunov N., Ryabchikova T. A., Stempels H. C., Weiss W. W., 1999, A&AS, 138, 119

Landau L. D., 1955, in Pauli W., ed., Neils Bohr and the Development of Physics. McGraw-Hill, New York, NY, USA, p. 52

Landau S. J., Harari D. D., Zaldarriaga M., 2001, Phys. Rev. D, 63, 083505

Landau S. J., Vucetich H., 2002, ApJ, 570, 463

Langacker P., Segrè G., Strassler M. J., 2002, Phys. Lett. B, 528, 121

Lanzetta K. M., Bowen D. V., 1992, ApJ, 391, 48

Lanzetta K. M., Bowen D. V., Tytler D., Webb J. K., 1995, ApJ, 442, 538

Lauroesch J. T., Meyer D. M., Blades J. C., 2000, ApJ, 543, L43

Le Brun V., Bergeron J., 1998, A&A, 332, 814

Le Brun V., Bergeron J., Boisse P., 1996, A&A, 306, 691

Ledoux C., Srianand R., Petitjean P., 2002, A&A, 392, 781

Levshakov S. A., Dessauges-Zavadsky M., D'Odorico S., Molaro P., 2002a, MNRAS, 333, 373

Levshakov S. A., Dessauges-Zavadsky M., D'Odorico S., Molaro P., 2002b, ApJ, 565, 696

Levshakov S. A., Molaro P., Centurión M., D'Odorico S., Bonifacio P., Vladilo G., 2000, A&A, 361, 803

Levy-Leblond J. M., 1979, in Toraldo di Francini G., ed., Proc. Enrco Fermi Int. School Phys. Vol. 52, Problems in the foundations of physics. Elsevier, Netherlands, p. 237

Li L., Gott J. R. III, 1998, Phys. Rev. D, 58, 103513

Lineweaver C. H., Tenorio L., Smoot G. F., Keegstra P., Banday A. J., Lubin P., 1996, ApJ, 470, 38

Liske J., 2003, A&A, 398, 429

Litzen U., Brault J. W., Thorne A. P., 1993, Phys. Scr., 47, 628

Livio M., Stiavelli M., 1998, ApJ, 507, L13

Lopez S., Reimers D., Rauch M., Sargent W. L. W., Smette A., 1999, ApJ, 513, 598

Lu L., Sargent W. L. W., Barlow T. A., Churchill C. W., Vogt S. S., 1996, ApJS, 107, 475

Lu L., Sargent W. L. W., Womble D. S., Takada-Hidai M., 1996, ApJ, 472, 509

Lynds R., 1971, ApJ, 164, L73

Maeda K. I., 1988, Mod. Phys. Lett. A, 3, 242

Magueijo J., 2000, Phys. Rev. D, 62, 103521

Magueijo J., Barrow J. D., Sandvik H. B., 2002, Phys. Lett. B, 549, 284

Maller A., Somerville R. S., Prochaska J. X., Primack J. R., 1999, in Bunker A. J., van Breugel W. J. M., eds, ASP Conf. Ser. Vol. 193, The Hy-Redshift Universe: Galaxy Formation and Evolution at High Redshift. Astron. Soc. Pac., San Francisco, CA, U.S.A, p. 608

Marciano W. J., 1984, Phys. Rev. Lett., 52, 489

Marcy G. W., Butler R. P., 1992, PASP, 104, 270

Martin W. C., Zalubas R., 1983, J. Phys. Chem. Ref. Data, 12, 323

Martins C. J. A. P., ed., 2003, Proceedings of JENAM2002, The cosmology of extra dimensions and varying fundamental constants. Kluwer, Netherlands

Martins C. J. A. P., Melchiorri A., Trotta R., Bean R., Rocha G., Avelino P. P., Viana P. T. P., 2002, Phys. Rev. D, 66, 023505

Maurette M., 1976, Annu. Rev. Nuc. Sci., 26, 319

McDonald P., Miralda-Escudé J., 1999, ApJ, 519, 486

Menten K. M., Reid M. J., 1996, ApJ, 465, L99

Mills I., Cvitas T., Homann K., Kallay N., Kuchitsu K., 1988, in Quantities, Units

and Symbols in Physical Chemistry. Blackwell Scientific Publications, Oxford, UK

Milne E. A., 1935, Relativity, Gravitation and World Structure. Clarendon Press, Oxford, UK

Milne E. A., 1937, Proc. R. Soc. A, 158, 324

Miralda-Escude J., Cen R., Ostriker J. P., Rauch M., 1996, ApJ, 471, 582

Moffat J., 1993, Int. J. Mod. Phys. D, 2, 351

Mohr P. J., Taylor B. N., 2000, Rev. Mod. Phys., 72, 351

Molaro P., Bonifacio P., Centurión M., D'Odorico S., Vladilo G., Santin P., Di Marcantonio P., 2000, ApJ, 541, 54

Molaro P., Levshakov S. A., D'Odorico S., Bonifacio P., Centurión M., 2001, ApJ, 549, 90

Monaghan J. J., 1971, MNRAS, 152, 509

Moore C. E., 1971, Atomic Energy Levels as Derived from Analyses of Optical Spectra. Natl. Stand. Rel. Data Ser. Vol. 1–3, Natl. Bur. Stand. (USA), US Govt. Printing Office, Washington DC, USA

Morton D. C., 1991, ApJS, 77, 119

Morton D. C., 1992, ApJS, 81, 883

Morton D. C., Dinerstein H. L., 1976, ApJ, 204, 1

Murphy M. T., Curran S. J., Webb J. K., 2003b, MNRAS, 342, 830

Murphy M. T., Webb J. K., Flambaum V. V., 2003c, MNRAS, accepted, preprint (astro-ph/0306483)

Murphy M. T., Webb J. K., Flambaum V. V., Churchill C. W., Prochaska J. X., 2001b, MNRAS, 327, 1223

Murphy M. T., Webb J. K., Flambaum V. V., Curran S. J., 2002, in Dong S., Burchat P., eds, Proceedings of the XXII Physics in Collision Conference. Stanford, CA, U.S.A, p. 116

Murphy M. T., Webb J. K., Flambaum V. V., Curran S. J., 2003a, Ap&SS, 283, 577

Murphy M. T., Webb J. K., Flambaum V. V., Drinkwater M. J., Combes F., Wiklind T., 2001d, MNRAS, 327, 1244

Murphy M. T., Webb J. K., Flambaum V. V., Dzuba V. A., Churchill C. W., Prochaska J. X., Barrow J. D., Wolfe A. M., 2001a, MNRAS, 327, 1208

Murphy M. T., Webb J. K., Flambaum V. V., Prochaska J. X., Wolfe A. M., 2001c, MNRAS, 327, 1237

Nagourney W., Dehmelt H. G., 1981, Bull. Am. Phys. Soc., 26, 805

Naudet R., 1974, Bull. Inf. Sci. Tech., 193, 1

Nave G., Learner R. C. M., Thorne A. P., Harris C. J., 1991, J. Opt. Soc. Am. B, 8, 2028

Nollett K. M., Lopez R. E., 2002, Phys. Rev. D, 66, 063507

Norlén G., 1973, Phys. Scr., 8, 249

Nulsen P. E. J., Barcons X., Fabian A. C., 1998, MNRAS, 301, 168

O'Dea C. P., Baum S. A., Stanghellini C., Dey A., van Breugel W., Deustua S., Smith E. P., 1992, AJ, 104, 1320

Olive K. A., Pospelov M., Qian Y.-Z., Coc A., Cassé M., Vangiona-Flam E., 2002, Phys. Rev. D, 66, 045022

Outram P. J., Carswell R. F., Theuns T., 2000, ApJ, 529, L73

Outram P. J., Chaffee F. H., Carswell R. F., 1999, MNRAS, 310, 289

Pagel B. E. J., 1977, MNRAS, 179, 81P

Palmer B. A., Engleman R., 1983, Technical report, Atlas of the Thorium spectrum. Los Alamos National Laboratory, NM, USA

Patnaik A. R., Browne I. W. A., King L. J., Muxlow T. W. B., Walsh D., Wilkinson P. N., 1993, MNRAS, 261, 435

Peacock J. A., 1999, Cosmological physics. Cambridge Univ. Press, Cambridge, UK

Peck E. R., Reeder K., 1972, J. Opt. Soc. Am., 62, 958

Peebles P. J., Dicke R. H., 1962, Phys. Rev., 128, 2006

Peebles P. J. E., 1993, Principles of physical cosmology. Princeton Univ. Press,

Princeton, NJ, USA

Perlman E. S., Carilli C. L., Stocke J. T., Conway J., 1996, AJ, 111, 1839

Petitjean P., Rauch M., Carswell R. F., 1994, A&A, 291, 29

Petitjean P., Srianand R., Ledoux C., 2000, A&A, 364, L26

Petitjean P., Srianand R., Ledoux C., 2002, MNRAS, 332, 383

Petrov Y. V., 1977, Sov. Phys. Uspekhi, 20, 937

Pettini M., King D. L., Smith L. J., Hunstead R. W., 1997, ApJ, 478, 536

Pickering J. C., Donnelly M. P., Nilsson H., Hibbert A., Johansson S., 2002, A&A, 396, 715

Pickering J. C., Thorne A. P., Murray J. E., Litzén U., Johansson S., Zilio V., Webb J. K., 2000, MNRAS, 319, 163

Pickering J. C., Thorne A. P., Webb J. K., 1998, MNRAS, 300, 131

Pickett H. M., Poynter R. L., Cohen E. A., Delitsky M. L., Pearson J. C., Muller H. S. P., 1998, J. Quant. Spectrosc. Radiat. Transfer, 60, 883

Piskunov N. E., Kupka F., Ryabchikova T. A., Weiss W. W., Jeffery C. S., 1995, A&AS, 112, 525

Poppe G. P. M., Wijers C. M. J., 1990, Trans. Math. Software, 16, 38

Potekhin A. Y., Ivanchik A. V., Varshalovich D. A., Lanzetta K. M., Baldwin J. A., Williger G. M., Carswell R. F., 1998, ApJ, 505, 523

Prestage J. D., Tjoelker R. L., Maleki L., 1995, Phys. Rev. Lett., 74, 3511

Price R. J., Crawford I. A., Barlow M. J., 2000, MNRAS, 312, L43

Prochaska J. X., 2003, ApJ, 582, 49

Prochaska J. X., Wolfe A. M., 1996, ApJ, 470, 403

Prochaska J. X., Wolfe A. M., 1997, ApJ, 474, 140

Prochaska J. X., Wolfe A. M., 1999, ApJS, 121, 369

Prochaska J. X., Wolfe A. M., 2000, ApJ, 533, L5

Prochaska J. X. et al., 2001, ApJS, 137, 21

Randall L., Sundrum R., 1999a, Phys. Rev. Lett., 83, 3370

Randall L., Sundrum R., 1999b, Phys. Rev. Lett., 83, 4690

Rao S. M., Turnshek D. A., 2000, ApJS, 130, 1

Rauch M., 1998, ARA&A, 36, 267

Riazuelo A., Uzan J., 2002, Phys. Rev. D, 66, 023525

Rosman K. J. R., Taylor P. D. P., 1998, J. Phys. Chem. Ref. Data, 27, 1275

Safronova M. S., Johnson W. R., 2001, Phys. Rev. A, 64, 52501

Sandvik H. B., Barrow J. D., Magueijo J., 2002, Phys. Rev. Lett., 88, 31302

Savedoff M. P., 1956, Nat, 178, 689

Schaye J., 2001, ApJ, 559, L1

Schmidt M., 1963, Nat, 197, 1040

Shlyakhter A. I., 1976, Nat, 264, 340

Sievers J. L. et al., 2002, ApJ, submitted, preprint (astro-ph/0205387)

Smoot G. F. et al., 1992, ApJ, 396, L1

Sommerfeld A., 1911, Z. Phys., 12, 1057

Songaila A., Cowie L. L., 1996, AJ, 112, 335

Songaila A. et al., 1994, Nat, 371, 43

Sortais Y. et al., 2001, Phys. Scr., T95, 50

Srianand R., Petitjean P., 1998, A&A, 335, 33

Srianand R., Petitjean P., Ledoux C., 2000, Nat, 408, 931

Stockton A. N., Lynds C. R., 1966, ApJ, 144, 451

Struve O., Elvey C. T., 1934, ApJ, 79, 409

Teller E., 1948, Phys. Rev., 73, 801

Theuns T., Leonard A., Efstathiou G., 1998a, MNRAS, 297, L49

Theuns T., Leonard A., Efstathiou G., Pearce F. R., Thomas P. A., 1998b, MNRAS, 301, 478

Thompson R. I., 1975, Astron. Lett., 16, 3

Timmes F. X., Clayton D. D., 1996, ApJ, 472, 723

Tripp T. M., Lu L., Savage B. D., 1998, ApJ, 508, 200

Tubbs A. D., Wolfe A. M., 1980, ApJ, 236, L105

Uzan J., 2003, Rev. Mod. Phys., 75, 403

Valenti J. A., Butler R. P., Marcy G. W., 1995, PASP, 107, 966

Varshalovich D. A., Levshakov S. A., 1993, J. Exp. Theor. Phys. Lett., 58, 237

Varshalovich D. A., Panchuk V. E., Ivanchik A. V., 1996, Astron. Lett., 22, 6

Varshalovich D. A., Potekhin A. Y., 1995, Space Sci. Rev., 74, 259

Varshalovich D. A., Potekhin A. Y., 1996, Astron. Lett., 22, 1 (VP96)

Varshalovich D. A., Potekhin A. Y., Ivanchik A. V., 2000, in Dunford R. W., Gemmel D. S., Kanter E. P., Kraessig B., Southworth S. H., Young L., eds, AIP Conf. Proc. Vol. 506, X-Ray and Inner-Shell Processes. Argonne National Laboratory, Argonne, IL, USA, p. 503 (VPI00)

Vogt S. S. et al., 1994, in Crawford D. L., Craine E. R., eds, Proc. SPIE Vol. 2198, Instrumentation in Astronomy VIII. p. 362

Walker M., Wardle M., 1998, ApJ, 498, L125

Weast R. C., 1979, Handbook of Chemistry and Physics, 60th edn. CRC Press, Boca Raton, FL, USA

Webb J. K., 1987, PhD thesis, Univ. Cambridge

Webb J. K., Flambaum V. V., Churchill C. W., Drinkwater M. J., Barrow J. D., 1999, Phys. Rev. Lett., 82, 884 (W99)

Webb J. K., Murphy M. T., Flambaum V. V., 2003, in preparation

Webb J. K., Murphy M. T., Flambaum V. V., Curran S. J., 2003, Ap&SS, 283, 565

Webb J. K., Murphy M. T., Flambaum V. V., Dzuba V. A., Barrow J. D., Churchill C. W., Prochaska J. X., Wolfe A. M., 2001, Phys. Rev. Lett., 87, 091301

Weinberg S., 1983, Phil. Trans. R. Soc. London, 310, 249

Wells R. J., 1999, J. Quant. Spectrosc. Radiat. Transfer, 62, 29

Whaling W., Anderson W. H. C., Carle M. T., Brault J. W., Zarem H. A., 1995, J.

Quant. Spectrosc. Radiat. Transfer, 53, 1

Wheeler J. A., 1980, in Woolf H., ed., Some strangeness in the proportion. Addison-Wesley, London, UK, p. 341

Wiklind T., Combes F., 1994, A&A, 286, L9

Wiklind T., Combes F., 1995, A&A, 299, 382

Wiklind T., Combes F., 1996, A&A, 315, 86

Wiklind T., Combes F., 1997, A&A, 328, 48

Wiklind T., Combes F., 1998, ApJ, 500, 129

Wolfe A. M., Brown R. L., Roberts M. S., 1976, Phys. Rev. Lett., 37, 179

Wolfe A. M., Davis M. M., 1979, AJ, 84, 699

Wolfe A. M., Prochaska J. X., 2000, ApJ, 545, 603

Wu Y., Wang Z., 1986, Phys. Rev. Lett., 57, 1978